THE UNIVERSITY *of* EDINBURGH

Assessment of DNA Degradation in Live Spermatozoon using Laser Tweezers Raman Microspectrometry

Ruby Raheem-Kizchery

A thesis submitted for the degree of
Doctor of Philosophy

The University of Edinburgh
June 2012

Declaration

I declare that this thesis is an original report of my research, has been written by me and has not been submitted for any previous degree. The experimental work is almost entirely my own work; the collaborative contributions have been indicated clearly and acknowledged. Due references have been provided on all supporting literatures and resources.

Name: Ruby Raheem-Kizchery **Date**: 30th June 2012

Abstract

Purpose: Sperm nuclear proteins and DNA integrity have been implicated in infertility and treatment failures. High stallion to stallion variability is observed in sperm cryopreservation protocols. The cells are destroyed with harsh chemicals prior to using biochemical assays to test sperm DNA quality. The feasibility of using Raman spectrometry in combination with a laser trap for non-destructive micromanipulation and characterization of DNA damage in motile stallion and human sperm is experimentally investigated in this thesis.

Methods: Live stallion sperms were subjected to controlled cellular damage: (a) four grades of chemically induced oxidative stress using Xanthine – Xanthine Oxidase (b) three grades of osmotic stress using PBS and (c) membrane damage using thermal shock. Live human sperm DNA disintegration with time and oxidative stress were explored on fresh, cryopreserved and swim-up categories. The specimens ranged from sub-fertile patients to fertile donors in a limited study.

Post-treatment sperms resuspended in sperm media, placed on a quartz coverslip were trapped with a 785 nm, 25 mW laser, using a 1.4 NA, 60X, water immersion microscope objective. A Raman spectrum of a trapped cell was acquired for 20 – 30 seconds. The spectra from 20 – 40 cells from each specimen were analysed in the 630 cm^{-1} – 1630 cm^{-1} region using statistical variance and PCA.

Results: The Raman spectra from trapped motile sperm head contain intense peaks that did not require smoothing prior to analysis. PCA of the Raman spectra could not resolve the different grades of applied osmotic and oxidative stress in stallion cells. PCA showed high variability between specimens from the same stallion and between stallions, with distinct clustering by ejaculate. Membrane damage study and spectra from extended trapping also showed distinct specimen to specimen difference within and between stallions. Specimen to specimen variability is observed in motility and viability tests on 1000s of stallion cells using CASA and flow cytometry. Human sperms showed some clustering by category, time, stress and motility and appeared more sensitive to the tests than stallion sperms.

Conclusions: Raman spectra originate from the dense region of the trapped sperm head and resemble the fingerprint of dense calf thymus DNA. The cells show species specific response to the applied stress/damage. Stallion sperms show high variability between ejaculates that could not be differentiated by stallions. Human cells appear more sensitive to the applied processes. LTRS of live sperms needs further detailed research, cross correlated with other established complementary techniques, to identify spectral bands that are most sensitive to the various grades of induced DNA and membrane damage.

Acknowledgement

I am grateful to Alistair Elfick for the opportunity to do research in biophotonics, for the EPSRC funding, for supporting me in my OSA student chapter activities, travel grant applications (RSE Lessell's and RAE) and especially for supporting me in my application to train at CBST and Texas Medical Centre in the US.

Members of IMP have been very supportive throughout – Professor Easson, Professor Hall, Professor Ingram, Professor Sefiane and team. To Dr. Konstantin I am grateful for his support in the finishing years and the opportunity to teach his thermodynamics lab in the early years. Bobby Hoggs (now retired) and team at the workshop for their innumerable help. Vlastmil Srsen for help in the IBEE labs and for helping me test my first comet assay protocol. June and team have often kept me company on those days I worked into the wee hours.

Fellow PhD students within our group and IMP kept each other motivated when we felt stranded. Those weekend trips to Firbush made my day and my year – what a beautiful lakeside campus! An idyllic place for creativity and contemplation!

A few post-docs need special mention - Daniel Fredrich, a fellow OSA IONS member, and Jochen Arlt – for sharing their knowledge.

The Graduate Office team also need special mention as they have been very supportive and encouraging – Carol Ward, Sarah Wyse and the rest. Avril Davies and Sue Simpson – they have been the backbone of IMP and a tremendous help. Sue always found solutions to pressing problems and encouraged us always.

The George Square campus has been an exciting place to wander off to – to escape from the burdens of thesis. Harriet Harris, Ali Newell, the wonderful students and staff who came together to make sense out of the senseless! They made all the difference in the last couple of years – without their moral support the thesis would not have been completed. Thank you my good friends - Teodor, Ellinor.

Special thanks to these people for going out of their way to help me -

Professor Steve Block at Stanford guided me through the tricky part of building tweezers, for the lengthy emails and talks! **Dr. Rod Balhorn**, Division Head at Livermore Labs at the time I met him, made it possible for me to get research internship to train at CBST. Dr. Balhorn followed through with his commitments, even though changes were happening at Livermore that involved his career.

Prof Kit Lam, Head of Hematology and Oncology, a wonderful, compassionate individual – who made time to listen to my worries about my father's worsening

health. He is one in a million and I could not have hung in there at CBST, for as long as I did, without his moral support and encouragement.

Dr. Earnest Zeringue and Deborah Johnson at California IVF were very encouraging and interested in my research. They arranged for me to shadow them during various stages of IVF treatment, including egg extraction, ICSI and embryo biopsy. Without the shadowing, I would have struggled to visualise the procedures. Thank you ever so much for your encouragement. *For what it's worth, this thesis is dedicated to you and team, Dr. Zeringue.*

To Michael Martin and team at Berkeley Labs for the many sessions at the ALS and FTIR; and for the many clarifications when communication failed between the languages of biology and physics.

Keith Jewel and Paul Sheldon taught me how to use Minitab for PCA. Without their help, it would have been laborious. Keith showed me how to overcome some of the limitations of Minitab to do large scale data processing. Thank you Keith and Paul.

CBST: To Dr. Steve Lane and Professor Dennis Matthews for the research internship; to **Professor Stuart Meyers** who made this thesis possible with the opportunity to train in his lab, for the design of experiments and help with samples. Kenneth Wong at UC Davis Med Center helped with specimens; Dr. Doug Taylor, Frank Chuang, Dr. Thomas Husar, Cynthia Pagba, Tobias Moritz, and many others at CBST for the various training in LTRS, biochemical methods and cell culturing procedures. To Sabastian Wachsmann and team for the weekly soccer matches.

I also had the wonderful opportunity to train in Professor Randolph Glickman's lab at San Antonio Medical School. As a result my very first comet at Edinburgh worked! I thank Professor Hadziselimovic for his feedback on my early chapters - efforts at learning to speak biology.

To KiKi L'Italien, Meredith Smith and many wonderful people at OSA, who encouraged me to start the first OSA student chapter in Scotland; thank you for all the science communication opportunities.

I also must thank all my old school educators, PCK, PTM High School, Providence, Central – all the dedicated and talents faculty who invested in us and encouraged us to think outside the box and to take risks.

I relied on Google and Wikipedia for finding resources and basic information.

To my family, friends and kindred spirits – there is no need for words. Vellimma, you are always with me.

Table of Contents

List of Tables

List of Figures and Illustrations

Chapter One: Introduction to ART

Chapter Two: Human and Equine Spermatozoon

Chapter Three: Sperm DNA and Damage and Assessment with Biochemical Assays

Chapter Four: Raman Spectroscopy and Optical Traps for Assessing Sperm DNA Damage

Chapter Five: The Experiment

Chapter Six: The Experimental Results

Chapter Seven: The Discussion

Appendix:

Glossary

ART	Assisted Reproductive Technology
AI	Artificial Insemination
AZF	Azoospermia factor - a region in the long arm of human Y chromosome
CASA	Computer Assisted Sperm Analysis
DNA	Deoxyribose nucleic acid
DTT	Dithiothreitol
GPX	Glutathione peroxidase
HFEA	Human Fertility and Embryology Authority
H_2O_2	Hydrogen peroxide
HOST	Hyper-osmotic swelling test
HP	Human protamine
HCP	Hexagonal close packed crystalline structure
ICM	Inner cell mass - blastocyst stage of embryo
ICSI	Intracytoplasmic sperm injection
IVF	In *vitro* fertilisation
LTRS	Laser tweezers Raman spectrometer
PAGE	Polyacrylamide gel electrophoresis – nuclear protein study
PCA	Principal component analysis – a statistical method
PC	Principal component
PIXE	Proton induced x-ray emission – absolute technique for quantification of elements within a cell.
PM	Progressive Motility
ROI	Region of interest
RS	Raman Spectroscopy
SEM	Scanning electron microscopy

SOD	Superoxide dismutase
TEM	Transmission electron microscopy
TGCT	Testicular germ cell tumours
TM	Total Motility
TSH2B	Testis specific histone 2B
UDT	Cryptorchidism or undescended testes. The testes remain inside the abdomen of a male new-born baby.
WHO	World Health Organisation
ZP	Zona pellucida, a glycoprotein membrane of eggs

1

Introduction

Trust thyself: every heart vibrates to that iron string.
The eye was placed where one ray should fall, that it might testify of that particular ray.
Speak your latent conviction, and it shall be the universal sense; ...

Ralph Waldo Emerson (1803-1882)

1.0 The Mammalian Sperm Health

In 1678, Anton van Leeuwenhoek, a superb lens maker, known as the father of microbiology, first reported the finding of motile sperms, 'little animals', in semen. Since then, there have been several efforts to use artificial insemination (AI) for breeding purposes. AI was successfully used to produce pups in 1794; a century later, many countries adopted this method to raise rabbits and dogs. By the end of the 19th century, protocols were established for horse breeding for military purposes; these protocols were later adapted to breed cattle for dairy and meat. AI techniques had to be modified to improve the reproductive outcome in each species; sheep and horse and their reproductive cells did not respond well. These advances in AI paved the way to investigate cures for human infertility and assisted reproduction in humans started out cautiously in the 1940s [1, 2].

Sperms and eggs, collectively known as gametes or germ cells, have a singular role - to propagate the species [3]. What are the factors that contribute to their reproductive success? Why is it that some couples are able to conceive naturally while some others succeed with medical help? Why are some couples unable to have children? Why is breeding cattle using AI easier than breeding horses? Considerable research on mice and men, from embryo to adulthood, has shed light on the vital role of sperm in the success of a pregnancy. Horse and humans are researched in this thesis to gain molecular level understanding of mammalian spermatozoa.

Male factor infertility is summarised in this chapter. The structure of human and stallion spermatozoon and sperm DNA contribution to reproductive success are investigated using published literature, in the next two chapters.

1.1 Infertility

The socially accepted concept on the reproductive role of humans is that the man delivers the paternal heredity traits through the sperm to the egg and the woman bears complete responsibility for the success of the pregnancy. These roles cannot be taken for granted as both men and women can suffer from infertility – a state described by World Health Organisation (WHO) as the inability to get pregnant after

24 months of trying to conceive [4, 5]. Sperm health has a significant role in the success of the pregnancy. Recent research has revealed that the sperm also participates in early stages of embryo development [6, 7].

The average world fertility rate in 2009 ranged from 1.7 in the industrially developed countries to 4.6 in the least developed countries; where fertility rate is defined as the average number of childbirths per woman, within a region or population [8]. Worldwide fertility levels have dropped since 1970s, due to postponement of childbearing age and prevalent use of contraceptives. The average fertility in industrially developed nations has dropped from 2 children per woman in the 1970s to about 1.3 in the 1990s; with about 10% of older women remaining childless [9, 10].

1.2 In Vitro Fertilisation (IVF)

Childlessness is not always a choice and about 15% of couples worldwide suffer from infertility. Assisted reproduction in the form of artificial insemination has been used for over two centuries to help childless couples [2]. Assisted reproductive technology (ART) came into the limelight in 1978 when the world's first 'test tube baby', conceived outside the womb, was delivered in the UK [11]. The procedure of fertilising eggs in a glass dish is known as '*in vitro* fertilisation' (IVF). Australia in 1980, the US in 1981 and Sweden in 1982 succeeded in delivering their first IVF babies. Since then, IVF has been widely used to treat infertility [12].

Couples with poor sperm quality did not benefit from this conventional form of IVF. An advanced technique was developed in 1991 that resulted in pregnancies and live births - a sperm was injected into an egg by puncturing its membrane, the *zona pellucida* (ZP) [13]. After the success of this technique, sperm injection became popular as it had higher fertilisation rate than conventional IVF. This advanced form of IVF is known as intracytoplasmic sperm injection (ICSI); it is the only effective treatment for many cases of male factor infertility. Despite such advances that have helped many couples to have children, a large number of infertile couples remain childless, even after several IVF or ICSI treatment (see **section 1.4** for details) [14]. About 60% of the known causes of infertility are equally due to poor sperm and egg quality [3, 11].

1.3 Overview of Male Factor Infertility

WHO guidelines identify a range of characteristics to investigate male fertility - semen quality, sperm concentration, morphology and motility [15]. While WHO assessment criteria remain a good predictor of sperm quality, the assessment cannot determine the DNA integrity of individual sperms. Sperm assessment criteria cannot be used in the treatment of infertility caused by asthenozoospermia (low motility sperms), oligoasthenozoospermia (low sperm count and motility), teratozoospermia (low morphological normalcy), necrozoospermia (no live sperms), oligo-astheno-teratozoospermia (low, count, motility and morphological normalcy) and globozoospermia - round headed sperms [16].

Male infertility is on the rise. Environment, health and lifestyle are implicated [11, 17-21]. Sperms with a high level of DNA strand breakage are implicated in early pregnancy failures [22-25]. Many donor sperms are cryopreserved in liquid nitrogen at -196 ^{o}C and the freeze - thaw process induce damage to the cells [26]. Idiopathic infertility [27, 28] is a case where pregnancy failure occurs even though sperm morphology and count are normal. Aneuploidy, a genetic condition, accounts for some early pregnancy failures, where the chromosome count differs from the '22 + X/Y' found in normal sperms [29]. Obstructive and non-obstructive azoospermia are conditions in which sperms are absent in the semen. Surgically extracted sperms from testicular tissue are morphologically different from epididymal and ejaculate sperms; testicular sperms have been successfully used in ICSI [30-33].

1.4 Risk Factors with Infertility Treatment

Several cycles of IVF treatment are often required to achieve a live birth. The fertility tests, ovarian stimulation drugs that are used to produce multiple eggs and multiple births are a health risk to the mother and child [11, 34, 35]. Multiple embryo transfers are often used to increase the probability of a live birth [15, 36-39]. Multiplets are more likely to be miscarried, born premature or die young, and represent the highest source of health risk to both mother and child [11, 40]. Multiplets accounted for 2% of natural pregnancies; twins and triplets accounted for 23% - 32% of IVF births in the UK, Europe and the US, during 2005 – 2007 [11, 41].

DNA abnormalities have been associated with a large proportion of the male factor infertilities. Infertility and subnormal sperm quality have been observed in men with genetic disorders. IVF babies from infertile men with genetic disorders are likely to inherit the problem and compound the infertility trend in future generations [41, 42].

1.5 Motivation for live sperm DNA qualification

Infertility treatment has made tremendous strides; yet, the live birth rate in the UK in 2007 was only 30% for infertile women under 30 years of age and 3% for women in their 40s. About 30% of IVF treatments were for male factor, 28% for female factor, and the rest were for health and unknown factors. Nearly half (48%) of IVF treatments used ICSI [11, 43]. The IVF treatment statistics in the US during 2007 also showed a similar trend [44].

About 50% of the world's IVF treatment takes place in Europe. Data for the period from 1997 to 2006 showed increase in IVF usage. The average pregnancy rate was about 30% per embryo implant in 2006; about 67% of the treatment used ICSI [45].

The live birth rate has not improved significantly since the 1980s. **Figure 1.1** shows the charts for the first 15 years following ICSI usage in the UK (Human Fertility and Embryology (HFEA)). Conventional IVF and ICSI usage increased significantly over the 15-year period **(Chart A)**. The trend in the live birth rates over the ten-year period between 1996 and 2006, shown in **Chart B,** indicates, approximately 5% improvement [43].

ICSI has demonstrated higher success rates than conventional IVF in inducing first time pregnancies [46, 47]; about half the IVF treatments in the UK in 2007 used ICSI in both male and female factor infertility cases [11]. ICSI usage across Europe, the US, Australia & New Zealand increased significantly (2006 report) [45]. Since ICSI bypasses most of the natural sperm selection barriers, there is some concern that children conceived through ICSI could be susceptible to genetic defects, cancer and other health abnormalities [48-52]. Multiplets have been used to improve pregnancy rates; but with health risks to mother and child [53].

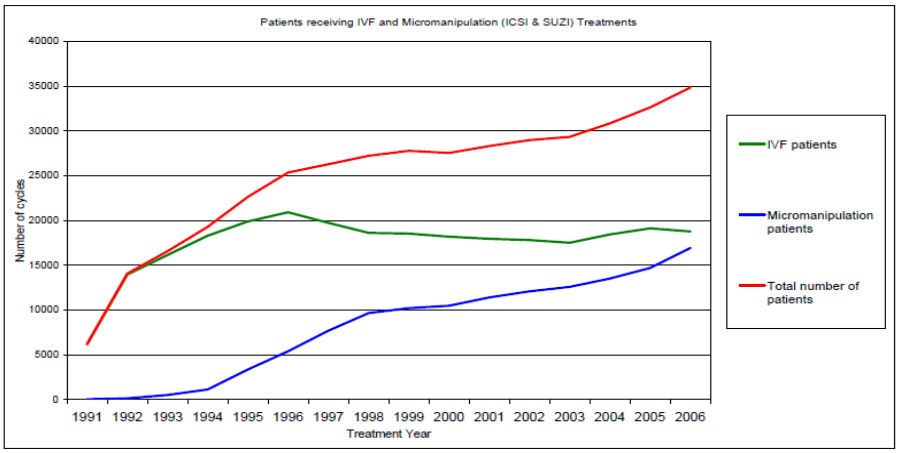

Chart A

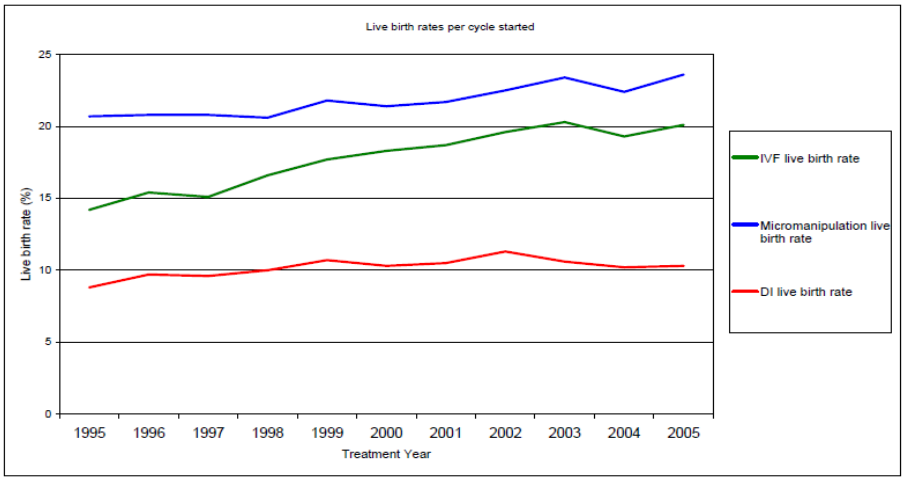

Chart B

Figure 1.1: HFEA statistics for IVF trend and live birth rates in the UK for the period 1991 – 2006 [43] . **Chart A:** IVF, ICSI and total IVF usage between the years 1991 – 2006. **Chart B:** IVF, ICSI and donor insemination (DI) live birth rates for the period 1996 – 2005.

Sperm morphology is not an absolute indicator of sperm health or live birth rates [54-56]. IVF clinics use biochemical assays like comet [57] and TUNEL [58] assays to test the DNA quality of sperm specimens used in IVF treatment; these tests are time consuming and require sacrifice of the cells. A large percentage of male factor pregnancy failures can be attributed to limitations in determining molecular level health of the sperm selected for ICSI [57-59].

With growing need for IVF treatment, decreasing number of sperm donors, declining sperm quality [18, 20, 60], cryopreservation induced sperm damage [61] and only marginal improvement in live birth rates in the last two decades [11], it has become increasingly necessary to gain molecular level understanding of sperm and egg interactions and their DNA health. Sperm malfunction has multiple and complex contributing factors that result in DNA damage [62, 63]. A fast, non-destructive and reliable technique for screening individual sperms and eggs for DNA damage prior to ICSI is therefore necessary [64, 65]. This research focuses on evaluating technologies for live sperm DNA quality assessment.

1.6 Raman spectroscopy for live sperm DNA assessment

The feasibility of using Raman spectroscopy (RS) as a potential tool to detect and discriminate between different degrees of DNA damage is explored in this research. RS is a study of molecular vibrations and has wide application in medical technology due to the ease of use and simplicity of the technique [66]. It has been successfully used for *in situ* diagnoses of diseases in real time [67]. RS with near infrared (NIR) radiation has been successfully used in the analysis of live cells [68], and has applications in bacteriology and virology [69, 70]. It has been used for real time *in vivo* cancer diagnosis [71] and to monitor the metabolic and developmental processes in single yeast cells [72]. Live cells have been continuously trapped by low power laser tweezers/traps without disrupting the cell cycle or functions which were continuously monitored [73, 74].

As a precedent for this thesis, DNA in various forms has been characterised using RS. Purified calf thymus DNA, synthetic DNA and the effect of temperature and chemical environment on the integrity of DNA have been studied in the Raman

spectral fingerprint region 600 cm^{-1} – 1700 cm^{-1} [75-78]. These papers provide detailed information on the DNA peaks. Various sperm DNA structures have also been investigated using Raman spectroscopy [79-81]. These literatures indicate that the optical tweezers and RS combination can be used to trap and analyse motile sperms without destroying the cells.

The biochemical structure of healthy sperm DNA is different from that of damaged or fragmented sperm DNA [82]. As a result, the Raman spectra of healthy sperms and DNA damaged sperms are expected to be different [81]. The cells can be rapidly examined in their physiological environment using Raman spectroscopy [69] and the technique can be used in place of time consuming biochemical assays for monitoring cryopreservation protocols and for clinical fertility tests. If laser tweezers do not induce cell damage and if the Raman spectrometers can achieve the sensitivity of biochemical techniques, this tool could be used in live sperm manipulation. The purpose of this research is to investigate the feasibility of using Raman microscope and optical tweezers to study live sperms.

1.7 The Experimental Approach

The human and horse are members of the placental mammalian family and share many common traits, including pregnancy and giving birth to offspring. Research on stallion sperm health and stress induced sperm DNA damage have been used to improve horse breeding using AI [83-87]. Stallion sperms were used to study the impact of stress and membrane damage on the sperm DNA quality. This research was carried out in collaboration with the Department of Veterinary Medicine, University of California (UC), Davis, and the Center for Biophotonics Science and Technology (CBST), a multidisciplinary research facility affiliated to the UC Davis Medical Center in Sacramento, funded by the US National Science Foundation (NSF).

Clinical specimens of human sperms obtained from the Andrology lab at UC Davis Medical Center and The California IVF Clinic, Davis, were used to compare Raman spectra of fresh and cryopreserved sperms and sperms separated using swim up techniques.

1.8 Outline of Thesis Chapters

Artificial insemination, infertility, male factor infertility, infertility treatments, benefits, risks and limitations of the treatment and the need for research at the molecular level to understand sperm DNA quality, are summarised in **Chapter One**. The motivation for using laser tweezers and RS combination to test live/motile sperm DNA quality is outlined.

The structure of the human and stallion sperm, sperm health and the environment are reviewed in **Chapter Two.** The history of AI and human infertility treatment are also reviewed. Horse (equine) species and their reproductive capability, managed horse breeding and its limitations as well as stress induced sperm DNA damage are summarised**.** The similarities and differences between the horse and human sperms are tabulated. The information gained from this literature review is summarised.

Cellular sources of reactive oxygen species (ROS) and free radicals that damage sperm DNA are summarised in **Chapter Three**. Basics of DNA and chromosome structure and DNA damage in horse and humans are summarised. Overview of the bio-chemical assays used to investigate DNA damage, with emphasis on single cell tests, are included.

Raman spectroscopy and laser tweezers are reviewed in **Chapter Four**. Applications of Raman spectroscopy in biological and medical sciences are summarised. Raman peaks of sperms, DNA and nuclear proteins are tabulated. Trapping with laser beam, application of laser traps in biology, laser trapping induced damage to cells and laser tweezers Raman spectroscopy (LTRS) – the tool used in this research – and applications of LTRS are reviewed.

The experimental design used for the study of live stallion and human sperms is described in **Chapter Five**. Sperm preparation techniques, the chemicals, viability test procedures, LTRS equipment, calibration procedure and statistical methods are outlined. The basic statistical methods, fundamentals of Principal Component Analysis (PCA) and its use in spectral analysis are also summarised in this chapter.

The outline of the experiments and the experimental results are reviewed in **Chapter Six**. Raman spectra of stallion sperms exposed to different types and grades of chemical stress are examined. The spectra of live and membrane damaged motile and immotile stallion sperms are compared. Fresh and swim-up human specimens from the andrology lab, and thawed donor sperms from the IVF clinic are also analysed using Raman spectroscopy.

The results from the experimental work are reviewed and discussed in **Chapter Seven**. These results are compared with published work on Raman spectroscopy of sperm cells. The findings from this research, conclusions, limitations of the experimental work and the scope for future research are summarised in **Chapter Eight**.

References

1. Foote, R.H., *The history of artificial insemination: Selected notes and notables.* Journal of Animal Science, 2002. **80**(E-Suppl_2): p. 1-10.
2. Ombelet, W. and J. Van Robays, *History of Human Artificial Inseminaton*, in *Facts Views and Vision in ObGyn*. 2010, Artificial Insemination: Belgium. p. 5.
3. Alberts, B., et al., *Molecular Biology of The Cell*. Fourth ed. 2002, New York: Garland Science.
4. Rowe, P.J., et al., eds. *WHO manual for the standard investigation and diagnosis of the infertile couple*. 1993, Cambridge University Press. 83.
5. World Health Organisation, ed. *WHO Laboratory Manual for the Examination of Human Semen and Sperm-Cervical Mucus Interaction*. 4 ed., ed. W.H. Organization. 1999, Cambridge University Press, UK. 128.
6. Tesarik, J., C. Mendoza, and E. Greco, *Paternal effects acting during the first cell cycle of human preimplantation development after ICSI.* Hum. Reprod., 2002. **17**(1): p. 184-189.
7. Nanassy, L. and D. Carrell, *Paternal effects on early embryogenesis.* Journal of Experimental & Clinical Assisted Reproduction, 2008. **5**(1): p. 2.
8. Haub, C. and M.M. Kent, *World Population Data Sheet 2009*, P.R. Bureau, Editor. 2009, PRB: Washington DC.
9. Anatoly G. Vishnevsky (1995) *Family, Fertility, and Demographic Dynamics in Russia: Analysis and Forecast*. Rand Corporation - a non-profit institution.
10. United Nations, *World Fertility Report 2003*. 2003, Department Economic & Social Affairs.
11. Human Fertilisation and Embryo Authority, *Fertility Facts & Figures 2007* HFEA, Editor. 2009, HFEA, United Kingdom: London.
12. Cohen, J., et al., *The early days of IVF outside the UK.* Hum Reprod Update, 2005. **11**(5): p. 439-460.
13. Palermo, G., et al., *Pregnancies after intracytoplasmic injection of single spermatozoon into an oocyte.* Lancet, 1992. **340**(8810): p. 17-18.
14. de Mouzon, J., et al., *Tenth ESHRE Report on Assisted reproductive technology in Europe, 2006: results generated from European registers by European Society of Human Reproduction and Embryology (ESHRE).* Hum. Reprod., 2010. **25**(8): p. 1851-1862.
15. Effy Vayena, Patrick J. Rowe, and P. David Griffin, eds. *Current practices and controversies in assisted reproduction : report of a WHO meeting*. 2002, World Health Organization, Geneva, Switzerland: Geneva.
16. Dam, A.H.D.M., et al., *Globozoospermia revisited.* Hum Reprod Update, 2007. **13**(1): p. 63.
17. Bujan, L., et al., *Time series analysis of sperm concentration in fertile men in Toulouse, France between 1977 and 1992.* BMJ, 1996. **312**(7029): p. 471-472.
18. Irvine, S., et al., *Evidence of deteriorating semen quality in the United Kingdom: birth cohort study in 577 men in Scotland over 11 years.* BMJ, 1996. **312**(7029): p. 467-471.
19. Andolz, P., M.A. Bielsa, and J. Vila, *Evolution of semen quality in North-eastern Spain: a study in 22 759 infertile men over a 36 year period.* Hum. Reprod., 1999. **14**(3): p. 731-735.
20. Shine R, P.J., Birdsall M,, *Declining sperm quality in New Zealand over 20 years.* The New Zealand Medical Journal, 2008. **121**((1287)): p. 50-56.
21. Vine, M.F., *Worldwide decline in semen quality might be due to smoking.* BMJ, 1996. **312**(7029): p. 506.
22. Ahmadi, A. and S.-C. Ng, *Fertilizing ability of DNA-damaged spermatozoa.* The Journal of Experimental Zoology, 1999. **284**(6): p. 696-704.
23. Irvine, D.S., et al., *DNA integrity in human spermatozoa: relationships with semen quality.* Journal of Andrology, 2000. **21**(1): p. 33-44.
24. Ramadan, A.S., et al., *Negative effects of increased sperm DNA damage in relation to seminal oxidative stress in men with idiopathic and male factor infertility.* Fertility and sterility, 2003. **79**: p. 1597-1605.
25. Zini, A., et al., *Sperm DNA damage is associated with an increased risk of pregnancy loss after IVF and ICSI: systematic review and meta-analysis.* Hum. Reprod., 2008. **23**(12): p. 2663-2668.

26. Esteves, S.C., et al., *Cryopreservation of human spermatozoa with pentoxifylline improves the post-thaw agonist-induced acrosome reaction rate.* Hum. Reprod., 1998. **13**(12): p. 3384-3389.
27. Collodel, G., et al., *Semen Quality of Male Idiopathic Infertile Smokers and Nonsmokers: An Ultrastructural Study.* J Androl, 2009: p. jandrol.109.007773.
28. Ambrosini, A., et al., *Idiopathic infertility: susceptibility of spermatozoa to in-vitro capacitation, in the presence and the absence of palmitylethanolamide (a homologue of anandamide), is strongly correlated with membrane polarity studied by Laurdan fluorescence.* Mol. Hum. Reprod., 2003. **9**(7): p. 381-388.
29. Shi, Q. and R.H. Martin, *Aneuploidy in human spermatozoa: FISH analysis in men with constitutional chromosomal abnormalities, and in infertile men.* Reproduction, 2001. **121**(5): p. 655-666.
30. Mercan, R., et al., *Outcome of testicular sperm retrieval procedures in non-obstructive azoospermia: percutaneous aspiration versus open biopsy.* Hum. Reprod., 2000. **15**(7): p. 1548-1551.
31. Fahmy, I., et al., *ICSI using testicular sperm in male hypogonadotrophic hypogonadism unresponsive to gonadotrophin therapy.* Hum. Reprod., 2004. **19**(7): p. 1558-1561.
32. Moghadam, K.K., et al., *The Motility of Epididymal or Testicular Spermatozoa Does Not Directly Affect IVF/ICSI Pregnancy Outcomes.* Journal of Andrology, 2005. **26**(5): p. 619-623.
33. Khalili, M.-A., M.-A. Manouchehri, and V. Dehghani, *Treatment Outcome Following Intracytoplasmic Injection Of Sperm Retrieved From Ejaculate, Epididymis, Or Testis Of Infertile Men.* Archives of Iranian Medicine, 2004. **7**(3): p. 232-236.
34. Santos, M.A., E.W. Kuijk, and N.S. Macklon, *The impact of ovarian stimulation for IVF on the developing embryo.* Reproduction, 2010 **139**(1): p. 23-34.
35. Gelbaya, T.A., *Short and long-term risks to women who conceive through in-Vitro fertilization.* Human Fertility, 2010 **13**(1): p. 19-27.
36. Wright, V.C., et al., *Assisted Reproductive Technology Surveillance --- United States, 2002*. 2005, CDC. p. 1-24.
37. Barri, P.N., *Multiple pregnancies: a plea for informed caution.* Hum Reprod Update, 2005. **11**(1): p. 1-2.
38. Greco, E., et al., *Limiting the number of injected oocytes to three impairs ICSI outcomes in patients with nonobstructive azoospermia.* Hum. Reprod., 2006. **21**(6): p. 1521-1524.
39. Van Voorhis, B.J., *Outcomes From Assisted Reproductive Technology.* Obstet Gynecol, 2006. **107**(1): p. 183-200.
40. USGovernment, R., *Use of assisted reproductive technology — United States, 1996 and 1998.* Morbidity and Mortality Weekly Report 2002.
41. Basatemur, E. and A. Sutcliffe, *Follow-up of Children Born after ART.* Placenta, 2008. **29**(Supplement 2): p. 135-140.
42. Singh, A.R., et al., *Genetic Factors in Male Infertility and their Implications.* International Journal of Human Genetics 2006. **6**(2): p. 163-169.
43. HFEA, *A long term analysis of the HFEA Register data 1991-2006*, HFEA, Editor. 2007, Human Fertilisation and Embryo Authority. p. 1-100.
44. USA Division of Reproductive Health, *Assisted Reproductive Technology (ART) Report: US National Summary Table: 2007*, C.f.D.C.a.P. Department of Health and Human Services, Editor. 2009, Center for Disease Control and Prevention.
45. de Mouzon, J., et al., *Tenth ESHRE Report on Assisted reproductive technology in Europe, 2006: results generated from European registers by ESHRE.* Hum. Reprod., 2010. **25**(8): p. 1851-1862.
46. Hwang, J.-L., et al., *IVF versus ICSI in sibling oocytes from patients with polycystic ovarian syndrome: a randomized controlled trial.* Hum. Reprod., 2005. **20**(5): p. 1261-1265.
47. Bartoov, B., et al., *Pregnancy rates are higher with intracytoplasmic morphologically selected sperm injection than with conventional intracytoplasmic injection.* Fertility and Sterility, 2003. **80**(6): p. 1413.
48. Campbell, A.J. and D.S. Irvine, *Male infertility and intracytoplasmic sperm injection (ICSI).* Br Med Bull, 2000. **56**(3): p. 616-629.
49. Fraser, L.R., *ART: Boon or bane?* Nature Cell Biology 2002. **4**(S1): p. S10_S13.
50. Hristova, R., et al., *Chromosome Abnormalities in Sperm From Infertile Men with Asthenoteratozoospermia* Biol Reprod, 2002. **66**(6): p. 1781-1783.

51. Gamiz, P., et al., *The effect of pronuclear morphology on early development and chromosomal abnormalities in cleavage-stage embryos.* Hum. Reprod., 2003. **18**(11): p. 2413-2419.
52. Gandini, L., et al., *Full-term pregnancies achieved with ICSI despite high levels of sperm chromatin damage.* Hum. Reprod., 2004. **19**(6): p. 1409-1417.
53. Jain, T., S.A. Missmer, and M.D. Hornstein, *Trends in Embryo-Transfer Practice and in Outcomes of the Use of Assisted Reproductive Technology in the United States.* N Engl J Med, 2004. **350**(16): p. 1639-1645.
54. Celik-Ozenci, C., et al., *Sperm selection for ICSI: shape properties do not predict the absence or presence of numerical chromosomal aberrations.* Hum. Reprod., 2004. **19**(9): p. 2052-2059.
55. De Vos, A., et al., *Influence of individual sperm morphology on fertilization, embryo morphology, and pregnancy outcome of intracytoplasmic sperm injection.* Fertility and Sterility, 2003. **79**(1): p. 42-48.
56. Keegan, B.R., et al., *Isolated teratozoospermia does not affect in vitro fertilization outcome and is not an indication for intracytoplasmic sperm injection.* Fertility and Sterility, 2007. **88**(6): p. 1583-1588.
57. Morris, I.D., et al., *The spectrum of DNA damage in human sperm assessed by single cell gel electrophoresis (Comet assay) and its relationship to fertilization and embryo development* Hum. Reprod., 2002. **17**(4): p. 990-998.
58. Groves-Kirkby, N., *Male factor infertility: TUNEL evaluation of sperm DNA damage.* Nat Rev Urol, 2010. **7**(8): p. 421-421.
59. Benchaib, M., et al., *Sperm DNA fragmentation decreases the pregnancy rate in an assisted reproductive technique.* Hum. Reprod., 2003. **18**(5): p. 1023-1028.
60. Magnusdottir, E.V., et al., *Persistent organochlorines, sedentary occupation, obesity and human male subfertility.* Hum. Reprod., 2005. **20**(1): p. 208-215.
61. Ozkavukcu, S., et al., *Effects of cryopreservation on sperm parameters and ultrastructural morphology of human spermatozoa.* Journal of Assisted Reproduction and Genetics 2008. **25**(8): p. 403-411.
62. Barratt, C., V. Kay, and S. Oxenham, *The human spermatozoon - a stripped down but refined machine.* Journal of Biology, 2009. **8**(7): p. 63.
63. Donnelly, E.T., et al., *Assessment of DNA integrity and morphology of ejaculated spermatozoa from fertile and infertile men before and after cryopreservation.* Hum. Reprod., 2001. **16**(6): p. 1191-1199.
64. Zini, A. and M. Sigman, *Are Tests of Sperm DNA Damage Clinically Useful? Pros and Cons.* J Androl, 2009. **30**(3): p. 219-229.
65. Simon, L., et al., *Clinical significance of sperm DNA damage in assisted reproduction outcome.* Hum. Reprod., 2010. **25**(7): p. 1594-1608.
66. Maquelin, K., et al., *Identification of medically relevant microorganisms by vibrational spectroscopy.* Journal of Microbiological Methods 2002. **51** p. 255- 271.
67. Hanlon, E.B., et al., *Prospects for in vivo Raman spectroscopy.* Physics in Medicine and Biology, 2000. **45**(2): p. R1.
68. Matthews, Q., et al., *Variability in Raman Spectra of Single Human Tumor Cells Cultured in Vitro: Correlation with Cell Cycle and Culture Confluency.* Appl. Spectrosc., 2010. **64**(8): p. 871-887.
69. Notingher, I. and L.L. Hench, *Raman microspectroscopy: a noninvasive tool for studies of individual living cells in vitro.* Expert Review of Medical Devices, 2006. **3**(2): p. 215-234.
70. Lambert, P., et al., *Raman spectroscopy: the gateway into tomorrow's virology.* Virology Journal, 2006. **3**(1): p. 51.
71. Kaminaka, S., et al., *Near-infrared multichannel Raman spectroscopy toward real-time in vivo cancer diagnosis.* Journal of Raman Spectroscopy, 2002. **33**(7): p. 498-502.
72. Huang, Y.-S., et al., *In Vivo Raman Spectroscopy And Imaging Of A Single Living Fission Yeast Cell.* Proceedings of the XIX International Conference on Raman Spectroscopy, 2004.
73. Singh, G.P., et al., *Real-Time Detection of Hyperosmotic Stress Response in Optically Trapped Single Yeast Cells Using Raman Microspectroscopy.* Analytical Chemistry, 2005. **77**(8): p. 2564 - 2568.
74. Creely, C.M., G.P. Singh, and D. Petrov, *Dual wavelength optical tweezers for confocal Raman spectroscopy.* Optics Communications, 2005. **245**: p. 465-470.
75. Duguid, J.G., et al., *DNA melting investigated by differential scanning calorimetry and Raman spectroscopy.* Biophysical Journal, 1996. **71**(6): p. 3350-3360.

76. Benevides, J.M. and J. G.J. Thomas, *Characterization of DNA structures by Raman spectroscopy: high-salt and low-salt forms of double heical poly(dG-dQ in H21 and D20 solutions and application to B, Z and A-DNA**. Nucleic Acids Research, 1983. **11**(16).
77. Deng, H., et al., *Dependence of the Raman Signature of Genomic B-DNA on Nucleotide Base Sequence.* Biopolymers:, 1999. **50**: p. 656-666.
78. Erfurth, S.C., Ernest J. Kiser, and W.L. Peticolas, *Determination of the Backbone Structure of Nucleic Acids and Nucleic Acid Oligomers by Laser Raman Scattering.* Proceedings of the National Academy of Sciences of the U S A, 1972. **69**(4): p. 938-941.
79. Ke, W., D. Yu, and J. Wu, *Raman spectroscopic study of the influence on herring sperm DNA of heat treatment and ultraviolet radiation.* Spectrochimica Acta Part A: Molecular and Biomolecular Spectroscopy, 1999. **55**(5): p. 1081-1090.
80. Huser, T., et al., *Raman spectroscopy of DNA packaging in individual human sperm cells distinguishes normal from abnormal cells.* Journal of Biophotonics, 2009. **2**(5): p. 322-332.
81. Mallidis, C., et al., *In situ visualization of damaged DNA in human sperm by Raman microspectroscopy.* Human Reproduction, 2011. **26**(7): p. 1641-1649.
82. Bennetts, L.E. and R.J. Aitken, *A comparative study of oxidative DNA damage in mammalian spermatozoa* Molecular Reproduction and Development, 2005. **71**(1): p. 77-87.
83. Samper, J.C., *Equine Breeding Management and Artificial Insemination* 2ed. 2009: Elsevier.
84. McKinnon, A.O. and J.L. Voss, eds. *Equine Reproduction*. 2005, Blackwell Publishing.
85. Baumber, J., et al., *Reactive Oxygen Species and Cryopreservation Promote DNA Fragmentation in Equine Spermatozoa.* J Androl, 2003. **24**(4): p. 621-628.
86. Meyers, S.A., *Spermatozoal response to osmotic stress.* Animal reproduction science, 2005. **89**(1): p. 57-64.
87. Pommer, A.C., J. Rutllant, and S.A. Meyers, *The role of osmotic resistance on equine spermatozoal function.* Theriogenology, 2002. **58**(7): p. 1373-1384.

2

Horse and Human Spermatozoon

"It is not for us to know why, or, how.
Grace comes with the creation word, Be."
Jalaluddin Rumi (1207-1273)

2.0 Introduction to Sperm Development

Search for the primordial sperm cells dates back to over a century. Embryos, foetuses, immature and mature testes at various stages of development have been studied with light microscopy, scanning electron microscopy (SEM) and transmission electron microscopy (TEM) after histochemical and immunohistochemical staining. The growth environment that these reproductive organs and cells encounter in the womb, also contribute to their adult health and fertility [1].

Human gametes have a single set of 23 chromosomes (haploid configuration) in the cell nucleus; whereas somatic cells (all other cells in the body) have 46 (23 pairs) chromosomes (diploid configuration). Gametes are capable of two types of cell division – mitotic (splitting into two diploid cells, each with an identical copy of the chromosomes) and meiotic (splitting a diploid cell into two haploid cells). Somatic cells are only capable of mitotic cell division [1].

Fertilisation occurs when a sperm fuses with an egg to create a new diploid cell called a 'zygote'. The zygote, enclosed by the *zona pellucida* (ZP), is formed within 18 hours [2]. The chromosomes of the zygote are derived from the combination of the sperm (23,X or 23,Y) and egg (23,X) chromosomes. The sex of the embryo is established at fertilisation; the zygote gaining a Y chromosome develops into a male offspring [3].

During the embryo/foetal growth, its reproductive organs, sex cells and sex hormones transition through various stages of development. Germ (reproductive cell) and gonad (reproductive organ) related genes and hormones are activated within days of embryo implantation in the womb. Any delay or error during germ and gonad development could result in a variety of growth defects and health problems, including infertility [4-7].

Human sperm structure is described in **Section 2.1**. Sperm health and environment is explored in **Section 2.2**. History of artificial insemination (AI) and evolutionary

facts about *Equus* species and research on stallion sperms are reviewed in **Sections 2.3** and **2.4.** The stallion sperm is described in **section 2.5.** Human and stallion sperms are compared in **section 2.6.**

2.1 Human Sperm Structure

A morphologically normal human sperm (**Figure 2.1**) is about 60 microns long with an oval shaped head that is 4 - 5.5 μm long and 2.5 - 3.5 μm wide. The length to width ratio is 1.5 - 1.75. The acrosomal region is well defined and covers 40-70 % of the head. The 50 μm long tail diameter is 1 - 2 μm and capable of propelling the cell forward [8]. The genomic DNA is condensed to almost crystalline density and is bound by sperm nuclear proteins known as protamines and histones [9].

A micron long flexible junction, known as the **neck,** forms a narrow bridge between the sperm head and midpiece. Calcium signals originate in the neck region. The proximal centriole (microtubular structure associated with the sperm tail) resides in the neck [10]. The **mid-piece** is a rigid structure and has a 7 μm long spiral fibrous rib enclosing several mitochondria. The mitochondrion provides energy for sperm motility and has a set of its own DNA (mtDNA). The mid-piece terminates at the **principal piece.** The annulus, a ring-like electron-dense cytoskeleton linked to flagellar integrity and cell motility, is found between the midpiece and the **principal-piece** in mammalian sperms [11].

Mature sperms have fully developed flagella; the skeletal structure extends from the base of the distal centriole to the tip of the tail. The axis of the flagella consists of a pair of central tubules surrounded by nine pairs of tubules, as shown in **Figure 2.1.** The principal-piece is 40 μm long, and the **end-piece** is 5 – 10 μm long. Together they formed the flagellum. Powered by the mitochondria, the flagellum produces helical movement and forward momentum in a fluid environment. This forward momentum or progressive motility (PM) is essential for natural pregnancy [8]. During the sperm's natural encounter with the egg, its acrosomal vesicle reacts with the chemical environment surrounding the egg and ruptures, exposing the sperm nuclear membrane [1].

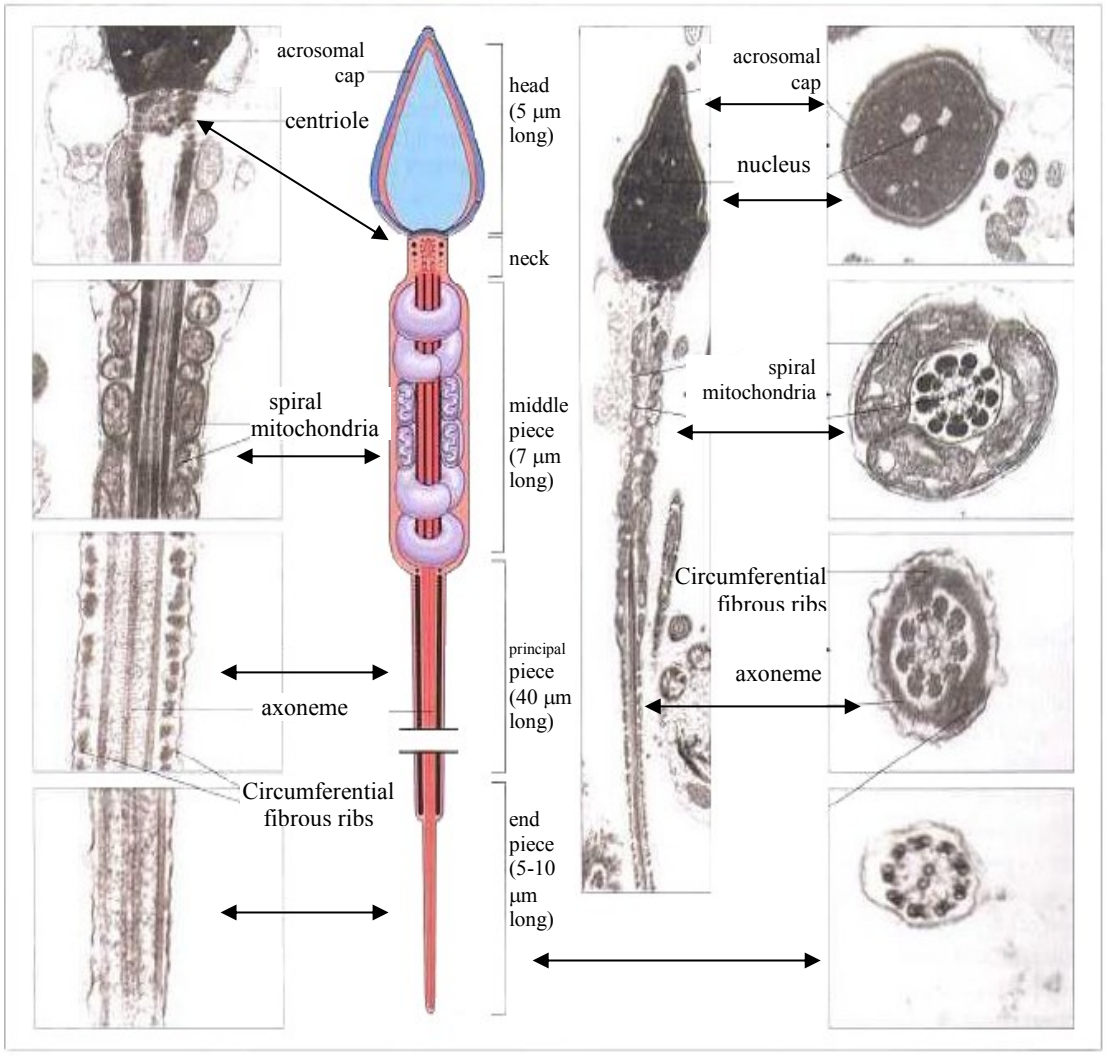

Figure 2.1 The diagram of a mature human spermatozoon and the scanning electron microscope (SEM) images of a whole sperm and its cross-sections *Adapted from Human Histology* [12] , *Chapter 16*

2.2 Sperm Health and the Environment

Environmental factors [13-15], oxidative stress [16], pesticides [17], geographical region [18], perfluoroalkyl compounds (PFCs) and plastics [19, 20], smoking [21], age [22-26], obesity and sedentary lifestyle [27, 28] and cancer [29-31] contribute to low fertility, low sperm count, low sperm morphology and high sperm DNA fragmentation.

2.2.1 Protamination and sperm DNA damage

During the maturation process, the nuclear proteins in the large spermatid are replaced by basic proteins known as protamines or P1. This aids nuclear condensation and the cell volume at maturation reduces to approximately a 10^{th} of its volume. The sperm head adopts a spear like shape and expels most of the cell plasma. The probability for DNA damage is high during condensation. The two types of protamines that bind the human sperms are known as HP1 and HP2 and have approximately the same ratio. These protamines form thiol cross-links with the highly reactive DNA to form a chemically neutral structure that protects the genetic heritage. About 15% of the human sperm is also bound by nuclear histones. Abnormal HP1: HP2 ratio has been associated with poor sperm morphology, low forward motility and reduced fertilisation capability [32-34]. Low HP1: HP2 ratio and low protamine concentrations were found in infertile men with high sperm DNA fragmentation [35-40].

Semen morphology of smokers revealed low sperm motility, reduced membrane integrity and high nuclear DNA damage. Low HP1 and HP2 concentration and high HP1: HP2 ratio were observed in the smoking population [41].

2.2.2 Effect of Environment, Lifestyle and Cancer on Sperm DNA

External factors like lifestyle, environment, drugs, nutrition, hormones, radiation and higher temperature could disturb spermatogenesis and result in malformed spermatids, misshapen or missing flagellum and midpeice, poorly attached acrosomal cap and disturbed nuclear condensation [42]. Obesity is found to negatively impact germ cell count [43, 44].

Two types of enzymes - endogenous sperm nuclease found in the sperm nucleus of hamster, mice and men, and exogenous DNAse - are capable of inducing sperm apoptosis by binding to DNA and cleaving the strands. Addition of Ca^{2+} and Mg^{2+} ions to the incubating medium will speed up the process; the DNA strands are cleaved into small fragments of approximately 50 kbp size loops within 15 to 30 minutes. Longer enzymatic exposure reduced the strands to 500 bp size in fertile and 8 bp size in infertile sperm samples. The human sperm DNA is easier to damage than hamster or mice sperm DNA due to its high histone content. Endonuclease can be activated in human sperms by freezing and thawing the sperms resuspended in cryoprotectant free media [45].

Alcohol during pregnancy could have an adverse effect on foetal germ cells. Semen volume and sperm count of adult sons of mothers who drank 4.5 units per week during pregnancy, was 32% lower compared to sons exposed to less than 1.0 unit of drink per week during their foetal life. Sperm motility, morphology and testosterone remained unaffected [46].

Dysfunctional centrioles have been linked to infertility [47]. The distal centriole, from which the axoneme originates, has been found in degenerate condition in many motile sperms. The proximal centriole located in the neck region appeared structurally intact [48]. Some infertility is linked to sperms with no axoneme [49, 50]. Malformed or absent axoneme causes infertility; ICSI has helped couples with such cases, to have babies [51]. High motility sperms with high morphological normalcy were divided into groups with straight and tapered midpiece. Sperms with straight midpeice were superior in fertilising bovine eggs and had higher aster formation rates [52].

The storage time scale of 6 months to over 14 years had no significant effect on the progressive motility of cryopreserved sperms used in clinical IVF, but sperms from incompletely filled straws showed decreased motility [53]. Antioxidant levels in bovine sperms dropped significantly after a single freeze-thaw cycle [54].

2.2.3 Genetic Abnormalities and Idiopathic Infertility

Genetic abnormalities account for 15% – 30% of male factor infertility [55]. Deleted in azoospermia-like' (Dazl) located in the Y-chromosome in mammals, regulate the differentiation and development of germ cells. Dazl has been linked to various gene functions in mice sperms, and could have a role in the haploid phase of sperm maturation; mutation in this gene could lead to sterility. Some azoospermic men were found to have diminished Dazl gene function. Microdeletions in the azoospermia factor (AZF) region on the Y chromosome have not resulted in chromosomal karyotype abnormalities [56, 57].

Patients with idiopathic infertility, cryptorchidism and varicocele displayed normal karyotype; the abnormal sperm morphology in the latter two cases is attributed to the high temperature in the testicular environment [58]. Low testosterone levels in cryptorchid children during early childhood could also account for poor fertility in adults [59, 60].

2.2.4 Age and Sperm Health

Age does not have a significant impact on sperm morphology; however, a noticeable decrease in sperm motility, semen volume and sperm count have been observed in older men. Reduced testosterone, increased lipid droplets in the testicular environment, arteriosclerotic lesions, thickening and hernia-like protrusions of basal membrane occur increasingly with age. Although numerical chromosomal abnormalities are comparable with that of young men, an increase in structural aberrations is observed in the sperms of older men. Children of elderly fathers show a 20% higher risk for autosome related diseases and neurological disorders, like dwarfism, Huntington's disease, schizophrenia, autism and early onset bipolar disorder (BPD). While children of men over 29 years are susceptible to BPD, children born to men over 54 years were at highest risk, based on a large population study involving inpatient and psychiatric care in Switzerland. These disorders have been attributed to mutation resulting from the many meiotic and mitotic processes experienced by the stem cells. The American Fertility Society has recommended that sperm donor age be limited to men under 50 years [61, 62].

Testes sections from elderly men showed great variation, ranging from healthy to severely damaged, affecting testicular size, tubular volume and quality, Sertoli and Leydig cell functions, sperm count and quality. Men between 50 – 90 years had lower sperm count and lower testosterone levels and higher lipid droplets and crystalline inclusions in the testis, than younger men. Spermatogenesis was found to be regular in some seminiferous tubules and reduced in others; large regions devoid of germ cells were also found. Increased abnormalities in spermatogenesis - multiple sperm heads and high germ cell degeneration that progressively spread from spermatids to spermatogonia, were also observed [63-67].

2.3 History of Artificial Insemination and ART

The success of commercial dairy farms in Europe in 1930s encouraged the UK and the US to invest in AI commercial dairy farm research. Sperm life was prolonged using egg yolks and sodium citrate. Antibiotics were added to semen extenders to prevent transmission of venereal and other disease, and techniques to minimise cold shocks to sperm cells were developed in the US. AI soon converted dairy farms into a multimillion dollar dairy industry. Bull semen was shipped across nations in cooled straws for select breeding of cattle that produced high volume milk. Cold storage using solid CO_2 at -79 ^{o}C was used to cryopreserve and prolong sperm life. In 1949, the UK researchers used glycerol to freeze chicken sperm for the first time. Liquid nitrogen usage for cryopreservation (at -196 ^{o}C) was introduced in 1950s. Since then, sperm cells have been frozen to last many years, paving the way for joint venture of cryopreservation and breeding industry [68, 69].

The breeding industry extended their business into increasing meat revenue. The hormone cycles of the cattle were artificially regulated and synchronised to breed in spring alongside feed crops like corn, using cryopreserved and extended bull semen. During the last quarter of 1900s, cattle feed agriculture and animal farm industry grew rapidly. Meat production soared using minimised labour cost; commercial meat and milk in the developed world increasingly relied on cattle bred using AI [68, 69].

Following the success with cattle, the breeding industry focused on improving the stock of horses, boars, sheep, goats, poultry, guide dogs and endangered species. Sheep and horse and their reproductive cells did not respond well to AI. Inbreeding is common in endangered species living in protected environment, due to limited access to their reproductive cells. High levels of DNA fragmentation were observed in three species of endangered ungulates, as a result of high inbreeding. Species specific AI techniques were developed to improve the reproductive outcome of each species; however, not all the species embraced the technology with ease [68, 70].

AI usage in humans dates back to the late 18th century; Scottish born surgeon, Dr. John Hunter impregnated a woman with her husband's sperm in 1770s. A century later (1884) in America, donor semen was injected into the womb of a woman who had failed to conceive naturally, and this resulted in a live birth. After the birth of the first test tube baby in 1978 using IVF, the use of ART for human reproduction became widely accepted and widespread [69].

2.4 Introduction to Equus Species and Horse Breeding

Horses are single hooved large animals that belong to the *Equus* family which evolved from a small fox-sized animal with multiple hooved toes that lived 45–60 million years ago. Zebras and donkeys are evolutionary cousins of the horse. The zebras with three main sub-species, equus quagga, equus zebra and equus gravyi, have 16, 22 & 23 pairs of chromosomes respectively. Donkeys/asses have three main subspecies, equus hemionus, equus asinus and equus africanus, with 28, 31 and 31 chromosome pairs respectively. Mules, hinnies and zebroids are usually sterile offspring of crossbreeding between horses, asses and zebras. The horses commonly found in the wild, like the Mustang of the Americas and Brumby of Australia, have descended from previously domesticated horses that returned to the wild. The Mongolian wild horse, Przewalskii (Equus ferus przewalskii), found in Central Asia was never tamed, and is an endangered species of the true wild equus. Cross breeding between domestic horse, which has 32 pairs of chromosomes and the Przewalskii which has 33 pairs of chromosomes, produced fertile offspring with 65

chromosomes. The Tarpan (equus ferus ferus) which became extinct in 1875 in the wild in Eurasia, (and in 1919 in captivity) was never domesticated [71-74].

Horses are known to have been domesticated for over 6000 years; they have a species identity *Equus Ferus Caballus* and have an average lifespan of 25 – 30 years. Some horses have lived to be 40 years; there has been a report of a horse that lived to be 62 years. Horses have been raised for their speed, strength and endurance; they have been used in war, hunting, transportation and farm work. They are currently bred for sports and racing in many parts of the world [75].

2.4.1 Equine Reproduction

Spring is the time for foraging for many animal and bird species living in the temperate zones, as trees and plants renew life with the onset of warm temperatures and longer days. As an evolutionary precaution for their reproductive success, spring is also their mating season; and horses are seasonal breeders [75, 76]. Horses show reproductive readiness towards the end of winter, and foals are born in spring. Mares have a pregnancy period of about 11 months and give birth to singletons; rare twin births have also been observed. Foals can walk within a few hours of birth, and attain reproductive capability within a year. Mares are used for breeding after they attain skeletal maturity between 5 to 7 years [77, 78].

Research on pre-puberty testes development and hormonal changes in colts is limited. A study on 15 colts revealed that their average age for reproductive maturity was 83 weeks. Neuroendocrine activity appeared at nine months and testes grew rapidly at 12 months, followed by sperm output. Sperm morphological abnormality is high during early stages of puberty. Sperm count is optimised between 2 to 4 years of age. Serum testosterone level stabilised and serum FSH and LH peaked between 30 to 40 weeks after birth; LH, testosterone, inhibin B and FSH that regulate spermatogenesis are controlled by the HPG-axis and vary with the season. Sperm output is directly related to the testes size; significant variation in testes size between breeds and individual horses have been observed. Stallions reach skeletal maturity between 5 to 6 years of age [77-79].

Age related testicular changes have been observed in 1 to 25 year old stallions [80]. Stallion sperm quality and concentration is linked to sunlight, temperature, stress, environment and food. Basal spermatogonia count increased during the breeding season, resulting in increased sperm output. Semen volume in summer is twice that of winter. Morphologically normal winter sperms have poor membrane integrity. Ovulation declined by 90% in mares, during short winter days [75-79].

Stallions produce sperms throughout their adult life; however, the semen quality declined after 20 years. Breeding regulations in Northern Hemisphere have assigned 1st January as the birthday of foals born throughout that year; foals born earlier in the year have a physical advantage over foals born later in the year. Mares are encouraged to deliver in January and preferably on the 1st. This is a formidable task for the horses, leading to stress and poor pregnancy outcome. AI is an alternative approach to breed horses in winter. Equine reproductive health and behaviour have to be well understood for successful managed breeding with AI [75, 76, 79].

2.4.2 Equine Artificial Insemination and Sperm Cryopreservation

Natural encounter between stallions and mares produced the highest pregnancy rates, even though 30% to 60% pregnancy rates per AI cycle have been achieved. Sperm motility is a powerful indicator of fertility potential in stallions, because 90% of cases reported poor pregnancy with fresh sperms of low motility [81, 82]. During a natural act of procreation, about half a billion sperms are invested in a single mare. In a highly controlled study to minimise sperm wastage; mares were successfully impregnated with about 1000 sperm cells per cycle, with about 50% success rate in inducing pregnancy during each attempt [78].

Statistically significant data on equine gamete characteristics and pregnancy outcome are not available because horse breeding has specific focus for which only a few mares and stallions qualify [83]. Multiple factors - the environment in which the horses are prepared for reproduction, the season and the mare's readiness, contribute to the low equine pregnancy rates with AI. Unlike cattle, where fertility and sperm freezability are the major breeding criteria, horses are bred for their speed

or strength. The mare's reproductive capacity or stallion fertility does not always complement these physical attributes [75].

Managed mares have been made to ovulate during non-breeding seasons with the aid of artificial lights. Mares have not responded well to hormones used to control ovulation; and it has been difficult to precisely time the AI to match the mares' follicular readiness. IVF usage has produced uncertain results in horses. Superovulating the mares, egg maturation and *in-Vitro* manipulation of sperm capacitation has been tricky [84].

The biochemical composition and arrangement of glycoproteins in the ZP is species specific; hence cross species fertilisation is not possible unless they are closely related. Equine sperms have lower efficiency for acrosome reaction or oolemma fusion; the sperms failed to fertilise *in vitro,* equine eggs having intact ZP. The sperms were able to penetrate oocytes that were partially or completely stripped of ZP. Equine oocytes show superior fertilisation and pronuclear formation rate after ICSI. Equine chromatin decondensation rate were tested on bovine, human, equine and porcine gametes, using ICSI; species specific barriers were not observed [85].

Fresh stallion semen has a useful life expectancy between 30 seconds and an hour. The sperm metabolic rate can be slowed down and its useful life extended in low temperature environment. With the use of semen extenders and cooling agents, the semen can be diluted to inseminate many mares at the same time; when kept chilled at 4 ^{o}C, the highly sensitive sperm life expectancy can be extended to about 2 days. Equine semen in extender is as effective as fresh semen, when kept cooled at 5^{o}C and used within 24 hours [75, 78, 86].

The sperm membranes of different species respond to cryopreservation differently due to characteristic membrane phospholipids. The temperature has to be lowered well below freezing, to extend equine sperm life beyond a couple of days. Equine sperm plasma membrane contains 37% more cholesterol than bull sperm's, affecting stallion fertility and freezability. Stallion sperms revealed mixed outcome after cryopreservation; about 20% of the sperms consistently performed well and 20% of the sperms consistently performed badly. The high variation in sperm quality

between breeds, between stallions within a breed and between ejaculates of a stallion, limits the use of a single cryopreservation protocol; the freezing technique has to be tweaked in each case to be affective [83, 86].

Horse sperms are sensitive to cold shocks and even short term chilling reduces sperm motility and pregnancy rates. The critical temperature range for damage is between -5 ^{o}C to -15 ^{o}C. The permeability of the cell membrane and cellular chemical environment is altered when frozen, creating osmotic stress. Membrane phospholipids are susceptible to oxidative stress. Slow cooling increases exposure to osmotic stress and rapid cooling encourages crystal formation that damage plasma and mitochondrial membrane and acrosome sheath. The disulphide bonds rupture on thawing, affecting chromatin compaction. Cryopreserved sperms also tend to have higher membrane damage during centrifugation. Cryopreserved winter sperms with normal shape, suffered high acrosome damage, indicating poor membrane integrity. The sperm membrane and DNA damage affect cell motility and pregnancy rate; a trade-off is required to minimise overall sperm damage [75, 78, 86-88].

Rapid thawing within seconds followed by incubation at 37 ^{o}C has been shown to reduce membrane damage, increase cell viability, minimise premature acrosome reaction and improve forward motility in cryopreserved equine sperm samples [89]. Vitrification is a process by which sperms are dehydrated and rapidly frozen by plunging the cells in liquid nitrogen; this cryopreservation technique has met with some success. Programmed cooling and thawing at different rates for different temperature range has also been evaluated for optimal cell performance. Despite these detailed protocols, there is significant stallion to stallion and ejaculate to ejaculate variation in the sperm response to cryopreservation, that makes the process difficult to implement uniformly across the board [75, 78].

Semen extenders and additives have been researched for improving cooling techniques. Different antioxidants added to sperm medium have helped to improve post thaw motility and viability of the sperms from different mammals. Addition of α-tocopherol has been found to protect equine sperms from cryopreservation induced membrane damage. Addition of superoxide dismutase (SOD) increased sperm DNA damage; H_2O_2 by-product from the enzyme is implicated [90]. Egg yolk, sugar and

glycerol have been identified as sperm-friendly cryoprotectants that do not damage the cells. Antioxidants, egg yolk and milk added to sperm media or semen extenders simulate the protective role of semen plasma. Antibiotics are also added to protect against infection during AI and to protect the cells from bacteria or other toxic contaminants incorporated during sperm collection [75, 78, 83].

Sperm concentration, morphology, motility, mitochondrial and membrane integrity, and cryopreservation affects were tested in fresh, centrifuged and freeze-thawed sperms, to characterise sperm function and to correlate it with pregnancy outcome. Acrosome binding antibodies and immunoflourescent tests were used to evaluate plasma-acrosome membrane integrity. Multiple motion parameters and high speed motion tracking software were used to evaluate motility. Cryopreserved and thawed stallion sperms had shorter lifespan and suffered higher membrane damage that reduced their progressive motility; this did not negatively affect their fertilisability. Statistically significant tests on cryopreserved sperms did not predict pregnancy outcome consistently. Morphology and motility were not pregnancy predictors. Sperm concentration tests were inconclusive, as low concentration was compensated with additional straws. Excess sperms caused reaction in the uterus, negatively impacting the pregnancy. Membrane integrity and progressive motility consistently declined after each process step. Freeze-thaw produced maximum change in motility and these varied between collections and between stallions [83, 88, 91].

The first equine birth using AI was reported in 1956. Cryopreserved (at -79 ^{o}C) epididymal sperms extracted from castrated testes of a 2 year old Belgian stallion was injected into a 10 year old mare. Seven mares and epididymal sperms from two stallions were used in this first AI attempt that resulted in a single pregnancy [92].

2.5 Stallion Spermatozoon

The developmental stages of stallion germ cells in the seminiferous tubules are similar to human germ cells. The seminiferous tubules contain spermatogonia, spermatocytes, spermatids and motile haploid spermatozoa. Seasonal variation in degeneration rates of germ cells have been observed, with high cell counts in Summer [75, 78].

The sperm output of stallions with normal fertility is about the same in the two testes. Cell type apoptosis was evaluated in testes cross sections from 4 – 17 year old stallions of normal fertility; spermatogenetic efficiency was approximately 50% in fertile stallions [93].

Horse sperms resemble human sperms anatomically but are slightly larger in size (**Figure 2.5**). The cell has a long flagella powered by the mitochondria. The sperm length is 60-65 μm from head to tail. The flattened spear shaped head is 6-7 μm long and 3.5 – 4 μm wide and contains tightly packed chromatins. The proximal centriole is housed in the flexible neck. The midpiece is 8 - 10.5 μm long and 0.6 μm wide and contains 50 turns of double helical arrangement of several mitochondria. The principal piece is 30 to 44 μm long and the end piece is 4-5 μm in length. The axoneme originates at the base of the distal centriole in the neck, to form the flagella; it consists of nine pairs of doublet microtubules surrounded by a central pair of microtubules. Off-centred tail is common and morphologically acceptable; they execute wide circular motion. The stallion cells suffer thermal shock during semen extraction, resulting in sperms with bent neck and coiled tails [78, 94].

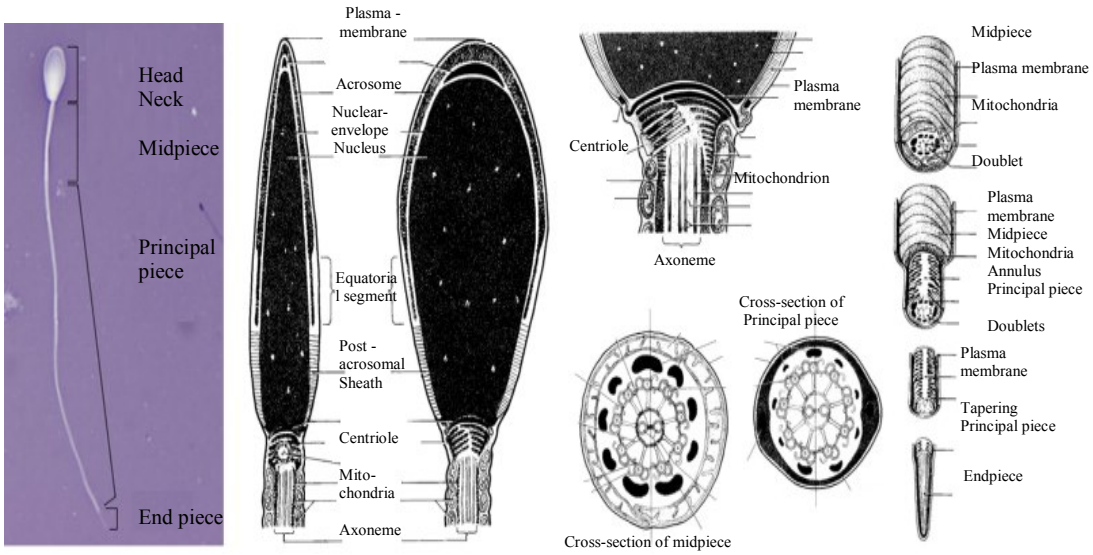

Figure 2.2: Anatomy of stallion spermatozoon [94]

Like human sperms, the stallion sperm head is two-thirds covered with the acrosomal cap. During natural breeding, equine sperms undergo capacitation in the mare's reproductive tracts. Typical stallion semen motility parameter for AI is 30-65% with a minimum of 35% progressive motility. Sperm head morphology varies between stallions. The sperm head shape is determined by the nuclear shape; and there is direct correlation between head defects and pregnancy failure rates. Large sperm head size is associated with subfertility. Long and narrow headed sperms have been found in subfertile stallions with lower sperm concentration and motility. Randomly distributed nuclear vacuoles have been observed in some sperms and these form during nuclear condensation [94, 95].

In a North Carolina based study, no significant seasonal difference in sperm morphology, concentration or motility was observed in fresh sperms; however, the cryopreserved sperms showed seasonal variation, with higher morphology and motility seen in the sperms collected during breeding season [96].

Equine sperms at different stages of development have different tolerance to temperature and endocrine disturbances. Illness, changes in nutrition, long distance transportation and unfamiliar environment create stress that disturb their hormones, and raise cortisol levels that cause sperm malformation. High temperature and hormonal disturbances cause mild testicular and sperm degeneration. Like humans, the testicular environment is kept 3-5 ^{o}C cooler than body core temperature. High environmental heat, excessive exercise and fever can expose the testes to increased temperature and cause damage to the sperms. Cryptorchidism, scrotal oedema and excess fat around the spermatic cord, act as temperature traps. Testosterones have been used for muscle growth in horses, and progestrogens have been used to suppress natural stallion playfulness that was perceived as aggression by their keepers; and these treatments have affected their sperm output. Sperm production returned to normalcy after a few months when these hormone treatments were stopped [94].

2.5.1 Stallion Sperm Nucleus

Protamines, P1 are found in all mammalian sperm chromatins. The number of P1 amino acid residues range from 47 to 50 in the mammals, with 52% - 54% having arginine rich amino acid residue and 12-18% having cysteine in the residue. The family of protamines known as P2 are found in the sperm nucleus of only a small subgroup of the placental mammals; their structure varies significantly between species. It is speculated that the primary role of P1 protamines is DNA binding and that P2 may have, in addition, a transcriptional role. Zinc is essential for sperm condensation, and has been found in the sperms of a few mammalian species, including human and horse. However, high zinc concentration is also associated with infertility in humans. Stallion ejaculate sperms have lower zinc content than testicular sperms - an indicating that the epididymal fluid absorbs some of the weakly bound zinc during disulphide bond formation in the epididymis [97-104].

Sperms specific histones have not been found in stallions; and this accounts for the tight cholesteric liquid crystal organisation observed in some stallion sperms. Highly organised triple layered chromatin packaging arrangement has also been found in stallion sperms and the nucleus also shows birefringence characteristics. This type of symmetry is absent in somatic cell nucleus or mammalian sperm nucleus with histones; human sperms exhibit HPC structure. Stallion sperm chromatins are highly resistant to decondensation as a result of this histone-free tight packaging. The disulphide bonds, dithiothreitol (DTT), decondense progressively from the apex of the head to the base of the neck, and from the periphery to the centre of the nucleus, during decondensation [105, 106].

2.6 Comparison of Horse and Human Sperm Cells

Unlike humans, horses are seasonal breeders and pregnancy rates are high in Feb-April [81]. Humans use AI for infertility treatment. AI and cryopreserved semen are used for breeding race horses out of season. Stallion infertility rate is 33%, with mare uterine and egg quality accounting for nearly 67% of the infertility. Male and female infertility in humans are comparable. The room temperature useful life of fresh horse sperms is 2 hours while that of human sperms is 48 hours [107].

Sperm concentration above 20 million per ml with 10% morphological normalcy is the baseline criteria for normal human male fertility. There are no established criteria for stallion fertility; 30-35% motile sperms, greater than 50% morphological normalcy and progressive motility are acceptable for commercial AI usage, provided the live/dead ratio is at least 6:4. Sperm concentration of 100 – 500 million cells per ml with at least 70% live cells and over 50% morphological normalcy are considered appropriate for stallion sperm cryopreservation. In the Netherlands, 300 million cells per ml showing progressive motility and morphological normalcy are required for commercial sale of frozen sperms. Forward motility, head shape, size and ratio are used to assess stallion and human sperm fertility. Motility degradation with time is used as a parameter to test stallion sperm quality. If 45% of the cells remained viable after 3hrs, and 10% remain viable after 8 hours, the specimens are considered acceptable for AI [78].

Both human and horse sperm nuclear DNA are packaged by protamines. Human P1 (HP1) is composed of 50 basic proteins with a higher arginine repeat sequence in the centre than in the periphery; it has 24 arginine and 6 cysteine basic protein residues. The larger P2 family of protamines - HP2, HP3 & HP4 have 57, 54 & 58 proteins respectively; they differ only in their N-terminal sequence, with 54 common sequences [108, 109]. HP2 has species specific binding sites that are different from HP1 binding sites. HP4 has 27 arginine and 5 cysteine components [110]. Unlike HP1, HP2 lacks tyrosine, has zinc binding sites and histidine residues [111, 112]. The ratio of HP2 : HP3 was difficult to resolve experimentally, but appeared to be 3:1 in normal fertility [32]. The distribution of protamine to DNA in sperms of normal fertility is 20%; higher ratio of protamines have been found in sperms of infertile men [113, 114].

Mature horse sperm DNA is packaged by both P1 (St1) and family of P2 (St2a and St2b); these differ by the amino acid sequence and content. St1 consists of 49 basic proteins [102, 115]. Stallion sperm DNA is packaged by 75% St1, 25% St2a and St2b [103, 116-119]. St2a and St2b have 27 arginine and 7 cysteine residues; the stallion sperm chromatin has very tight binding [115]. A comparison of the average human and stallion sperm parameters is provided in **Table 2.1.**

Characteristics	Human	Horse
Average sperm concentration cells/mL	60 million	600 million
Sperm head l/w	4.5/2.5	6.5/3.75
Sperm length	45 - 50 microns	60 - 65 microns
Chromosomes (haploid)	23	32
Sperm nuclear histones	10-15%	None
Sperm nuclear protamine-1	HP1	St1
P1: Amino acid sequences	**HP1 50** Arginine = 24 Cysteine = 6 Histidine = 1	**St1 49** Arginine = 27 Cysteine = 7 Histidine = 2
Protamine-2	P2: majority P3: 33%)?? P4: ??	St2a: 85% St2b: 14%
Protamine-1 : Protamine-2 ratio	~1:1	~3:1
P2 Amino acid residue	**HP2 57** Arginine = 27 Cysteine = 5 Histidine = 9	**St2a 62** Arginine = 27 Cysteine = 7 Histidine = ?
P3 Amino acid residue	**HP3 54** Arginine = 26 Cysteine = 5 Histidine = 8	**St2b 58** Arginine = 27 Cysteine = 7 Histidine = ?
P4 Amino acid residue	**HP4 58** Arginine = 27 Cysteine = 5 Histidine = 9	---

Table 2.1: Comparison of stallion and human sperms [102, 103, 111, 112, 116, 120, 121]

2.7 Chapter Two Conclusions

A simple set of underlying factors that contributes to infertility could not be identified, during this literature review. Sperm DNA damage/fragmentation has been consistently observed in male factor infertility; however the molecular level understanding of the type and nature of DNA fragmentation is still in its infancy. DNA damaged sperms fertilised eggs, but blastocyst development requires the participation of intra-species genomes – healthy DNA of both sperm and egg.

The protamine content and ratio has to be right for natural pregnancy and conventional IVF, but has no known impact on embryo development or ICSI outcome. Protamines provide a protective environment for the paternal genomes to mature. Can protamine less sperms be used in IVF successfully? High density sperms are morphologically superior but the density is not a criterion in sub fertility. Can the sperm density be influenced by the chromosomes? The presence of the large X chromosome in the 23, X sperm will make it denser than the 23, Y sperm. Is there an increased occurrence of female children born through density gradient selection of sperms? Such questions are worthy of investigation, though a digression to this thesis.

The precise nature of sperm-egg interaction in pregnancy is not clearly explained. Does the entire sperm, including the tail, enter the egg? Sperm equatorial proteins have a role in binding. Does the sperm plasma or nuclear membrane enter the egg or does it engage with the oolemma to form an extension of its envelope?

The absence of acrosome cap does not impact ICSI outcome. The acrosome content does not enter the egg in a natural pregnancy; it is not clear how it is discarded during ICSI. Can acrosome in the egg do damage to the foetus or cause pregnancy failure, or is the large chemical environment inside the egg capable of neutralising its toxicity?

The history of AI and its challenges in breeding was also helpful in understanding the technological progress that led to infertility treatment. While there are significant differences between horse and human sperms - the absence of histones, for example - the similarities dominate.

Stallion sperms were used in the major stress damage study described in **Chapter Five**, and this review has been critical in gaining insight into sperm molecular structure and content and the known factors that contribute to sperm health, DNA damage and infertility. Human sperms were used in the minor experimental study that compared cryopreserved, swim-up and fresh cells. The contents of this chapter have been necessary to comprehend published work on the subject. The review has helped to prepare the groundwork for identifying similarities and differences in the Raman spectra of horse and human.

Even though the horse and human are different species, the two sperm tales contribute to a better to understanding of the cellular and molecular nature of these cells than either of the tales reveal on their own. Together, the human and the horse sperms have added more light on the mystery and complexity of life, reproduction and infertility. In spite of the detailed work and literature on these cells, the knowledge at the molecular level, or even cellular level is in its infancy and more questions remain unanswered than before the start of this review.

Reference

1. Alberts, B., et al., *Molecular Biology of The Cell*. Fourth ed. 2002, New York: Garland Science.
2. Capmany, G., et al., *Cell Cycle regulations: The timing of pronuclear formation, DNA synthesis and cleavage in the human 1-cell embryo.* Mol. Hum. Reprod., 1996. **2**(5): p. 299-306.
3. Van Montfoort, A.P.A., et al., *Early cleavage is a valuable addition to existing embryo selection parameters: a study using single embryo transfers.* Hum. Reprod., 2004. **19**(9): p. 2103-2108.
4. Gianaroli, L., M.C. Magli, and A.P. Ferraretti, *Sperm and Blastomere Aneuploidy Detection in Reproductive Genetics and Medicine.* J. Histochem. Cytochem., 2005. **53**(3): p. 261-267.
5. Scott, H.M., J.I. Mason, and R.M. Sharpe, ***Steroidogenesis in the Fetal Testis and Its Susceptibility to Disruption by Exogenous Compounds***. Endocrine Reviews, 2009. **30**(7): p. 43.
6. Hughes, P.I.A., *How vulnerable is the developing testis to the external environment?* Archives of Disease in Childhood, 2000. **83**(4): p. 281-282.
7. Robinson, L.L.L., J. Townsend, and R.A. Anderson, *The Human Fetal Testis Is a Site of Expression of Neurotrophins and Their Receptors: Regulation of the Germ Cell and Peritubular Cell Population.* J Clin Endocrinol Metab, 2003. **88**(8): p. 3943-3951.
8. World Health Organisation, ed. *WHO Laboratory Manual for the Examination of Human Semen and Sperm-Cervical Mucus Interaction*. 4 ed., ed. W.H. Organization. 1999, Cambridge University Press, UK. 128.
9. Balhorn, R., L. Brewer, and M. Corzett, *DNA Condensation by Protamine and Arginine-Rich Peptides: Analysis of Toroid Stability Using Single DNA Molecules.* Molecular Reproduction And Development 2000. **56**: p. 230-234.
10. Bedu-Addo, K., et al., *Mobilisation of stored calcium in the neck region of human sperm – a mechanism for regulation of flagellar activity.* International Journal of Developmental Biology, 2008. **52**: p. 615-626.
11. Lhuillier, P., et al., *Absence of annulus in human asthenozoospermia: Case Report.* Hum. Reprod., 2009. **24**(6): p. 1296-1303.
12. Stevens, A. and J. Lowe, *Human Histology*. 1997: Mosby (imprint from Times Mirror). 408.
13. Sharpe, R.M., *Natural and anthropogenic environmental oestrogens: the scientific basis for risk assessment. Environmental estrogens and male infertility.* Pure & Applied Chemistry, 1998. **70**(9): p. 1685-1701.
14. Sharpe, R.M. and D.S. Irvine, *How strong is the evidence of a link between environmental chemicals and adverse effects on human reproductive health?* BMJ, 2004. **328**(7437): p. 447-451.
15. Jurewicz J, H.W., Radwan M, Bonde JP., *Environmental factors and semen quality.* International journal of occupational medicine and environmental health, 2010 **6**: p. 1-25.
16. Agarwal, A. and S.A. Prabakaran, *Mechanism, measurement, and prevention of oxidative stress in male reproductive physiology.* Indian Journal of Experimental Biology, 2005. **43**: p. 963-974.
17. Bian, Q., et al., *Study on the relation between occupational fenvalerate exposure and spermatozoa DNA damage of pesticide factory workers.* Occuppational and Environmental Medicine, 2004. **61**(12): p. 999-1005.
18. Jorgensen, N., et al., *Regional differences in semen quality in Europe.* Human Reproduction, 2001. **16**(5): p. 1012-1019.
19. Joensen, U.N.m., et al., *Do Perfluoroalkyl Compounds Impair Human Semen Quality?* Environ Health Perspect, 2009. **117**(6).
20. Migliore, L., et al., *Assessment of sperm DNA integrity in workers exposed to styrene.* Hum. Reprod., 2002. **17**(11): p. 2912-2918.
21. Sepaniak, S., et al., *The influence of cigarette smoking on human sperm quality and DNA fragmentation.* Toxicology, 2006. **223**(1-2): p. 54-60.
22. Eskenazi, B., et al., *The association of age and semen quality in healthy men.* Human Reproduction, 2003. **18**(2): p. 447-454.

23. Slama, R., et al., *Influence of Paternal Age on the Risk of Spontaneous Abortion.* Am. J. Epidemiol., 2005. **161**(9): p. 816-823.
24. Wyrobek, A.J., et al., *Advancing age has differential effects on DNA damage, chromatin integrity, gene mutations, and aneuploidies in sperm.* Proceedings of the National Academy of Sciences, 2006. **103**(25): p. 9601-9606.
25. Winkle, T., et al., *The correlation between male age, sperm quality and sperm DNA fragmentation in 320 men attending a fertility center.* Journal of Assisted Reproduction and Genetics, 2009. **26**(1): p. 41-46.
26. Sartorius, G.A. and E. Nieschlag, *Paternal age and reproduction.* Hum Reprod Update, 2009: p. dmp027.
27. Stewart, T.M., et al., *Associations between andrological measures, hormones and semen quality in fertile Australian men: inverse relationship between obesity and sperm output.* Hum. Reprod., 2009. **24**(7): p. 1561-1568.
28. Magnusdottir, E.V., et al., *Persistent organochlorines, sedentary occupation, obesity and human male subfertility.* Hum. Reprod., 2005. **20**(1): p. 208-215.
29. Meirow, D. and J.G. Schenker, *Infertility: Cancer and male infertility.* Hum. Reprod., 1995. **10**(8): p. 2017-2022.
30. Tempest, H.G., et al., *Sperm aneuploidy frequencies analysed before and after chemotherapy in testicular cancer and Hodgkin's lymphoma patients.* Hum. Reprod., 2008. **23**(2): p. 251-258.
31. Meseguer, M., et al., *The effect of cancer on sperm DNA fragmentation as measured by the sperm chromatin dispersion test.* Fertility and Sterility, 2008. **90**(1): p. 225-227.
32. Balhorn, R., S. Reed, and N. Tanphaichitr, *Aberrant protamine 1/protamine 2 ratios in sperm of infertile human males.* Cellular and Molecular Life Sciences, 1988. **44**(1): p. 52-55.
33. Carrell, D.T. and L. Liu, *Altered protamine 2 expression is uncommon in donors of known fertility, but common among men with poor fertilizing capacity, and may reflect other abnormalities of spermiogenesis.* J Androl, 2001. **22**(4): p. 604-610.
34. Aoki, V.W., L. Liu, and D.T. Carrell, *Identification and evaluation of a novel sperm protamine abnormality in a population of infertile males.* Human Reproduction, 2005. **20**(5): p. 1298-1306.
35. Yoshii, T., et al., *Fine resolution of human sperm nucleoproteins by two-dimensional electrophoresis.* Mol. Hum. Reprod., 2005. **11**(9): p. 677-681.
36. Tanaka, H., et al., *Single nucleotide polymorphisms in the protamine-1 and -2 genes of fertile and infertile human male populations.* Mol. Hum. Reprod., 2003. **9**(2): p. 69-73.
37. García-Peiró, A., et al., *Protamine 1 to protamine 2 ratio correlates with dynamic aspects of DNA fragmentation in human sperm.* Fertility and Sterility, 2010. **In Press, Corrected Proof**.
38. Aoki, V.W., et al., *Protamine Levels Vary Between Individual Sperm Cells of Infertile Human Males and Correlate With Viability and DNA Integrity.* J Androl, 2006. **27**(6): p. 890-898.
39. Aoki, V.W., L. Liu, and D.T. Carrell, *A novel mechanism of protamine expression deregulation highlighted by abnormal protamine transcript retention in infertile human males with sperm protamine deficiency.* Mol. Hum. Reprod., 2006. **12**(1): p. 41-50.
40. García-Peiró, A., et al., *Protamine 1 to protamine 2 ratio correlates with dynamic aspects of DNA fragmentation in human sperm.* Fertility and Sterility 2011. **95**(1): p. 105-109.
41. Hammadeh, M.E., et al., *Protamine contents and P1/P2 ratio in human spermatozoa from smokers and non-smokers.* Human Reproduction, 2010: p. 1-13.
42. Holstein, A.-F., W. Schulze, and M. Davidoff, *Understanding spermatogenesis is a prerequisite for treatment.* Reproductive Biology and Endocrinology, 2003. **1**(1): p. 107.
43. Winters, S.J., et al., *Inhibin-B Levels in Healthy Young Adult Men and Prepubertal Boys: Is Obesity the Cause for the Contemporary Decline in Sperm Count Because of Fewer Sertoli Cells?* J Androl, 2006. **27**(4): p. 560-564.
44. Stewart, T.M., et al., *Associations between andrological measures, hormones and semen quality in fertile Australian men: inverse relationship between obesity and sperm output.* Human Reproduction, 2009. **24**(7): p. 1561-1568.
45. Sotolongo, B., et al., *An Endogenous Nuclease in Hamster, Mouse, and Human Spermatozoa Cleaves DNA into Loop-Sized Fragments.* Journal of Andrology, , 2005. **26**(2): p. 272 - 280.
46. Ramlau-Hansen, C.H., et al., *Maternal alcohol consumption during pregnancy and semen quality in the male offspring: two decades of follow-up.* Human Reproduction, 2010: p. 140.

47. Nakamura, S., et al., *A trial to restore defective human sperm centrosomal function.* Hum. Reprod., 2005. **20**(7): p. 1933-1937.
48. Manandhar, G., C. Simerly, and G. Schatten, *Highly degenerated distal centrioles in rhesus and human spermatozoa.* Human Reproduction, 2000. **15**(2): p. 256-263.
49. Baccetti B, Burrini AG, and P. V., *Spermatozoa and cilia lacking axoneme in an infertile man.* Andrologia, 1980. **12**(6): p. 525-32.
50. Neugebauer, D.C., et al., *'9 + 0' Axoneme in spermatozoa and some nasal cilia of a patient with totally immotile spermatozoa associated with thickened sheath and short midpiece.* Hum. Reprod., 1990. **5**(8): p. 981-986.
51. Richard J. Kordus, et al., *Successful twin birth following blastocyst culture of embryos derived from the immotile ejaculated spermatozoa from a patient with primary ciliary dyskinesia: A case report.* Journal of Assisted Reproduction and Genetics 2008. **25**(9-10): p. 437-443.
52. Ugajin, T., et al., *The shape of the sperm midpiece in intracytoplasmic morphologically selected sperm injection relates sperm centrosomal function.* Journal of Assisted Reproduction and Genetics, 2009. **27**(2): p. 75-81.
53. Yogev, L., et al., *Long-term cryostorage of sperm in a human sperm bank does not damage progressive motility concentration.* Hum. Reprod., 2010: p. deq041.
54. Bilodeau, J.-F., et al., *Levels of antioxidant defenses are decreased in bovine spermatozoa after a cycle of freezing and thawing.* Molecular Reproduction and Development, 2000. **55**(3): p. 282-288.
55. O'Flynn O'Brien, K.L., A.C. Varghese, and A. Agarwal, *The genetic causes of male factor infertility: A review.* Fertility and Sterility. **93**(1): p. 1-12.
56. Kerr, C.L. and L. Cheng, *The Dazzle in Germ Cell Differentiation.* J Mol Cell Biol, 2010. **2**(1): p. 26-29.
57. Brekhman, V., et al., *The DAZL1 gene is expressed in human male and female embryonic gonads before meiosis.* Molecular Human Reproduction, 2000. **6**(5): p. 465-468.
58. Dada, R., N.P. Gupta, and K. Kucheriac, *Yq Microdeletions—Azoospermia Factor Candidate Genes and Spermatogenic Arrest.* Journal of Biomolecular Techniques, 2004. **15** (3): p. 176-183.
59. Dunkel, L., V. Hirvonen, and K. Erkkilä, *Clinical aspects of male germ cell apoptosis during testis development and spermatogenesis.* Nature, 1997. **4**(3): p. 171-179.
60. Hadziselimović, F. and B. Herzog, *Treatment with a luteinizing hormone-releasing hormone analogue after successful orchiopexy markedly improves the chance of fertility later in life.* The Journal of urology, 1997. **158**(3 Pt 2): p. 1193-5.
61. Plas, E., et al., *Effects of aging on male fertility?* Experimental Gerontology, 2000. **35**(5): p. 543-551.
62. Frans, E.M., et al., *Advancing Paternal Age and Bipolar Disorder.* Arch Gen Psychiatry, 2008. **65**(9): p. 1034-1040.
63. Paniagua, R., et al., *Ultrastructure of the aging human testis.* Journal of Electron Microscopy Technique, 1991. **19**(2): p. 241-260.
64. Trainer, T.D., *Histology of the Normal Testis.* The American Journal of Surgical Pathology, 1987. **11**(10): p. 797-809.
65. Amann, R.P., *The Cycle of the Seminiferous Epithelium in Humans: A Need to Revisit?* J Androl, 2008. **29**(5): p. 469-487.
66. Anand-Ivell, R., et al., *Peripheral INSL3 concentrations decline with age in a large population of Australian men.* International Journal of Andrology, 2006. **29**(6): p. 618-626.
67. Schulze, W. and C. Schulze, *Multinucleate Sertoli cells in aged human testis.* Cell and Tissue Research, 1981. **217**(2): p. 259-266.
68. Foote, R.H., *The history of artificial insemination: Selected notes and notables.* Journal of Animal Science, 2002. **80**(E-Suppl_2): p. 1-10.
69. Ombelet, W. and J. Van Robays, *History of Human Artificial Inseminaton*, in *Facts Views and Vision in ObGyn*. 2010, Artificial Insemination: Belgium. p. 5.
70. Ruiz-Lopez, M.J., et al., *High Levels of DNA Fragmentation in Spermatozoa Are Associated with Inbreeding and Poor Sperm Quality in Endangered Ungulates.* Biology of Reproduction, 2010. **83**(3): p. 332-338.
71. Fredga, K., *Chromosomal Changes in Vertebrate Evolution.* Proceedings of the Royal Society of London. Series B, Biological Sciences, 1977. **199**(1136): p. 377-397.

72. Buckland, R.A., J.M. Fletcher, and A.C. Chandley, *Characterization of the domestic horse 'Equus caballus' karyotype using G-and C-banding techniques.* Cellular and Molecular Life Sciences, 1976. **32**(9): p. 1146-1149.
73. Trujillo, J.M., et al., *Cromosomes of the horse, the donkey, and the mule.* Chromosoma, 1962. **13**(3): p. 243-248.
74. Lear, T.L. and E. Bailey, *Equine clinical cytogenetics: the past and future.* Cytogenetic and Genome Research, 2008. **120**(1-2): p. 42-49.
75. Mina, C.G. and D. Morel, *Equine Reproductive Physiology, Breeding and Stud Management*. Third ed. 2008: CAB International
76. Nagy, P., D. Guillaume, and P. Daels, *Seasonality in mares.* Animal Reproduction Science, 2000. **60-61**: p. 245-262.
77. McKinnon, A.O. and J.L. Voss, eds. *Equine Reproduction*. 2005, Blackwell Publishing.
78. Samper, J.C., *Equine Breeding Management and Artificial Insemination* 2ed. 2009: Elsevier.
79. Blottner, S., et al., *Morphological and functional changes of stallion spermatozoa after cryopreservation during breeding and non-breeding season.* Animal Reproduction Science, 2001. **65**(1-2): p. 75-88.
80. Jones, L.S. and W.E. Berndtson, *A quantitative study of Sertoli cell and germ cell populations as related to sexual development and aging in the stallion.* Biology of Reproduction, 1986. **35**(1): p. 138-148.
81. Blanchard, T.L., et al., *Some Factors Associated With Fertility of Thoroughbred Stallions.* Journal of Equine Veterinary Science, 2010. **30**(8): p. 407-418.
82. Vidament, M., et al., *Equine frozen semen freezability and fertility field results.* Theriogenology, 1997. **48**: p. 907 - 917.
83. Kuisma, P., et al., *Fertility of frozen-thawed stallion semen cannot be predicted by the currently used laboratory methods.* Acta Veterinaria Scandinavica, 2006. **48**(1): p. 14.
84. Galli, C., et al., *Pregnancy: A cloned horse born to its dam twin.* Nature, 2003. **424**(6949): p. 635-635.
85. Mugnier, S., et al., *New Insights into the Mechanisms of Fertilization: Comparison of the Fertilization Steps, Composition, and Structure of the Zona Pellucida Between Horses and Pigs.* Biology of Reproduction, 2009. **81**(5): p. 856-870.
86. Aurich, C., *Factors affecting the plasma membrane function of cooled-stored stallion spermatozoa.* Animal Reproduction Science, 2005. **89**(1-4): p. 65-75.
87. Meyers, S.A., *Spermatozoal response to osmotic stress.* Animal reproduction science, 2005. **89**(1): p. 57-64.
88. Sardoy, M.C., M.I. Carretero, and D.M. Neild, *Evaluation of stallion sperm DNA alterations during cryopreservation using toluidine blue.* Animal Reproduction Science, 2008. **107**(3-4): p. 349-350.
89. Bradford, L.L. and M.M. Buhr, *Function of cryopreserved horse semen is improved by optimized thawing rates.* Journal of Equine Veterinary Science, 2002. **22**(12): p. 546-550.
90. Baumber, J., B.A. Ball, and J.J. Linfor, *Assessment of the cryopreservation of equine spermatozoa in the presence of enzyme scavengers and antioxidants.* American Journal of Veterinary Research, 2005. **66**(5): p. 772-779.
91. Blach, E.L., et al., *Changes in quality of stallion spermatozoa during cryopreservation: Plasma membrane integrity and motion characteristics.* Theriogenology, 1989. **31**(2): p. 283-298.
92. Barker, C.A.V. and J.C.C. Gandier, *Pregnancy In A Mare Resulting From Frozen Epididymal Spermatozoa.* Canadian Journal of Comparative Medicine, 1957. **XXI**(2): p. 47-51.
93. Heninger, N.L., et al., *Germ cell apoptosis in the testes of normal stallions.* Theriogenology, 2004. **62**(1-2): p. 283-297.
94. Brito, L.F.C., *Evaluation of Stallion Sperm Morphology.* Clinical Techniques in Equine Practice, 2007. **6**(4): p. 249-264.
95. Casey, P.J., et al., *Morphometric differences in sperm head dimensions of fertile and subfertile stallions.* Theriogenology, 1997. **47**(2): p. 575-582.
96. Wrencha, N., et al., *Effect of season on fresh and cryopreserved stallion semen.* Animal Reproduction Science, 2010. **119** p. 219-227.
97. Dadoune, J.-P., *Expression of mammalian spermatozoal nucleoproteins.* Microscopy Research and Technique, 2003. **61**(1): p. 56-75.

98. McKay, D.J., B.S. Renaux, and G.H. Dixon, *The amino acid sequence of human sperm protamine P1.* Bioscience Reports, 1985. **5**(5): p. 383-391.
99. Balhorn, R., *The protamine family of sperm nuclear proteins.* . Genome Biology, 2007. **8** (9): p. 227.
100. Bench, G.S., et al., *DNA and total protamine masses in individual sperm from fertile mammalian subjects.* Cytometry, 1996. **23**(4): p. 263-271.
101. Love, C.C. and R.M. Kenney, *Scrotal Heat Stress Induces Altered Sperm Chromatin Structure Associated with a Decrease in Protamine Disulfide Bonding in the Stallion.* Biol Reprod, 1999. **60**(3): p. 615-620.
102. Ammer, H. and A. Henschen, *The major protamine from stallion sperm. Isolation and amino-acid sequence.* Biological Chemistry Hoppe-Seyler, 1987. **368**(12): p. 1619-26.
103. Bélaïche, D., et al., *Isolation and characterization of two protamines St1 and St2 from stallion spermatozoa, and amino-acid sequence of the major protamine St1.* Biochimica et Biophysica Acta (BBA) - Protein Structure and Molecular Enzymology, 1987. **913**(2): p. 145-149.
104. Corzett, M., J. Mazrimas, and R. Balhorn, *Protamine 1: Protamine 2 stoichiometry in the sperm of eutherian mammals* Molecular Reproduction and Development, 2002. **61**(4): p. 519-527.
105. Livolant, F., *Cholesteric organization of DNA in the stallion sperm head.* Tissue and Cell, 1984. **16**(4): p. 535-555.
106. Blanc, N.S., et al., *DNA in Human and Stallion Spermatozoa Forms Local Hexagonal Packing with Twist and Many Defects.* Journal of Structural Biology 2001. **134**: p. 76-81.
107. Gravance, C.G., et al., *Sperm head morphometry analysis of ejaculate and dismount stallion semen samples.* Animal Reproduction Science, 1997. **47**(1-2): p. 149-155.
108. de Yebra, L., et al., *Detection of P2 Precursors in the Sperm Cells of Infertile Patients Who Have Reduced Protamine P2 Levels.* Fertility and Sterility, 1998. **69**(4): p. 755-759.
109. Oliva, R., *Protamines and male infertility.* Human reproduction update, 2006. **12**(4): p. 417-35.
110. Oliva, R., *Protamines and male infertility.* Hum Reprod Update, 2006. **12**: p. 417 - 435.
111. Ammer H, Henschen A, and L. CH., *Isolation and amino-acid sequence analysis of human sperm protamines P1 and P2. Occurrence of two forms of protamine P2.* Biological Chemistry Hoppe Seyler, 1986. **367**(6): p. 515-22.
112. Arkhis, A., et al., *Molecular structure of human protamine P4 (HP4), a minor basic protein of human sperm nuclei.* European Journal of Biochemistry, 1991. **200**(2): p. 387-392.
113. Castillo, J., et al., *Protamine/DNA Ratios and DNA Damage in Native and Density Gradient Centrifuged Sperm From Infertile Patients.* J Androl, 2011. **32**(3): p. 324-332.
114. Mengual, L., et al., *Marked Differences in Protamine Content and P1/P2 Ratios in Sperm Cells From Percoll Fractions Between Patients and Controls.* J Androl, 2003. **24**(3): p. 438-447.
115. Pirhonen, A., et al., *Protamine P1 sequences in equids: comparison with even-toed animals.* Theriogenology, 2002. **58**(5): p. 1007-1015.
116. Pirhonen, A., et al., *Primary structures of two protamine 2 variants (St2a and St2b) from stallion spermatozoa.* Biochimica et Biophysica Acta (BBA) - Protein Structure and Molecular Enzymology, 1990. **1039**(2): p. 177-180.
117. Pirhonen, A., A. Linnala-Kankkunen, and P.H. Mäenpää, *Comparison of partial amino acid sequences of two protamine 2 variants from stallion sperm Structural evidence that the variants are products of different genes.* FEBS Letters, 1989. **244**(1): p. 199-202.
118. Sabeur, K., et al., *Characterization of a novel, testis-specific equine serine/threonine kinase.* Molecular Reproduction and Development, 2008. **75**(5): p. 867-873.
119. Pirhonen, A., A. Linnala-Kankkunen, and P.H. Maenpaa, *Identification of Phosphoseryl Residues in Protamines from Mature Mammalian Spermatozoa.* Biology Of Reproduction, 1994. **50**: p. 981-986.
120. Pesch, S. and M. Bergmann, *Structure of mammalian spermatozoa in respect to viability, fertility and cryopreservation.* Micron, 2006. **37**(7): p. 597-612.
121. McKay, D.J., B.S. Renaux, and G.H. Dixon, *Human sperm protamines.* European Journal of Biochemistry, 1986. **156**(1): p. 5-8.

3

Sperm DNA and Damage Assessment with Biochemical Assays

We are built to make mistakes, coded for error.
The capacity to blunder slightly is the real marvel of DNA

Lewis Thomas (1913 - 1993)

3.0 Structure of DNA and Chromosomes

Study of cellular structure and proteins, using biochemical techniques, dates back to the 1800s. These studies led to the discovery of deoxyribonucleic acid (DNA) and protamines by Swiss medical scientist, Johannes Friederich Miescher in 1874. DNA, contains the genetic identity of all living creatures, and is found in the cells of plants, bacteria, fish, insects, birds, animals and all forms of lives. The mammalian DNA exists as a double-stranded, linear, polymer chain that assumes a helical shape as shown in **Figure 3.1a.** Different species have different DNA length and genetic information. Within the *Homo-sapiens*, each individual has a unique DNA which codes for the colour of the eyes, height, features and health inheritance. There are trillions of cells in the human body; and a copy of the DNA is located within the nucleus of most cells. The exception is - the red blood cell. The red blood cell has no nucleus or DNA. The organelle, mitochondrion has multiple copies of its own DNA, mtDNA. The mtDNA has a double stranded ring shape, resembling a bacterial DNA [1, 2].

The nucleotide is the basic unit of a DNA strand. It consists of a sugar-phosphate backbone unit, covalently attached to a nitrogenous base unit as shown in **Figure 3.1b.** Both adenine and guanine are nitrogenous bases having a purine structure (as shown in **Figure 3.2a)**, with 4 nitrogen and 5 carbon atoms, forming two rings in a plane. The bases, thymine and cytosine have pyrimidine structure (**Figure 3.2b)** with 2 nitrogen and 4 carbon atoms forming a ring in a plane. Deoxyribose (**Figure 3.2c)** is a polar sugar molecule consisting of 5 non-symmetric carbon atoms, 3 hydroxyl (OH) ions and a CH_2 ion with the formula $C_5H_{10}O_4$. The OH ion attached to the C1′ atom is covalently bonded to a base to form one of the four nucleosides - deoxyadenosine (dA), deoxyguanosine (dG), deoxycytosine (dC), or deoxythymidine (dT). Each hydroxyl ion attached to the C3′ and C5′ atoms in the sugar molecule, bonds covalently with a negatively charged phosphate ion (a process known as phosphorylation), to form the alternating sugar - phosphate (phosphodiester) bonds of the DNA backbone [1].

Double stranded DNA is composed of a linear polymer chain of phosphodiester – purine (pyrimidine) molecules bonded with another antiparallel phosphodiester – pyrimidine (purine) molecules as shown in **Figure 3.2d.** In the energetically favoured structure, the double stranded DNA is helical in shape as shown in **Figure 3.2e**. Purine – pyrimidine bases have weak hydrogen bond of equal length, with A-T forming a double and C-G forming a triple bond as shown in **Figure 3.3a**. These core nitrogenous bonds are hydrophobic in nature and the peripheral backbones of the double strand have negative polarity. When the DNA double strand is viewed along the helical axis, as shown in **Figure 3.3b,** the hydrophobic core forms a strong non-reactive centre that preserves the genetic code; and the exterior forms a negatively charged hydrophilic envelop that is highly reactive [3].

The natural forms of DNA helical structures are right handed A-DNA with 11 base pairs (bp) per turn, B-DNA with 10 bp per turn and left handed Z-DNA with 12 bp per turn. Human and mammalian DNA usually exists as the energetically favoured B-DNA which has a pitch of 3.4 nm and a bp spacing of 0.34 nm. The DNA strands are conventionally assigned 5′ to 3′ direction, with the C5′ end known as the leading end and the C3′ end known as the lagging end [3].

Even though the same DNA exists in various types of cells in different regions of the human body, the instructions for the growth, maturation and apoptosis of different cell types are unique to the particular cell and its local environment. Different segments of the DNA are coded for transcription in different cell types and at different stages of growth; and these segments have weaker bindings in the chromatin compared to the inactive segments that have tight binding [1, 3].

A **chromatin** in a somatic cell is a DNA tightly coiled around special nuclear proteins known as histones. Each histone consists of four pairs of unit proteins, H2A, H2B, H3 and H4, and a linking protein H1. The nucleosome, a basic unit of a chromatin, is illustrated in **Figure 3.4**; many nucleosomes are linked to form the chromatin. About 147 DNA bp are wrapped around a core histone to form a nucleosome and about 20 bp of DNA are supported by H1 [4].

a:

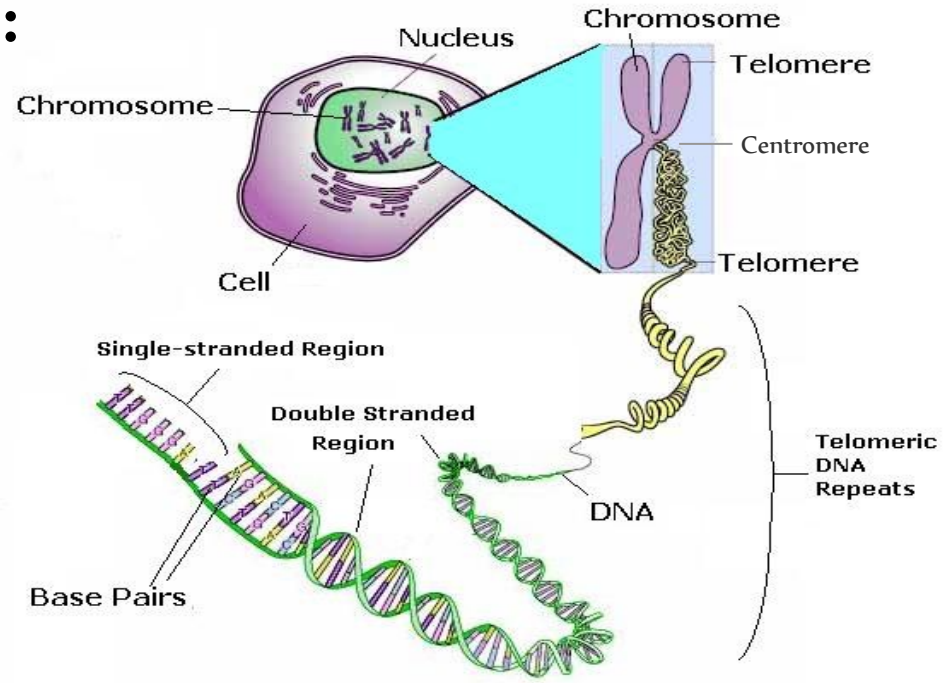

b:

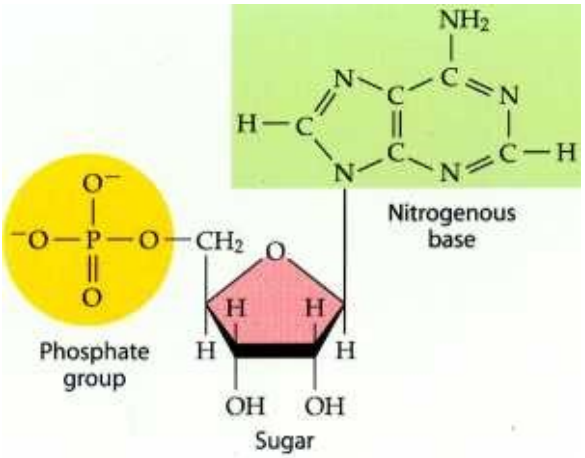

Figure 3.1 The cell, chromosome, DNA and the nucleotide

a: Schematics of a chromosome, DNA and nucleotides in a cell nucleus

b: chemical structure of a nucleotide

Images retrieved in January 2011from the websites

http://www.ch.ic.ac.uk/local/projects/burgoine/origins.txt.html

https://www.msu.edu/course/isb/202/ebertmay/notes/snotes/02_15_07_genes_evo2.html

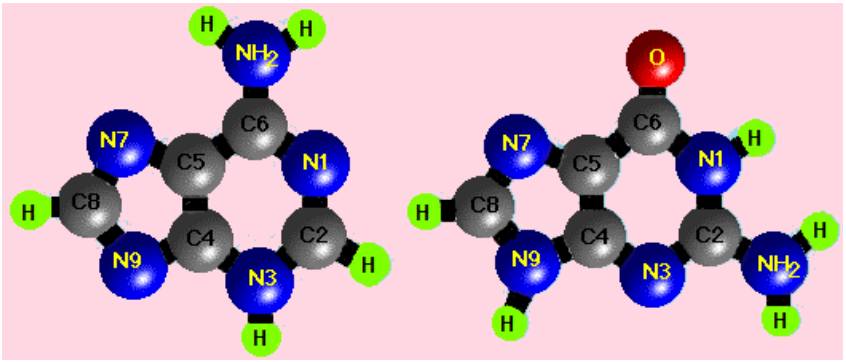

3.2a: Purine bases, adenine and guanine

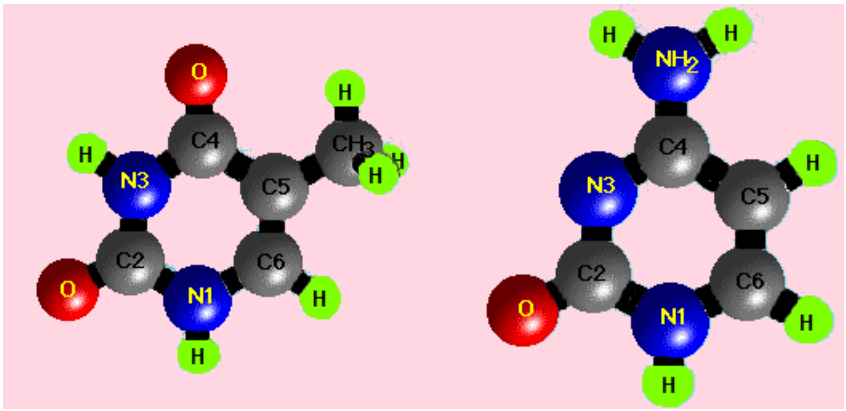

3.2b: Pyrimidine bases, thymine and cytosine

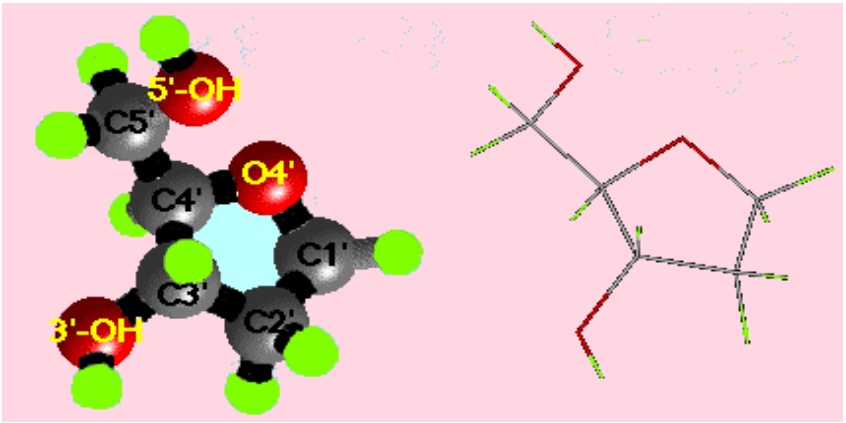

3.2c: Sugar molecule, deoxyribose

Figure 3.2 Molecular structures of DNA components

a: Purine bases, adenine and guanine

b: Pyrimidine bases, thymine and cytosine

c: Sugar molecule, deoxyribose

Extracted and adapted on 11 January 2011) *Copyright 1995, Richard B. Hallick. All rights reserved*
http://www.blc.arizona.edu/molecular_graphics/dna_structure/dna_tutorial.html#deoxyribose

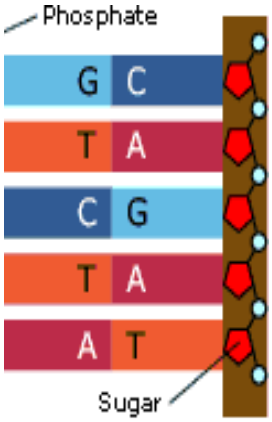

3.2d

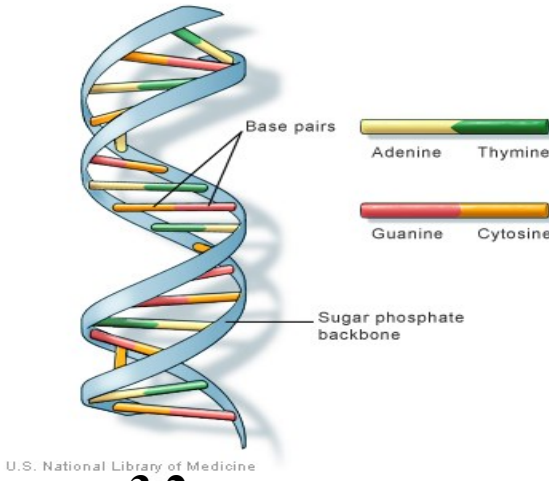

3.2e

Figure 3.2 (continued) Molecular structure of DNA components

d: Schematics of DNA [5]

e: Helical structure of DNA [6]

When the chromatin forms a dense linear structure, it is known as a chromosome. The chromosome has a constricted region known as the centromere, which can be located anywhere along the length of the chromosome. The centromere divides the chromosome into two arms, with the ends of the arms known as 'telomeres' [7]. Chromosomes in the process of mitotic division are connected at the centromere as shown in **Figure 3.5a**. While human, horse, toad and mouse have about 3 billion total DNA bp in the sperm nucleus, the total numbers of chromosomes are different in these species. As an example, the onion plant has about 17 billion bp, 5 times more DNA bp than the human has, but it has only 8 pairs of chromosomes [1, 3].

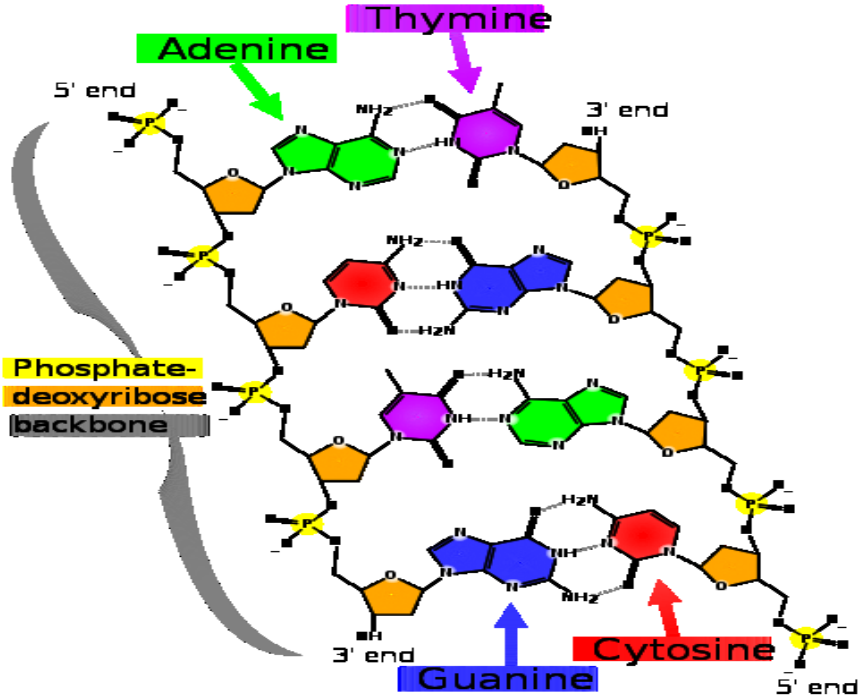

a

http://en.wikipedia.org/wiki/File:DNA_chemical_structure.svg
(extracted January 11th 2011)

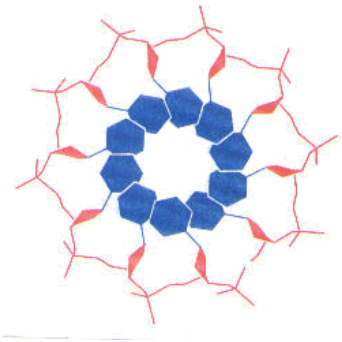

b

http://www.chemcases.com/cisplat/cisplat14.htm
extracted on 11th January 2011

Figure 3.3 DNA double strand

a Segment consisting of A-T, C-G, T-A and G-C bases with the two strands of antiparallel.sugar-phosphate chains. The triple hydrogen bonds of C-G and double hydrogen bonds of A-T .

b A top view of the helical double stranded DNA showing the hydrophobic core and hydrophilic exterior

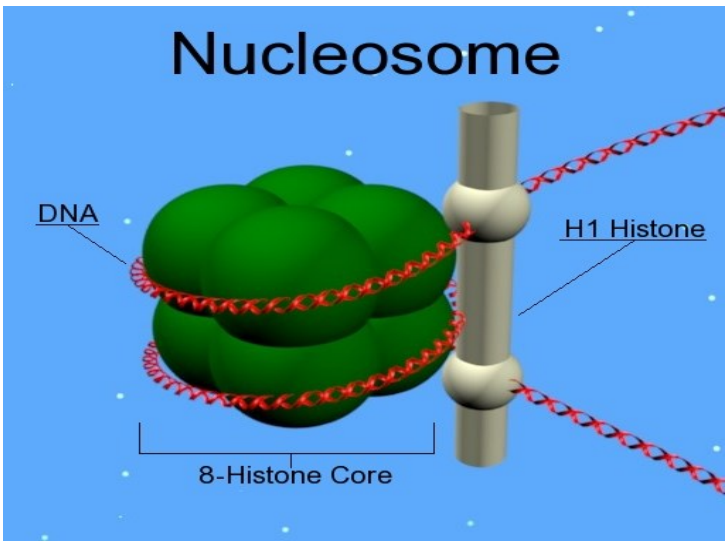

Figure: 3.4 A nucleosome – a unit of DNA wrapped around binding histones. Several such units form a chromatin in a somatic cell. *Extracted and adapted on 11 January 2011: http://commons.wikimedia.org/wiki/File:Nucleosome.jpg*

Men and women have 22 chromosome pairs that are identical in the somatic cell; these are known as autosomes. The 23rd chromosome pair is known as sex chromosomes. Men have an X and a Y sex chromosome forming the 23rd pair, whereas women have two X chromosomes in the pair. Deviation from this normal karyotype causes health and developmental abnormalities. The human chromosomes are arranged according to size, in **Figure 3.5b.** The largest human chromosome is an autosome with 246 million bp and the smallest autosome has 46 million bp in its DNA. The medium sized X chromosome has 153 million bp, and the small Y chromosome has 50 million DNA bp. Each diploid cell nucleus in the human has over 6.1 billion bp. The mature human sperm has over three billion bp [7].

Protamines were first observed in 1870 by Johann Friedrich Miescher, the Swiss biologist, who discovered DNA. In 1896, Albrecht Kossel, Professor of Physiology, at the University of Heidelberg in Germany, characterised protamines as a set of positively charged basic small proteins. David Bloch completed a detailed catalogue of sperm nuclear proteins from various species, which was published in 1969 [2]. Protamines are arginine rich (50% -70%) proteins that bind DNA and consist of

protamine-1 (P1) and family of P2 protamines. P1 is common to all mammalian sperms; P2 and P1 to P2 ratio vary within the species [8, 9] and is approximately '1' in a healthy human sperm [10, 11]. Human protamines, HP1 and family of HP2 are essential for normal sperm development, function and morphology [9, 12-14] .

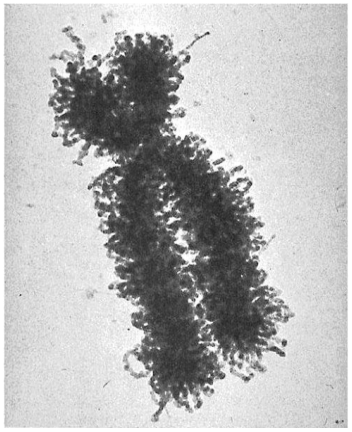

Figure 3.5a SEM image of human chromosome pair, showing centromere and telmeres (Dr. E Du Praw) (Extracted from http://cnx.org) January 2011

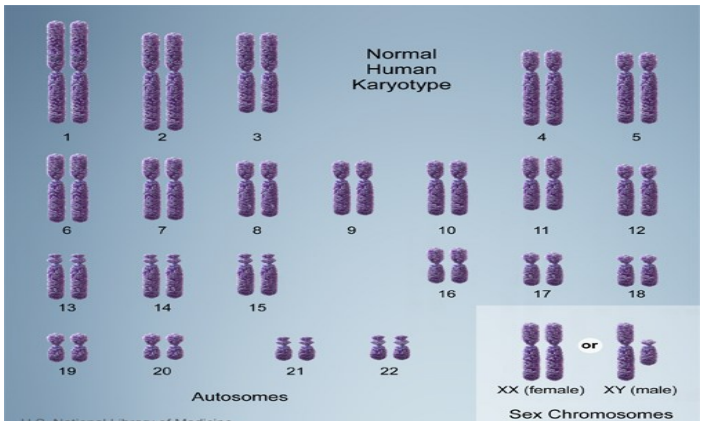

Figure 3.5b Image of a complete set of human chromosomes, with the autosomes arranged by size showing 22 pairs of autosomes and the X and Y pairs (Extracted from http://ghr.nlm.nih.gov/handbook/illustrations/normalkaryotype)

Figure: 3.5 The human chromosomes

The genes responsible for protamine synthesis and DNA condensation are located on chromosome 16 in humans [12, 15]. During sperm nuclear condensation, the somatic histones are replaced by positively charged, arginine rich, transition proteins; and then by arginine and cysteine rich HP1 and HP2 protamines and testis specific histones (TSH). HP1 binds 10 – 11 DNA bp and HP2 family of protamines bind 15 DNA bp. TSH provides tighter binding than histones in somatic cells [10, 15]. The protamines are anchored to the nuclear matrix, a sponge-like flexible skeletal meshwork that provide organisational structure to nuclear chromatins [16].

Even though horses have 32 chromosomes, they are smaller than human chromosomes in size. The stallion sperm chromosomes contain 2.5 to 2.7 billion bp. The stallion Y chromosome has between 45 – 50 million bp and is comparable in size with human Y [17]. **Figure 3.6** shows the image of a mare's chromosomes.

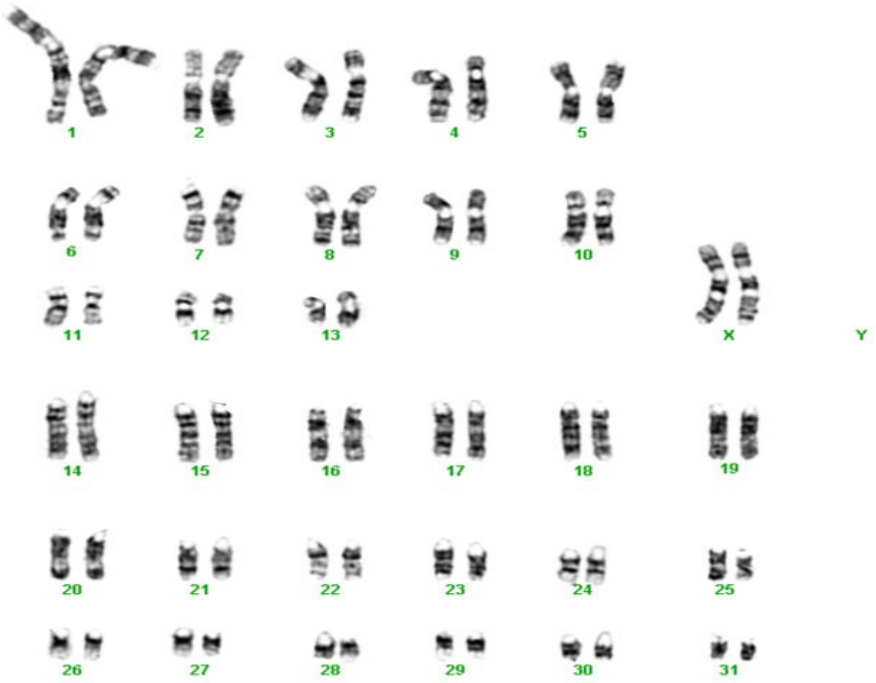

Figure 3.6 The equine chromosomes
Image of a complete set of chromosomes from a mare, showing 31 pairs of autosomes and the X pair. Extracted Jan 2011from http://www.ca.uky.edu/gluck/LearT_Proj_Clinical.asp

DNA replication is a process by which a double-stranded DNA splits into two single stranded DNA templates to create two new identical double-stranded DNAs (**Figure 3.7**). The instructions for generating specific proteins that are characteristic of the species are coded onto small sections of the DNA double strands in specific sequences of the bp, and these are known as genes; in a human, these genes vary in size from a 1000 to a million bp per gene. Only a small fraction of the DNA strand is coded for gene expression; and the rest of the DNA contain large segments of repeat sequences; the functions of these segments are unclear. The DNA also has regions containing gene fragments or damaged genes [3, 7].

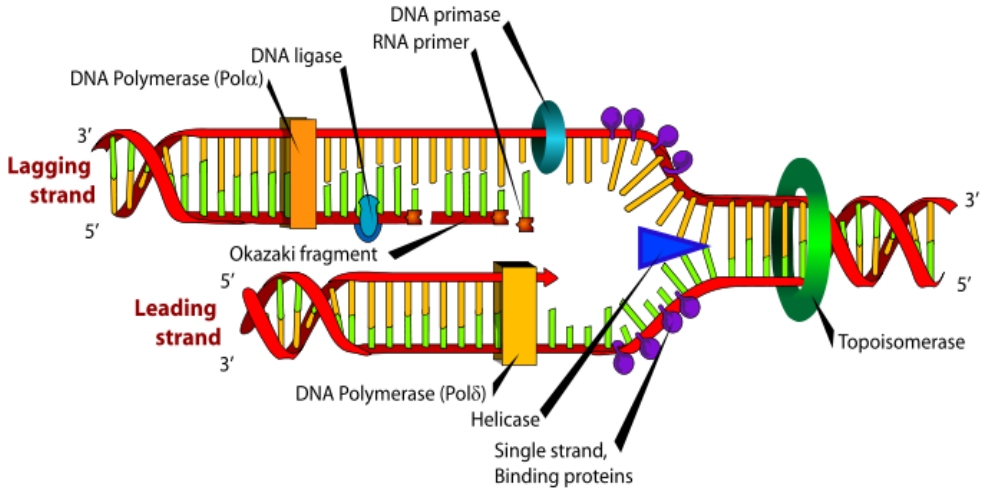

Figure 3.7 Schematic of **a** DNA replication process
http://www.replicationfork.com/ (retrieved on 14th January 2011)

Humans have 20,000 to 25,000 genes; over 1056 genes expressed by human sperms have been identified; and that included enzymes, receptors and regulator genes. Nearly 50% of the genes are involved in metabolic functions [7, 18]. Horses have fewer genes than humans; and about 53% of the genomic arrangement in horses and human autosomes are similar. The gene arrangements in the equine and human X chromosomes are highly correlated, including the position of the centromere [19-21].

3.1 DNA Damage and Repair

Identical copies of double stranded DNA are found in the several trillions of cellular nuclei in a human body. The DNAs experience frequent divisions, replications, recombinations and protein synthesis during embryo/fetal development, childhood and early adulthood, leading to 10,000 to 200,000 cellular changes per day. The process slows down in old age but is not totally absent. Coding errors are inevitable when trillions of nucleotides split, add, divide, subtract and multiply, as they participate in normal growth and metabolic process. Some of the errors are injurious to health and others pave way for evolutionary changes [3].

The DNA strands have inherent vibration and natural flexibility to shift in space, and this can cause replication errors. A variety of enzymes with capacity to repair specific errors/DNA damage exist within cells. Usually 99% of the errors are corrected instantly during proof reading, shrinking the error frequency to about one in ten million. Spontaneous errors in the replication of genes are sources of novel mutations, which, over several lifetimes, introduce evolutionary changes. Hair and eye colours, blood types, and human races with their genetic advantages and disadvantages, are some of the evolutionary consequences of spontaneous coding errors [22].

External factors like stress, environment, illness, chemotherapy and drugs can cause DNA damage. Radiation (UV, X-ray and γ-ray) and alkyl groups from tumour suppressing agents can modify or remove bases from DNA. DNA damage is also caused by cancerous gene activities, excess reactive oxygen species (ROS) and cell apoptosis. ROS and their by-products inflict more damage to mtDNAs than to nuclear DNA, due to mitochondrial proximity to ROS species. Accumulated errors can limit the affect of repair mechanism and cause adverse health affects. Cells with excess DNA damage could remain inactive, suffer apoptosis or produce tumours [6, 22]. The major forms of DNA damages (**Figure 3.8)** are**:**

- Single and multiple base damages including cross-links
- Single strand breaks (SSB)
- Double strand breaks (DSB)
- Cluster damage

Special sensor proteins in the cell nucleus identify DNA damage, move to the location, act as recognition centres for repair proteins to track and inhibit damage propagation. DNA bp mismatches/coding errors are repaired by mismatch repair (MMR) proteins. Base excision repair (BER) mechanism removes modified bases. Extensive base damages are repaired by nucleotide excision repair (NER) mechanism. Bulk damages due to UV light and other high energy radiation exposure are repaired by nucleotide excision repair (NER) pathway. Inter-strand crosslink damages are repaired by recombination DNA repair mechanisms [23-25].

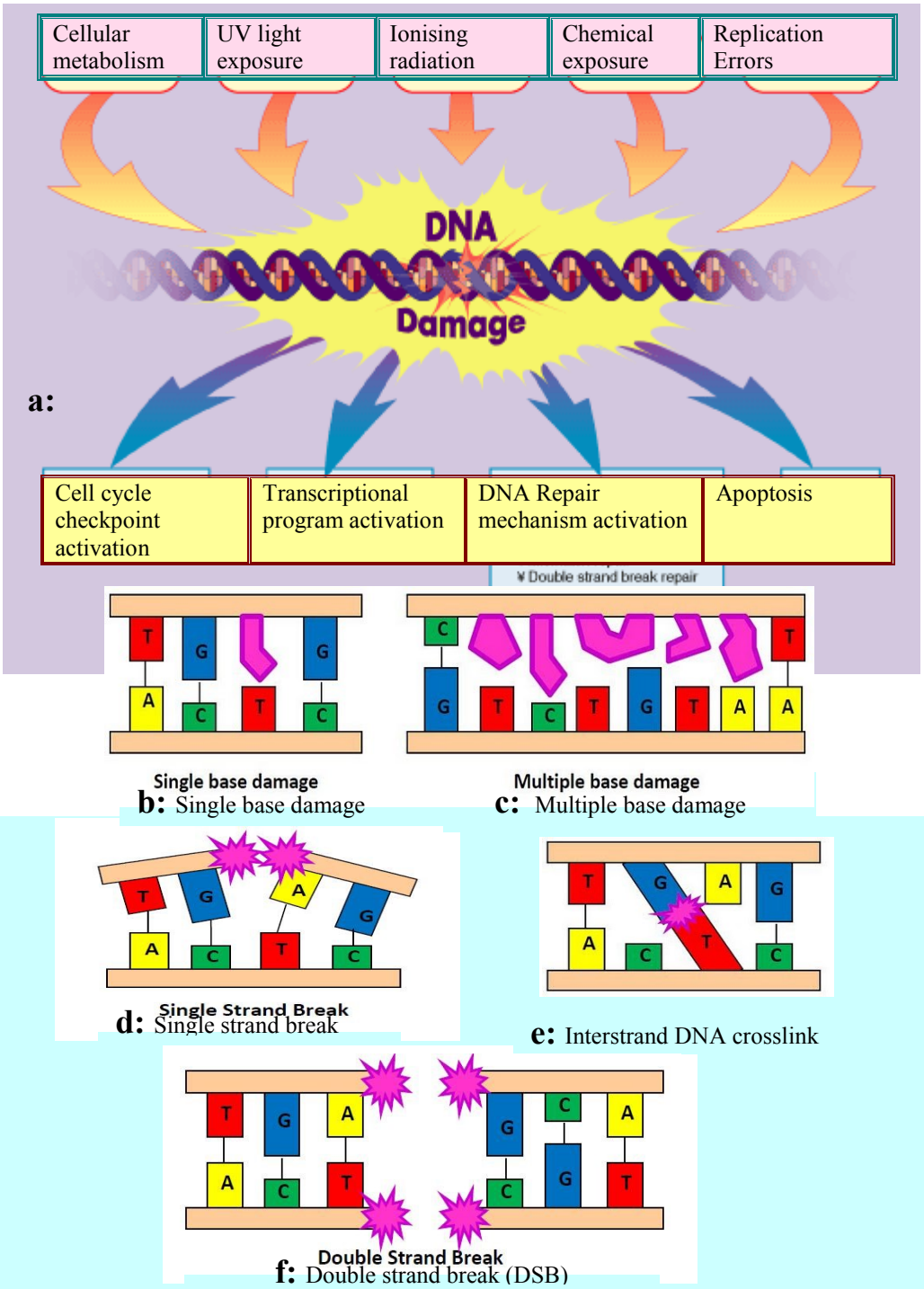

Figure 3.8 Types of DNA damages
http://www.rndsystems.com/mini_review_detail_objectname_MR03_DNADamageResponse.aspx
http://ozradonc.wikidot.com/types-of-dna-lesions

SSBs are created by direct damage to sugar molecules, resulting in a dangling 5′-deoxyribose phosphate (5′-dRP) end, or indirectly during DNA damage repair process. Special enzymes are involved in SSB repair pathway. Damage to BER could lead to major illness [23, 26].

DSBs have been identified as the most harmful form of DNA damage, as these can destroy the cell or damage its DNA integrity. Various proteins are involved in the signalling and repair of DSBs. Following the recognition of a DSB, the cell cycle activities are suspended until the damage is fixed. When a cell fails to repair the DSB, the cell apoptosis mechanism is invoked to protect the integrity of the region. Occasionally the DSB escapes detection and the damaged cells proliferate, giving rise to cell mutations or chromosomal aberrations [27, 28].

Cluster damages are externally generated base damages or SSBs or a combination of the two such that two or more damaged sites are located in close proximity (within 1-2 helical length of the DNA strands). Ionising radiations are the major external source of cluster damages and these damages lead to cell mutation [29].

Coding errors in genes could result in mutation of the genes and disrupt their functions. When mutations occur in polymerase genes, cell division and repair mechanisms are impaired; the residual errors are bound to be significantly high, causing cancer and other serious illness. When such errors occur during embryogenesis, it causes embryo growth arrest. Errors in sex chromosomes could be passed down through the generations, causing inherited illnesses or disorders [6, 22].

When DSBs occur in double strand repair genes, the cells become highly sensitive to damage sources like ionising radiations. Immunodeficiency, growth delay, mental retardation, neurodegeneration, cancer predisposition, lymphoid tumours, insulin-resistant diabetes, immune deficiency syndromes, cancer and premature aging are some of the illnesses caused by damage to double strand repair genes [27, 28].

Mutation of mtDNA cause mitochondrial dysfunction. Nuclear DNA integrity can be compromised by damaged mtDNA. Accumulated damage over time in organs like the heart, brain, muscles and other tissues, contributes to aging. Mitochondria

have their own independent mtDNA repair pathways and machineries, like mitochondrial BER (mtBER) and MMR (mtMMR). Base damages in mtDNA are repaired by complex multistage BER proteins by creating intermediary SSB as a by-product of the repair chain activity. The mtBER is the most common repair mechanism in mammalian mtDNAs. Decrease in mtBER quantity and quality results in mtDNA instability and dysfunction [23].

DNA double strand lesion, 8-hydroxi-guanime (8-oxo-G) is found in mtDNA, and can be identified by markers. Two other recently identified, equally frequent DNA lesions due to oxidative stress, are 2,6-diamino-4-hydroxy-5-formamidopyrimidine (FapyG) and 4,6-diamino-5-formamidopyrimidine (FapyA) . Cigarette smoke caused DNA SSB in human cells when cultured in polyphenols found in cigarette smoke. It generated H_2O_2 and caused SSB in the cellular DNA. Catalase and superoxide dismutase (SOD) inhibited SSB when added to the culture; catalase appeared more efficient at repairing SSBs [30]. Energetic Fe ions, Gamma rays and X-rays damage isolated DNA in solution creating cluster damage and DSBs. The amount of induced damage has been shown to be proportional to the radiation doses [31].

3.1.1 DNA Damage Mechanism in Sperms

Six significant mechanisms for sperm DNA damage have been identified [32].

1. **Apoptosis induced DNA damage:** Apoptotic markers are used to damage the DNA during spermatogenesis to eliminate unhealthy cells and regulate cell population. This accounts for 50-60% of cell deaths during spermiogenesis.
2. **Nick repair mechanism failure after DNA protamination:** Nicks found in spermatids release torsional stress during histone replacement, and are repaired during normal DNA condensation.
3. **Oxidative stress induced DNA damage in the epididymis:** Disulphide bonds are formed by an oxidative process during sperm epididymal transportation. Testicular sperms have lower DNA damage level than ejaculate sperms.
4. **Activation of apoptosis inducing enzymes**: Caspases and endonucleases (enzymes that break DNA backbones - phosphodiester bonds) are activated in damaging environments like exposure to free radicals or high temperature.
5. **Testicular cancer**: Radiation/chemotherapy induce DNA damage to sperms

6. **Environment and life style:** Atmospheric pollutants, habitual smoking and life-styles can cause sperm DNA damage.

The ejaculates of fertile and infertile men contain significant percentage of spermatozoa with 'apoptotic markers', as these cells are not completely eliminated by Sertoli cells, and their numbers vary within individuals. AnnexinV (AV) proteins selectively bind to cell membranes with apoptotic markers, and were used to separate the marked (AV+) and unmarked (AV-) sperms from a fertile donor. AV+ and AV- cells penetrated hamster oocytes; the DNA decondensation rate with AV- was comparable to the unsorted control sperms and superior to that of AV+ cells. Cryopreservation, drugs, radiation and excess oxidative stress are external sources of DNA damage that activate the apoptosis process [32, 33].

Density gradient, electrophoretic technique and markers for membrane integrity are some techniques used to investigate sperm quality [32, 34, 35]. Fertile and infertile men have sperm DNA SSBs; a high percentage of the cells from infertile men have diffuse and extensive SSBs, an indication of extensive DNA damage. They appear as small isolated spots after immuno-histochemical staining. SSBs located in the periphery of the sperm nucleus are linked to histone and telomere damage [36].

Abnormal protamine DNA ratio and chromatin condensation cause DNA strand breaks, as it undermines the electro-mechano-chemical stability of sperm chromatin. During the condensation phase of spermeogenesis, small torroidal protamine subunits replace the large nucleosome bindings, adding stress in the smaller DNA loops. Topoisomerase enzymes create nicks in the DNA to reduce this stress. Any imbalance in the enzyme increases the risk of sperm DNA damage [32, 37].

3.2 Reactive Oxygen Species

The harmful affects of oxygen and nitrogen in the form of free radicals and reactive agents – collectively known as reactive oxygen species (ROS) and reactive nitrogen species (RNS) - was first identified in 1954. ROS have been implicated in sperm DNA damage. Oxygen is essential for normal metabolic functions of various cells within the human body and for producing energy. ROS are naturally present in the

human body at the cellular level, through the metabolic process of breathing, food processing, exercising and growth. Mitochondria and the endoplasmic reticulum are the common sources of free radicals in cells. ROS are beneficial in low doses to combat infection; they participate in cellular signalling and regulate muscle force. Excess ROS create oxidative stress damage to DNA, proteins and lipids. Cells can neutralise low levels of internally or externally generated ROS due to natural internal defence mechanism. Oxidative stress occurs when ROS levels exceed the body's own natural antioxidant defence capacity, causing cellular damage [38, 39].

The most common forms of cellular ROS are superoxide (O_2^-), nitric oxide (NO) and hydrogen peroxide (H_2O_2). NO is highly reactive and is produced in cells containing L-arginine. NO interacts with iron in the blood (haemoglobin), and with superoxide to form peroxinitrite, $NO3^-$, an isomer of nitrate. Peroxinitrite is also highly reactive and can damage DNA, thiols and proteins. Superoxide is a by-product of respiration within cells and is also produced during immune system response to infections. Although not highly reactive, superoxide can diffuse into cells over time and react with iron-sulphur clusters in proteins, damaging the cell. Hydrogen peroxide (H_2O_2), a stable molecular by-product of enzymatic reaction within the body, can penetrate cell membranes. It is capable of blocking enzyme activities and creating OH ions during reactions with the metals in molecules. Hydroxyl radical (OH) is highly reactive and can damage cells in their neighbourhood. ROS can produce highly reactive by-products through chain reactions inside cells and can inflict extensive damage to the cells and surrounding regions [39, 40].

3.3 Mitochondria and ROS

The mitochondrion is a complex cellular organelle, with several compartments enclosed by a double layered, smooth, porous outer membrane. The outer membrane is protein permeable allowing adenosine triphosphate (ATP) and large molecules to pass through. The intermembrane space separates the deeply wrinkled inner membrane, which permits small molecules like oxygen, water and CO_2 to pass through to the enclosure known as the 'matrix'. The matrix contains a variety of

enzymes and multiple copies of mtDNA. The mtDNA is small with 16,000 – 17,000 bp in mammals (16,569 bp in humans and 16,640 +/- 560 in horses) that encode 37 specific small (15 to 20 kb) genes. The mitochondrion produces its own enzymes, proteins and RNAs. Cells normally have identical mtDNAs [41, 42].

ROS in the mitochondria was first noticed in 1966, but was only recognised as a by-product of mitochondrial activity when H_2O_2 production in the heart muscles of avian mitochondria was demonstrated by Boveris and Chance in 1971. The mitochondrion has different shapes and functions in different cell types and species. The primary role of mitochondria is the synthesis and distribution of mechanical, chemical and osmotic energy using electron transportation. ROS are the inherent metabolic by-product of this function. H_2O_2 and superoxide are the primary ROS and multiple processes within the mitochondria generate ROS. At least nine enzymatic sources of mitochondrial ROS have been identified; their nature, functions and quantity differ in mammalian species and in different cell type [38, 39].

External sources of ROS include automobile exhaust fumes, cigarette smoke, UV light, asbestos, pesticides, herbicides, radioactive decays, forest fires and burning of organic matters [43]. Oxidative stress can be hereditary or environmentally induced; it can also be a by-product of excessive physical activity [40]. Lifestyle (smoking, diet, alcohol and stress), age, obesity and environment (heat, pollution, plastics, pesticide/herbicide and heavy metals) are sources of oxidative stress in humans [44].

ROS induced cellular damage can be due to (a) inherently reduced efficiency of the mitochondrial function, (b) damage suffered by the mitochondria during illness, (c) overproduction of the toxins (d) one or more combinations of these [38]. The ROS turns toxic when it exceeds the optimal ROS detoxification capacity of the cellular region. Excess ROS has been identified as a pathway for aging, cancer, neurological disorders such as Alzheimer's and Parkinson's, cardiovascular disease, diabetes, rheumatoid arthritis [39], cataract and age related macular degeneration of the eye [45], prostate cancer and male infertility [46].

The cell has multiple complex defence mechanisms in the form of enzymatic and non-enzymatic antioxidants that are capable of protecting themselves and

neighbouring cells from the damaging affects of ROS and their by-products. The lipids in the mitochondrial membrane contain antioxidants that are capable of scavenging the ROS; and this lipid antioxidant capacity can be regenerated by enzymes and other antioxidants within the membrane and within the cell [38, 47].

Experiments have shown that healthy mitochondria do not produce excess ROS; residual ROS in the cellular region is a result of damage to mitochondria or lack of sufficient antioxidant proteins and enzymes. Isolated brain cell mitochondria and intact heart cells of mice were used to demonstrate that the mitochondria had the capacity to remove or neutralise ROS at about ten times the rate at which it generated ROS. A simple laboratory test model showed that steady H_2O_2 production in healthy isolated mitochondria was in the order of a few micromoles. Oxidative stress damage to the cell is due to the failure of mitochondrial defence mechanism rather than due to mitochondrial ROS generation [38].

3.4 Oxidative Stress and Sperm

The dual role of oxygen - beneficial and harmful, in sperm function was recognised by MacLeod in 1943. Fifty years later, the beneficial roles of ROS were identified in DNA condensation, maturation, motility, capacitation, acrosome reaction, fusion and embryo development [48, 49].

The human and equine seminal plasma has the capacity to protect sperms against ROS induced damage. Catalase, SOD and glutathione peroxidise (GPX) are enzymes that protect against the damaging affects of ROS in seminal plasma. The concentration and efficiency of these ROS scavengers vary between species. The enzyme concentration varies between equine breeds and within a breed [48, 50].

High ROS levels during spermiogenesis, cause early maturation of sperms before completing cytoplasmic expulsion. Immature sperms and sperms with poor morphology often have excess cytoplasmic residue; and the enzymes in the cytoplasm generate additional ROS that can damage cell membranes and their DNAs. The sperm has a limited supply of defensive enzymes such as GPX, catalase and SOD; hence proteins and unsaturated fatty acids in plasma membranes are

susceptible to ROS damage [51-54]. Comet assay analysis of fresh and frozen macaque sperm cells, and cytogenetic studies of motile and immotile sperms injected into mice eggs, indicate that high motility sperms have a higher likelihood of possessing undamaged DNA [55].

The sperm mitochondria are sources of ROS that support sperm function. Healthy sperms can withstand the ROS. Low density, defective and abnormal sperms produce excess ROS; the mtDNA and the cell membranes are susceptible to ROS induced damage. Histones neutralise some levels of ROS, but are absent in sperm mitochondria. ROS induced lipid peroxidation, membrane and DNA damages were observed in sperms from infertile men. Poor DNA condensation combined with ROS exposure may be a factor in the damage [56-58]. Antioxidant intake has helped infertile couples with high sperm DNA damage to become pregnant [59].

Peroxide exposures of 250, 1000 & 5000 μM induced mtDNA strand break rates of 0.062, 0.134, & 0.142 per 1000 bp, reducing cell motility and function [60]. High motility sperms from fertile men, isolated using a density gradient, were incubated in peroxide of 10, 100 and 200 μM (micro-molar) concentrations for two hours. Dose dependent decrease in motility was observed with doses $\geq$ 100 μM. The DNA damage was proportional to peroxide concentration, but the peroxide had little impact on the plasma membrane integrity [61].

When the seminal plasma is removed for cryopreservation, the cells are exposed to a variety of ROS, especially H_2O_2. H_2O_2 caused more damage to equine sperms than other ROS species. Freeze-thaw causes damage to sperm membranes, proteins and chromatins. Loss of motility is the first sign of ROS induced damage in cooled or frozen equine semen [48, 62, 63]. Centrifugation and density gradient wash strip the seminal fluid and its antioxidants from the sperm environment, creating oxidative stress. ROS of non-mitochondrial origin have been detected during cryopreservation of human sperms; the plant extract, genistein, was found to protect the cells from ROS induced damage [44, 50, 64, 65].

The leukocytes and the ROS, commonly found in equine semen, become sources of oxidative stress in sperms, during illness or sperm preparation for cryopreservation

[48]. Superoxide anion (O_2^-), the major ROS generated by equine sperm, is rapidly converted to H_2O_2 that damage DNA. Cryodamaged sperms generate excess ROS. A swollen midpiece in cryopreserved stallion sperm cells is indicative of mitochondrial damage [48]. ROS is also generated by the equine sperm head membrane during capacitation. Low levels of ROS do not damage the equine sperm plasma membrane. The high calcium content found in cryopreserved sperms could indicate premature capacitation in the high ROS environment [66].

Neutrophils, the predominant form of leukocytes in semen, produce 1000x more ROS than sperms do during capacitation. High leukocyte levels in semen (leukocytospermia) occur during urogenital tract infection or inflammation. Epididymal sperms, spermatogonia and spermatocytes are vulnerable to oxidative stress during the infection or inflammation. Low non-enzymatic antioxidants and high leukocytospermia have been found in men with idiopathic infertility and linked to early pregnancy failures [67, 68].

Semen from infertile men contains 40-fold more ROS than semen from fertile men. High levels of ROS and low levels of antioxidants were found in morphologically normal semen of men suffering from idiopathic infertility. High ROS levels were found in the testes of cryptorchid men; their antioxidant capacity was unaffected and the DNA damage occurred in spermatogonia-spermatocyte phase [44, 69].

Protamine deficient sperm cells suffer ROS induced DNA damage. Guanine transforms to 8-hydroxydeoxyguanosine (8-OHdG) when exposed to oxidative stress. Tests using 8-OHdG antibody biomarkers, flow cytometry, TUNEL assay and fluorescence microscopy on low and high density sperms separated by density gradient wash revealed that cells with damaged mitochondrial membrane have 8-OHdG formation [56, 70].

Clinical study of ROS levels and total antioxidant capacity (TAC) in semen from men suffering from vericocele infertility (enlargement of the veins in the spermatic cord) and idiopathic infertility showed high DNA damage. Vericocele accounts for 20% to 40% of infertility. Sperm concentration and morphology improved and DNA damage level decreased after varicocelectomy (surgical removal of vericocele) [71-73].

Gametes are exposed to ROS during IVF treatment. The incubation and in-*vitro* culture media create oxidative stress, as it does not perfectly mimic the natural protective environment of gametes and embryos. Low fertility sperms experience higher oxidative stress damage when extracted from the seminal plasma. The in-*vitro* eggs and embryos are also exposed to oxidative stress, and the embryos generate large amount of ROS through their high metabolic activities [74].

Statistical analyses of IVF outcome and sperm DNA damage using Medline database over the period 1999 – 2008, revealed that sperm DNA damage correlated with pregnancy loss in both ICSI and conventional IVF [75]. Sperm DNA damage could be used as a biomarker of male infertility [76]. Sperms from 70% of the infertile men with low sperm count were unable to fuse with the egg [77]. Pregnancies failed at the blastocyst stage when sperms with high levels of DNA damage were used [44]. Men with spinal chord injuries had high sperm DNA damage, low sperm concentration, low sperm motility and abnormally high ROS levels [78, 79].

Certain environment and lifestyle can cause oxidative stress damage to sperms. Chemotherapy and related drugs, paracetamol and aspirin can increase apocytochrome activity that damage sperm cells. The semen of smokers has high ROS and low antioxidant levels, due to the oxidants in cigarettes. Both nicotine and DNA fragmentation were identified in the semen of smokers. 8-OHdG lesion in DNA was 50% higher in smokers than non-smokers; and the antioxidant α-tocopherol was depleted by 30%. Alcohol lowers antioxidant and testosterone levels, increases testicular ROS and induces oxidative damage to serum lipids. Exposure to phthalates through food, skin or inhalation, disturbs spermatogenesis and creates oxidative stress damage to sperms. Heavy metals such as cadmium and lead can cause oxidative stress damage to sperms. Infertility and miscarriage has been high among welders, painters and factory workers who made batteries. Experiments on mice sperms showed herbicides and pesticides induced oxidative stress damage to the sperms [44, 80, 81].

Radiation damage tests on the testicular germ cells from mice neonates showed that the germ cells had different damage response and different capacities to repair the

induced DNA DSBs at different stages of growth [82]. When sperms from fertile and infertile men were exposed to H_2O_2 and X-rays, the sperms from infertile men suffered significantly more damage than those from fertile men, indicating that radiation and ROS sources did not easily damage healthy human sperm cells [83].

Gamma rays, with intensities of 5, 10, 50 or 100 Gy, were used to artificially induce DNA damage in human and hamster sperms. All four categories of the irradiated sperms were able to fertilise hamster eggs. However, the number of blastocysts decreased with increased gamma ray exposure; full term pregnancy and normal offspring in mice were possible only with the lowest dose of 5Gy and undamaged control sperms. Caffeine can block the sperm DNA repair mechanism in eggs; hamster eggs was used to demonstrate the ability of eggs to repair low levels of sperm DNA damage caused by caffeine. The eggs repaired sperm DNA DSB breaks of less than 8% caused by a dose of 5 Gy [84].

Morphologically normal bovine sperms were exposed to x-rays of intensities 0.6, 1.25, 2.5, 5, and 10 Gy and gamma rays ranging from 5Gy to 300 Gy. The radiation did not impact cell membrane, acrosome cap, cell motility and morphology. However, dose dependent DNA strand breaks were observed, even in doses as low as 0.6Gy. The cells did not block fertilisation or early embryo development after exposure to X-ray doses of 0.6 to 10Gy; the embryos appeared morphologically normal. The number of blastocysts was not affected at 0.6Gy exposure. The number of blastocysts decreased with 1.25Gy and significantly decreased with 2.5Gy doses. Further embryo development was also negatively impacted by radiation dosages over 2.5Gy. Hatching was severely reduced at 2.5Gy and arrested at 10 Gy [85].

3.5 Osmotic Stress and Sperm

Water transportation across a porous membrane is achieved by a force known as osmotic force, and is regulated by the soluble molecular content in the solution. The net unidirectional pressure of water flow is known as osmotic stress, and it ceases when the concentration of the solutes across the membrane equalises. The membrane structure, molecular content, number and size of pores and temperature contribute to water transport rate across cellular membranes; the bulk transport

characteristics of the membrane is known as semipermeability. Osmotic stress is measured in units of osmolality and sperm osmotic stress is expressed in 10^{-3} of an osmol (mOsm) [86].

Different mammalian species have shown different degrees of tolerance to sperm cryopreservation methods. This is attributed to species specific variations in the nature and content of the membrane lipids. The sperm cells suffer permanent membrane damage from the accumulated injuries caused by thermal shock, ice crystal formation, osmotic stress and oxidative stress encountered during cryopreservation. During freezing, the cells expel water and shrink, creating hyperosmotic stress; during thawing the cells takes in water and stretch the cell membrane and cause hyposmotic stress. At sufficiently high values, the stress causes permanent damage to cell membranes. The lipids and proteins are oxidised by the induced ROS. Cold shock and subzero temperatures reduce signalling capacity and fertilisability of the cell, as the Ca^{++} and K^{+} transportation across the membrane is effected [87].

Lipid peroxidation is low in fresh sperms and high in cryopreserved sperms and it varies within stallions as well as between ejaculates from a single stallion. Lipid peroxidation is predominantly confined to the midpiece section. Sperms with high membrane integrity and mitochondrial membrane potential suffer low damage. Caspase activity induced cell death has been triggered by lipid peroxidation, as well as oxidative and osmotic stress following cryopreservation [88].

Stallion sperms are exposed to a variety of oxidative and osmotic stresses during their journey through the testicular epididymis and then through the mare's uterine tracts; the cells have natural resilience to these stresses. However, during semen collection, the cells are exposed to thermal shock in addition to osmotic shock from the water soluble lubricants and urine, which generate high hyperosmotic stress in excess of 800 mOsm. Stallion sperm cells produce superoxide anion, a ROS, in response to osmotic stress. The ROS is responsible for the reduced number of viable sperms. Membrane activity and phosphoprotein expression are altered in stallion sperms exposed to hyper or hypo osmotic stress. The anti-oxidants neutralise some

of the ROS; their efficiency vary with the nature and concentration of the anti-oxidants and the extent of osmotic stress damage. While some anti-oxidants have no affect on the ROS, others like tiron (a superoxide scavenger) in low doses, reduced the ROS and in high doses, increased the ROS production [89, 90].

Sperm handling is critical to the fertility potential of horses. The motility of equine spermatozoa is reduced when exposed to osmotic stress. Motility dropped to 10% at 100 and 500 mOsm. Hypo-osmotic stress caused irreversible membrane damage and motility loss after the cell reached its maximum volume, while hyper-osmotic stress up to 600 mOsm had no noticeable affect on membrane integrity. Glycerol added to the media helped to reduce, but not eliminate, cell membrane damage and motility decline. Rapid addition of glycerol and other cryoprotectants also caused osmotic shock - membrane damage and motility loss. Unlike stallion and boar sperms, human and mouse sperms appeared less sensitive to osmotic stress and regained some motility on removing the stress. The impact of cold shock is more pronounced on progressive motility than on the membrane integrity [91-93].

Tail deformation - swelling and coiling, was first reported in 1993, when live sperms with high membrane integrity were exposed to hypo-osmotic stress test (HOST) [94]. When equine sperms were incubated for 30 minutes at 37^{o}C in fructose, sucrose, and lactose solutions of 300, 150, 100, 50, and 25 mOsm, the cells were found to be most sensitive to 25 – 100 mOsm, and least sensitive to 300 mOsm solutions. This response was found to be consistent and reproducible, and became a test for equine sperm viability [93]. Cell motility, viability, and membrane integrity of the sperms decreased after HOST test and a large fraction of the cells suffered irreversible membrane damage, rendering them unsuitable for AI [92].

Post-thaw sperm viability test with HOST has become a vital part of the stallion sperm function test, as it has shown consistent relationship to pregnancy outcome. Test samples of sperms are suspended in hypo-tonic solutions of 75-129 mOsm for 15 minutes, and the % of viable cells counted using special computer aided software. Similar tests with hyper-osmotic solutions produced inconsistent results, and hence have not been used in cell viability protocols [95].

Membrane integrity and forward motility of human sperms are useful predictors of post-thaw sperm function. Human sperms are most sensitive to HOST at 68 Osm/L with 2% NaCl in double distilled water; and the technique is a sensitive predictor of normospermia, teratospermia and oligospermia. These tests also have excellent correlation to WHO sperm assessment protocol. However, the test sperms do not regain their original motility when returned to isotonic conditions, indicating irreversible membrane damage, affecting capacitation and fertilisation [91, 96, 97]

Sperms with high membrane integrity can become immotile after osmotic stress induced mitochondrial damage. Sperm motility and membrane integrity tests have good agreement in fresh semen; the correlation decreased with time. Sperm motility and membrane integrity decreased after each process step of cryopreservation, with more pronounced motility decay [98].

A variety of biochemical staining techniques that target specific lipids, proteins, organelles like mitochondria or acrosome are available to test localised molecular level integrity of the spermatozoa [99]. Different types of stains interact with different molecules in the cell. Test kit containing SYBR-14 and propidium iodide (PI) stain green in sperm cells with undamaged membrane, and red in cells with damaged membrane, and are used to test sperm viability. The molecular mechanism in HOST is different from that of stains and often has different result. Stains measure the level of physical damage to membranes and HOST distinguish between 'live and dead cells' by testing membrane function and biochemical activity [100].

3.6 *Overview of Chemical Assays for Testing DNA Damage*

Many biochemical techniques for testing and quantifying proteins and DNA in the cells were perfected in the 1980s. Light and fluorescence spectroscopy, nuclear magnetic resonance spectroscopy (NMR), SEM and transmission electron microscopy (TEM) provided atomic or molecular level information of biochemically labelled, dissected, extracted or denatured cells, and were used in conjunction with various biochemical assays to obtain detailed DNA information [101].

'Alkaline Single cell gel electrophoresis (Comet assay)', first reported by Narendra Singh and team in 1988 [102]; 'terminal deoxynucleotidyl transferase-mediated dUDP nick-end labelling (TUNEL)' assay, first reported from the University of Dusseldorf in Germany in 1991 [103], and 'sperm chromatin dispersion assay (SDC)' first designed by Roti and team in 1987 [104] were used for detecting DNA strand breaks in single sperm cells. 'Sperm chromatin structure assay (SCSA)', designed by Evenson and team in 1980 [105], measured the ratio of damaged to undamaged sperm cells in the sample; and several thousands to millions of cells were analysed very quickly. The sensitivity and merits of some of these assays for detecting sperm DNA fragments has been investigated [106]. While many more biochemical assays have been developed for specific tests and cell types, the four techniques summarised are extensively used to quantify sperm DNA damage [107-110].

3.6.1 Single Cell Gel Electrophoresis - Comet Assay

Neutral, alkaline and pulsed forms of comet assays have been used to investigate DNA integrity of cells; these assays are capable of detecting DNA SSBs and DSBs. Both somatic and sperm nuclear DNA damage have been investigated using these techniques. The electrophoretic solution has pH 10 in neutral comet assay and pH 13 in alkaline comet assay. These techniques show different sensitivity to DNA unwinding. The DNA fragments produce a comet shaped fluorescence image (**Figure 3.9**), which is a measure of the DNA damage [111]. The basic procedure of alkaline comet assay is described and consists of five sequential steps [112, 113].

(1) Sample preparation: Cell monolayers are embedded in a thin flexible gel film substrate on glass. The porous gel traps large cells but allows free movement of DNA strands. The surface distribution of the cells is maintained with cell spacing large enough to prevent overlap of comet tails.

(2) Cell lysing: The cells embedded in the gel layer are placed in a lysing solution that destroys the membranes and proteins in the cells.

(3) DNA unwinding: The slides are immersed in neutral or alkaline electrophoretic solution to allow the DNA strands to unwind. Damaged DNA strands unwind faster than the undamaged DNA strands.

(4) DNA strand migration: An appropriate voltage applied across the electrophoretic solution causes DNA fragments to drift towards the anode.

(5) Fluorescence Imaging: The slides are stained using fluorescent dye and imaged to highlight DNA strand migration (comet tail). Undamaged cells produce a circular halo and damaged cells produce a comet tail.

Radiation and ROS are used to artificially induce DNA damage in cells. Single cells in low concentration are re-suspended in low melting point agarose (LMPA) gel and mono-layered on glass slides pre-coated with a thin film of normal agarose. After the gel sets, the substrates are immersed in a standard lysing solution made of concentrated salt and detergents (EDTA, Tris and NaCl) for an hour, rinsed in a buffer solution and placed in pH 13 alkaline electrophoresis solution consisting of 300mM NaOH and 1mM EDTA. The DNA takes about an hour to unwind. A voltage of ~ 1 volt/cm is applied across the electrodes in the chamber and the fluid level is adjusted to generate 300 mA current across the immersed slides. The DNA strands are exposed to the field for about 40 minutes; the amount and extent of DNA fragment migration is directly related to the strand size and the applied field. The slides are removed and stained using SYBR-green and examined under a fluorescence microscope. The images of undamaged and damaged cells are shown using neutral comet assay in **Figure 3.9**. The technique is highly sensitive and capable of detecting DNA strand breaks of a few kilobytes [83, 113, 114].

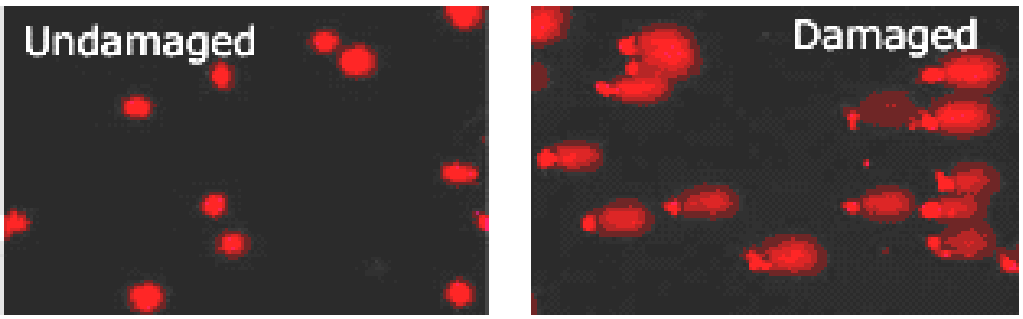

Figure 3.9 Images of undamaged and damaged sperm DNA with Comet Assay [115]

The comet assay has been modified for mammalian sperm DNA analysis. Additional chemicals like triton X, proteinase K, RNAse, mercaptoethanol and/or dithiothreitol (DTT) are added to the standard lysing solutions to break down the lipids and proteins in the highly resistant membranous perinuclear theca and protamine disulphide crosslinks. This technique has been used to quantify the degree of sperm DNA damage and its impact on fertility [109, 116]. The lysing solution in the assay is modified to suit the characteristics of each species. RNAse enzyme, proteinase K and beta-mercaptoethanol have been used to breakdown the highly resistant stallion sperm nuclear proteins [117, 118].

Comet assay technique is highly sensitive for quantifying DNA damage; however, it is time consuming and takes over 24 hours. Hence it is not suitable for routine fresh semen analysis. Flash frozen raw human semen in liquid nitrogen has the same amount of DNA damage as fresh semen, and was used to preserve the semen for time consuming comet test using neutral comet assay [119].

3.6.2 dT-mediated dUTP Nick-End Labelling (TUNEL) Assay

Nick translation, first reported by Rigby and team [120], utilises DNA polymerase-I enzyme to nick the 3′-OH bond in the active region of the DNA and attach itself to the break. The 5′-OH section of the DNA is displaced (translated). Specific fluorescent labelled enzymes that attach to SSBs and DSBs in the DNA are used to identify and quantify damage. A modified nucleotide, dUTP, 2′-Deoxyuridine 5′-Triphosphate, with the enzyme, terminal deoxynucleotidyl transferase (TdT) that attaches to the 3′-OH end is known as TUNEL assay. TUNEL assay is capable of detecting both SSBs and DSBs and is popularly used in clinical sperm DNA tests. The intensity of the fluorescence image is used as a measure of the damage [121]. **Figure 3.10** shows an image of sperm damage using TUNEL assay.

TUNEL assay and annexin V were used to test DNA fragmentation in normosperms exposed to H_2O_2 or γ-rays. Motility decreased after 15 minutes of exposure to 25 μmol/l of H_2O_2; DNA damage increased with time and maximised within an hour. The DNA damage was proportional to γ-radiation dose. Motile cells suffered less damage when compared immotile cells [122].

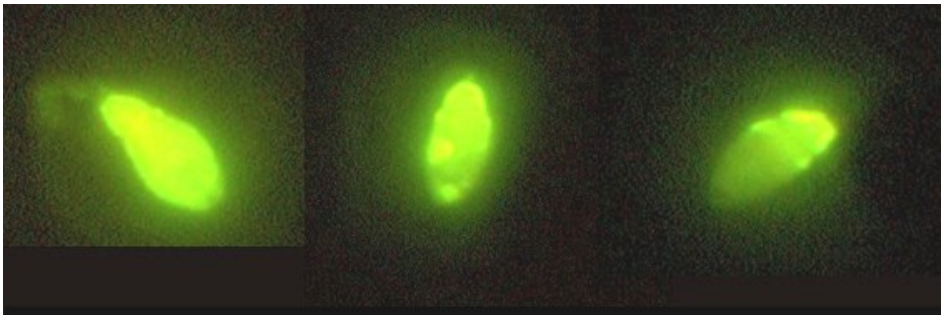

Figure 3.10 Images of sperm DNA damage using TUNEL assay
(left) granularity (middle) vacuoles (right) homogeneous [123]

3.6.3 Sperm Chromatin Dispersion (SCD) Test

SCD test is similar to Comet assay tests, without the same extended time commitment; however, its role as a sensitive metrology tool is yet to be established. The samples are prepared on slides, using Comet assay procedure, immersed in 0.08 N HCl solution to create DNA SSBs, and immersed in lysing solution to destroy membranes and proteins. The slides are rinsed with Tris-borate-EDTA buffer to cause the DNA strands to unwind and dehydrated in ethanol baths of increasing concentrations. The slides are dried and stained for fluorescence imaging. The image generated by sperms from fertile men with low DNA damage has been found to be different from that of infertile men with high DNA fragmentation [108, 124].

3.6.4 Sperm Chromatin Structure Assay

Sperm Chromatin Structure Assay (SCSA) is a technique where large number of sperms are exposed to heat or stress and stained using acridine-orange. The vulnerable cells suffer damage. Using flow cytometry, where a beam of light interacts with each sperm nucleus causing the stained DNA to fluoresce, a few thousand sperms are evaluated rapidly. The dye fluoresces green in the cells with undamaged DNA and orange in the cells with damaged DNA. With computer aided signal counter, the ratio of DNA damaged cell to the total cells, known as DNA

fragmentation index (DFI), is obtained on 10s of 1000s of cells within minutes. The DFI of left over specimens from IVF clinics were measured; ejaculates were grouped into fertile (with 0-15% DFI) and low pregnancy potential (with >30% DFI) [107, 125].

However, pregnancy and live birth with ICSI was achieved with sperms having DFI of 32%. Various studies indicate that the DFI is not a simple predictor of pregnancy outcome. Pregnancies and live births could be achieved using natural, normal, ICSI and IVF techniques using fresh and cryopreserved sperms. The sperm preparation techniques influenced the DFI; the DFI of neat semen, swim-up and density gradient preparations of the same ejaculate are different [101, 126-129]. SCSA predicted spontaneous abortion but not fertilisation or embryo quality in IVF and ICSI [128].

3.6.5 Mammalian Sperm DNA Damage Tests

The enzyme DNAseI and H_2O_2 were used to damage the DNA of human, mice and bull sperms. Bull has only P1, whereas mice and men have P1 and P2 protamines and nuclear histones. Alkaline and neutral comet assay, TUNEL assay and SCSA were used to measure the induced DNA damage. DNAseI attacks the DNA phosphodiester bonds to create DNA damage; and the damage is related to the nature and integrity of the protamine bindings within each species. The tests revealed species specific response to DNAseI, with human sperms most sensitive and the bull sperm least sensitive to the enzyme attack. The free radicals released by H_2O_2 create SSBs and base damages. The sperm response to H_2O_2 appeared to be less dependent on the binding. In this study, good agreement between TUNEL and Comet was observed, whereas, SCSA had a different correlation [130].

The effect of X-Rays on germ cell development in mice testes was evaluated using comet and SCSA. The mature ejaculate sperms were most resistant to radiation induced damage. The damage sustained by spermatocytes was passed on to the mature sperms. The affect of radiation was temporary, and new cell cycles did not show radiation damage [131]. Radiation did not cause membrane damage nor impair motility or block fertilisation and early embryo development in bull sperms. Dose

dependent increase in SSBs were observed with TUNEL assay and blastocyst formation was blocked [85].

H_2O_2 at different concentrations were used to induce sperm DNA damage in human, tammar wallaby and mice sperms, and tested with comet assays. Mice sperms were most resistant to peroxide damage and wallaby sperms, lacking disulphide cross-link, were least resistant [60].

Vacuoles in sperms are visible under high magnification microscopes. Human sperm cells with different size and concentration of vacuoles were tested for chromatin integrity and DNA damage using TUNEL and comet assay. The tests showed that vacuoles did not cause additional DNA damage [123, 132]. Sperm DNA damage in testicular cancer patients were evaluated using TUNEL, comet and SCSA. The patients with morphologically normal looking sperms had high DNA damage [116].

3.6.6 Stallion Sperm DNA Damage Tests

Comet assay was used to determine cryopreservation and ROS induced DNA damage in stallion sperms. Four stages of lysing - standard lysing, RNase, proteinase K and mercaptoethenol added to fresh lysing solutions were needed to destroy the membranes and proteins. Ethidium bromide was used for staining. Different strengths of xanthine – xanthine oxidase were used to induce DNA fragmentation [63, 118]. A density gradient protocol was tested using comet assay [133].

SCSA has been designed for clinical equine sperm DNA damage assessment [134]. SCD did not detect stallion sperm DNA damage in fresh, thawed or chilled samples incubated at 37 ^{o}C. However, damage was observed following prolonged incubation of over an hour. After 48 hours, 100% of the samples suffered damage [135]. SCD was used on post-thaw stallion sperms to test a cryopreservation protocol on two different density gradient centrifugation protocol and different freezing semen extenders. SCD revealed reduced DNA damage after 4 hours of thawing [136].

3.7 *Biochemical Assays in Clinical IVF Applications*

The biochemical assay tests clearly indicated that sperm DNA damage has a negative impact on pregnancy outcome. Many assays, specifically designed to test sperm DNA damage prior to IVF treatment, were impractical for routine clinical usage, as they were complex, time consuming and inconclusive in many cases. SCSA and TUNEL were used to compare clinical pregnancy with sperm DNA quality, and the small but statistically significant study did not show sufficient correlation between percentage of sperm DNA damage to pregnancy, in order to incorporate these tools into routine clinical procedures for IVF [137]. Toluidine blue (TB) is a simple, fast and inexpensive test that correlated with both SCSA and TUNEL tests. TB has been identified as a fast and simple technique for routine clinical application to test sperm DNA damage [138].

TUNEL assay was used to compare DNA damage in fresh sperms to pregnancy rates, during a 4 months clinical trial involving 50 IVF and 54 ICSI patients with male infertility. Samples from men of normal fertility had 6-8% DNA damage. Samples from men with low sperm count had 12 - 16% DNA fragmentation. The pregnancy rate was low with sperms that had DNA fragmentation greater than 10%; and sperms with DNA fragmentations of 18-20% did not result in pregnancy with ICSI. DNA fragmentation did not appear to have a significant impact on pregnancy using conventional IVF [139]. Alkaline comet assay tests showed that DNA fragmentation was high in cryopreserved sperms from infertile men; whereas the sperms of normal fertility did not show similar increase in DNA damage [140].

Various studies indicate that the DFI index in SCSA is not a simple predictor of pregnancy outcome. Since pregnancies and live births are achieved using a variety of techniques - natural, ICSI and conventional IVF with fresh or cryopreserved sperms, prepared using neat semen, swim up or density gradient, the DFI for each method has to be evaluated separately. The DFI of neat semen, swim-up and density gradient preparations on the same ejaculate are not same [101, 126, 128, 129]. SCSA predicted spontaneous abortion but did not predict fertilisation rate or embryo quality in IVF and ICSI [128]. Pregnancy and live birth using ICSI was achieved with sperm

preparation that had high DFI of 32% indicating the limitations of predictive value of DFI in infertility treatment [127].

3.8 Summary of Chapter Three

The molecular structure of DNA, DNA replication, coding errors and repair mechanisms provided a glimpse into the complex and miraculously orderly nature of cell life and death, health and diseases, aging, cancer, genetic disorders, DNA damage and evolutionary changes. There are different types of DNA damages; the nature and location of DNA damages play a role in fertility. This review also helped to understand the chromosomal similarities and differences between horse and humans.

Many papers list ROS as a major source of sperm DNA damage; hence, the nature of internally and externally generated ROS, the role of mitochondria in ROS generation and neutralisation were reviewed. Study of oxidative and osmotic stress in human and stallion sperms were very useful for designing the experimental work. Artificial sources of ROS were reviewed, as hydrogen peroxide generated from xanthine - xanthine oxidase was used to induce DNA damage for oxidative stress damage study in this research. This chapter provided background information for the design of the core experimental work in this thesis.

It had also been the intention to use comet or TUNEL assay to compare the induced sperm DNA damage with Raman spectroscopy analysis. Such a comparative study was not possible in the timeframe of the PhD. As a result, the thesis relies on published papers to explain the experimental spectroscopy study. The review of the different assays helped to interpret the difference in the techniques and their outcome, when comparing these techniques with Raman spectroscopy.

Multiple factors contribute to the inability to standardise sperm DNA damage measurement techniques. Discussion with researchers, who used biochemical assays on stallion sperms, claimed limited success with stallion sperms because of the highly resistant disulphide cross-links. Various biochemical assays have been used in quantifying human sperm DNA damage and to correlate it with pregnancy

potential, but this has produced inconsistent results. These tests measure different types of damage and could account for the different DFIs.

This review shows that a comparative study of Raman fingerprint of live sperms with biochemical assays require in-depth knowledge of sperm biochemistry, the nature of the live cell interaction with the laser, the nature and interaction of the assays with the cells, the nature and location of DNA damage and any time dependent change that happens to the chemically stressed cells. Such knowledge is in its fledgling stage [101, 141, 142].

Reference

1. Alberts, B., et al., *Molecular Biology of The Cell*. Fourth ed. 2002, New York: Garland Science.
2. Lewis, J.D., et al., *A walk though vertebrate and invertebrate protamines.* Chromosoma, 2003. **111**: p. 473 - 482.
3. Strachan, T. and A.P. Read, *Human Molecular Genetics* 2nd edition ed. 1999, New York: Wiley-Liss.
4. Redon, C., et al., *Histone H2A variants H2AX and H2AZ.* Current Opinion in Genetics & Development, 2002. **12**(2): p. 162-169.
5. Fredholm, L. *The Discovery of the Molecular Structure of DNA - The Double Helix*. [website] 2003 [cited 2011 11 Jan]; Atricle and images]. Available from: http://nobelprize.org/educational/medicine/dna_double_helix/readmore.html.
6. National Library of Medicine, N., *Genetics Home Reference, Your Guide to Understanding Genetic Conditions*, D.o.H.a.H. Services, Editor. 2011, National Library of Medicine, Lister Hill National Center for Biomedical Communications. p. 147.
7. HGMIS, H.G.M.I.S., *Human Genome Project Information*, U.S. Department of Energy Office of Science, Editor. 2008, Office of Biological and Environmental Research,Oak Ridge National Laboratory.
8. Bench, G.S., et al., *DNA and total protamine masses in individual sperm from fertile mammalian subjects.* Cytometry, 1996. **23**: p. 263 - 271.
9. Brewer, L., M. Corzett, and R. Balhorn, *Condensation of DNA by Spermatid Basic Nuclear Proteins.* J. Biol. Chem., 2002. **277**(41): p. 38895-38900.
10. Yoshii, T., et al., *Fine resolution of human sperm nucleoproteins by two-dimensional electrophoresis.* Molecular Human Reproduction, 2005. **11**(9): p. 677-681.
11. Balhorn, R., S. Reed, and N. Tanphaichitr, *Aberrant protamine 1/protamine 2 ratios in sperm of infertile human males.* Cellular and Molecular Life Sciences, 1988. **44**(1): p. 52-55.
12. Oliva, R., *Protamines and male infertility.* Hum Reprod Update, 2006. **12**(4): p. 417-435.
13. Hammadeh, M.E., et al., *Protamine contents and P1/P2 ratio in human spermatozoa from smokers and non-smokers.* Human Reproduction, 2010: p. 1-13.
14. Aoki, V.W. and D.T. Carrell, *Human protamines and the developing spermatid: their structure, function, expression and relationship with male infertility.* Asian J Androl, 2003. **5**(4): p. 315 - 324.
15. Balhorn, R., *The protamine family of sperm nuclear proteins.* Genome Biology, 2007. **8** (9): p. 227.
16. Kramer, J.A. and S.A. Krawetz, *Nuclear Matrix Interactions within the Sperm Genome.* Journal of Biological Chemistry, 1996. **271**(20): p. 11619-11622.
17. Raudsepp, T., et al., *A detailed physical map of the horse Y chromosome.* Proceedings of the National Academy of Sciences of the United States of America, 2004. **101**(25): p. 9321-9326.
18. Mark, A.B., et al., *Identification of gene products present in Triton X-100 soluble and insoluble fractions of human spermatozoa lysates using LC-MS/MS analysis.* PROTEOMICS - Clinical Applications, 2007. **1**(5): p. 524-532.
19. Wade, C.M., et al., *Genome Sequence, Comparative Analysis, and Population Genetics of the Domestic Horse.* Science, 2009. **326**(5954): p. 865-867.
20. Raudsepp, T., et al., *Exceptional conservation of horse - human gene order on X chromosome revealed by high-resolution radiation hybrid mapping.* Proceedings of the National Academy of Sciences of the United States of America, 2004. **101**(8): p. 2386-2391.
21. Chowdhary, B.P., et al., *The First-Generation Whole-Genome Radiation Hybrid Map in the Horse Identifies Conserved Segments in Human and Mouse Genomes.* Genome Research, 2003. **13**(4): p. 742-751.
22. Pray, L.A., *DNA Replication and Causes of Mutation.* Nature Education 2008 **1**(1).
23. Gredilla, R., *DNA Damage and Base Excision Repair in Mitochondria and Their Role in Aging.* Journal of Aging Research, 2011. **2011**: p. 1-9.
24. Widlak, P., M. Pietrowska, and J. Lanuszewska, *The role of chromatin proteins in DNA damage recognition and repair -Mini-review.* Histochemistry and Cell Biology, 2006. **125**(1): p. 119-126.

25. de Laat, W.L., N.G.J. Jaspers, and J.H.J. Hoeijmakers, *Molecular mechanism of nucleotide excision repair.* Genes & Development, 1999. **13**(7): p. 768-785.
26. Ma, W., et al., *The Transition of Closely Opposed Lesions to Double-Strand Breaks during Long-Patch Base Excision Repair Is Prevented by the Coordinated Action of DNA Polymerase {delta} and Rad27/Fen1.* Mol. Cell. Biol., 2009. **29**(5): p. 1212-1221.
27. Bohgaki, T., M. Bohgaki, and R. Hakem, *DNA double-strand break signaling and human disorders.* Genome Integrity, 2010. **1**(1): p. 15.
28. Cromie, G.A., J.C. Connelly, and D.R.F. Leach, *Recombination at Double-Strand Breaks and DNA Ends: Conserved Mechanisms from Phage to Humans.* Molecular Cell, 2001. **8**(6): p. 1163-1174.
29. Mourgues, S., M.E. Lomax, and P. O' Neill, *Base excision repair processing of abasic site/single-strand break lesions within clustered damage sites associated with XRCC1 deficiency.* Nucleic Acids Research, 2007. **35**(22): p. 7676-7687.
30. Nakayama, T., et al., *Cigarette smoke induces DNA single-strand breaks in human cells.* Nature, 1985. **314**(6010): p. 462-464.
31. Sutherland, B.M., et al., *Clustered DNA Damages Induced in Human Hematopoietic Cells by Low Doses of Ionizing Radiation.* Journal of Radiation Research, 2002. **43**(S): p. S149-S152.
32. Sakkas, D. and J.G. Alvarez, *Sperm DNA fragmentation: mechanisms of origin, impact on reproductive outcome, and analysis.* Fertility and Sterility, 2010. **93**(4): p. 1027-1036.
33. Said, T., et al., *Selection of Nonapoptotic Spermatozoa As a New Tool for Enhancing Assisted Reproduction Outcomes: An In Vitro Model.* Biology of Reproduction, 2006. **74**(3): p. 530-537.
34. Ainsworth, C., et al., *First recorded pregnancy and normal birth after ICSI using electrophoretically isolated spermatozoa.* Human Reproduction, 2006. **22**(1): p. 197-200.
35. Fleming, S.D., et al., *Prospective controlled trial of an electrophoretic method of sperm preparation for assisted reproduction: comparison with density gradient centrifugation.* Human Reproduction, 2008. **23**(12): p. 2646-2651.
36. Zhang, X., et al., *Localization of single-stranded DNA in human sperm nuclei.* Fertility and Sterility, 2007. **88**(5): p. 1334-1338.
37. Hekmatdoost, A., N. Lakpour, and M.R. Sadeghi, *Sperm Chromatin Integrity: Etiologies and Mechanisms of Abnormality, Assays, Clinical Importance, Preventing and Repairing Damage* Avicenna Journal of Medical Biotechnology 2009. **1** (3): p. 147 to 160
38. Andreyev, A., Y. Kushnareva, and A. Starkov, *Mitochondrial metabolism of reactive oxygen species.* Biochemistry (Moscow), 2005. **70** (2): p. 200-14.
39. Valko, M., et al., *Free radicals and antioxidants in normal physiological functions and human disease.* The International Journal of Biochemistry & Cell Biology, 2007. **39**(1): p. 44-84.
40. Powers, S.K. and M.J. Jackson, *Exercise-Induced Oxidative Stress: Cellular Mechanisms and Impact on Muscle Force Production.* Physiol. Rev., 2008. **88**(4): p. 1243-1276.
41. St John, J.C., R.P. Jokhi, and C.L.R. Barratt, *Men with oligoasthenoteratozoospermia harbour higher numbers of multiple mitochondrial DNA deletions in their spermatozoa, but individual deletions are not indicative of overall aetiology.* Mol. Hum. Reprod., 2001. **7**(1): p. 103-111.
42. George, M. and O.A. Ryder, *Mitochondrial DNA evolution in the genus Equus.* Molecular Biology and Evolution, 1986. **3**(6): p. 535-546.
43. Nagendrappa, G., *An appreciation of free radical chemistry 3. Free radicals in diseases and health.* Resonance, 2005. **10**(4): p. 65-74.
44. Tremellen, K., *Oxidative stress and male infertility--a clinical perspective.* Hum Reprod Update, 2008. **14**(3): p. 243-258.
45. Fletcher, A.E., *Free Radicals, Antioxidants and Eye Diseases: Evidence from Epidemiological Studies on Cataract and Age-Related Macular Degeneration.* Ophthalmic Research, 2010. **44**(3): p. 191-198.
46. Agarwal, A., S.A. Prabakaran, and T.M. Said, *Prevention of Oxidative Stress Injury to Sperm.* J Androl, 2005. **26**(6): p. 654-660.
47. Goodsell, D.S., *The Molecular Perspective: Cytochrome c and Apoptosis.* Oncologist, 2004. **9**(2): p. 226-227.
48. Ball, B.A., *Oxidative stress, osmotic stress and apoptosis: Impacts on sperm function and preservation in the horse.* Animal Reproduction Science, 2008. **107**(3-4): p. 257-267.
49. Aitken, R.J. and M.A. Baker, *Oxidative stress and male reproductive biology.* Reproduction, Fertility and Development, 2004. **16**(5): p. 581-588.

50. Ricci, G., et al., *Semen preparation methods and sperm apoptosis: swim-up versus gradient-density centrifugation technique.* Fertility and Sterility, 2009. **91**(2): p. 632-638.
51. Aitken, R.J., et al., *Reactive oxygen species generation by human spermatozoa is induced by exogenous NADPH and inhibited by the flavoprotein inhibitors diphenylene iodonium and quinacrine.* Molecular Reproduction and Development, 1997. **47**(4): p. 468-482.
52. Alvarez, J.G. and B.T. Storey, *Evidence for increased lipid peroxidative damage and loss of superoxide dismutase activity as a mode of sublethal cryodamage to human sperm during cryopreservation.* J Androl, 1992. **13**(3): p. 232-241.
53. Ford, W.C.L., *Regulation of sperm function by reactive oxygen species.* Hum Reprod Update, 2004. **10**(5): p. 387-399.
54. Sanocka, D. and M. Kurpisz, *Reactive oxygen species and sperm cells.* Reproductive Biology and Endocrinology, 2004. **2**(1): p. 12.
55. Li, M.W., et al., *Damage to Chromosomes and DNA of Rhesus Monkey Sperm Following Cryopreservation.* J Androl, 2007. **28**(4): p. 493-501.
56. De Iuliis, G.N., et al., *DNA Damage in Human Spermatozoa Is Highly Correlated with the Efficiency of Chromatin Remodeling and the Formation of 8-Hydroxy-2'-Deoxyguanosine, a Marker of Oxidative Stress.* Biology of Reproduction, 2009. **81**(3): p. 517-524.
57. Koppers, A.J., et al., *Significance of Mitochondrial Reactive Oxygen Species in the Generation of Oxidative Stress in Spermatozoa.* J Clin Endocrinol Metab, 2008. **93**(8): p. 3199-3207.
58. Williams, A.C. and W.C.L. Ford, *Relationship between reactive oxygen species production and lipid peroxidation in human sperm suspensions and their association with sperm function.* Fertility and Sterility, 2005. **83**(4): p. 929-936.
59. Gil-Villa, A.M., et al., *Role of male factor in early recurrent embryo loss: do antioxidants have any effect?* Fertility and Sterility, 2009. **92**(2): p. 565-571.
60. Bennetts, L.E. and R.J. Aitken, *A comparative study of oxidative DNA damage in mammalian spermatozoa.* . Molecular Reproduction and Development, 2005. **71**(1): p. 77-87.
61. Kemal Duru, N., M. Morshedi, and S. Oehninger, *Effects of hydrogen peroxide on DNA and plasma membrane integrity of human spermatozoa.* Fertility and Sterility, 2000. **74**(6): p. 1200-1207.
62. Ball, B., *The effect of oxidative stress on equine sperm function, semen storage and stallion fertility.* Journal of Equine Veterinary Science, 2000. **20**(2): p. 95-96.
63. Baumber, J., et al., *Reactive Oxygen Species and Cryopreservation Promote DNA Fragmentation in Equine Spermatozoa.* J Androl, 2003. **24**(4): p. 621-628.
64. Thomson, L.K., et al., *Cryopreservation-induced human sperm DNA damage is predominantly mediated by oxidative stress rather than apoptosis.* Human Reproduction, 2009. **24**(9): p. 2061-2070.
65. De Iuliis, G.N., et al., *DNA Damage in Human Spermatozoa Is Highly Correlated with the Efficiency of Chromatin Remodeling and the Formation of 8-Hydroxy-2â€²-Deoxyguanosine, a Marker of Oxidative Stress.* Biology of Reproduction, 2009. **81**(3): p. 517-524.
66. Neild, D.M., et al., *Membrane changes during different stages of a freeze-thaw protocol for equine semen cryopreservation.* Theriogenology, 2003. **59**(8): p. 1693-1705.
67. Oliva, A. and L. Multigner, *Ketotifen improves sperm motility and sperm morphology in male patients with leukocytospermia and unexplained infertility.* Fertility and Sterility, 2006. **85**(1): p. 240-243.
68. Ricci, G., et al., *Leukocyte detection in human semen using flow cytometry.* Human Reproduction, 2000. **15**(6): p. 1329-1337.
69. Ramadan, A.S., et al., *Negative effects of increased sperm DNA damage in relation to seminal oxidative stress in men with idiopathic and male factor infertility.* Fertility and sterility, 2003. **79**: p. 1597-1605.
70. Oger, I., et al., *Evaluating human sperm DNA integrity: relationship between 8-hydroxydeoxyguanosine quantification and the sperm chromatin structure assay.* Zygote, 2003. **11**(04): p. 367-371.
71. Zini, A., et al., *Beneficial effect of microsurgical varicocelectomy on human sperm DNA integrity.* Hum. Reprod., 2005. **20**(4): p. 1018-1021.
72. Saleh, R.A., et al., *Varicocele in infertile men is significantly correlated with increased levels of sperm nuclear DNA damage.* Fertility and Sterility, 2002. **78**(Supplement 1): p. S259-S259.
73. Smith, R., et al., *Increased sperm DNA damage in patients with varicocele: relationship with seminal oxidative stress.* Human Reproduction, 2006. **21**(4): p. 986-993.

74. du Plessis, S.S., et al., *Impact of oxidative stress on IVF.* Expert Review of Obstetrics & Gynecology, 2008. **3**(4): p. 539-554.
75. Zini, A., et al., *Sperm DNA damage is associated with an increased risk of pregnancy loss after IVF and ICSI: systematic review and meta-analysis.* Hum. Reprod., 2008. **23**(12): p. 2663-2668.
76. Simon, L., et al., *Clinical significance of sperm DNA damage in assisted reproduction outcome.* Human Reproduction, 2010. **25**(7): p. 1594-1608.
77. Aitken, R.J. and J.S. Clarkson, *Cellular basis of defective sperm function and its association with the genesis of reactive oxygen species by human spermatozoa.* J Reprod Fertil, 1987. **81**(2): p. 459-469.
78. Brackett, N.L., et al., *Higher Sperm DNA Damage in Semen From Men With Spinal Cord Injuries Compared With Controls.* J Androl, 2008. **29**(1): p. 93-99.
79. Padron, O.F., et al., *Seminal reactive oxygen species and sperm motility and morphology in men with spinal cord injury.* Fertility and Sterility, 1997. **67**(6): p. 1115-1120.
80. Kulkarni, S.R., et al., *Levels of plasma testosterone, antioxidants and oxidative stress in alcoholic patients attending de-addiction centre.* Biology and Medicine, 2009. **1**(4): p. 11-20.
81. Fraga, C.G., et al., *Smoking and low antioxidant levels increase oxidative damage to sperm DNA.* Mutation Research/Fundamental and Molecular Mechanisms of Mutagenesis, 1996. **351**(2): p. 199-203.
82. Forand, A., et al., *Similarities and Differences in the In Vivo Response of Mouse Neonatal Gonocytes and Spermatogonia to Genotoxic Stress.* Biology of Reproduction, 2009. **80**(5): p. 860-873.
83. McKelvey-Martin, V.J., et al., *Two potential clinical applications of the alkaline single-cell gel electrophoresis assay: (1) human bladder washings and transitional cell carcinoma of the bladder; and (2) human sperm and male infertility.* Mutation Research/Fundamental and Molecular Mechanisms of Mutagenesis, 1997. **375**(2): p. 93-104.
84. Ahmadi, A. and S.-C. Ng, *Fertilizing ability of DNA-damaged spermatozoa.* The Journal of Experimental Zoology, 1999. **284**(6): p. 696-704.
85. Fatehi, A.N., et al., *DNA Damage in Bovine Sperm Does Not Block Fertilization and Early Embryonic Development But Induces Apoptosis After the First Cleavages*. Journal of Andrology, 2006. **27**(2): p. 176-188.
86. Rand, R.P., *Intracellular osmotic action.* Cellular and Molecular Life Sciences, 2000. **57**(7): p. 1018-1032.
87. Meyers, S.A., *Spermatozoal response to osmotic stress.* Animal reproduction science, 2005. **89**(1): p. 57-64.
88. Ortega Ferrusola, C., et al., *Lipid peroxidation, assessed with BODIPY-C11, increases after cryopreservation of stallion spermatozoa, is stallion-dependent and is related to apoptotic-like changes.* Reproduction, 2009. **138**(1): p. 55-63.
89. Devireddy, R.V., et al., *Measured effect of collection and cooling conditions on the motility and the water transport parameters at subzero temperatures of equine spermatozoa.* Reproduction, 2002. **124**(5): p. 643-648.
90. Burnaugh, L., et al., *Osmotic stress stimulates generation of superoxide anion by spermatozoa in horses.* Animal Reproduction Science, 2010. **117**(3-4): p. 249-260.
91. Ball, B.A. and A. Vo, *Osmotic tolerance of equine spermatozoa and the effects of soluble cryoprotectants on equine sperm motility, viability, and mitochondrial membrane potential.* Journal of Andrology, 2001. **22**(6): p. 1061-1069.
92. Pommer, A.C., J. Rutllant, and S.A. Meyers, *The role of osmotic resistance on equine spermatozoal function.* Theriogenology, 2002. **58**(7): p. 1373-1384.
93. Neild, D., et al., *Hypoosmotic test in equine spermatozoa.* Theriogenology, 1999. **51**(4): p. 721-727.
94. Noiles, E.E., et al., *Determination of water permeability coefficient for human spermatozoa and its activation energy.* Biology of Reproduction, 1993. **48**(1): p. 99-109.
95. Mina, C.G. and D. Morel, *Equine Reproductive Physiology, Breeding and Stud Management*. Third ed. 2008: CAB International
96. Celik-Ozenci, C., et al., *Cryopreservation/thawing and function of human sperm: sperm that remain motile also maintain their plasma membrane integrity and hyaluronic acid binding properties.* Fertility and Sterility, 2002. **78**(Supplement 1): p. S213-S213.

97. Misro, M.M. and S.P. Chaki, *Development of a rapid, sensitive, and reproducible laboratory test kit for the assessment of plasma membrane integrity of human sperm.* Fertility and Sterility, 2008. **89**(1): p. 223-227.
98. Foster, M.L., et al., *Agreement between measures of total motility and membrane integrity in stallion sperm.* Theriogenology, 2011. **75**(8): p. 1499-1505.
99. Silva, P.F.N. and B.M. Gadella, *Detection of damage in mammalian sperm cells.* Theriogenology, 2006. **65**(5): p. 958-978.
100. Aurich, C., *Factors affecting the plasma membrane function of cooled-stored stallion spermatozoa.* Animal Reproduction Science, 2005. **89**(1-4): p. 65-75.
101. Makhlouf, A.A. and C. Niederberger, *DNA Integrity Tests in Clinical Practice: It Is Not a Simple Matter of Black and White (or Red and Green).* Journal of Andrology, 2006. **27**(3): p. 316-323.
102. Singh, N.P., et al., *A simple technique for quantitation of low levels of DNA damage in individual cells.* Experimental Cell Research, 1988. **175**(1): p. 184-191.
103. Fehsel, K., V. Kolb-Bachofen, and H. Kolb, *Analysis of TNF alpha-induced DNA strand breaks at the single cell level.* The American Journal of Pathology, 1991. **139**(2): p. 251-254.
104. Roti, J.L.R. and W.D. Wright, *Visualization of DNA loops in nucleoids from HeLa cells: assays for DNA damage and repair.* Cytometry, 1987. **8**(5): p. 461-7.
105. Evenson, D.P., Z. Darzynkiewicz, and M.R. Melamed, *Relation of mammalian sperm chromatin heterogeneity to fertility.* Science, 1980. **210**(4474): p. 1131-1133.
106. Chohan, K.R., et al., *Comparison of Chromatin Assays for DNA Fragmentation Evaluation in Human Sperm.* Journal of Andrology, 2006. **27**(1): p. 53-59.
107. Boe-Hansen, G.B., et al., *The sperm chromatin structure assay as a diagnostic tool in the human fertility clinic.* Hum. Reprod., 2006: p. del019.
108. Fernandez, J.L., et al., *The Sperm Chromatin Dispersion Test: A Simple Method for the Determination of Sperm DNA Fragmentation.* J Androl, 2003. **24**(1): p. 59-66.
109. Morris, I.D., et al., *The spectrum of DNA damage in human sperm assessed by single cell gel electrophoresis (Comet assay) and its relationship to fertilization and embryo development* Hum. Reprod., 2002. **17**(4): p. 990-998.
110. Olive, P.L., D. Wlodek, and J.P. Banaith, *DNA Double-Strand Breaks Measured in Individual Cells Subjected to Gel Electrophoresis.* Cancer Research, 1991. **51**(17): p. 4671-4676.
111. McArt, D.G., et al., *Comet sensitivity in assessing DNA damage and repair in different cell cycle stages.* Mutagenesis, 2010. **25**(3): p. 299-303.
112. Singh, N.P., et al., *Abundant alkali-sensitive sites in DNA of human and mouse sperm.* Experimental Cell Research, 1989. **184**(2): p. 461-470.
113. Glickman, R.D., et al., *Laser Bioeffects Associated with Ultrafast Lasers: Role of Multiphoton Absorption.* Journal of Laser Applications, 2008. **20**(89): p. 1-9.
114. Olive, P.L. and J.P. Banath, *The comet assay: a method to measure DNA damage in individual cells.* Nat. Protocols, 2006. **1**(1): p. 23-29.
115. Duty, S.M., et al., *The Relationship between Environmental Exposures to Phthalates and DNA Damage in Human Sperm Using the Neutral Comet Assay.* Environmental Health Perspectives 2002. **111**: p. 1164-1169.
116. O'Flaherty, C., et al., *Characterization of sperm chromatin quality in testicular cancer and Hodgkin's lymphoma patients prior to chemotherapy.* Human Reproduction, 2008. **23**(5): p. 1044-1052.
117. Wagner, T.E., D.R. Mann, and R.C. Vincent, *The role of disulfide reduction in chromatin release from equine sperm.* Journal of Experimental Zoology, 1974. **189**(3): p. 387-393.
118. Linfor, J.J. and S.A. Meyers, *Detection of DNA damage in response to cooling injury in equine spermatozoa using single-cell gel electrophoresis.* J Androl, 2002. **23**(1): p. 107-113.
119. Duty, S.M., et al., *Reliability of the comet assay in cryopreserved human sperm.* Human Reproduction, 2002. **17**(5): p. 1274-1280.
120. Rigby, P.W.J., et al., *Labeling deoxyribonucleic acid to high specific activity in vitro by nick translation with DNA polymerase I.* Journal of Molecular Biology, 1977. **113**(1): p. 237-251.
121. Gorczyca, W., J. Gong, and Z. Darzynkiewicz, *Detection of DNA Strand Breaks in Individual Apoptotic Cells by the in Situ Terminal Deoxynucleotidyl Transferase and Nick Translation Assays.* Cancer Research, 1993. **53**(8): p. 1945-1951.
122. Ramos, L. and A.M.M. Wetzels, *Low rates of DNA fragmentation in selected motile human spermatozoa assessed by the TUNEL assay.* Human Reproduction, 2001. **16**(8): p. 1703-1707.

123. Barroso, G., et al., *Developmental sperm contributions: fertilization and beyond.* Fertility and Sterility, 2009. **92**(3): p. 835-848.
124. Muriel, L., et al., *Value of the sperm deoxyribonucleic acid fragmentation level, as measured by the sperm chromatin dispersion test, in the outcome of in vitro fertilization and intracytoplasmic sperm injection.* Fertility and Sterility, 2006. **85**(2): p. 371-383.
125. Evenson, D.P., et al., *Utility of the sperm chromatin structure assay as a diagnostic and prognostic tool in the human fertility clinic.* Hum. Reprod., 1999. **14**(4): p. 1039-1049.
126. Spano, M., et al., *Nuclear chromatin variations in human spermatozoa undergoing swim-up and cryopreservation evaluated by the flow cytometric sperm chromatin structure assay.* Molecular Human Reproduction, 1999. **5**(1): p. 29-37.
127. Gandini, L., et al., *Full-term pregnancies achieved with ICSI despite high levels of sperm chromatin damage.* Hum. Reprod., 2004. **19**(6): p. 1409-1417.
128. Bungum, M., et al., *The predictive value of sperm chromatin structure assay (SCSA) parameters for the outcome of intrauterine insemination, IVF and ICSI.* Hum. Reprod., 2004. **19**(6): p. 1401-1408.
129. Bungum, M., et al., *Sperm chromatin structure assay parameters measured after density gradient centrifugation are not predictive for the outcome of ART.* Hum. Reprod., 2008. **23**(1): p. 4-10.
130. Villani, P., et al., *Sperm DNA fragmentation induced by DNAse I and hydrogen peroxide: an in vitro comparative study among different mammalian species.* Reproduction, 2010. **140**(3): p. 445-452.
131. Cordelli, E., et al., *Evaluation of DNA Damage in Different Stages of Mouse Spermatogenesis after Testicular X Irradiation.* Radiation Research, 2003. **160**(4): p. 443-451.
132. Watanabe, S., et al., *An investigation of the potential effect of vacuoles in human sperm on DNA damage using a chromosome assay and the TUNEL assay.* Human Reproduction, 2010. **26**(5): p. 978-986.
133. Costa, A., et al., *Single Layer Centrifugation with Androcoll-E™ improved progressive motility and percentage of live spermatozoa with intact acrosome of chilled stallion semen but did not have an effect on DNA integrity. Open Journal of Animal Sciences*, 2012. **2**: p. 159-165.
134. Love, C.C., *The sperm chromatin structure assay: a review of clinical applications.* Animal Reproduction Science, 2005. **89**: p. 39-45.
135. Lopez-Fernandez, C., et al., *Dynamics of sperm DNA fragmentation in domestic animals: II. The stallion.* Theriogenology, 2007. **68**(9): p. 1240-1250.
136. Gutierrez-Cepeda, L., et al., *The effect of two pre-cryopreservation single layer colloidal centrifugation protocols in combination with different freezing extenders on the fragmentation dynamics of thawed equine sperm DNA.* Acta Veterinaria Scandinavica C7 - 72, 2012. **54**(1): p. 1-8.
137. Collins, J.A., K.T. Barnhart, and P.N. Schlegel, *Do sperm DNA integrity tests predict pregnancy with in vitro fertilization?* Fertility and Sterility, 2008. **89**(4): p. 823-831.
138. Erenpreiss, J., et al., *Toluidine blue cytometry test for sperm DNA conformation: comparison with the flow cytometric sperm chromatin structure and TUNEL assays* Human Reproduction, 2004. **19**(10): p. 2277-2282.
139. Benchaib, M., et al., *Sperm DNA fragmentation decreases the pregnancy rate in an assisted reproductive technique.* Hum. Reprod., 2003. **18**(5): p. 1023-1028.
140. Donnelly, E.T., et al., *Assessment of DNA integrity and morphology of ejaculated spermatozoa from fertile and infertile men before and after cryopreservation.* Human Reproduction, 2001. **16**(6): p. 1191-1199.
141. Aitken, R.J., et al., *The source and significance of DNA damage in human spermatozoa; a commentary on diagnostic strategies and straw man fallacies.* Molecular Human Reproduction, 2013. **19**(8): p. 475-485.
142. Schulte, R., et al., *Sperm DNA damage in male infertility: etiologies, assays, and outcomes.* Journal of Assisted Reproduction and Genetics, 2010. **27**(1): p. 3-12.

4

Raman Spectroscopy and Optical Traps for Assessing Sperm DNA Damage

Oh, Pauli, Fermi guide us
Banish our illusions
And elevate our hunches
To sensible conclusions

Frederick Reines (1918 - 1998)

4.0 *Spectroscopy*

With the discovery of electrons by JJ Thomson in 1897, many of the emerging details of microscopic structures could no longer be supported by classical physics. In the early 1900s, a new theory 'quantum mechanics' started to take shape. Einstein explained photoelectric effect in 1906 and stated that radiant energy was exchanged in discrete packets. Bohr created the electron orbitals in 1913 to explain all the series of the hydrogen spectral lines. He was awarded the Nobel Prize in 1922 for the work. In 1924 de Broglie, a French prince and history student turned physicist, proposed the wave nature of matter. When Davisson and Germer discovered electron diffraction in 1927, de Broglie was awarded the Nobel Prize in 1929 for his novel wave-particle theory. In 1926 Shroedinger came up with his famous 'equations' that used 'probability density functions', and 'momentum and energy operators', to describe atomic scale characteristics of materials. He used the quantum version of the ideal harmonic oscillator, to model the hydrogen atom and characterise its spectral lines. The word 'photon', derived from Greek word for light $\varphi\omega\varsigma$, was used by G. N. Lewis in a paper in 1926, to describe a 'particulate of light' [1, 2].

A new and exciting period had emerged in physics, and scientists were flocking to explore the discrete world of atoms and molecules using spectroscopy. Professor C. V. Raman was one of them.

4.1 History of Raman Spectroscopy

Professor CV Raman was born in South India in 1888 and graduated from Madras Presidency College with gold medal in 1904; and in 1906, he completed an MA with distinction. He developed a research interest in optics and acoustics very early on, and during his student years, published papers on diffraction (1906) in well-known scientific journals. He started his career in Civil Services before accepting a Professorship of Physics at the University of Calcutta. Unlike most scientists of recent years, Professor Raman had no professional training in research [3].

Professor Raman published a letter in Nature on the impact of scattering angle on the intensity of scattered radiation in 1919, and an article on light scattering by sulphur particle suspensions in 1921. The same year he travelled to Britain by sea for the first time, and was fascinated by the spectacular blue of the Mediterranean Sea. He demonstrated that the blue of the sea was not due to reflection of the blue of the sky in water, but due to scattering of sunlight by water molecules [3, 4].

In 1922, Professor Raman published are article 'Molecular Diffraction of Light' in a campus newspaper, which explored the concept of energy exchange between photons and molecules. A year later, Compton demonstrated inelastic scattering of X-rays (Compton Effect), and won the Nobel Prize in 1927. Mandelstam and Landsberg in the Soviet Union, Jean Cabannes and Yves Rocord in France, and Raman worked independently, researching inelastic scattering with visible light [3].

Professor Raman and his students spent the next six years working on light scattering experiments. He used violet spectral lines extracted from sunlight and liquid media for his early scattering research. He dismissed the observation of green light alongside scattered violet light in 1923, and several such phenomena, in a variety of liquid media, as weak fluorescence. Two years later, when the green radiation was found to be polarised, he recognised it as a new phenomenon, but hesitated to publish the observations without further evidence [3]. By the end of 1927, his team had observed a wavelength shifted radiation effect in optical grade glass and ice crystals. He called it 'modified scattering'. Professor Raman sent a cable to 'Nature' on 16th February 1928, summarising their findings in a letter titled, 'A New Type of Secondary Radiation'. Using 435.8 nm line from a mercury vapour lamp, his team improved the experimental results; Professor Raman published a detailed account of the experiment and the observation of high frequency lines, the more intense low frequency lines and their polarisation states, in the Indian Journal of Physics on 31st March 1928. The frequencies, ranging from a few cm^{-1} to 3800 cm^{-1}, appeared as sharp lines with ice and as diffuse lines with water or glass scatterers [3, 5].

The French team Rocard and Cabannes had developed a theoretical model for inelastic scattering in November 1927 and used it to calculate the frequencies and

molecular structures that gave rise to the scattered signals. The theoretical findings were published in 23 April 1928 [3].

Landsberg and Mandelstam in Moscow used quartz and an electric discharge lamp for their scattering experiments. On 21st February 1928, the Russian team independently demonstrated inelastic light scattering, the intensity of which was related to the absolute temperature of the scatterer. The team published their work on 6th May. They associated the large change in frequency to the excited IR frequencies of the crystal, and called it 'combination scattering' [3].

Professor Raman was awarded the Nobel Prize in 1930 for this discovery, two years after the historic Raman Effect was demonstrated; and its scope in the study of materials was well anticipated even though monochromatic source in the form of lasers were yet to be invented [3].

The quantum mechanical scattering theory that explained the Raman Effect required intense and complex analysis of the Eigen functions associated with the scatterer and a precise knowledge of all its eigenstates. Quantum chemistry was still in a fledgling state at the time and the application of this theory remained elusive. However, in 1934, Placzek, a Czech scientist [6], used molecular symmetry, stationary nuclei, non-degenerate states, and a scattering frequency much greater than the excitation energies of the molecules, to explain Raman Effect. Using this simplified model, he calculated the intensities of the scattered signals for the ground state of molecules. He derived the inelastic scattering components using the nuclear coordinates, a 9 x 9 polarisability tensor and its derivatives. Since then, using molecular structure and symmetry characteristics of molecules, Placzek's technique has been used to theoretically analyse Raman signals [3].

In the early days, narrow regions of light were extracted from powerful lamps or sunlight. Spectrometers and handcrafted gratings with limited resolution were used to resolve the weak signals. Photographic plates that required several hours of exposure were used to capture these Raman signals. Raman spectroscopists required patience and dedication; as a result, the applications of Raman spectroscopy developed very slowly for many decades.

In the first quarter of the 20th century, many revolutionary new concepts in physics paved the way, not only for Raman spectroscopy, but also for the concept of 'stimulated emission', as theorised by Einstein in his 1917 publication [7]. On 16th May 1960, the first laser was invented by Theodore Maiman of Hughes Research Laboratory in California, using stimulated emission from a solid state ruby crystal. For the first time, monochromatic light sources with narrow line widths were produced without the need for dispersion elements and filters. Peter Sorokin at IBM research laboratories in Yorktown Heights, New York, produced a high power laser using calcium fluoride crystal for lasing. The same year Ali Javan and team at Bell Labs invented a continuous emission, low power laser of very narrow frequency range, using helium neon gas. In 1962, Robert Hall and team at GE, New York, invented the first semiconductor laser, which found wide applications from barcode readers and laser pointers to optical communications [8]. Following the invention of lasers, research in Raman spectroscopy gained momentum, and nearly a quarter of a million papers were published on the subject by 1978 [3].

Small, low powered Nd:YAG (yttrium-Al-garnet) diode lasers emerged in the 1980s, with narrow emission wavelengths ranging from 532 nm in the visible to 1064 nm in the NIR range. Digital imaging devices appeared in the consumer market at about the same time. Photodiode arrays and charge coupled devices (CCD) capable of high resolution, high speed digital image recording at multiple wavelengths, with superior sensitivity and signal to noise ratio (SNR) replaced photographic films [9]. Personal computers became affordable when Advanced Micro Devices AMD) competed with Intel in manufacturing X86 microprocessors in 1986. Computer controlled equipment became affordable and easy to use; computer technology was utilised to improve signal acquisition and data processing. These events paved way for affordable commercial Raman tools; Raman affect was applied in materials research, product development, manufacturing and medical applications [9].

4.2 Introduction to Light Scattering Techniques

When light is incident on matter, it can be absorbed, emitted, transmitted or elastically (Rayleigh, Debye and Thomson) and inelastically (Raman, Compton and Brillouin) scattered - a physical process where the signal direction is altered. In

1800, Herschel, a self-taught British Astronomer of German origin, discovered heat generating invisible 'calorific rays' that behaved like visible light. In the mid-1800s, Kirchhoff, a Prussian born German physicist, discovered that atoms and molecules absorbed and emitted characteristic radiation. IR spectroscopy, as absorption spectroscopy is popularly known today, was nearly a century old before Raman Effect was discovered [10].

The nature of light-matter interaction depends on the wavelength of the light and the molecules in the material. Thomson and Compton Effect occur when the incident photons interact with the bound, free or quasi-free electrons in the material. Compton Effect is an inelastic scattering event in which high energy photons - usually x-rays and γ-rays - transfer momentum and energy to the electrons in the scattterer; the scattered light has wavelengths different from that of the incident beam. When the energy of the incident radiation is << the rest energy of the electron ($m_e c^2$), the scattered radiation does not suffer measurable energy loss; the scattering is treated as elastic, and the phenomenon is known as Thomson scattering [11].

Rayleigh scattering and Mie/Debye scattering are elastic scattering and the most dominant effect in light-matter interaction. Mie (Debye) scattering covers large and small particle scattering [12]; when the particle size is << than the wavelength of the incident light, the scattering is known as Rayleigh scattering; it has strong wavelength dependence and the intensity of the scattered light varies as $\frac{1}{\lambda^4}$ [13].

Brillouin scattering is caused by thermal fluctuations and acoustic phonons, and is observed in condensed matters and solids when light interacts with the inhomogeneities in the material. The standing wave pattern of refractive index fluctuation caused by acoustic phonons is utilised to design thin film coatings for wavelength specific optical fibres, Bragg gratings and optical sensors [14].

4.3 Overview of Raman Spectroscopy

All atoms and molecules have intrinsic vibrational modes, even at 0 K. Each mode of vibration has an associated discrete energy state. In crystalline materials, where several planes of atoms and/or molecules vibrate in phase, the vibrations are known as phonons. Phonons are the quantum mechanical equivalent of classical acoustic

waves. In this thesis the word 'phonon' is used to denote a vibrational mode. The term 'degrees of freedom' for a molecule defines the number of independent ways in which the atoms in the molecule can oscillate, and is related to the number of atoms in the molecule. A single molecule represented as a rigid body (having size and shape) has 6 degrees of freedom - 3 translational and 3 rotational. A molecule consisting of N atoms in bound state has 3N – 6 degrees of freedom; in a linear structure, the molecule has 3N – 5 degrees of freedom [15].

Raman Spectroscopy (RS) is the study of light matter interaction, in which the incident light is absorbed in small packets, 'quanta', to change the polarisation state of the molecular phonons, as they transition from one state to another. The re-emitted photons have slightly different energies, and they carry information of the molecular bonds and vibrational modes [16]. The energy states of phonons obey Bose-Einstein statistical distribution [17],

$$\frac{n_i}{g_i} = \frac{1}{Be^{\frac{\varepsilon_i}{kT}} - 1},$$

where n_i is the population of the energy state, ε_i,

k is Boltzmann constant and T is the absolute temperature

g_i is the total number of states at energy ε_i (degeneracy).

B $\geq$1 is a constant associated with temperature of the system.

4.3.1 Linear and Nonlinear Raman Effects

There are two basic types of Raman scattering – linear and non-linear. The photon–phonon interaction is a superposition of linear and nonlinear Raman contributions. Various methods of sample preparation are used to enhance the weak Raman signals - resonance Raman, surface enhanced Raman (SERS), tip enhanced Raman and combinations of these techniques [16]. The experimental work in this thesis use NIR radiation and linear Raman scattering.

4.3.2 Linear Raman Effect

In linear Raman techniques, the dominant contribution is from linear interaction, such that the scattered signal intensity is proportional to the incident signal intensity at a given scattering angle. Energies in the UV and visible range are needed to cause

electronic excitations [18]; however, electronic excitations from NIR range has been reported in Cr doped YAG at low temperatures [19].

Rotational energy states provide information on the centre of mass (CM) of the molecules, and apply primarily to gases and liquids where the CM of the fluid molecules are not rigidly bound. Rotational scattering frequencies are in the microwave range, and consist of evenly spaced peaks that are largely responsible for spectral line broadening in liquids and gases [3, 15].

4.3.3 Diatomic Molecular Vibrations

Homonuclear diatomic molecules like C_2, N_2, O_2 and H_2 have symmetric charge distribution; they have symmetric vibrations and do not contribute to IR spectra. Hence, the vibrational spectra of these molecules can only be studied using Raman spectroscopy. The classical simple harmonic oscillator (SHO) model cannot explain discrete spectral lines or multiple frequencies observed in molecular spectra [15]. The one- dimensional quantum mechanical oscillator (QMO) model has been able to explain the discrete spectral lines, the 'non-zero' energy at 0 K and low energy spectra of diatomic molecules. This symmetric potential cannot explain the vibrational transitions between non-adjacent states, the energy bands at higher energy states or dissociation at high energies that are different for different diatomic molecules with different bond strengths [15].

Real vibrational potential is not symmetric about the equilibrium position. During the molecular vibration, the high energy, short range inter-nuclear repulsive force dominates at minimum inter-atomic spacing; the long range, low energy van der Waal attractive force dominates at maximum inter-atomic spacing. This affect, is known as anharmonicity. The anharmonic quantum mechanical oscillator (AQMO) is a more realistic model of diatomic molecular energy states, permitting multilevel transitions, dissociation and energy bands. The QMO and AQMO with their corresponding discrete energy levels are shown in **Figure 4.1**. D_e is the energy of dissociation and D_o is the depth of the potential well. The anharmonic potential has no exact solutions. Analytical approximations like variational method and

perturbation theory are used to model the binding potentials; and many models exist that reproduce higher frequency spectra of particular molecules [20].

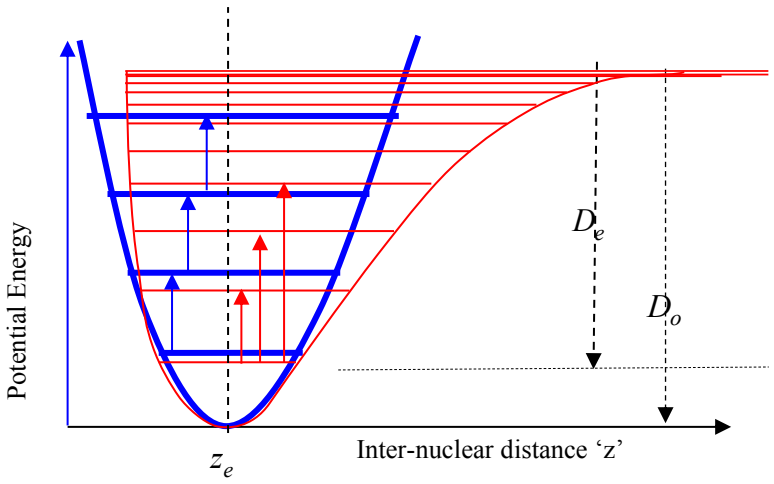

Figure 4.1 The energy states as a function of the bond length for a linear diatomic molecule oscillating in AQMO (red) is compared to the QMO (blue) about the equilibrium inter-nuclear spacing z_e. Adapted from [15].

A popular anharmonic potential is the Morse potential with an exponential function that has an exact solution for a diatomic molecule [21] ,

$$V(z) = D_e(1 - e^{-a(z-z_e)})^2$$

where D_e is the dissociation potential and the constant a is characteristic of the diatomic molecular bond. As $z \to \infty$, $V(z) \to D_e$. However, as $z \to 0$ V(z) $\neq \to \infty$. Despite this obvious limitation, Morse potential and its modifications are used to determine low energy states of many diatomic and polyatomic molecules [15, 22].

4.3.4 Triatomic Molecular Vibration

CO_2 is a linear tri-atomic molecule with four degrees of freedom (**Figure 4.2)**. Due to linear charge symmetry, the non-homonuclear and non-polar CO_2 molecule has vibrational modes that are either Raman or IR active [23]. The two perpendicular bending modes have the same magnitude; the molecule produces three vibrational spectra in an isotropic material. The symmetric linear stretching is Raman active, the asymmetric linear stretching mode and the bending modes are IR active [15].

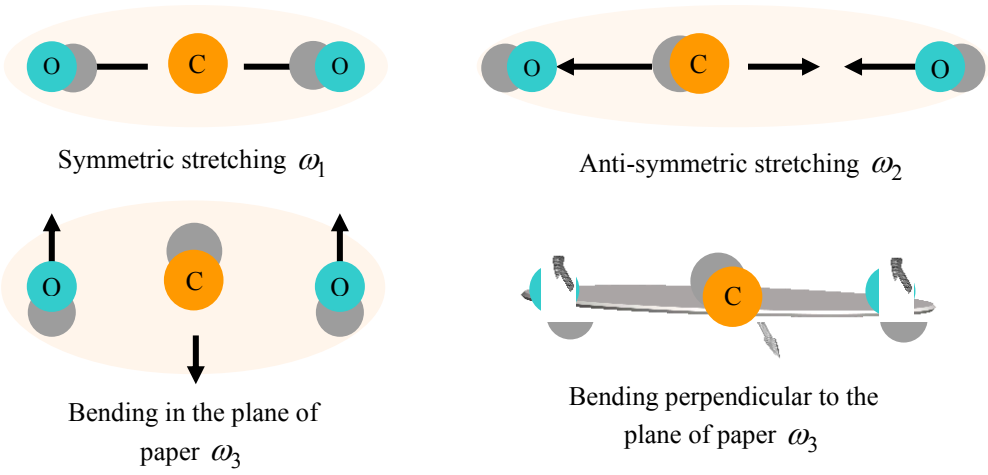

Figure 4.2 CO_2 with charge symmetry about the CM, is used as an example of a linear tri-atomic molecule executing fundamental vibrational motions along the molecular axis.

H_2O (water molecule) is a typical example of a tri-atomic non-linear molecule. It is a polar molecule with non-centrosymmetric charge distribution with the H atoms making 104.5 degrees with the 'O' atom. H_2O has 3 degrees of freedom, consisting of bending, asymmetric and symmetric stretching modes. H_2O molecule also rotates about the heavier O atom and the strong roto-vibrational coupling produces rocking vibrations (librations) along the three axes as depicted in **Figure 4.3**.

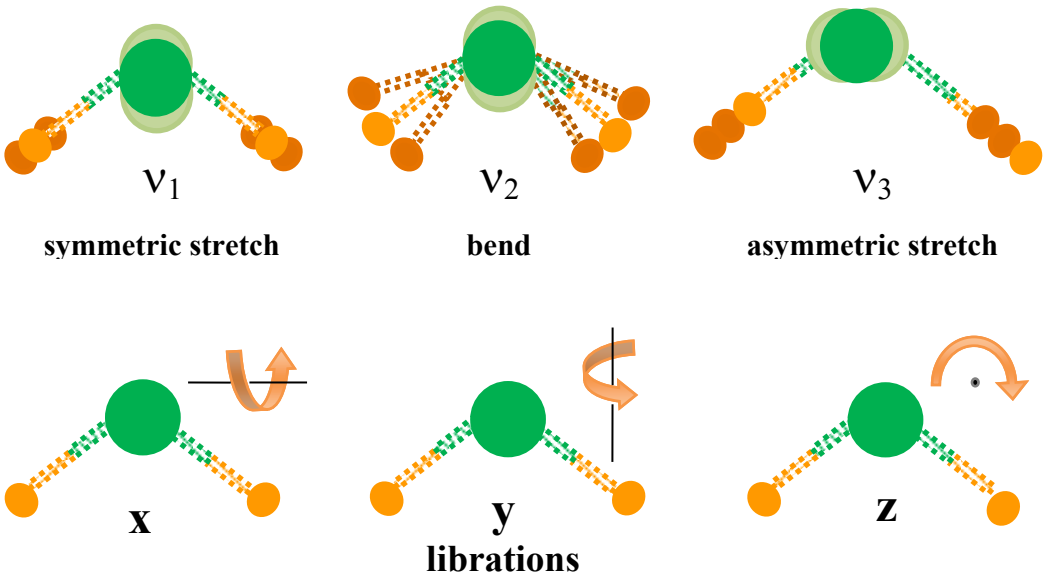

Figure 4.3 A non-linear tri-atomic molecule, H_2O, with 3 degrees of freedom, executing vibrational motion and libration (rocking motion) [24]

These vibrations are weakly Raman active but strongly IR active, due to their strong dipole moment and give rise to sharp IR vapour phase peaks. Convolution of librational, rotational and vibrational modes gives rise to millions of vibrational overtone spectra that account for spectral line broadening in water. The complex vibrations of polyatomic molecules can be decomposed into fundamental modes of vibration, as demonstrated with diatomic and tri-atomic molecules. These modes and their Raman and IR activities can be investigated using quantum chemistry, point groups and symmetry properties [24, 25].

4.3.5 Comparison of IR and Raman Vibrational Modes

Both IR and Raman scattering studies are required to obtain more details of molecular bonds, as can be seen in the spectra of benzene in **Figure 4.4** [26].

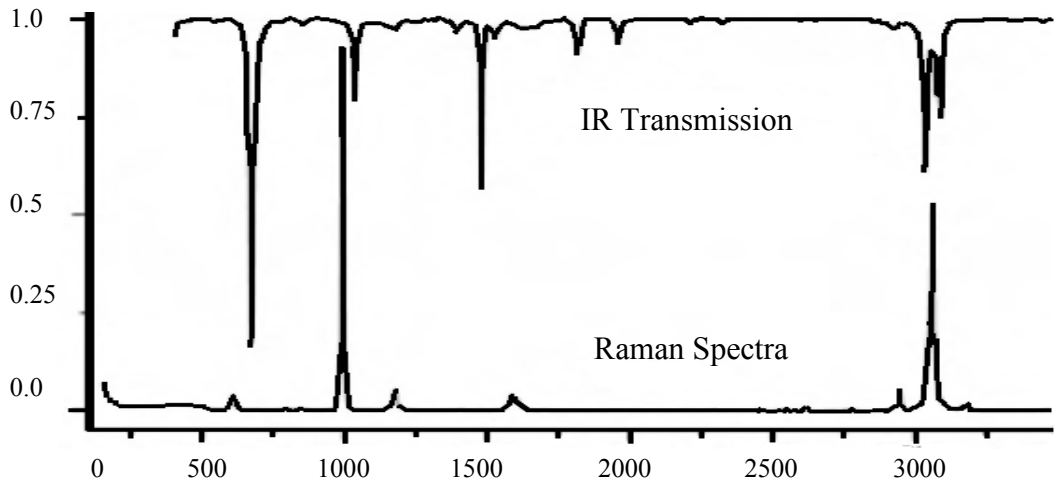

Figure 4.4 Raman and IR spectra of benzene. Extracted and adapted from [26]

The QMO model provides some information on phonon states and allowed transitions, but does not distinguish between Raman and IR activity. Raman scattering is due to molecular 'polarisability' - the ease with which the electron cloud deform in the electric field of the radiation [27].

Symmetric vibrations in centrosymmetric poly-atomic molecular bonds have zero dipole moment and are Raman active; their non-symmetric vibrations are IR active.

Non-linear and non-centrosymmetric poly-atomic molecular bonds are both Raman and IR active, with overlapping modes. Typically, covalent bonds are strongly Raman active, and ionic bonds are strongly IR active. Polar molecules have strong IR absorption peaks and weak Raman peaks. Stretching vibrations have stronger Raman peaks than bending vibrations. Heteronuclear diatomic molecules are non-symmetric and hence polar. The vibrations exhibit both Raman and IR activity. The molecular polarisability and dipole moment with the bending and symmetric stretching modes of CO_2 are illustrated in **Figure 4.5** [16, 27].

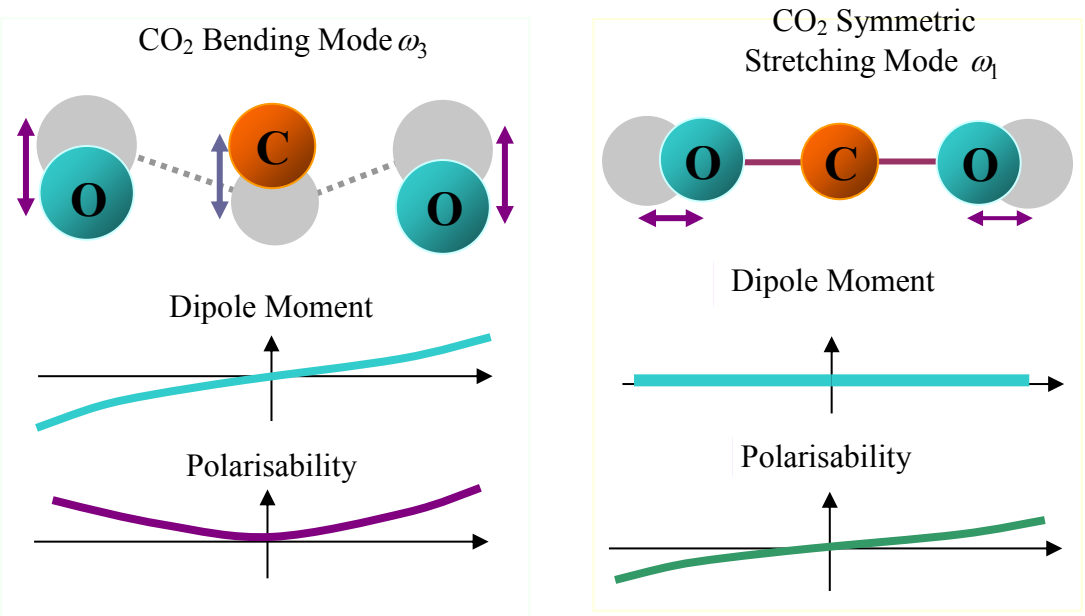

Figure 4.5 (**Left**) The CO_2 bending mode vibration has no Raman spectra, as the net polarisability slope is '0' at equilibrium and the slope of the dipole moment is non-zero. (**Right**) The CO_2 symmetric stretching mode vibration has no IR spectrum, and has a non-zero polarisability slope at equilibrium position [27].

4.3.6 Polarisability Tensors and Raman Scattering Theory

During light scattering, the induced oscillating molecular multipole moments can be treated as superposition of permanent and induced dipole, quadrupole and higher order moments of progressively decreasing magnitude that can be expanded as a Taylor series,

$$\boldsymbol{\mu} = \boldsymbol{\mu}_0 + \boldsymbol{\mu}_1 + \frac{\boldsymbol{\mu}_2}{2!} + \frac{\boldsymbol{\mu}_3}{3!} + \ldots$$

The oscillating electric field vector **E** of the incident radiation is

$\mathrm{E} = E_0 \mathrm{e}^{i(\mathbf{k}.\mathbf{r}-\omega_0 t)}$, where E_0 is the amplitude of the incident light along the propagation direction, **r,** with propagation constant **k**

$\boldsymbol{\mu_0}$ is the permanent dipole moment. (In spherically symmetric molecules, $\boldsymbol{\mu_0} = 0$)

$\boldsymbol{\mu}_1 = \alpha \mathrm{E}$ is the induced linear dipole moment vector and α is the polarisability factor

$\boldsymbol{\mu}_2 = \beta \mathrm{E.E}$ is the induced non-linear quadrupole moment vector and β is known as hyperpolarisability factor

……..
……..

$$\boldsymbol{\mu} = \boldsymbol{\mu_0} + \alpha \mathrm{E} + \frac{1}{2}\beta \mathrm{E.E} + \frac{1}{6}\gamma \mathrm{E.E.E} + \frac{1}{12}\eta \mathrm{E.E.E.E} \ldots [27]$$

The hyperpolarisability contributions are about 35 orders of magnitude smaller in single photon laser scattering techniques, and hence, practically non-existent in linear Raman scattering. Surface enhanced and resonant hyper-Raman spectroscopy are useful to study these overtones in small molecules. Hyperpolarisability spectroscopy is a better alternative to study large molecular spectra, since linear Raman spectra of large molecules are diffuse [27, 28].

Ignoring the negligible higher order contributions from hyperpolarisability factors and ignoring permanent dipoles, the multipole moment can be reduced to

$$\boldsymbol{\mu} = \boldsymbol{\mu}_1 = \alpha \mathrm{E} \qquad (1)$$

The polarisability factor, α is a simple vector for diatomic and tri-atomic linear modes of vibration. In polyatomic molecules, the polarisability factor is represented by a complex ellipsoid, whose surface changes with the induced oscillating dipole moment. The linear polarisability factor α is represented mathematically by a tensor of rank two; α has different magnitudes along different surface normals and measures the charge cloud distortion along that direction, as shown in **Figure 4.6**

(right) [16]. The dipole moment along the three axis are related to the axial component of the E – field and can be expressed as three linear equations,

$$\mu_{1x} = \alpha_{xx}E_x + \alpha_{xy}E_x + \alpha_{xz}E_x$$
$$\mu_{1y} = \alpha_{yx}E_x + \alpha_{yy}E_x + \alpha_{yz}E_x$$
$$\mu_{1z} = \alpha_{zx}E_x + \alpha_{zy}E_x + \alpha_{zz}E_x$$

Due to symmetry in most isotropic materials, only six distinguishable polarisability components exist, as

$$\alpha_{xy} = \alpha_{yx}, \quad \alpha_{xz} = \alpha_{zx} \quad \text{and} \quad \alpha_{yz} = \alpha_{zy}$$

For a spherically symmetric molecule, the tensor reduces to a vector, with the polarization vector oriented along the direction of the applied field (**Figure 4.6 (**left**)**). In a highly polar molecule, the electron cloud is an elongated ellipsoid, with the long axis along the bond axis. The α_{zz} component will be dominant, when the field E = E_z, is directed along the z-axis, as shown in **Figure 4.6 (**centre**)**.

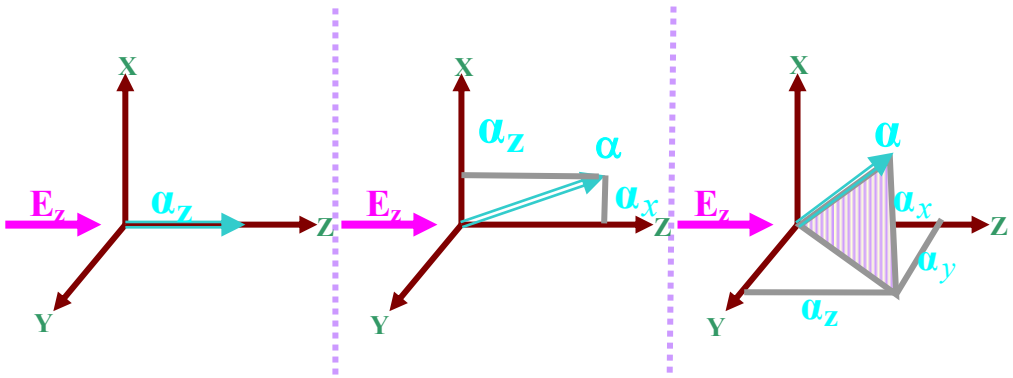

Figure 4.6 The three possible orientations of polarisability with respect to the incident electric field vector along z-axis influenced by the molecular charge distribution, the individual bonds and charge symmetry. Adapted from [27]

The linear polarisability factor is different for different phonon modes. The fundamental modes of vibration have the strongest scattering cross-sections. Higher order phonon modes and multiphonon coupling decrease with increasing order. Using Taylor expansion for 'α', for diatomic vibration along z-axis [15, 27],

$$\alpha = \alpha_0 + \left(\frac{d\alpha}{dz}\right)_0 z + \frac{1}{2}\left(\frac{d^2\alpha}{dz^2}\right)_0 z^2 + \ldots \quad (2)$$

α_0 is the polarisability ellipsoid tensor at equilibrium.

$\left(\frac{d\alpha}{dz}\right)_0$ is the first order change in polarisability tensor

Substituting equation (2) in (1), and assuming harmonic oscillations along the z-axis with frequency ω and amplitude Z_0 for the ground state vibrational mode,

$$\boldsymbol{\mu}_1 = \left\{\alpha_0 + \left(\frac{d\alpha}{dz}\right)_0 Z_0 e^{i\omega t} + \frac{1}{2}\left(\frac{d^2\alpha}{dz^2}\right)_0 Z_0 e^{i2\omega t} + \ldots\right\} \mathrm{e}^{i(\mathbf{k}.\mathbf{z}-\omega_0 t)} \quad (3)$$

Expanding (3), using only the first two significant terms, factoring out common terms and rearranging

$$\boldsymbol{\mu_1} = \alpha_0 E_0 \mathrm{e}^{i(\mathbf{k}.\mathbf{z}-\omega_0 t)} + \left(\frac{d\alpha}{dz}\right)_0 Z_0 E_0 \mathrm{e}^{i(\mathbf{k}.\mathbf{z}+(\omega-\omega_0)t)} \quad (4)$$

When the periodic oscillations of the incident E field are represented in a complex plane, the real terms remain unaltered by the change in phase,

$$\Re e\, \mathrm{e}^{-i\omega_0 t} = \Re e\, \mathrm{e}^{i\omega_0 t}$$

Hence, $$\boldsymbol{\mu}_1 = \alpha_0 E_0 \mathrm{e}^{i(\mathbf{k}.\mathbf{z}+\omega_0 t)} + \left(\frac{d\alpha}{dz}\right)_0 Z_0 E_0 \mathrm{e}^{i(\mathbf{k}.\mathbf{z}+(\omega+\omega_0)t)} \quad (5)$$

Adding (4) and (5), rearranging and using trigonometric identities,

$$\boldsymbol{\mu}_1 = \frac{1}{2}\alpha_0 E_0 \mathrm{e}^{i(\mathbf{k}.\mathbf{z}-\omega_0 t)} + \frac{1}{2}\left(\frac{d\alpha}{dz}\right)_0 Z_0 E_0 \left\{ \mathrm{e}^{i(\mathbf{k}.\mathbf{z}-(\omega_0-\omega)t)} + \mathrm{e}^{i(\mathbf{k}.\mathbf{z}-(\omega_0+\omega)t)} \right\} \quad (6)$$

Equation (6) consists of two terms that represent the scattered signals. The first term, with the same frequency as the incident light, accounts for Rayleigh or elastic scattering; it is the dominant scattering signal. About one in 10^7 scattered photon frequencies are slightly red shifted from the Rayleigh frequency (the second term in equation (6)); the frequency, $\omega_S = \omega_0 - \omega$, corresponds to a ground state molecule absorbing energy from the incident radiation to transition to the first excited state; the re-emitted light had slightly lower frequency (Stokes). The blue shifted

frequency, $\omega_{AS} = \omega_0 + \omega$, corresponds to a molecule in the excited state absorbing energy from the incident light to return to the ground state, re-emitting signals at a higher frequency (anti-Stokes). Stokes and anti-Stokes Raman scattering is illustrated in **Figure 4.7.**

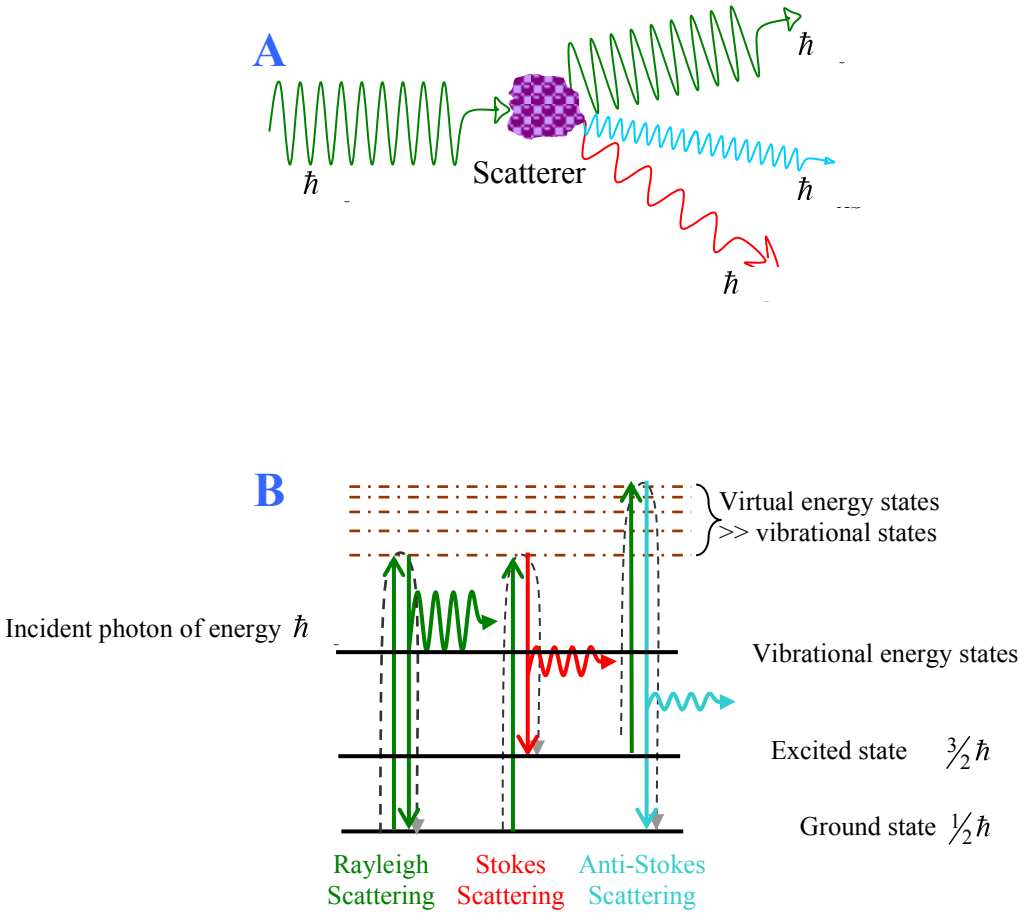

Figure 4.7 **A:** Scattering from an incident green laser source gives rise to blue and red shifted Raman signals and the predominant Rayleigh scattering. Stoke's, ω_S (red), anti-Stoke's, ω_{AS} (blue) and Rayleigh lines ω_0 (green) are shown, with their amplitudes denoting intensities. **B**: QMHO energy level diagram of scattering modes

Stokes and anti-Stokes Raman frequencies are symmetric with respect to the central intense Rayleigh frequency. Depending on the scattering molecules, induced dipoles can vibrate in the same plane as the **E** field vector or in a different plane, influencing the plane of polarisation of the scattered light. The number of spectral lines is

usually less than the total number of phonon modes, as many phonons are degenerate and other phonons are weak scattererers [27]. The quantum mechanical conditions to be satisfied for photon-phonon interaction in equation (6) are:

(a) $\alpha_0 \neq 0$ for Rayleigh scattering

(b) $\left(\frac{d\alpha}{dz}\right) \neq 0$ at equilibrium for Raman scattering

The probability of scattering amplitude and the solutions require perturbation or variational method; which is a specialised field, and beyond the scope of this research [27].

The intensity of a Raman frequency is material property, material phase, molecular bonds, pressure, temperature and scattering angle dependent. Most room temperature measurements exploit Stokes Raman signals, as the temperature dependent anti-Stokes signal intensities are very weak. The relative intensities of Stokes and anti-Stokes lines obey Bose-Einstein statistical distribution for a large range of temperatures, and are given by [17, 29]

$$\frac{I_{A-S}(\omega)}{I_S(\omega)} = \left(\frac{N(\omega)}{N(\omega)+1}\right) = e^{-\frac{\hbar}{2kT}}$$

$$\text{where } N(\omega) = \left(\frac{1}{e^{\frac{\hbar}{2kT}} - 1}\right)$$

4.3.7 Lattice Phonons and Raman Scattering in Crystalline Solids

Crystalline solids have highly organised atomic and molecular arrangements with long range order that can be modelled using periodic structures. A Raman spectrum is sensitive to crystalline structures of the same molecule, due to changes in bond strength, bond length and polarity. Mammalian DNA has some crystalline symmetry, especially in the structure of the sugar-phosphate backbone [30-32].

Like molecular symmetry planes and symmetry groups, crystals also display a variety of symmetries, including, translation, reflection, rotation and inversion. Since there are hundreds of crystal symmetry groups, the crystal structures are often identified by well-known crystals like diamond or zinc-blende or sodium chloride.

The crystal can be composed of a single species, as in pure metals – silver (Ag), iron (Fe), copper, gold, or minerals like silicon (Si), germanium (Ge) and diamond; or it can be a composite crystalline material such as quartz (SiO_4), sodium chloride (NaCl), ice (H_2O) and alumina (Al_2O_3) [31].

A perfect crystalline material is composed of repeating unit cells with identical atomic or molecular arrangement in each cell. The dimensions of the unit cells are called lattice parameters or lattice vectors, and Bravais lattices are a group of simple models that depict crystalline structures. Wurzite (hexagonal close packed (HCP)) and Zinc Blende - cubic close packed (CCP) - are Bravais lattices commonly encountered in semiconductor materials used in electronics and display. The group of atoms or molecules in a unit cell are known as basis; the position of each basis is called lattice point. The unit cells are abstract boundaries and the interatomic or inter-molecular bonds are not isolated within the unit cells, in real life [31].

Lattice parameters are also represented using reciprocal lattice vectors (RLV). The RLV equivalent of the unit cell is known as a Brillouin zone. The low frequency vibrations of crystalline materials are due to oscillations of lattices and symmetry planes, and are known as lattice phonons. These phonons are characteristic of the crystal lattice, and the phonon amplitude is much less than the lattice spacing. However, the wavelength of the lattice phonons can be several times the size of the lattice parameters [31].

The QMO model can be extended to derive scattering energies of lattice phonons. The modes of vibration of the atoms in a crystalline material are not independent; they behave like a coupled HO. An ideal linear crystalline chain along the z-axis, consisting of a single atom of mass M in each basis, with lattice parameter **a,** is shown in **Figure 4.8** (top array). The vibrations of each unit cell matching (or nearly matching) those of the nearest neighbouring cells, in both amplitude and phase, as shown in **Figure 4.8** (middle array)**,** are known as acoustic phonons. Acoustic phonons have long wavelengths and low restoring force. The vibrations parallel to the direction of the wave vector **k** are known as longitudinal acoustic (LA) phonons; the vibrations perpendicular to **k** are called transverse acoustic (TA) phonons. The

vibration in opposite phase, as illustrated in **Figure 4.8 (**bottom array), are called optical phonons; their frequencies are higher than those of acoustic phonons. A lattice with a single basis has only acoustic phonons. There are two transverse and a longitudinal acoustic phonon associated with each **k**. When p basis are present in a lattice, it has 3p branches of phonons with 3 acoustic phonons (1 LA + 2TA) and 3p-3 optical phonons [31]. Real two-dimensional and three-dimensional lattices with only nearest neighbour interactions involve approximations and complex calculations beyond the scope of this literature review.

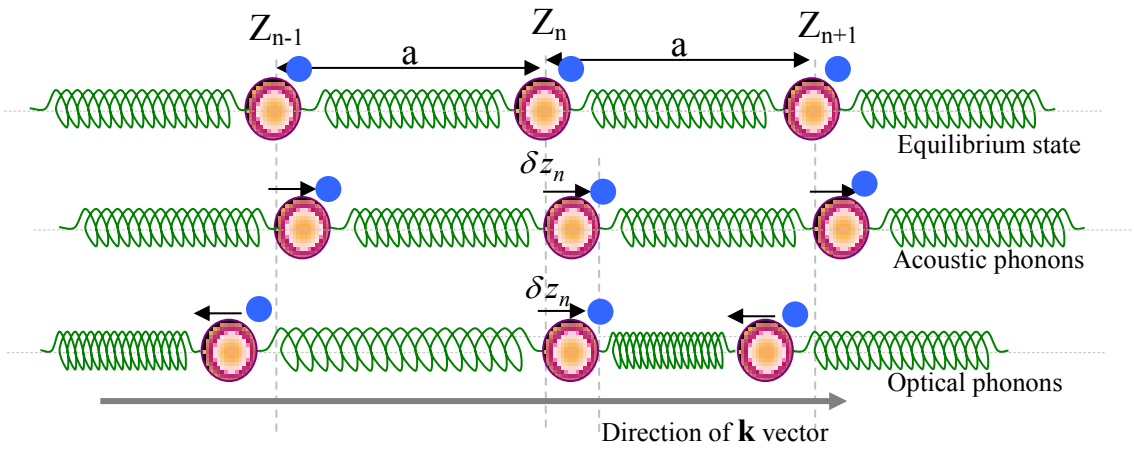

Figure 4.8 A 1-d crystal displaying acoustic and optical vibrational modes

4.4 Applications of Raman Spectroscopy

The materials studied using Raman spectroscopy range from highly ordered solid state or crystalline materials like silicon and germanium used in semiconductor technology, to highly disordered or amorphous materials like amorphous silicon, carbon and glass. Material purity and bond integrity can be tested with Raman spectroscopy and hence it has been extensively used in material process control and geological mineral tests [33, 34].

Raman spectrum is used to analyse phase and refractive index changes in materials, as it is sensitive to material pressure, temperature, chemical environment and density. Raman spectroscopy has been applied in geology, archaeology, semiconductor technology, polymer chemistry, pharmacy research, and organic semiconductor

research. With improvement in detector technology, Raman spectroscopy has been extensively used to analyse complex molecular structures in biological specimens [35].

4.4.1 Raman Scattering in some Crystalline and Glass Substrate Materials

Silicon (Si), germanium (Ge), glass and quartz are used as substrates in many applications, including Raman spectroscopy. Both Si and Ge are natural semiconductors whose crystalline properties have been extensively studied for making electronic and opto-electronic devices. Si unit cell is composed of 8 Si atoms and has FCC tetrahedral structure [36]. The Si 520 cm^{-1} and Ge 300 cm^{-1} Raman peaks correspond to the triply degenerate TO phonon modes, as depicted in **Figure 4.9** [37]. Raman spectra of Si is sensitive to temperature changes [17], and structural changes - cubic, diamond, polycrystalline and amorphous [38].

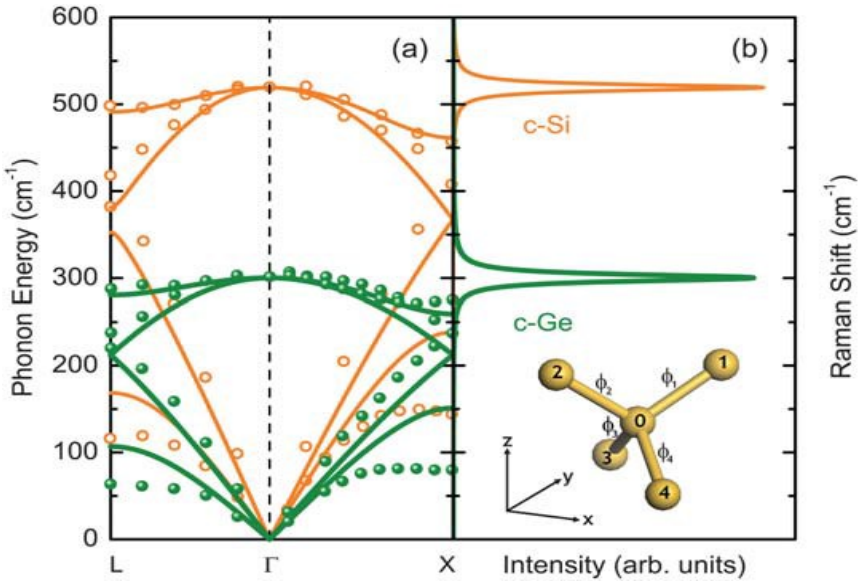

Figure 4.9 **(Left)** Theoretical (solid lines) and experimental neutron scattering data (circles) on c-Si (orange) and c-Ge (green) acoustic and optical phonons. **(Right)** Raman spectra of c-Si and c-Ge plotted with phonon energy on the vertical axis. Extracted from [37]

SiO_2 structures include amorphous silica, fused silica and crystalline quartz. Fused silica and quartz have some similarities to H_2O. Ice and quartz are the crystalline states of the two chemicals (sand and water) that are abundant in nature. Both SiO_2

and H_2O have tri-atomic nonlinear structure that form tetrahedral bond with their nearest neighbours. The SiO_2 angle is 109 ^{o}, while that of H_2O is 104.5 ^{o}. The tetrahedral structure in H_2O is formed by weak hydrogen bonds, and that in fused silica and quartz is formed by strong covalent bonds. Quartz has three distinct Raman peaks in the low energy region – an intense peak at 464 cm^{-1} due to bending mode of the tetrahedron, and two less intense peaks at 205 and 128 cm^{-1} [39-41]. The Raman spectra of quartz and glass coverslip in the 600– 1800 cm^{-1} is shown in Figure 4.10 [42].

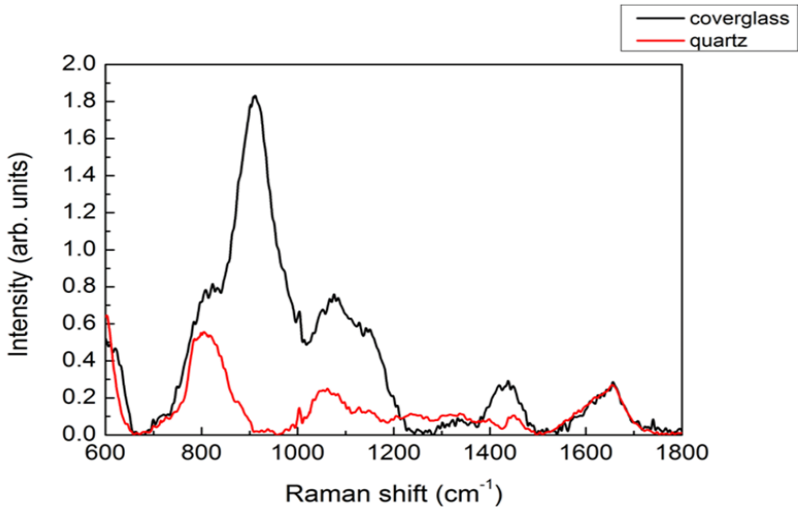

Figure 4.10 The Raman spectra of quartz and glass coverslips [42] suppl material.

Polarised scattering sources and depolarisation ratios (DR) are used to study crystalline geometry of materials. DR is the ratio of scattered perpendicular polarisation to parallel polarisation, measured with respect to the incident light polarisation. Amorphous materials, liquids and gases in Brownian motion have randomly oriented polarisation, with DR $\leq$ 0.75. Materials with highly symmetric vibrations tend to retain the polarisation orientation of the incident light, and have very small DRs [43].

4.4.2 Raman Scattering in H_2O

At normal pressure, the common structure of solid H_2O is hexagonal ice. All three vibrational modes of ice are strongly IR active and weakly Raman active. A Raman peak of the bending mode of H_2O is located at 1650 cm^{-1}. The O-H stretching

(symmetric and antisymmetric) in ice and water are located at energies over 3000 cm^{-1}. Ice has a sharp peak at 3140 cm^{-1}, and a broad higher energy band due to strong inter-molecular interactions of the O-H stretching vibrations with libration and overtones of bending modes [44-46]. Sharp low frequency peaks at 225 cm^{-1} and broader peak at 306 cm^{-1} attributed to lattice modes, have been observed in ice [47]. Low frequency acoustic phonons at 65-70 cm^{-1} and 164 – 181 cm^{-1} have been observed in cubic and hexagonal ice; the optical phonons are seen at energies over 330 cm^{-1} [48].

H_2O has many temperature and pressure dependent solid state structures, including hexagonal, cubic, polycrystalline and amorphous state. H_2O molecules stick together via weak hydrogen bonds to form instantaneous strong hydrogen bonds in ice and tetrahedral bond in water [48]. Natural ice found on earth has hexagonal structure. Compressed phase transitions of ice crystal structures have applications in geophysics, planetary evolution, astro-biology and search for extra-terrestrial planetary water. Raman spectroscopy has been used to study low vibrational frequencies of ice, short O-O bond lengths, shortening of hydrogen bonds and lattice phonons [49]. Long term study of the microphysical structure of ice formation in clouds using Raman remote sensing, may shed light on the role of clouds in radiation trapping and climate change [50].

All three fundamental modes of vibrations of ice are peak shifted in water and steam. Vapour phase O-H vibrations exhibit bending mode at 1595 cm^{-1}, symmetric stretching at 3657 cm^{-1} and asymmetric stretching at 3756 cm^{-1}. As the temperature decreased, the inter-molecular spacing decreased and hydrogen bond strength and dipole moment increased. The O-H stretching peaks are red shifted and the bending mode energy is blue shifted when H_2O transitions from vapour to liquid to ice. H_2O has broad Raman bands, which is attributed to vibrational coupling with complex overtones and librations. The stretching mode of water starts at about 3200 cm^{-1}; it has broader band width (300 cm^{-1} to 400 cm^{-1} wide) than ice. Low frequency acoustic phonons have been observed in water at 60 cm^{-1} (TA) and 175 cm^{-1} (LA); these indicate a tetrahedral structure [24, 44, 48, 51].

4.4.3 Applications of Raman Scattering in Biological Materials

Raman spectroscopy is used to study structural biology. Raman spectra of macromolecules are highly complex and difficult to interpret, but the spectra of small complexes like ligand-receptor and enzyme-substrate binding sites are important biological structures that are easier to analyse [52]. Raman spectra of L-histidine in aqueous solution [53], and spermine and spermidine (polyamines) interaction with oligonucleotides [54, 55]; provide insight into molecular level DNA packaging.

Raman spectroscopy has gained wide acceptance in medical microbiology because of the minimal sample preparation and handling requirements. Rapid identification of medically significant micro-organisms, and the use of statistical techniques for standardisation have simplified the analytical approach [56]. Raman spectroscopy has also been identified as a suitable tool for in-*situ* diagnoses of diseases in real-time [57], and NIR has been identified as a suitable wavelength to minimise damage and fluorescence contribution in the study of live cells and tissues, and in bacteriology and virology [58, 59]. Raman spectroscopy has been used to monitor in real-time, the in *vivo* metabolic and developmental processes [60], multipotent stem cell research and tissue engineering [61, 62], study of protein folding [63] and cancer diagnosis [64].

Scanning confocal Raman microspectroscopy with Ti-Sapphire laser sources at 720nm and 850nm has been used to obtain layer-by-layer, images and molecular spectra of 1- 4mm thick live skin. Blood flow through dermal capillary and secretion of sweat duct in sebaceous glands (glands at the base of hair follicle) have been monitored in *vivo* [65]. Green fluorescent protein probes attached to the nucleus of yeast cells have been used to monitor their mitotic process in real time, using confocal Raman spectroscopy [66].

Raman spectra of differentiated and undifferentiated human embryonic stem cells have been monitored using 785 nm, 100 mW laser source. A 20x objective, 6x50 μm spot size and 200 sec exposure time were used for each spectrum. The expression of a stem cell self-renewal gene was unaffected following the exposure to the high laser power at the focus, as the stem cell proliferation and pluripotency was not impaired [67]. Human mesenchymal stem cells (derived from bone marrow) can

differentiate into bone cartilage and adipose tissue (fat storing cells). Raman spectroscopy was used to monitor the differentiation of these cells to form bone tissue in a study that lasted from 7 to 28 days. The spectral bands of crystalline mineral species associated with bone were identified through their specific spectral fingerprint [68].

Healthy tooth enamel has high polarisation anisotropy compared to teeth with dental caries. Polarised Raman spectroscopy and depolarisation ratio was used to detect dental caries. The symmetric vibration of PO_4^{3-} at 959 cm^{-1} corresponding to the enamel crystallites was most sensitive to the degree of damage caused by caries [69].

The photoreceptors in the retinal segments from pigs' eyes were mapped using 514 nm (10mW), 633 nm (20 mW) and 785 nm (100 mW) lasers; all three wavelengths were found suitable for studying the DNA and protein rich regions [70]. Micro-Raman mapping was used to investigate the distribution of DNA, proteins and cytoplasm in apoptotic and non-apoptotic HeLa cells [71]. Embryo development was investigated using chemically fixed mice cells and Raman mapping [72].

Raman spectra using 1064 nm pulsed laser of 120 mW power provided fluorescence-free Raman signals with high SNR of cancerous and healthy lung tissue, with 91% sensitivity [73]. Chemically induced cell apoptosis of human lung carcinoma was monitored with a 785nm, 120mW laser Raman spectrometer. Time-dependent changes in protein and lipid content and DNA disintegration were observed [74].

The nucleus and cytoplasm of neutrophilic, eosinophilic and basophilic granulocytes were compared using Raman spectroscopy. The nuclear spectra of the three granulocytes were identical; the cytoplasmic spectra revealed compositional differences in the enzyme peroxidase [75]. Live bacteria grown on CaF_2 substrates were studied using micro-Raman spectroscopy with a 632.8 nm, 8 mW tightly focused laser and 3 minutes exposure time. Characteristic granulose and protein peaks of differentiated bacteria with different growth phases were identified [76, 77].

Developmental phases and growth cycles of cultured human tumour cell line were monitored progressively from one cell division to the next, using Raman

spectroscopy. The cycles, regulated by cell cycle regulatory drugs, were accompanied by changes in the Raman spectra of DNA/RNA and proteins from each cell [78].

4.4.4 Raman Spectroscopy of DNA and Nuclear Proteins

Proteins and DNAs are composed of a variety of complex biomolecules with complex vibrational modes; the normal modes of vibration from these biomolecules are superposed in a DNA or protein to produce characteristic fingerprints. The Raman spectra/fingerprint of a biomolecule, calf thymus DNA, is shown in **Figure 4.11**. The spectrum from the aqueous suspension of dense freeze-dried commercial calf thymus B-DNA at room temperature (11 ^{o}C) consists of averaged data from several 100 accumulations of 30 second duration each; the spectrum was acquired with a 514.5 nm argon laser of 200 mW power [32].

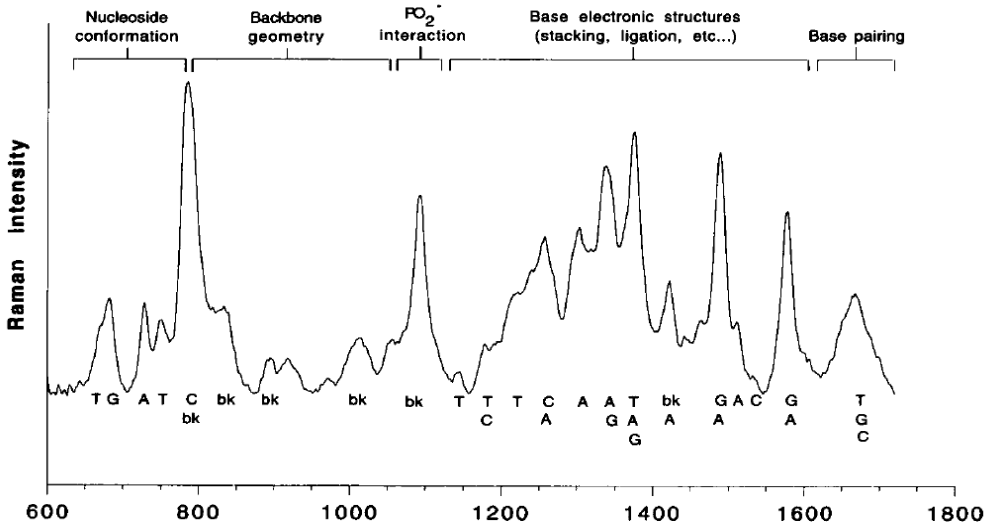

Figure 4.11 Raman spectrum of freeze-dried calf thymus B-DNA [32]

Solid and solution forms of dimethyl and diethyl phosphate compounds, representing simple models of DNA, were used to analyse the Raman bands of phosphodiester groups and their depolarisation ratios in the crystalline solids [79, 80]. Temperature dependence of vibrational modes of bases and sugar-phosphate molecules have also been extensively characterised [81, 82]. The vibrational modes of sugar-phosphate

backbone and their relationship to DNA conformation were analysed using A, B & Z DNA fibres. The phosphate peaks in the region 750 cm^{-1} - 850 cm^{-1} revealed strong conformation dependence [83].

Protein bands were identified in eukaryotic chromosomes at 622, 647, 826, 949, 1003, 1157, 1177, and 1269 cm^{-1}, corresponding to phenylalanine, tyrosine and tryptophan amino acids. A band in the 1220 cm^{-1} - 1300 cm^{-1} region corresponds to amide III modes and that in the 1656 cm^{-1} - 1669 cm^{-1} region corresponds to amide I modes. The DNA secondary structure in the 600 cm^{-1} – 700 cm^{-1} region corresponds to guanine ring breathing mode; the energy was also found to be dependent on the bond angle between the base and sugar molecule. The peaks at 625, 665 and 682 cm^{-1}s correspond to C3′ - vibrations of Z, A and B DNA respectively [84-86].

Raman spectroscopy and differential scanning calorimetry were used to study the molecular mechanism of thermal denaturation of B-DNA encountered during DNA replication and gene expression. Synthetic DNA consisting of poly dA-dT bases, calf thymus DNA fragments (160 kb size) were used in DNA melting experiments in temperatures of 10 - 93 ^{o}C range. The results show temperature dependence of DNA helical confirmation; the hydrogen bond dissociated between 66 - 80 ^{o}C, to form single strands. Stacked base pairs separated, disturbing the B-DNA helical structure and the stability of sugar-phosphate backbone. The size and nature of the base stacks and the DNA environment (salt, water and pH) also affected the melting temperature. Raman peaks from unstacked bases and separated base pairs had higher energy than the peaks from stacked base pairs in the helical double strands. Unlike the DNA backbone peaks at 786 cm^{-1}, 1014 cm^{-1} and 1092 cm^{-1}, Raman peaks at 834 cm^{-1} from phosphodiester, 1240 cm^{-1} from thymine ring and the 1668 cm^{-1} band from dT, dG and dC were sensitive to temperatures. No noticeable spectral changes were observed at post melting (75 - 85 ^{o}C) temperatures [87, 88].

Some Raman peaks of DNA in solution were found to be affected by salt and heavy water. Synthetic helical double stranded DNA had Z-confirmation in high salt solutions; they had B-confirmation in low salt solutions. C=O and phosphodiester stretching modes of the backbone in the 750 cm^{-1} -850 cm^{-1} region and guanine mode in the 600 - 700 cm^{-1} range had characteristic peaks for the three conformations [89].

The intensity of the phosphodioxy group, PO_2^- stretching mode peak at 1100 cm^{-1} in solid DNA was unaffected by thermal or radiation induced damage. The peak energy shifted to 1094 cm^{-1} in 95% humidity, due to change in helical conformation. The appearance of peaks and shoulders in the 873 cm^{-1} -875 cm^{-1} range, 976 cm^{-1} - 985 cm^{-1} range, and at 1077 cm^{-1} and 1087 cm^{-1} indicate PO_3^- stretching vibration from single stranded DNA (ssDNA) or denatured double strand DNA (dsDNA) [90].

The stable phosphodioxy stretching mode at 1092 cm^{-1} appeared unaffected by the base composition and sequence in B-DNA; however, the mode shifted to 1100 cm^{-1} in A-DNA. B-DNA base sequences affected the deoxyribose linked phosphodiester ring breathing peak at 835 cm^{-1}; the peak shifted to 830 cm^{-1} when only C-G were in the base sequences, and to 840 cm^{-1} when only A-T were in the base sequences. The phosphodiester peak at 785 cm^{-1} is a composite peak with contributions from dT (790 cm^{-1}) and dC (780 cm^{-1}). Presence of a peak at 807 cm^{-1} has been identified as a marker for A-DNA [91].

Raman peaks from dG in calf thymus DNA are located in the 620 cm^{-1} - 685 cm^{-1} energy range and the sugar-phosphate peaks are in the 800 cm^{-1} - 1100 cm^{-1} energy range. The peaks in the 1200 cm^{-1}- 1600 cm^{-1} region contain purine and pyrimidine ring vibrations. B-DNA conformation has a characteristic peak at 834 cm^{-1} and the transient Z-DNA conformation [92] has a characteristic peak at 850 cm^{-1}. The thermal stability of B-DNA decreases in solutions with high concentrations of divalent cations such as magnesium. Raman spectra of nucleosides, with and without metal ion bindings, show different thermal denaturation patterns, in dT and dC peaks at 1240 cm^{-1} and 1257 cm^{-1}. The stable DNA peak at 1092 cm^{-1} band is sensitive to heavy metal ions, and especially to Cu binding; the peak red shifted due to reduction in PO_2^- stretching energy. The broad band at 1668 cm^{-1} is sensitive to changes in dT, dC and dG. The stability of condensed DNA in the presence of different concentrations of divalent cations and metal ions was modelled using cylindrical shape for the DNA helix. High ionic concentrations of transition metals or heavy elements destabilised the DNA bases as they preferentially bound to bases to create cross-links that damaged the DNA [32, 82, 93]. The DNA peaks discussed in this subsection are summarised in **Table 4.1.**

Energy (cm^{-1})	Molecular component/bond	Comments
594	dC, dT	Deformation C=O [90]
681	dG C2′-endo/anti dG conformation	Intensity dropped, red shifted to 660 on melting [87]. Displaced to 665 when converted to C3′ -endo/anti dG conformation [32, 90]. Intensity low with low pH [94]
729	dA ring breathing	Blue shifts to 734, intensity gain DNA melting [87, 90]
750	dT C2′-endo/anti ring breathing	Peak broadened, intensity dropped slightly and red shifted to 738 on melting [87, 90]
785	C3′-OPO-C5′ + dC and dT(wk)	Phosphodiester sym-stretch and cytosine ring breathing; dC was temp invariant [87, 90]
835	OPO anti-symmetric stretching	Specific to B-DNA. Localised vibration of the phosphodiester group was sensitive to temperature, intensity dropped slightly [87]
850	bk Z-DNA	[86] backbone (bk)
895	bk	Localised vibration of the phosphodiester group was sensitive to temperature, intensity dropped slightly [87]
923	bk	Local vibration of phosphodiester group, sensitive to temp, slight intensity dropped [87]. Many bk peaks (868 -1024) affected by irradiation [86, 90]
1014	bk dioxyribose dT, dG, dC ring	Weak sugar backbone band – temperature and divalent metal ion binding invariant [87]
1054	*v*CO of bk	Sugar C-O stretching mode [86, 87]
1092, 1094	PO_2^- Phosphodioxy sym stretch.	pH, temperature invariant [95], [87]. Solid DNA peak at 1100 cm^{-1} [90]
1145	Medium peak, various assignments	1141 dT [90] 1148 deoxyribose-Phosphate [86]
1178-1187	dT, dC	1172 – 1187 due to dG, dT, dC [86, 87, 90]
1197	dT	1199 unassigned [86] dT [96]
1218	dT	1218 [87]; dC and dT [90]
1240	dT with minor dC contribution	Thymine ring intensity gain on thermal denaturation [87]

Energy (cm^{-1})	Molecular component/bond	Comments
1244-1258	dC, dA(?) dT	Large dC band at 1258 [87] minor intensity gain on thermal denaturation and large intensity gain on mercuric chloride binding [32]. 1244 due to dC & dT [90]
1292-1295	dC	dC ring mode [87] C4′ exo-anti [86]
1302-1305	dA	dA [87], dA, dC ring mode [90], disordered DNA [86]
1320	dG	dG [87]
1335	dA, dG	dA, dG [87], C2-N3 stretching in dA & dG [90]
1376	dT, dA, dG,	Sensitive to hydrophobic/philic environment, peak shifts down [87], C5-H3 deformation of dT, dA & dC [90]
1421	dA, bk 2'CH2 def	[86, 87]
1485-1490	dG strong, dA	dG marker at 1489 dominant pk with dA a weak pk at 1482. Peak sensitive to hydrogen bond, metal ion and protein binding at N7 site. Shift to lower energy with increased intensity on bond melting [32, 87]
1512-1514	dA medium pk	dA marker [87], deform N_2H_6 + ring dA at 1508 [90]
1532	dC small pk	dC N3-C4 stretching at 1530 [90] and at 1532 dC [87]
1578	dG, dA strong pk	dA dG equally dominant. Peak sensitive to hydrogen bond and protein binding at N7 site. Shift to lower energy with increased intensity on bond melting [87, 90]
1602	dC	Very weak [87]
1645	dT	C2=O dT stretch [90]
1668	Band due to C=O stretch and N-H stretch from dT, dG & dC	Temp sensitive Carbonyl group from T,G & C. Increase in intensity and red shift to 1658 due to rupture of hydrogen bond [87]. C4=O dT stretch at 1670 [90]
1688	vC=O, NH_2 def, dT, dG, dC	A broad and strong band [87]

Table 4.1 Wavenumbers and some associated Raman vibrational peaks of calf thymus DNA components

4.4.5 Raman Spectroscopy and Sperm Cells

There are very few reports on IR and Raman spectroscopic study of sperm molecular structures. Chromosomes, located in the cell nucleus and are tightly bound DNA - protein complexes. Histones and or protamines bind segments of DNA to form a dense organised structure. The DNA-histone structure showed coiled DNA molecules and histone bridges with 3.5 – 3.7 nm spacing when investigated over 50 years ago using X-ray diffractometry [97]. DNA - protamine complexes was analysed using X-ray diffractometry; protamine-bound nucleotides adopted B-DNA conformation. Each unit cell, represented by HCP structure, contained a single protamine bound DNA molecule separated by a protamine bridge from the next unit cell [98]. Histones in chromatin from intact salmon sperm heads revealed C-N stretching vibration at 1156 cm^{-1}. The weak peaks at 1178 cm^{-1} and 1269 cm^{-1} were from ring breathing modes of tyrosine. CH_2 vibrational peaks associated with fatty acids were observed at 1443 cm^{-1}, 1456 cm^{-1} and 1471 cm^{-1} [86].

Raman spectra of live salmon sperm chromosomes, aqueous solutions of synthetic B-type DNA oligomers and other natural purified DNAs were compared, to identify cellular and nuclear environmental effects on DNA conformation. Despite the highly compacted and condensed state of salmon sperm nuclei, Raman peaks from its nuclei showed high correlation with the Raman peaks from synthetic B-DNAs [86, 99].

The effect of heating (40 ^oC, 91 ^oC & 200 ^oC) and UV radiation (253.7 nm for 30 and 60 minutes) on herring sperm DNA fibres was investigated using Raman spectroscopy with 514 nm Ar laser. The spectra showed temperature dependent damage above melting point, with clumping of the strands at 91 ^oC and above. UV radiation (3.2 W/m^2) induced damage on the herring sperm DNA in aqueous solution was more severe than heat induced damage to the DNA fibre at melting temperature [30]. The effect of UV-A and UV-B irradiation on calf thymus DNA in aqueous solution for 3 hrs (0.5 W/m^2) caused blue-shift of PO_2^- peak. Damage to B-DNA and A-DNA were observed along with increased background noise [96].

Even though sperms of different species differ in appearance and genetic coding, their P1 protamines are basic proteins containing arginine residues; and in mammalian cells P1 are of similar size with about 50% arginine. Salmine-DNA

complex - salmon sperm protamine combined with calf thymus B-DNA and DNA-arginine complex suspended in different salt concentrations were analysed using 488 nm argon-ion laser Raman spectroscopy with laser power less than 100 mW at the sample plane. DNA-protamine complexes had a slightly modified B-DNA conformation, and the bases were not as tightly stacked as in pure DNA helix. The DNA-protamine bindings were observed along the major DNA grooves [100]. Hydrogen bonded stable secondary structures and non-hydrogen bonded alpha helix and beta turns were found in salmon and squid protamines investigated with IR spectroscopy. The protamine caused the DNA to condense into HCP structures [101].

Buffalo sperm cells were incubated with melatonin - an anti-oxidant, to minimise ROS induced DNA damage during sex selection, and tested with laser tweezers Raman spectrometry (LTRS). The spectral intensity of previously frozen sperms was weaker than that of fresh and sorted cells (**Figure 4.12)** and showed melatonin induced difference in thawed and stained cells. The melatonin induced difference was not observed in fresh and sorted cells. The mitochondrial activity increased significantly with melatonin exposure [102].

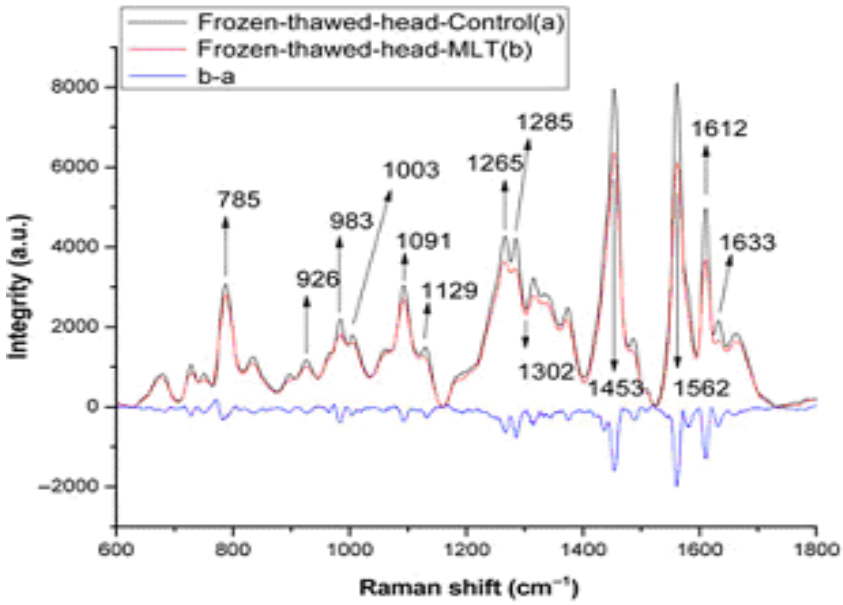

Figure 4.12 Raman spectrum of frozen and thawed buffalo sperm with and without melatonin [102]

FTIR was used to investigate temperature dependent molecular phase changes in stallion and rhesus monkey sperms [103]. Temperature dependent phase changes caused lipid separation and aggregation in cellular membranes during cryopreservation. Cryopreservation without cryoprotectants caused permanent membrane damage to stallion sperms during freezing and thawing [104].

Filtered sperms from infertile men were dried on silicon coverslips and analysed using FTIR spectroscopy and multivariate statistical analyses. The ratio of 1087 cm^{-1} (symmetric $PO2^-$ stretching) and 966 cm^{-1} (C-O and C-C stretching) spectral peaks from DNA backbone were constant in uncontaminated sperm samples. The ratio of the two peaks differed for different cell types in a human body. Amide I band at 1657 cm^{-1} was due to C=O stretching of peptide backbone; the band at 1547 cm^{-1} was due to N-H bending and C-N stretching in amide II. The ratio of a DNA backbone band to amide II protein band and the ratio of amide I and amide II bands were used to characterise sperm DNA to binding protein ratio. FTIR was used to characterise normal and dysfunctional sperms and seminal plasma parameters [105].

The chromosomes of morphologically normal and abnormal human sperm heads were examined using Raman spectroscopy (**Figure 4.13**). Abnormal protamine content and improper DNA packaging was attributed to the abnormal sperm head morphology. The sperms from fertile donors were filtered, deposited on quartz coverslips, and their tails and cellular membranes chemically removed to eliminate Raman signals from membrane proteins. Raman spectra from the chromosomes were collected for 5 minutes with a 488 nm, 50 mW laser source. The power at the focal plane was ~100 kW/cm^2. A 1200 lines/mm grating produced spectral resolution of 4 cm^{-1}. The Raman spectra were compared with that of calf thymus DNA and fixed whole sperm heads. The ratio of protein to DNA was calculated using 1092 cm^{-1} and methylene deformation in proteins at 1442 cm^{-1}. Proteins to DNA ratios of normal sperm heads were 1.1 to 1.5. The protein peak appeared to be sensitive to the abnormal shape of the sperm head [106] .

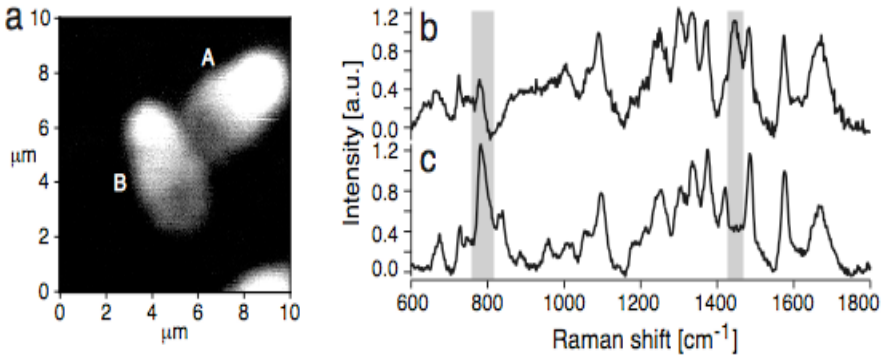

Figure 4.13 Fluorescence image of a normal (A) and pear-shaped (B) human sperm head **(b)** Raman spectrum of normal human sperm head **(c)** Raman spectrum of calf-thymus DNA gel. The spectral difference are highlighted by grey bands [106].

Mitochondria in the midpiece are responsible for sperm motility; and confocal Raman microspectroscopy of human sperm mitochondria was investigated using fibre coupled, 532 nm, 10 mW, laser source and a Zeiss microscope. A Nikon Fluor 100X/0.9 NA objective was used to focus the laser on the sample and collect the backscattered signals which was imaged onto a 1024 x 127 pixel CCD camera. The spectral range of the Raman spectra was 400 cm^{-1} to 3400 cm^{-1} and the spectral resolution was < 4 cm^{-1}. UV radiation has been shown to penetrate cellular membranes and cause gene mutation; and the effect of UV damage to sperm organelles was also investigated in this research using 365 nm source and 0.6mW/cm^2 irradiance. UV exposure time ranged from 0 to 60 minutes, and the spectra was taken at 15 minutes interval. High motility sperms from healthy donors were selected using swim-up procedure and smeared on coverslips with single cell spacing. Raman maps with image sizes of 30 μm x 30 μm, in both spot and line modes were obtained. The Raman spectra from the nucleus, neck and midpiece had distinct peaks. The peaks at 751 cm^{-1} and 1375 cm^{-1} were identified as originating from mitochondrial membranes and bases. Radiation effect on mitochondria was visible in the spectrum after 15 minutes of UV exposure. The time dependent effect of UV radiation on sperm head is shown in **Figure 4.14** [107].

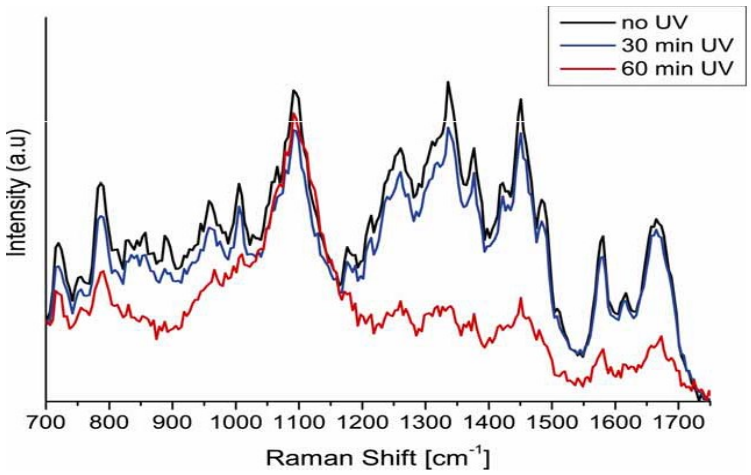

Figure 4.14 Average Raman spectrum of human sperms smeared on a glass slide, after k-means cluster analysis of nuclear cluster. The black spectra is from undamaged sperms, the blue from cells exposed to UV light for 30 minutes and the red spectra is from cells exposed to UV light for 60 minutes [107].

Raman spectroscopy and acridine orange tests were used to study UV (312 nm for 10 minutes) damage to sperms. Human sperms from fertile donors in seminal plasma and in PBS were smeared and air dried on quartz slides. 200 cells per test were analysed using Horiba Jobin Raman microspectrometer consisting of an Olympus BX41 microscope with Olympus 100X/0.9 NA objective, a 15mW He-Ne laser source, a 600 lines/mm grating and a Peltier cooled CCD camera. Silicon 520 cm^{-1} peak was used for calibration; the peak resolution was 6.7 cm^{-1}. Raman map, with 50 nm step size, delineated the head, midpiece and tail. Low frequency background noise was subtracted and outliers deleted before spectral analysis. PCA was used to differentiate the UV exposed from the unexposed samples. The UV irradiated samples revealed significant change in the otherwise stable 1092 cm^{-1} peak and a new peak formation, (**Figure 4.15),** was observed at 1042 cm^{-1}. **Note:** The intensity of the UV light was not specified in the report [108].

Raman spectra of sperms in seminal plasma were analysed with two laser sources. The spectral intensity from 632 nm laser was superior to that from 785 nm laser. Tests using 1%, 25%, 50% and 100% of source power (not explicitly stated) did not affect the peaks, but the SNR improved with increased laser intensity. Cell damage

was observed after full power exposure at a spot for 10-30 minutes. The full power is assumed to be 15 mW at 632 nm and 30 mW at 785 nm. The 1092 cm^{-1} peak was visible only in the spectra from the back of the sperm head, whereas the prominent 785 cm^{-1} peak was visible in the spectra from the acrosome region [108].

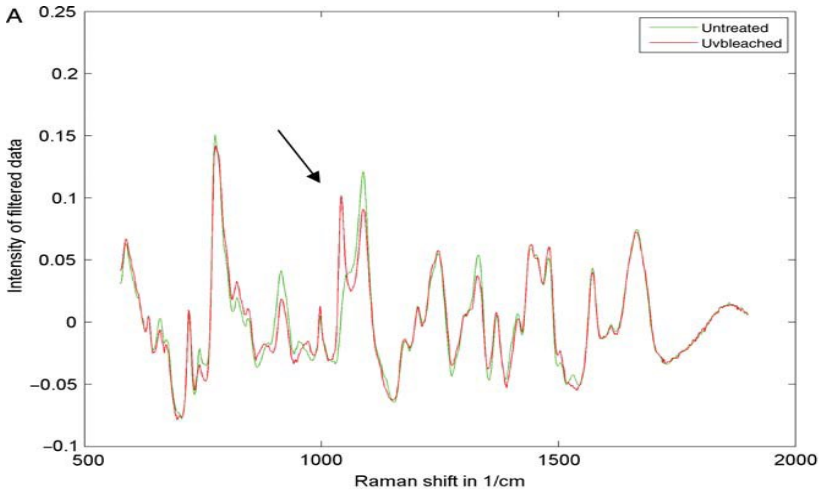

Figure 4.15 Average Raman spectra of air dried human sperm (green) and UVB irradiated (red) [108]

4.5 Live Cell Manipulation with Optical Tweezers

The basics of optical trapping is summarised in this section. Photon has energy and momentum and is capable of exerting radiation pressure. It is the same radiation pressure that keeps the sun and stars from gravitational collapse and the tail of the comets directed away from the sun. The force exerted by radiation pressure was first demonstrated by Ashkin in 1970. When a one Watt laser beam was focused to a spot size of a micron near a one micron sized particle of density 1 gm/cm^3, the particle accelerated at the rate of $10^9/cm^3$ in the direction of beam propagation [109].

Transparent latex spheres suspended in water not only experienced the force of the laser beam, causing them to accelerate in the direction of the beam, but the beads in the periphery of a tightly focused Gaussian beam were pulled into the high intensity region of the beam and remained with the beam focus; they resumed Brownian motion only when the beam was switched off. The unexpected capability of a

tightly focused laser beams to trap optically dense micron sized particles, was summarised by Ashkin and team in their 1986 seminal paper [110].

The radiation pressure is caused by changes in photon (frequency, ν) momentum,

$\frac{\partial p}{\partial z}$, where $\mathrm{p} = \frac{h\nu}{\lambda}$ is the incident momentum vector directed along the z-axis.

The total momentum of a laser beam containing N photons is N**p** = **P**. The force from the photon experienced by an ideal opaque particle is 2**P**/c per second in the direction of the incident beam.

The radiation force experienced by a transparent particle is related to the radiation flux across its surface, and the refractive index of the particle with respect to that of the medium, *n*. The total force '**F**' exerted by the radiation is [110],

$$\mathbf{F} \propto \frac{n}{c}\mathbf{P}$$

A laser beam with a Gaussian profile has high intensity gradient at the focus of a sufficiently high numerical aperture (NA) microscope objective. Small optically dense neutral particles are held in place when the scattering force exerted on the particle is balanced by the gradient force pulling the sphere towards the focus, just outside the focal point; this is a 3-d affect. The ray diagram of the force experienced by a transparent bead is shown in **Figure 4.16**. The transverse differential photon momentum caused by the large cross-sectional intensity gradient of the beam refracted by an optically dense bead, pulls the bead towards the high intensity region of the beam. The axially directed scattering force by the beam propels the bead forward, until the net force by the intensity gradient is in equilibrium with the axial scattering force, as shown in the figure. The force on an optically rare bead pushes the bead away from the beam axis; a single beam cannot trap such beads [110].

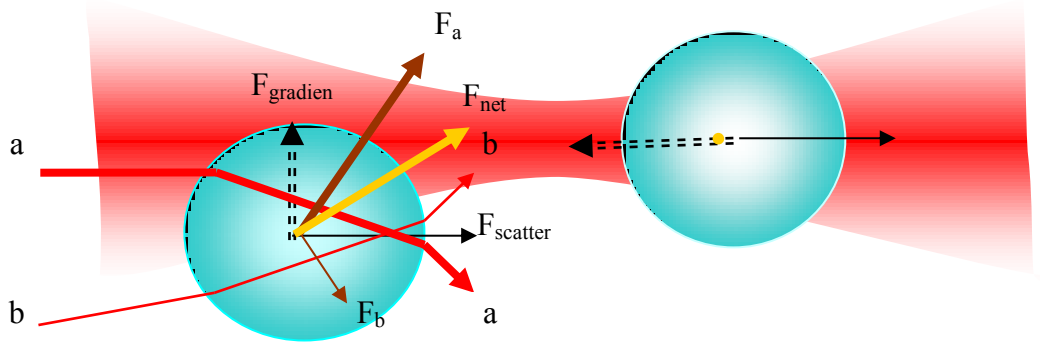

Figure 4.16 Trapping profile of an optically dense particle in the focal region of the laser beam is illustrated using ray optics. The unbalanced force on the particle (left of focus) and equilibrium state of the particle (right of focus) are also depicted.

Since the discovery of laser traps, the technique has been used for particle levitation, and to trap atoms, molecules and dielectric spheres (submicron to ~100 microns). Two oppositely directed beams are used to trap opaque or optically rare particles. Optical tweezers have applications in the study of low temperature physics – Bose-Einstein condensate, colloidal science and crystallites, cellular and molecular bio-mechanics, biological cell trapping and manipulating cellular components [111-113]

Liquid crystal spatial light modulators and high speed optical switches are used to control the pattern and speed of arrays of optical traps; these are used to trap and manipulate multiple, rapidly moving particles, simultaneously [114]. Optical traps are used in cell sorting by size and refractive index. Moving light patterns are used to trap, isolate or arrange multiple particles in colloidal suspensions or in fluid flow, into different patterns [115]. Programmable optical trap arrays have been created using Shack-Hartman wavefront sensor technique [116]. High intensity laser beam arrays with separate control of position, intensity, size and shape of individual beams with phase modulation has been used for both static and dynamic trapping of multiple micro-spheres in suspension [117]. Two beam interference patterns were used to trap hollow spheres and low index particles [118]. Weakly focused laser beam was used to trap micro-sphere clusters, and coherent scattering from these clusters create optical binding forces that attract nearby particles [119].

Optical aberration can affect the quality of optical traps when trapping deep within large samples. Optical elements in the beam path and the trapped sample can contribute to the aberrations. Deformable mirrors and diffractive optics elements (DOE), along with dye stained polystyrene beads have been used to correct trap aberrations [120]. Trapping efficiency of AlGaAs diode laser was improved by 40%, when anamorphic prism was used to correct ellipticity and astigmatism [121]. Dual axes adaptive optics with acousto-optic modulation and remote trap alignment has been used in laser tweezers array for International Space Station (ISS) micro-gravity research; it has also been used to investigate colloid crystallisation [122].

4.5.1 Optical Traps in Biological Applications

Ashkin used 100 mW argon lasers (514.5 nm) to trap rod shaped tobacco mosaic viruses and live motile bacteria in suspension, for the first time. Trapped bacteria survived in laser powers of ~ 5mW, even after several minutes of trapping [123]. Since then, laser traps have been used in biological applications [124].

Optical traps were used to investigate cell division, cell motility, torsion and strain in tethered cells using single beams to trap small cells and oppositely directed beams to trap large cells. Optical traps have been used to explore micro-environment (viscosity and elasticity) inside cellular cytoplasm [125, 126]. Oppositely directed lasers were used to axially stack several trapped colloidal particles, including red blood cells and yeast cells, to improve their Raman signal intensity [127].

Transport of lipid droplets in the periphery of drosophila embryos, at various stages of development, was investigated using optical traps. The critical force exerted by a laser trap to stall lipid droplets was used to characterise the force of the vesicle as a function of the developmental stages of embryo [128]. Cyclical behaviour of processive enzymes like polymerases, the motion of polymerase during RNA transcription, the pico-Newton force exerted by bio-motors, kinesins and myosin, have been studied with highly sensitive position sensors and optical traps [126, 129].

Mechanical properties of DNA, microtubules and filaments were tested using dual beams for simultaneous trapping and stretching [130]. The force required to unzip base pairs from tethered DNA double strand segments was studied using dye on

polystyrene beads attached to the free end of a DNA [131]. Optical traps and fluorescence microscopy were used to study RNA-polymerase interaction with DNA [132]. When bacteria trapped with IR laser was exposed to visible light resonance excitation, the bacteria suffered damage by the exposure [133].

A 1064 nm, 2 mW laser beam was used to continuously trap *Saccharomyces cerevisiae* yeast cells and a 785 nm laser of about 10 mW power was used to acquire Raman spectrum of the trapped cells in culture. Cell proliferation was unaffected during the continuous trapping for 150 minutes; spectra were acquired every 3 minutes with 3 minutes accumulation. Molecular changes were observed during the process of budding. The effect of heat, hyperosmotic stress and chemical stress on the trapped cells were monitored in real time using Raman signature of glycerol and ethanol in the cell. Continuous trapping of a for over two hours did not disrupt budding yeast cells or the cell cycle [134, 135].

Laser traps have been used for vesicle manipulation and positioning within large cells and for transporting bacteria inside hollow fibres [111]. Holographic optical tweezers were used to generate multiple beams to trap different sections of floating cells to prevent the cells from spinning/rotating inside the trap; they were also used for spatially resolved studies such as Raman mapping [136, 137].

4.5.2 Laser Tweezers Raman Spectroscopy (LTRS)

The use of a single laser beam for simultaneous trapping and Raman spectral acquisition was first reported by a team of researchers from East Carolina University, NC, in the US in 2002. A 785nm laser source was used to trap live red blood and yeast cells, using 2mW power. During Raman data acquisition, the laser power was raised to 20 mW for 2 seconds. Molecular changes to the live cells were investigated using these dual power technique [138].

A 785 nm, 5 mW laser and a 100x oil immersion objective were used to acquire Raman spectra for 180 seconds from trapped *Saccharomyces cerevisiae* (yeast) cell culture incubated in a 30^{o}C environment. The continuously trapped cells were supplied with nutrients in the culture; spectral changes were observed during the process of budding and other growth phases. The effect of continuous trapping was

also investigated on 5 μm sized yeast cells trapped for 3 hours. While phase related spectral changes were observed, the peaks did not indicate trapping induced stress damages. The budding time of trapped and untrapped cells were the same, indicating that trapping had no obvious effect on budding [136].

LTRS and generalised discriminate analysis were used for the first time to obtain Raman fingerprints of human chromosomes. This technique was fast, reliable, non-destructive and simple, when compared to the labour intensive G-banding, using complex staining technique, that was done during mitotic metaphase [139]. LTRS has also been used to investigate different bacteria, the transgenic characteristics of pine cell nuclei and temperature effects on trapped yeast cells, with 785 nm diode laser, a 1.3 NA, 100X objective and 2 mW trapping power. Changes to characteristic Raman peaks caused by heat induced changes in yeast cell structure were analysed using 15 mW laser power; denaturation of bio-molecules were observed in the cells. *In vitro* Raman spectra of the nucleus within optically trapped live spores, blood cells and bacteria were also investigated [140, 141].

A bespoke LTRS at the Centre for Biophotonics Science and Technology (CBST), (USA), was used to investigate Raman signature of blood cancer cells [142], protein inclusions from brain cells [143] and nucleotide structures [144]. The details of the LTRS are provided in **Chapter 5,** as it was used for this research.

4.6 Laser Trapping Induced Cellular Damage

Ashkin demonstrated, using tobacco mosaic viruses, that trapped bacteria and viruses could be destroyed – opticuted - with radiation power. The photochemical effects from low intensity light irradiation on biological materials are directly proportional to the total irradiance. However, laser induced live cell damages are related to its wavelength, intensity and its potential for multiphoton generation. Low power, short laser pulses can inflict instant damage to biological materials as a result of multiphoton interaction. Multiphotons from 532 nm (green) and 266 nm (UV) pulsed lasers caused cellular alterations in rat kidney tissue [145]. When Nd:YAG, 1064 nm, 50 mW laser was used to trap *Escherichia coli (E. coli)* bacteria in water, the bacteria not only remained alive for over an hour, but it also divided into two live

bacteria. The divided bacteria also divided when trapped; indicating no damage to the cell function by the 1064 nm trapping. Trapped yeast cells also reproduced while remaining trapped by the laser tweezers [123].

Wavelength and oxygen dependent damages were observed in tethered *E. coli* bacteria, using laser traps ranging from 790 nm to 1064 nm, with and without oxygen in their environment. Anaerobic conditions at 970 nm produced the least cellular damage. Single photon involved photo-damage and other complex factors that have not been clearly understood, also contributed to the observed nonlinear damage [146].

Extended trapping with He-Ne laser at 633 nm and 0.4 mW power negatively impacted budding in yeast cells [136]. Trapped bacteria were studied using two strains of *E. coli* cells and three types of lasers. Tunable Ti:sapphire ring laser (780nm – 970nm), diode laser at 991nm and Nd:YAG laser at 1064nm with different laser shapes were used. Oxygen and wavelength dependent damages were observed in the study [146]. Pulsed laser traps caused DNA damage to live cells. DNA strand breaks were detected in bovine RPE cells exposed to 810 nm CW and femto-second pulsed laser, using comet assay [147, 148].

Non-linear wavelength dependent cloning efficiency was observed with unstained, laser-trapped Chinese hamster ovaries (CHO) at 88 mW. CHO exposed to single mode 950 – 990 nm radiations exhibited the highest cloning efficiency in the study, and the ovaries exposed to 760 nm, 900 nm and 1064 nm showed least cloning efficiency. Cloning efficiency was inversely related to laser power and exposure time. The CHO could not clone after 20 seconds exposure to multimode 760 nm, 88 mW laser trap. CHO cloning efficiency declined after 300 seconds exposure when a single mode 760 nm, 88 mW laser trap was used [149-151].

CW and pulsed lasers at 1064 nm were used to study the impact of the laser power on trapped ovaries and sperms. The trapping beam produced diffraction limited spot-size of 0.8 μm with a 1.3 NA oil immersion objective. Temperature changes, pH changes and cell viability were tested on CHO and motile human sperms. Two photon fluorescence excitation using appropriate stains for cell viability (Acridine orange and Propidium Iodide (PI)) and pH (carboxy SNARF) were used to study

laser induced DNA damage. Laser powers from 100 mW to 400 mW were used in CW mode, to study human sperms. Laser powers of 20 mW to 200 mW were required to trap motile sperm cells. The fluorescent spectra indicated that low motility sperms could be trapped up to 2 minutes at 300 mW, without visible DNA damage. Slight temperature increase was observed but it was not sufficient to induce thermal denaturation. When the laser trap was operated in Q switched pulse mode (100 ns at 40 μJ/pulse) with an average power of 40 mW and peak power of 400 mW, the temperature rose rapidly to about 100^{o}C and damaged the sperm cells [152].

UV and visible laser traps have induced photo-stress in cells. NIR optical traps have been used in non-invasive biological surgery [126, 153, 154]. Human sperms were trapped at 40 mW with a 1064 nm laser for 120 seconds without any change observed in flagellar velocity [155]. NIR absorption by water dropped by a factor of 3 in the 750 – 1000 nm range, making this range superior to 1064 nm lasers for live cell trapping. Trapping induced damage to live human sperm cells were studied using 750 nm to 1064 nm laser frequencies. Due to the heterogeneity in sperms motility, the laser intensities varied from 50 mW – 150 mW and the trapping power ranged from 15 MW/cm^2 – 40 MW/cm^2, creating photon fluxes in excess of 10^{26}/cm^2/second. Both endogenous and exogenous fluorescence were observed, on lightly stained sperms with multimode lasers, creating significantly higher excitation. When the cells were trapped for 10 minutes by 70 mW sources at wavelengths 800 nm or higher, the sperms remained viable, and displayed green fluorescence with PI staining. When a 780 nm source was used at the same power, the average lifetime was ~ 580 seconds (range of ~ 400 -1000 seconds). The cell viability decreased significantly when multimode 760 nm laser was used, and displayed green fluorescence for about 60 seconds. With single mode laser, the lifetime improved to ~ 400 seconds at 760 nm. The damage was attributed to two- photon excitation. Damage to sperm cells by UV lasers was significantly high at very low powers and exposure time [149-151]. The force required to trap motile sperms was tested using a 760 nm laser. The cells were trapped at 300 mW and the intensity decreased until the cell escaped from the trap; the average laser power for escape was 60 +/- 40mW. The escape power doubled during hyper-activation and tripled when sperm reached the egg [156].

4.7 Chapter Four Digest

The history of spectroscopy provided insight into the discovery and development of Raman spectroscopy. The theoretical and experimental struggles in the early 20th century and the rapid progress in Raman applications before the turn of the Millennium in the 21st century were summarised. A brief overview of the theory using the simplest of models was helpful in understanding vibrational spectroscopy.

Applications of Raman spectroscopy in biological sciences and medical applications have grown exponentially in the last 20 – 30 years, and a variety of applications were investigated through literature review. Simple sample preparation and weak scattering by water has made Raman spectroscopy popular in live cell studies. Raman fingerprints of cellular and synthetic DNA and its components were examined in some detail, as the focus of the research is on sperm DNA damage. Available literature on Raman and IR spectroscopy of mammalian sperms and human sperms were also reviewed in detail. The published work on Raman spectroscopy of live sperm cells, at the time of submitting the thesis, was limited.

The techniques of optical trapping and applications of laser tweezers were summarised, as Raman spectra were taken on trapped sperms cells in this research. Damage inducing capability of laser traps were also reviewed in detail, as the laser intensity at the focus is sufficiently high and can induce photo-damage. Lasers in the UV and visible energy range were found to induce cellular damage, even at low laser powers. NIR region of the spectrum induced less damage, with near NIR (<800 nm) causing wavelength dependent damage that has not been fully investigated. The choice of laser wavelength and beam intensities for LTRS are critical to minimise heat induced and wavelength induced cellular damage. However, at the low power (~25 mW) and exposure times (~ 30 seconds) with the narrow a line width laser used in this research, a normal sperm should not suffer stress damage.

Stains and biochemical assays were used in some of the reported studies to evaluate laser induced damage. In other studies, the cellular functions were tested while continuously trapped. The information contained in **Section 4.6** is critical in evaluating laser induced damage to sperm cells. The section contains several reports

on damage evaluation to instil confidence in the experimental work undertaken and to deduce that low power NIR laser traps do not damage live healthy sperm cells.

While somatic cells are easy to damage, sperm cells have not only double membranous layers protecting the DNA (Chapter Two) these layers cannot be destroyed with the chemicals used to destroy the membranes of somatic cells. In addition, the protamine cross links add further chemical stability to the sperm nucleus. Healthy sperms have not been damaged by gamma rays (Chapter Three).

The biochemical assays described in **Chapter Three** for somatic cell applications were modified to study sperm cells. Yet, it was challenging for the experts, to produce consistent and reproducible results with stallion sperms; very likely, due to the tight, histone free crosslinks. While the stain test on trapped sperms would have been useful to directly investigate DNA damage on the cells, such resources were not available at the time of the experiments; hence, I had to rely on the papers referenced in **Section 4.6.** The literature also indicate that low power, narrow line width, NIR lasers do not induce DNA damage on healthy sperm cells.

The literature survey and basic theory completed in this and the preceding chapters have prepared the ground work for the appropriate design of the experimental work, using available resources. These chapters also contain most of the information required for the analyse of the results and discussion of their limitations, presented in the next three chapters. Both horse and human sperms have high variability. The variability within breeds and within stallions, makes them difficult specimens for feasibility studies. However, with much re-design of the original plan, this experimental work has been completed, relying heavily on published literature than on experimental proof to support the outcome.

Reference

1. Subrahmanyam, N. and B. Lal, *A Textbook of Optics*. 22 ed. 1966, New Delhi: S Chand & Company Ltd.
2. Walker, C.T. and G.A. Slack, *Who named the -ON's?* American Journal of Physics, 1970. **38**(12): p. 1380-1389.
3. Krishnan, R.S. and R.K. Shankar, *Raman Effect: History of the Discovery.* Journal of Raman Spectroscopy, 1981. **10**(1): p. 1-8.
4. Raman, C.V., *The Colour of the Sea.* Nature, 1921. **108**(367): p. 10-11.
5. Nampoori, V.P.N., *A Co-traveler of Light, Colour and Beauty - Life and Work of CV Raman*, in *Photnics News*. 2002, Cochin University, Cochin, Kerala India: International School of Photonics (ISP) p. 17.
6. Fischer, J., *George Placzek - An Unsung Hero of Physics*, in *CERN Courier*. 2005, Institute of Physics for CERN.
7. Neuenschwander, D.E., *Bright Ideas: From Concept to Hardware in the First Lasers.* Americal Institute of Physics History Newsletter, 2010. **42**(1).
8. Garwin, L. and T. Lincoln, eds. *A Century of Nature: Twenty-One Discoveries that Changed Science and the World*. 2003, The University of Chicago Press.
9. McCreery, R.L., *Raman Spectroscopy for Chemical Analysis*. Vol. 157. 2000: John Wiley and Sons. 420.
10. Sampaolo, M., *Gustav Robert Kirchhoff*, in *Encyclopedia Brittanica* M. Sampaolo, Editor. 2006.
11. Sarachik, E.S. and G.T. Schappert, *Classical Theory of the Scattering of Intense Laser Radiation by Free Electrons.* Physical Review D, 1970. **1**(10): p. 2738.
12. Mei, G., *Contributions to the Optics of Turbid Media, Particularly of Colloidal Metal Solutions.* Annalen Der Physik, 1908. **25**(3): p. 377.
13. Miles, R.B., W.R. Lempert, and J.N. Forkey, *Laser Rayleigh scattering.* Measurement Science And Technology, 2001. **12**: p. R33-R51.
14. Cardona, M. and R. Merlin, eds. *Light Scattering in Solids: Volume IX, Novel Materials and Techniques*. Topics in Applied Physics. Vol. 9. 2007, Springer Science. 432.
15. Hollas, M.J., *Modern Spectroscopy*. Fourth ed. 1987: John Wiley & Sons, Ltd. 455.
16. Ferraro, J.R., K. Nakamoto, and C.W. Brown, *Introductory Raman Spectrosopy*. Second Edition ed. Vol. 1. 2003: Academic Press. 434.
17. Hart, T.R., R.L. Aggarwal, and B. Lax, *Temperature Dependence of Raman Scattering in Silicon.* Physical Review B, 1970. **1**(2): p. 5.
18. Nakamoto, K., *Infrared and Raman Spectra of Inorganic and Coordination Compounds: Theory and applications in inorganic chemistry*. Sixth ed. 2009: Wiley-Interscience.
19. Hoffman, K.R., et al., *On the emission and excitation spectrum of the NIR laser center in Cr:YAG.* Journal of Luminescence, 1992. **52**(5-6): p. 277-279.
20. Bonatsos, D. and C. Daskaloyannis, *Model of n coupled generalized deformed oscillators for vibrations of polyatomic molecules.* Physical Review A, 1993. **48**(5): p. 3611.
21. Morse, P.M., *Diatomic Molecules According to the Wave Mechanics. II. Vibrational Levels.* Physical Review, 1929. **34**(1): p. 57.
22. Al-Dossary, O.M., *Morse potential eigen-energies through the asymptotic iteration method.* International Journal of Quantum Chemistry, 2007. **107**(10): p. 2040-2046.
23. Wong, C.F. and J.C. Light, *Vibrational excitation and dissociative attachment of a triatomic molecule: CO2 in the collinear approximation.* Physical Review A, 1986. **33**(2): p. 954.
24. Chaplin, M. (2011) *Water Structure and Science*. Web Article **2011**, Web article.
25. Cook, R.L., F.C. De Lucia, and P. Helminger, *Molecular force field and structure of water: Recent microwave results.* Journal of Molecular Spectroscopy, 1974. **53**(1): p. 62-76.
26. Wartewig, S., *IR and Raman Spectroscopy: Fundamental Processing*. 2003 WILEY-VCH Verlag GmbH & Co. KGaA, Weinheim. 175.
27. Long, D.A., *The Raman Effect: A Unified Treatment of the Theory of Raman Scattering by Molecules.* First ed. 2002: John Wiley & Sons. 611.
28. Kielich, S. and T. Bancewicz, *Symmetric and Non-Symmetric Hyper-Raman Scattering: Its Polarisation States and Angular Dependences.* Journal of Raman Spectroscopy, 1990. **21**: p. 7.

29. Watanabe, J., M. Watanabe, and S. Kinoshita, *Stokes-to-anti-Stokes intensity ratio in the low-frequency light scattering of a paraelectric KH_{2}PO_{4} crystal near the ferroelectric-phase-transition temperature.* Physical Review B, 2006. **74**(13): p. 132105.
30. Ke, W., D. Yu, and J. Wu, *Raman spectroscopic study of the influence on herring sperm DNA of heat treatment and ultraviolet radiation.* Spectrochimica Acta Part A: Molecular and Biomolecular Spectroscopy, 1999. **55**(5): p. 1081-1090.
31. Kittel, C., *Introduction to Solid State Physics*. 8 ed. 2004: John Wiley & Sons. 680.
32. Duguid, J., et al., *Raman spectroscopy of DNA-metal complexes. I. Interactions and conformational effects of the divalent cations: Mg, Ca, Sr, Ba, Mn, Co, Ni, Cu, Pd, and Cd.* Biophysical Journal, 1993. **65**(5): p. 1916-1928.
33. Danichkin, S.A., et al., *Raman scattering parameters for gas molecules (survey).* Journal of Applied Spectroscopy, 1981. **35**(4): p. 1057.
34. Dickinson, R.G., R.T. Dillon, and F. Rasetti, *Raman Spectra of Polyatomic Gases.* Physical Review, 1929. **34**(4): p. 582.
35. Lutz, H.D. and H. Haeuseler, *Infrared and Raman spectroscopy in inorganic solids research.* Journal of Molecular Structure, 1999. **511-512**: p. 69–75.
36. Bernstein, N., M. J. Mehl, and D.A. Papaconstantopoulos, *Energetic, vibrational, and electronic properties of silicon using a nonorthogonal tight-binding model.* Physical Review B, 2000. **62**(7): p. 11.
37. Alfaro, P., et al., *Raman scattering by confined optical phonons in Si and Ge nanostructures.* Nanoscale, 2011. **3**: p. 1246-1251.
38. Kobliska, R.J. and S.A. Solin, *Raman Spectrum of Wurtzite Silicon.* Physical Review B, 1973. **8**(8): p. 3799.
39. Dracinsky, M., L. Benda, and P. Bour, *Ab initio modeling of fused silica, crystal quartz, and water Raman spectra.* Chemical Physics Letters, 2011. **512**(1-3): p. 54-59.
40. Enami, M., T. Nishiyama, and T. Mouri, *Laser Raman microspectrometry of metamorphic quartz: A simple method for comparison of metamorphic pressures.* American Mineralogist, 2007. **92**(8-9): p. 1303-1315.
41. Walrafen, G.E., Y.C. Chu, and M.S. Hokmabadi, *Interaction-induced Raman scattering from fused silica.* The Journal of Physical Chemistry, 1990. **94**(15): p. 5658-5661.
42. Hung, P.-S., et al., *Detection of Osteogenic Differentiation by Differential Mineralized Matrix Production in Mesenchymal Stromal Cells by Raman Spectroscopy.* PLoS ONE, 2013. **8**(5): p. e65438.
43. Pelletier, M.J., ed. *Analytical Applications of Raman Spectroscopy*. 1999, Blackwell Science. 478.
44. Garcia, C.S., et al., *Remote pulsed laser Raman spectroscopy system for detecting water,ice, and hydrous minerals.* Proceedings of SPIE, 2006. **6302**: p. 7.
45. Larsen, O., *Vibrational relaxation of the H2O bending mode in liquid water.* J. Chem. Phys., 2004. **121**(24): p. 12143.
46. Walrafen, G.E. and Y.C. Chu, *Linearity between Structural Correlation Length and Correlated-Proton Raman Intensity from Amorphous Ice and Supercooled Water up to Dense Supercritical Steam.* The Journal of Physical Chemistry, 1995. **99**(28): p. 11225-11229.
47. Prasad, P.S.R., Y. Sowjanya, and K.S. Prasad, *Micro-Raman investigations of mixed gas hydrates.* Vibrational Spectroscopy, 2009. **50**: p. 319-323.
48. Walrafen, G.E., *Raman spectrum of water: transverse and longitudinal acoustic modes below .apprxeq.300 cm-1 and optic modes above .apprxeq.300 cm-1.* The Journal of Physical Chemistry, 1990. **94**(6): p. 2237-2239.
49. Yoshimura, Y., et al., *Convergent Raman Features in High Density Amorphous Ice, Ice VII, and Ice VIII under Pressure.* The Journal of Physical Chemistry B, 2011. **115**.
50. Wang, Z., et al., *A new way to measure cirrus cloud ice water content by using ice Raman scatter with Raman lidar.* Geophysical Research Letters 2004. **31**(L15101): p. 4.
51. Auer, B.M. and J.L. Skinner[a], *IR and Raman spectra of liquid water: Theory and interpretation.* The Journal of Chemical Physics 2008. **128**(224511): p. 12.
52. Carey, P.R., *Raman Spectroscopy, the Sleeping Giant in Structural Biology, Awakes* 1999. **274**: p. 26625-26628.
53. Mesu, J.G., et al., *Infrared and Raman spectroscopic study of pH-induced structural changes of l-histidine in aqueous environment.* Vibrational Spectroscopy, 2005. **39**(1): p. 114.

54. Ruiz-Chica, A.J., et al., *Characterization by Raman spectroscopy of conformational changes on guanine-cytosine and adenine-thymine oligonucleotides induced by aminooxy analogues of spermidine.* Journal of Raman Spectroscopy, 2004. **35**(2): p. 93-100.
55. Deng, H., et al., *Structural basis of polyamine–DNA recognition: spermidine and spermine interactions with genomic B-DNAs of different GC content probed by Raman spectroscopy.* Nucieic Acid Research, 2000. **28**(17): p. 3379-3385.
56. Maquelin, K., et al., *Identification of medically relevant microorganisms by vibrational spectroscopy.* Journal of Microbiological Methods 2002. **51** p. 255- 271.
57. Hanlon, E.B., et al., *Prospects for in vivo Raman spectroscopy.* Physics in Medicine and Biology, 2000. **45**(2): p. R1.
58. Notingher, I. and L.L. Hench, *Raman microspectroscopy: a noninvasive tool for studies of individual living cells in vitro.* Expert Review of Medical Devices, 2006. **3**(2): p. 215-234.
59. Lambert, P., et al., *Raman spectroscopy: the gateway into tomorrow's virology.* Virology Journal, 2006. **3**(1): p. 51.
60. Huang, Y.-S., et al., *In Vivo Raman Spectroscopy And Imaging Of A Single Living Fission Yeast Cell.* Proceedings of the XIX International Conference on Raman Spectroscopy, 2004.
61. Manoharan, R., Y. Wang, and M.S. Feld, *Histochemical analysis of biological tissues using Raman spectroscopy.* Spectrochimica Acta Part A: Molecular and Biomolecular Spectroscopy, 1996. **52**(2): p. 215-249.
62. Azrad, E., et al., *Probing the effect of an extract of elk velvet antler powder on mesenchymal stem cells using Raman microspectroscopy: enhanced differentiation toward osteogenic fate.* Journal of Raman Spectroscopy, 2006. **37**: p. 480–486.
63. Blanch, E.W., et al., *Protein Fold Recognition And Structure Elucidation Using Raman Optical Activity* Proceedings of the XIX International Conference on Raman Spectroscopy, 2004.
64. Kaminaka, S., et al., *Near-infrared multichannel Raman spectroscopy toward real-time in vivo cancer diagnosis.* Journal of Raman Spectroscopy, 2002. **33**(7): p. 498-502.
65. Caspers, P.J., G.W. Lucassen, and G.J. Puppels, *Combined In Vivo Confocal Raman Spectroscopy and Confocal Microscopy of Human Skin.* Biophys. J., 2003. **85**(1): p. 572-580.
66. Huang, Y.-S., et al., *Molecular-level pursuit of yeast mitosis by time- and space-resolved Raman spectroscopy.* Journal of Raman Spectroscopy, 2003. **34**: p. 1-3.
67. Schulze, H.G., et al., *Assessing Differentiation Status of Human Embryonic Stem Cells Noninvasively Using Raman Microspectroscopy.* Analytical Chemistry, 2010. **82**(12): p. 5020-5027.
68. McManus, L.L., et al., *Raman spectroscopic monitoring of the osteogenic differentiation of human mesenchymal stem cells.* Analyst, 2011. **136**(12): p. 2471-2481.
69. Ko, A.C.-T., et al., *Detection of early dental caries using polarized Raman spectroscopy.* Optics Express, 2006. **14**(1): p. 203-215.
70. Beattie, J.R., et al., *Effect of excitation wavelength on the Raman spectroscopy of the porcine photoreceptor layer from the area centralis*. Molecular Vision 2005. **11**: p. 825-832
71. Uzunbajakava, N., et al., *Nonresonant Confocal Raman Imaging of DNA and Protein Distribution in Apoptotic Cells.* Biophysical Journal Volume 2003. **84**: p. 3968-3981.
72. Davidson, B., et al., *The changing biochemical composition and organisation of the murine oocyte and early embryo as revealed by Raman spectroscopic mapping.* Journal of Raman Spectroscopy, 2012. **43**(1): p. 24-31.
73. Yamazaki, H., et al., *The Diagnosis of Lung Cancer Using 1064-nm Excited Near-infrared Multichannel Raman Spectroscopy.* Radiation Medecine, 2003. **21** (1): p. 1-6.
74. Verrier, S., et al., *In situ monitoring of cell death using Raman microspectroscopy.* Biopolymers, 2004. **74**(1-2): p. 157-162.
75. Puppels, G.J., et al., *Studying single living cells and chromosomes by confocal Raman microspectroscopy.* Nature, 1990. **347**(6290): p. 301.
76. Schuster, K., et al., *Multidimensional information on the chemical composition of single bacterial cells by confocal Raman microspectroscopy.* Analytical Chemistry, 2000. **72**(22): p. 5529-34.
77. Schuster, K., Urlaub E, and G. JR, *Single-cell analysis of bacteria by Raman microscopy: spectral information on the chemical composition of cells and on the heterogeneity in a culture.* Journal of Microbiological Methods, 2000 **42**(1): p. 29-38.

78. Matthews, Q., et al., *Variability in Raman Spectra of Single Human Tumor Cells Cultured in Vitro: Correlation with Cell Cycle and Culture Confluency.* Appl. Spectrosc., 2010. **64**(8): p. 871-887.
79. Guan, Y., C.J. Wurrey, and J. George J. Thomas, *Vibrational Analysis of Nucleic Acids. I. The Phosphodiester Group in Dimethyl Phosphate Model Compounds: $(CH_3O_2)_2PO_2^-$, $(CD_3O)_2PO_2^-$, and $(^{13}CH3O)_2PO_2^-$* Biophysical Journal, 1994. **66**: p. 225-235.
80. Guan, Y. and J. George J. Thomas, *Vibrational Analysis of Nucleic Acids. V. Force Field and Conformation-Dependent Modes of the Phosphodiester Backbone Modeled by Diethyl Phosphate.* Biophysical Journal 1996 **71**: p. 2802-2814.
81. Benevides, J.M., S.A. Overman, and J. George J. Thomas, *Raman, polarized Raman and ultraviolet resonance Raman spectroscopy of nucleic acids and their complexes.* Journal of Raman Spectroscopy, 2005. **36**(4): p. 279-299.
82. Duguid, J.G. and V.A. Bloomfield, *Electrostatic Effects on the Stability of Condensed DNA in the Presence of Divalent Cations.* Biophysical Journal, 1996. **70** p. 2838-2846.
83. Erfurth, S.C., Ernest J. Kiser, and W.L. Peticolas, *Determination of the Backbone Structure of Nucleic Acids and Nucleic Acid Oligomers by Laser Raman Scattering.* Proceedings of the National Academy of Sciences of the U S A, 1972. **69**(4): p. 938-941.
84. Nishimura, Y., et al., *Raman diagnosis of nucleic acid structure: sugar-puckering and glycosidic conformation in the guanosine moiety.* Nucleic Acids Research, 1983. **11**(5): p. 1579-1588.
85. Benevides, J.M., et al., *The Raman spectra of left-handed DNA oligomers incorporating adenine-thymine base pairs.* Nucleic Acids Research, 1984. **12**(14): p. 5913-5925.
86. Peticolas, W.L., et al., *Laser Raman Microscopy of Chromosomes in Living Eukaryotic Cells: DNA Polymorphism In Vivo.* Journal of Raman spectroscopy 1996. **27** p. 571-578.
87. Duguid, J.G., et al., *DNA melting investigated by differential scanning calorimetry and Raman spectroscopy.* Biophysical Journal, 1996. **71**(6): p. 3350-3360.
88. Movileanu, L., J.M. Benevides, and G.J. Thomas, *Temperature dependence of the raman spectrum of DNA. Part I—Raman signatures of premelting and melting transitions of poly(dA–dT)·poly(dA–dT).* Journal of Raman Spectroscopy, 1999. **30**(8): p. 637-649.
89. Benevides, J.M. and J. G.J. Thomas, *Characterization of DNA structures by Raman spectroscopy: high-salt and low-salt forms of double heical poly(dG-dQ in H21 and D20 solutions and application to B, Z and A-DNA*.* Nucleic Acids Research, 1983. **11**(16).
90. Synytsya, A., et al., *Raman spectroscopic study of calf thymus DNA: an effect of proton- and gamma-irradiation.* Journal of Raman Spectroscopy, 2007. **38**(11): p. 1406-1415.
91. Deng, H., et al., *Dependence of the Raman Signature of Genomic B-DNA on Nucleotide Base Sequence.* Biopolymers:, 1999. **50**: p. 656-666.
92. Rich, A. and S. Zhang, *Z-DNA: the long road to biological function.* Nat Rev Genet, 2003. **4**(7): p. 566-572.
93. Duguid, J.G. and V.A. Bloomfield, *Aggregation of melted DNA by divalent metal ion-mediated cross-linking.* Biophysical Journal, 1995. **69**(6): p. 2642-2648.
94. Morari, C.I. and C.M. Muntean, *Numerical simulations of Raman spectra of guanine-cytosine Watson-Crick and protonated Hoogsteen base pairs.* Biopolymers, 2003. **72**(5): p. 339-344.
95. Benevides, J.M., ChulHee Kang, and J. George J. Thomas, *Raman Signature of the Four-Stranded Intercalated Cytosine Motif in Crystal and Solution Structures of DNA Deoxycytidylates d(CCCT) and d(C8).* Biochemistry 1996. **35**: p. 5747-5755.
96. Tang, Y.-L. and Z.-Y. Guo, *Raman Spectroscopic Analysis of the Effect of Ultraviolet Irradiation on Calf Thymus DNA.* Acta Biochimica et Biophysica Sinica, 2005. **37**(1): p. 39-46.
97. Wilkins, M.H.F., G. Zubay, and H.R. Wilson, *X-ray diffraction studies of the molecular structure of nucleohistone and chromosomes.* Journal of Molecular Biology, 1959. **1**(2): p. 179-IN10.
98. Suau, P. and J.A. Subirana, *X-ray diffraction studies of nucleoprotamine structure.* Journal of Molecular Biology, 1977. **117**(4): p. 909-926.
99. Kubasek, W., et al., *Raman spectra of the model B-DNA oligomer d(CGCGAATTCGCG)2 and of the DNA in living salmon sperm show that both have very similar B-type conformations.* Biochemistry, 1986. **25**(23): p. 7440-5.
100. Hud, N.V., F.P. Milanovich, and R. Balhorn, *Evidence of Novel Secondary Structure in DNA-Bound Protamine Is Revealed by Raman Spectroscopy.* Biochemistry, 1994. **33**(24): p. 7528.

101. Roque, A., I. Ponte, and P. Suau, *Secondary structure of protamine in sperm nuclei: an infrared spectroscopy study.* BMC Structural Biology, 2011. **11**(1): p. 14.
102. Li, X.X., et al., *Protective Effects of Melatonin against Oxidative Stress in Flow Cytometry-sorted Buffalo Sperm.* Reproduction in Domestic Animals, 2011: p. 1-9.
103. Meyers, S.A., *Dry storage of sperm: applications in primates and domestic animals.* Reproduction, Fertility and Development, 2005. **18**(2): p. 1-5.
104. Ricker, J.V., et al., *Equine Sperm Membrane Phase Behavior: The Effects of Lipid-Based Cryoprotectants.* Biology of Reproduction, 2006. **74**(2): p. 359-365.
105. Barcot, O., et al., *Investigation of Spermatozoa and Seminal Plasma by Fourier Transform Infrared Spectroscopy.* Appl. Spectrosc., 2007. **61**(3): p. 309-313.
106. Huser, T., et al., *Raman spectroscopy of DNA packaging in individual human sperm cells distinguishes normal from abnormal cells.* Journal of Biophotonics, 2009. **2**(5): p. 322-332.
107. Meister, K., et al., *Confocal Raman microspectroscopy as an analytical tool to assess the mitochondrial status in human spermatozoa.* Analyst, 2010. **135**(6): p. 1370-1374.
108. Mallidis, C., et al., *In situ visualization of damaged DNA in human sperm by Raman microspectroscopy.* Human Reproduction, 2011. **26**(7): p. 1641-1649.
109. Ashkin, A., *Acceleration and Trapping of Particles by Radiation Pressure.* Physical Review Letters, 1970. **24**(4): p. 156-159.
110. Ashkin, A., et al., *Observation of a single-beam gradient force optical trap for dielectric particles.* Optics Letter, 1986. **11**: p. 288-290.
111. Ashkin, A., *History of optical trapping and manipulation of small-neutral particle, atoms, and molecules.* Selected Topics in Quantum Electronics, IEEE Journal of 2000. **6**(6).
112. Lang, M.J. and S.M. Block, *Resource Letter: LBOT-1: Laser-based optical tweezers.* Americal Journal of Physics, 2003.
113. Nieminen, T.A., et al., *Physics of Optical Tweezers*, in *Methods in Cell Biology*. 2007, Academic Press. p. 207-236.
114. Hossack, W., et al., *High-speed holographic optical tweezers using a ferroelectric liquid crystal microdisplay.* Optics Express, 2003. **11** (17): p. 2053-2059
115. Dholakia, K., et al., *Cellular and Colloidal Separation Using Optical Forces*, in *Methods in Cell Biology*. 2007, Academic Press. p. 467-495.
116. Rodrigo, P.J., et al., *Shack-Hartmann multiple-beam optical tweezers.* Optics Express, 2003. **11**(3): p. 208.
117. Eriksen, R.L., V.R. Daria, and J. Glückstad, *Fully dynamic multiple-beam optical tweezers.* Optics Express 2002. **10**(14): p. 597.
118. MacDonald, M.P., et al., *Trapping and manipulation of low-index particles in a two-dimensional interferometric optical trap* Optics Letters, 2001. **26**(12): p. 863-865
119. Ahlawat, S., R. Dasgupta, and P.K. Gupta, *Optical trapping near a colloidal cluster formed by a weakly focused laser beam.* Journal of Physics D: Applied Physics, 2008. **41**(10): p. 105-7.
120. Theofanidou, E., et al., *Spherical aberration correction for optical tweezers.* Optics Communications, 2004. **236**(1-3): p. 145-150.
121. Escandon, G.J., et al., *Beam magnification and the efficiency of optical trapping with 790-nm AlGaAs laser diodes.* Photonics Technology Letters, IEEE, 1994. **6**(5): p. 597-600.
122. Resnick, A., *Design and construction of a space-borne optical tweezer apparatus.* Review of Scientific Instrument, 2001. **72**(11): p. 4059-4065.
123. Ashkin, A. and J. Dziedzic, *Optical trapping and manipulation of viruses and bacteria.* Science, 1987. **235**(4795): p. 1517-1520.
124. Svoboda, K. and S.M. Block, *Biological applications of optical forces.* . Annual Review of Biophysical and Biomolecular Structures, 1994. **23**: p. 247-285.
125. Jess, P.R.T., et al., *Dual beam fibre trap for Raman micro-spectroscopy of single cells.* Opt. Express, 2006. **14**(12): p. 5779-5791.
126. Block, S.M., *Optical tweezers: a new tool for biophysics* Noninvasive Techniques in Cell Biology, 1990. **9**: p. 375-401.
127. Jess, P.R.T., et al., *Simultaneous Raman micro–spectroscopy of optically trapped and stacked cells.* Journal of Raman Spectroscopy, 2007. **38**(9): p. 1082-1088.
128. Welte, M.A., et al., *Developmental Regulation of Vesicle Transport in Drosophila Embryos: Forces and Kinetics.* Cell, 1998. **92**(4): p. 547-557.
129. Lang, M.J., et al., *An Automated Two-Dimensional Optical Force Clamp for Single Molecule Studies.* Biophysical Journal, 2002. **83**(1): p. 491-501.

130. Berns, M.W., *Laser Scissors and Tweezers.* Scientific American 1998: p. 8.
131. Lang, M., P. Fordyce, and S. Block, *Combined optical trapping and single-molecule fluorescence.* Journal of Biology, 2003. **2**(1): p. 6.
132. Harada, Y., et al., *Single-Molecule Imaging of RNA Polymerase-DNA Interactions in Real Time.* Biophysical Journal, 1999. **76**(2): p. 709-715.
133. Mukerji, I., *Resonance Raman Spectroscopy*, in *eLS*. 2001, John Wiley & Sons, Ltd.
134. Singh, G.P., et al., *Real-Time Detection of Hyperosmotic Stress Response in Optically Trapped Single Yeast Cells Using Raman Microspectroscopy.* 2564 Analytical Chemistry , , 2005. **77**(8): p. 2564 - 2568.
135. Creely, C.M., G.P. Singh, and D. Petrov, *Dual wavelength optical tweezers for confocal Raman spectroscopy.* Optics Communications, 2005. **245**: p. 465-470.
136. Singh, G.P., et al., *The lag phase and G1 phase of a single yeast cell monitored by Raman microspectroscopy.* Journal of Raman Spectroscopy, 2006. **9999**(9999): p. n/a.
137. Creely, C.M., et al., *Raman imaging of floating cells.* Optics Express, 2005. **12**(16): p. 6105.
138. Xie, C., M.A. Dinno, and Y.-q. Li, *Near-infrared Raman spectroscopy of single optically trapped biological cells.* Opt. Lett., 2002. **27**(4): p. 249-251.
139. Ojeda, J.F., et al., *Chromosomal analysis and identification based on optical tweezers and Raman spectroscopy.* Opt. Express, 2006. **14**(12): p. 5385-5393.
140. Tang, W., et al., *Non-destructive analysis of the nuclei of transgenic living cells using laser tweezers and near-infrared raman spectroscopic technique.* Genomics Proteomics Bioinformatics, 2005. **3**(3): p. 169-78.
141. Xie, C., et al., *Real-time Raman spectroscopy of optically trapped living cells and organelles.* Optics Express, 2004. **12**(25): p. 6208-6214
142. Chan, J.W., et al., *Micro-Raman Spectroscopy Detects Individual Neoplastic and Normal Hematopoietic Cells.* Biophysical Journal, 2006. **90**(2): p. 648-656.
143. Moritz, T.J., et al., *Characterisation of FXTAS related isolated intranuclear protein inclusions using laser tweezers Raman spectroscopy.* J of Raman Spectroscopy, 2010. **41**(1): p. 33.
144. Pagba, C.V., S.M. Lane, and S. Wachsmann-Hogiu, *Conformational changes in quadruplex oligonucleotide structures probed by Raman spectroscopy.* Biomed. Opt. Express, 2011. **2**(2): p. 207-217.
145. Calmettes, P.P. and M.W. Berns, *Laser-Induced Multiphoton Processes in Living Cells.* PNAS, 1983. **80**(23): p. 7197-7199.
146. Neuman, K.C., et al., *Characterization of Photodamage to Escherichia coli in Optical Traps.* Biophysical Journal, 1999. **77**(5): p. 2856-2863.
147. Glickman, R.D., et al., *Laser Bioeffects Associated with Ultrafast Lasers: Role of Multiphoton Absorption.* Journal of Laser Applications, 2008. **20**(89): p. 1-9.
148. Glickman, R.D., *Phototoxicity to the Retina: Mechanisms of Damage.* International Journal of Toxicology, 2002. **21**(6): p. 473-490.
149. Konig, K., et al., *Cell damage in near-infrared multimode optical traps as a result of multiphoton absorption.* Optics Letters, 1996. **21**: p. 1090.
150. Konig, K., et al., *Effects of ultraviolet exposure and near infrared laser tweezers on human spermatozoa.* Human Reproduction, 1996. **11**(10): p. 2162-2164.
151. Liang, H., et al., *Wavelength dependence of cell cloning efficiency after optical trapping.* Biophysical journal, 1996. **70**(3): p. 1529-1533.
152. Liu, Y., et al., *Physiological monitoring of optically trapped cells: assessing the effects of confinement by 1064-nm laser tweezers using microfluorometry.* Biophysical Journal, 1996. **71**(4): p. 2158-2167.
153. Konig, K., *Laser tweezers and multiphoton microscopes in life sciences.* Histochemistry and Cell Biology, 2000. **114**(2): p. 79.
154. Liu, Y., et al., *Evidence for localized cell heating induced by infrared optical tweezers.* Biophysical Journal, 1995. **68**: p. 2137-2144.
155. Colon, J., et al., *Controlled micromanipulation of human sperm in three dimensions with an infrared laser optical trap: effect on sperm velocity.* Fertility and Sterility 1992. **57**(3): p. 695.
156. Westphal, L.M., et al., *Exposure of human spermatozoa to the cumulus oophorus results in increased relative force as measured by a 760 nm laser optical trap.* Human Reproduction, 1993. **8**(7): p. 1083-1086.

5

The Experimental Methods

The significant problems we face cannot be solved at the same level of thinking we were at when we created them.

--- Albert Einstein (1879 – 1955)

5.0 *Materials and Measurements*

This chapter includes the description of stallion and human sperm preparations, stallion cell viability tests, laser tweezers Raman spectrometer (LTRS), preliminary and preparatory Raman measurements, procedure for acquiring Raman spectra of stallion and human sperm cells and statistical techniques for analyses of the spectral data. The experimental work was conducted in two phases, with slightly different aims and experimental designs.

5.1 Stallion Sperm Preparation and Measurements

The stallions used for Raman spectroscopy research belonged to the Horse Facility associated with the Department of Animal Science, or the Barnyard associated with the Veterinary Medicine Teaching Hospital, at the University of California Davis (UC Davis). The stallions were fed grass-hay mixture, Omolene 200 (horse feed) and water, and exercised daily, adhering to Institutional Animal Care and Use Committee protocol. Research scientists from Meyers Lab, at the affiliated School of Veterinary Medicine arranged the stallions and semen collection. Semen was collected from a single horse at about 8 am, on the morning of LTRS booking. A fraction of the semen was processed for Raman spectroscopy; sperm preparation and exposure to biochemical stress were completed at ~ 1pm by research associate Megan McCarthy, from Meyers Lab. Her work is summarised in this **Section**.

The preliminary work with stallion sperms involved testing of two sperm extenders. HEPES-Biggers, Whitten and Whittingham (BWW) was a clear sperm medium and INRA 96 was a milky medium. These media have been successful in extending the useful life of stallion sperms for up to 48 hours. INRA 96 medium scattered light, making it difficult to trap sperms, and hence BWW was selected as the sperm media for this research.

5.1.1 Chemicals and Reagents

The following chemicals were used for the experiments. Unless otherwise stated, all other chemicals were purchased from Sigma Chemical Company.

Xanthine (X) -- *Calbiochem (La Jolla, Ca.)*

Xanthine Oxidase (XO) -- *Sigma Chemical Co. (St. Louis, Montana)*

10X Dulbecco's Phosphate Buffered Saline (DPBS) -- *Gibco Catalog #14050-055, 500 mL*

Percoll -- *Sigma Catalog #P1644*

Xanthine -- *Calbiochem – EMD Chemicals, catalog # 6820, 5g*

Xanthine Oxidase -- *Sigma, catalog # X4376-5UN*

LIVE/DEAD Sperm Viability Kit -- *InvitrogenLS7011*

HEPES (FW: 260.3)

Polystyrene beads (NIST traceable) – Polysience Inc.

5.1.2 Stallion Sperm Preparation Protocol

An artificial vagina equipped with a nylon mesh filter was used to separate the sperm rich seminal fluid from the thicker gel and debris. Sperm density was determined using densitometer. The semen was diluted to 50 million cells/mL using (BWW) medium containing 0.1% polyvinylalcohol (PVA). PVA is used to minimise cell flocculation. The filtered semen was maintained at ambient temperature in a portable enclosure and transported without delay to Meyers Lab, where a small portion was separately processed for Raman spectroscopy studies.

The procedures used to extract sperm cells from the seminal plasma are known as **sperm preparation**. Sperm cells are isolated from semen fluid and debris by centrifugation through a discontinuous density gradient buffer. Percoll buffer, consisting of polyvinyl pyrrolidone-coated silica particles of 17 nm size (average), used for this purpose, has been successfully used in the past, to separate biological cells and organelles based on their densities [1, 2].

Stallion sperm preparation: Percoll is diluted in Hepes 20X, an organic medium used in cell culturing, to create 84% and 42% density buffer solutions. 2.5 ml of the fresh semen is layered over 2 ml of 42% Percoll buffer, which is layered over 1 ml

of 84% Percoll buffer in a 15 ml polypropylene centrifuge tube (Corning ®) and centrifuged at 300g for 20 minutes, to separate the high density sperm cells from the fluid and debris in semen. The supernatant is discarded and residual sperm pellet is extracted using a micro-pipette. The pellet is placed in a clean centrifuge tube and resuspended in 5 ml BWW containing 1 mg/ml of PVA and washed (centrifuged) twice at 300g for 5 minutes, to remove residual colloidal suspensions from the percoll wash. The final sperm pellet consists of pure sperm cells.

The prepared sperm pellet was resuspended in 1 ml of BWW containing 1 mg/ml of PVA for this research. Sperm concentration was measured using haemocytometer; BWW/PVA medium was added to the cell suspensions to achieve a final sperm concentration of ~ $25x10^6$ cells /ml. The cell suspensions were transferred, in volumes of 500 µl aliquots, into Eppendorf tubes of 1 ml size, labelled and kept aside for stress exposure and viability tests, prior to transporting them in chilled containers, for Raman spectroscopy studies at CBST (20 to 30 minutes drive).

5.1.3 Oxidative Stress Treatment of Stallion Sperms

Four aliquots of 500 µl samples were used for oxidative stress damage studies. Xanthine (X) and xanthine oxidase (XO) were used to induce oxidative stress in the sperms. Three grades of X-XO used to induce ROS damage to stallion sperms were identified from previous research by Professor Meyers' team. X, measured in molar units, and XO, measured in units of volume percent, were mixed to create *low, medium* and *high* strength ROS; their ratios are summarised in **Table 5.1**. Both O_2^- and H_2O_2, identified as by-products of X-XO, damaged DNA bases and reduced cell motility. Cell viability and acrosome integrity remained unaffected, but exposure to high concentration of X-XO caused lipid peroxidation [3, 4].

The three strengths of ROS solutions were added to three appropriately labelled sperm aliquots. The control aliquot had no ROS added to it. All four tubes were incubated at 37 ºC in an environment containing 5% CO_2 in air. The tubes were removed at the end of 60 minutes and centrifuged at 300g for 5 minutes. The sperm pellets were extracted from each tube and transferred to clean, appropriately labelled tubes, and resuspended in fresh BWW + 1 mg/ml PVA.

(Cntrl) Control (no X-XO) Untreated 0.5 ml aliquot of prepared sperms suspended in BWW/PVA media
(Low) 0.1 mM X and 0.01 Units/ml XO Added to a 0.5 ml aliquot of prepared sperms suspended in BWW/PVA media
(Med) 0.5 mM X and 0.05 Units/ml XO Added to a 0.5 ml aliquot of prepared sperms suspended in BWW/PVA media
(High) 1 mM X and 0.1 Units/ml XO Added to a 0.5 ml aliquot of prepared sperms suspended in BWW/PVA media

Table 5.1 ROS solutions of different strengths created using X-XO in different ratios

5.1.4 Osmotic Stress Treatment of Stallion Sperms

Three aliquots containing the prepared sperm suspensions described in **Section 5.1.2** were used for osmotic stress experiments. The three osmotic stress grades used in the study - isotonic, hypotonic and hypertonic - were identified from previous research at Meyers' Lab [5, 6]. Each stress grade was prepared by diluting 10X DPBS using double distilled water (ddH_2O) in the ratio given in **Table 5.2**. A small volume of the solution was taken from each preparation, to test their osmolality. The final osmolality was adjusted to 100 (hypo), 300 (iso) and 600 (hyper) mOsm/kg using calibration standards on vapour pressure osmometer (model 5100 C; Wescor Inc. Logan, Utah), with an error margin of ± 5 mOsm/kg. The pH level was adjusted to ~7.3. The solutions were then filtered using 0.22 μm pore size and stored at 4 ^{o}C for applying osmotic stress on the sperm cells [7].

Table 5.2 summarises the ratio, pH readings and final osmolality measured on the solutions prepared for creating osmotic stress. Osmolality measurements were

tabulated for **Study One**. The solutions for **Study Two** were prepared using the same procedure, and hence the osmolality measurements were not tabulated.

Desired Osmolality (mOsm)	**10X DPBS (ml)**	**Volume of ddH_2O (ml)**	**pH reading**	**Measured Osmolality (mOsm)**
100	0.320	9.667	7.4	102
300	1.055	9.000	7.4	310
600	2.100	8.000	7.0	601

Table 5.2 The pH and Osm readings of the osmotic stress solutions

Three freshly prepared aliquots of sperms were centrifuged at 300g for 5 minutes, the sperm pellets extracted and re-suspended in the three 0.5 ml of osmotic solutions, maintained at room temperature. At the end of 30 minutes in the osmotic stressors, the three tubes were centrifuged at 300g for 5 minutes, sperm pellets extracted and re-suspended in clean Eppendorf tubes containing 500 µl of BWW media + 1 mg/ml of PVA.

5.1.5 Stallion Sperms Motility Tests

Cell motility was evaluated after every process step using computer assisted sperm assessment (CASA) on HTM-CEROS sperm analyser, version 12.2 g (*Hamilton Thorne Biosciences, Inc*, Beverly, Mass.), as summarised in **Table 5.3**. Four or more fields containing 200 or more cells per field were identified for CASA from the seven stressed stallion sperm aliquots described in **Section 5.1.3 and 5.1.4**. Sperm paths tracked on the monitor included forward, helical, zig-zag and circular or curved paths; some random tracks were also observed. Percent total motility (TM) and percent progressive motility (PM) were extracted for motility evaluation.

5.1.6 Stallion Sperm Membrane Damage using Cold Shock

Cell membrane damage was induced by subjecting sperm cells from a test specimen to repeated cold shock. Stallion cells are prepared as described in **Section 5.1.2**. A tube containing the cell suspensions in BWW + 1 mg/ml PVA is plunged into liquid nitrogen for 20 seconds and then placed in 37 ^{o}C water bath for 30 seconds. This process is repeated until cell viability tests as described in the next section, reveal 100% damaged cells. The cells are then mixed with undamaged (control) cells in BWW + 1 mg/ml PVA in two ratios -50% damaged cells and 90% damaged cells, labelled accordingly and kept aside for Raman spectroscopy and TUNEL assay study. This procedure is applied uniformly to all specimens.

5.1.7 Stallion Sperm Viability Test using Stains and Flow Cytometry

Sperm viability tests were completed, following exposure to oxidative and osmotic stress exposure, and is summarised in **Table 5.3**. About 500 µl of the cell suspensions from each aliquot was extracted for membrane damage tests using the LIVE/DEAD sperm viability assay kit. The kit consists of SYBR-14, a green fluorescent DNA stain, and propidium iodide (PI), a red fluorescent DNA stain. Peak emission wavelength from SYBR 14 stained cells was 516 nm (green) and that from PI stained cells was 617 nm (orange). SYBR-14 can penetrate healthy and damaged membranes to bind to DNA, whereas PI dye can only penetrate damaged membranes, to bind to the DNA. SYBR 14 was diluted to a concentration of 100 nM and PI was diluted to a concentration of 12 µM and added to each of the sample 500 µl aliquots. The stained samples were kept at 36 ^{o}C; the cells were exposed to the combined stains for 10 minutes and then diluted in BWW + 1% PVA to a concentration of 10^6 cells/ml, in preparation for flow cytometry.

Becton Dickenson FACScan™ flow cytometer is an automated system in which fluorescent signals are excited as stained cells flowed past a 15 mW, 488 nm, focused argon laser beam. By adjusting the cell flow rate to about 400 cells per second, spectral overlap can be eliminated/minimised and about 10,000 gated events analyzed per sample. The scattered fluorescent signals from the cells reach several detectors simultaneously. The signals from the SYBR 14 and PI are separated with the aid of two optical band pass filters - 530/30 and 585/42.

Cell Quest, an integrated software package, was used to analyse the scattered signals from the stained sperm cells, and several thousand cells were automatically analysed. The green emitting cells were marked as 'viable' and red-orange emitting cells marked as 'nonviable'. Cells displaying both red and green signals were marked as nonviable. Motility (TM and PM) and viability tests are tabulated in **Table 5.3**.

Chemical Process Steps	**Oxidative Stress**			**Osmotic Stress**		
	TM	**PM**	**Viability**	**TM**	**PM**	**Viability**
Before incubation	**X**	**X**		**X**	**X**	
After incubation	**X**	**X**		**X**	**X**	
After re-suspension	**X**	**X**	**X**	**X**	**X**	**X**

Table 5.3 Process steps at which motility and viability tests were completed following the osmotic and oxidative stress damage exposure

5.2 Human Sperm Resources and Preparation

Ethical usage of human material was reviewed and permission to work with human cells was sought from the UCD Institutional Review Board (IRB) / Ethics Committee, prior to embarking on this section of the research. Sperm donors for IVF treatment are pre-screened for infectious disease and genetic disorders and their cells are frozen prior to use. Processed/prepared human cells were obtained from the following two sites, and hence the chemicals and reagents described are based on information provided by these centers -

(1) Andrology laboratory at the UC Davis Medical Center, Department of Obstetrics and Gynaecology, University of California, Sacramento

(2) California IVF, Davis Fertility Center, Inc., Davis, California

Donor identities were not used in the research, nor were the samples prepared exclusively for this research. Surplus prepared sperms used in IVF treatment were obtained from California IVF, and surplus sperms used for fertility screening were obtained from the Andrology lab. Since only 20 to 40 cells were needed for Raman

study, there were plenty of cells in the left over medium. The donor samples had normal counts and morphology, while the rest of the samples had unknown fertility potential. Human sperm specimens include fresh sperms processed on the day, previously frozen and thawed sperms from donors, and sperms using swim up technique. Some of these cells were exposed to oxidative stress using 1mM and 2 mM peroxide and others were tested for daily variation in sperm quality; these were analysed using Raman spectroscopy.

5.2.1 Human Sperm Preparation Procedure

The human sperm preparation procedures are similar to that of stallion sperm preparation techniques. PureSperm®80 and Puresperm®40 are ready-to-use density gradient buffers of densities 80% and 40% respectively, and used by UC Medical Center for sperm preparation. The buffer consists of silane coated silica, with PureSperm®80 having twice the density of PureSperm®40 with pH range 7.4 – 7.8 and osmolality range 300 mOsm – 310 mOsm. The sperm survival in the buffer, which is free from bacteria and microbe contamination, is rated as 70% after 18 hours.

Equal volumes of PureSperm® 80 (bottom layer) and PureSperm®40 (second layer) are placed in a centrifuge tube and the semen is layered over it and centrifuged at 1800 RPM for 20 minutes. The extracted sperm pellet is resuspended in a clean tube containing sperm medium (Sydney IVF Sperm Medium K-SISM) and centrifuged at 1800 RPM for 10 minutes. The sperm pellet is extracted and resuspended in the final tube with 0.4 - 0.5 ml of sperm medium. Remains of the sperm preparations were kept aside to be picked up for the Raman spectroscopy study.

5.2.2 Sperm Swim-up Procedure

About 0.4 – 0.5 ml of liquefied semen are placed in a conical tube, below a layer of 1 ml sperm medium, using a sterile micro-pipette. Alternately, the sperm medium can be gently layered over the semen placed in the tube. The tube is held in an inclined position and placed in an incubator (maintained at 37 ^{o}C and 5% CO_2) for an hour. Sperms with high PM will swim up into the top medium, while those with low PM or abnormal motility remained in the bottom layer. This technique is useful to extract

morphologically superior sperms, but it is at the cost of sperm concentration, which is significantly reduced in many cases of male factor infertility.

5.3 Laser Tweezers Raman Spectrometer

A bespoke LTRS at CBST has been used exclusively for the study of cells in suspension, using Raman spectroscopy [8, 9]. The schematic of the system is shown in **Figure 5.1.** The laser source consists of a compact diode laser (CrystaLaser), an isolator and a 785 band pass filter. The 1.1 mm size, 785 nm, continuous wave laser beam of 70 mW intensity at the source is expanded (10X) with a telescopic arrangement using optical lenses. The beam is coupled to the base of an Olympus microscope objective (water immersion 60X/1.2 NA) on an inverted Olympus microscope IX-71, using two dichroic mirrors in the turret/base plane of the inverted microscope, for selective beam transmission and reflection. The dichroic mirror at the entrance port of the microscope unit reflects the 785 nm laser towards the base of the objective, as shown in the figure, and transmits the lower frequency backscattered Raman signals to the spectrometer. The backscattered light from the sample is collected by the same objective and consists of both Rayleigh and Raman signals. The second dichroic mirror (a short pass filter (SPF)), reflects the 785 nm signals into the objective, transmits the white light (illuminating the sample), to the webcam and reflects the Raman signals. The Raman signal is launched into the spectrometer - yellow highlighted region of **Figure 5.1**.

The spectrometer consists of a triple grating imaging monochromator spectrograph, with motorised mirrors, entrance and exit slits. A multimode optical fibre couples the transmitted signals to a notch filter (to remove residual Rayleigh signal) and dispersion elements. The dispersed Raman signal at the output slit is aligned to the centre of the CCD, a metal vacuum sealed, back illuminated, deep depletion PIXIS 100 camera from Princeton Instruments. The sensor consists of 1340 x 100 pixel arrays, with each pixel of size 20μm x20 μm. The camera is thermo-electric air-cooled to -80 ^{o}C; the temperature is stabilised at ~ -70 ^{o}C.

A charge coupled device (CCD) is used to capture the Raman signals. Winspec software (Roper series) controls the spectrometer and CCD operations as well as the

spectral calibration and data acquisition. The webcam is controlled by a separate program; the live images are used for sample positioning and tracking. It is used to position the laser beam at the centre of the screen and to adjust the working distance.

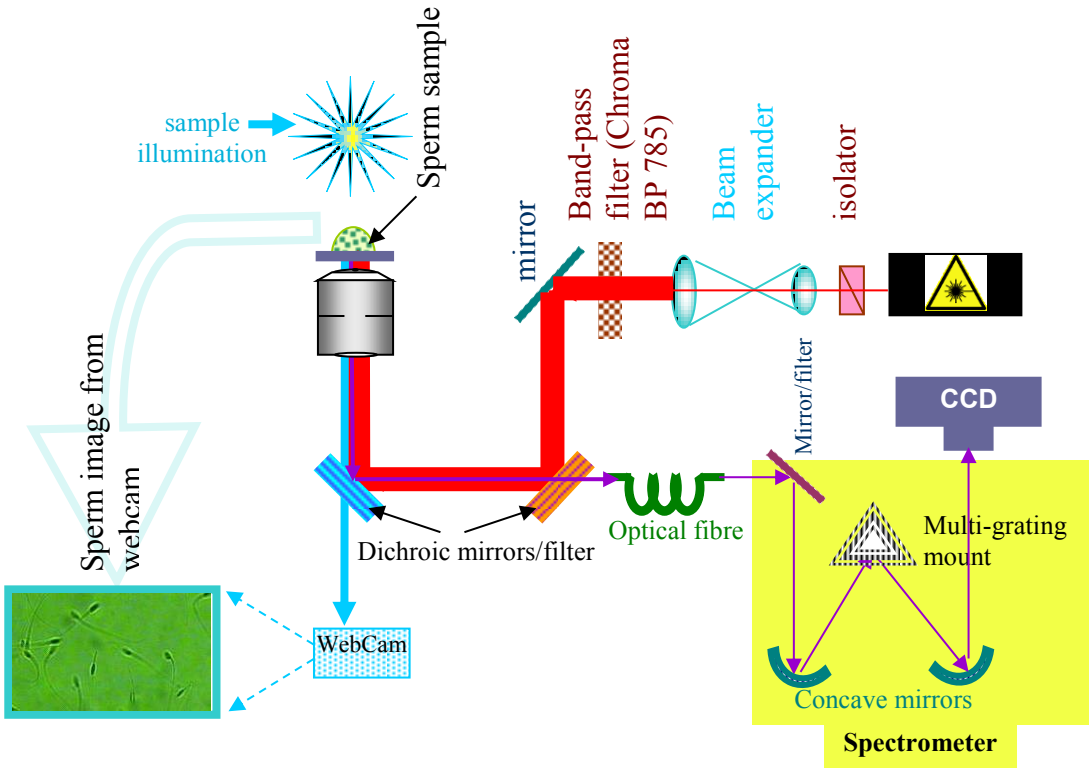

Figure 5.1 The schematics of the Laser Tweezers Raman Spectrometer

5.4 Preparatory Measurements using LTRS

Standard operating procedures for the LTRS equipment, developed at CBST were adopted. Preliminary tests were conducted to evaluate equipment performance, which included investigation of CCD image quality, laser exposure time, signal

accumulation parameters and spectral quality. Data files were automatically saved in .SPC format, and converted to ASCII format at the end of the experiment, using Winspec. The data analysis was completed using custom software and Minitab.

The terminologies used in the experiment are summarised below:

- ***data set***: A collection of 10 to 40 spectra from a single aliquot – examples: 10 to 40 sperm cells from a single stallion/human exposed to a single stress chemical or process environment, a single set of repeatability or reproducibility spectra from polystyrene beads or sperms.
- ***data group***: Data sets from several aliquots made from a single stallion or human semen and exposed to different chemical environments. Example: seven data sets from a stallion sperm collection, exposed to three grades of osmotic stress and four grades of oxidative stress.
- ***channel:*** Each pixel on the CCD detector is an energy channel. Each Raman spectrum consisted of 1340 pixels or channels.

5.4.1 Sample Preparation for Spectroscopy

Quartz coverslip was used for mounting the samples. While calcium fluoride (CaF_2) material produces significantly less background signal, CaF_2 coverslips of suitable dimensions were not easily available for this research. The quartz coverslip was mounted in a cylindrical steel holder from Molecular Probes® and positioned on the sample stage**.** The coverslips were washed in soap, methanol and deionised water and blow dried prior to each use. A drop of about 100 µl of sample suspension was placed on the coverslip so that 10 to 20 beads/sperm cells appeared in the field of view. The laser intensity at the sample plane was ~25mW. The laser was used to trap a bead/cell, the focus plane height adjusted to optimise Raman signal, and left undisturbed for the rest of the study. The overhead lights were switched off during the data acquisition.

Preparatory work included the following:

1. Selection and positioning of an appropriate grating. A 600 lines/mm grating was used, as the acquired spectral range, 200 cm^{-1} - 1900 cm^{-1}, included the

DNA fingerprint region, 600 cm^{-1} to 1800 cm^{-1}, that has been reported in papers. At grating position 1150 rel cm^{-1}, the DNA fingerprint region was approximately centred on the detector.

2. The pixel area for binning was set to 1340 x 10 pixels at the start.
3. Exposure time for samples. Appropriate data acquisition time for polystyrene bead was set at 2 seconds and that for sperms at 20 - 30 seconds (to minimise laser exposure). The sperm signal quality was comparable to that obtained at 60 – 120 seconds.

5.4.2 Wavelength Calibration Procedure

Calibration was done at the start of every study (data group) using NIST traceable polystyrene beads. The beads from Polyscience Inc. used in the first study were 3 μm (catalog id: 64060-15) with bead size ranging from 2.85μm – 3.15 μm; in the second study the beads used were 4 μm (catalog id: 64070-15) and the size ranged from 3.80 μm - 4.20 μm. About 50 μl of the concentrated bead suspension was diluted in 5 ml of deionised water and stored in a labelled tube for calibration usage in this experimental work.

The experimental work was carried out in two independent studies, **Study One** and **Study Two,** approximately six months apart in early winter and mid-summer. The calibration procedures used were slightly different for the studies. **Figure 5.2** is a polystyrene spectrum acquired on the LTRS. The six peaks, their standard wavenumbers and corresponding pixels are marked**.** Six polystyrene peaks in the range 620 cm^{-1} to 1602 cm^{-1} were selected for frequency calibration in **Study One**. Pixel numbers corresponding to each of the six peaks were identified from the acquired spectrum and entered in the calibration table in Winspec menu. Peak values in wavenumbers, obtained from a standard polystyrene spectrum from NIST (Aldrich #18,243-5) [10], were tabulated against the corresponding pixel values. Third order polynomial fit was used for the calibration**.** Second order fit and three peaks, 620 cm^{-1}, 1001.4 cm^{-1} and 1602 cm^{-1}, were used for calibrating the frequency in **Study Two**, as these were considered sufficient.

5.4.3 Repeatability and Reproducibility Study

Repeatability study and reproducibility study of polystyrene beads were used for calculating LTRS spectral resolution limits, intensity fluctuation and equipment stability over time. The calibration spectra were also used for comparing equipment stability over time.

The impact of extended laser trapping was explored on a select few horse and human cells from some processes, using repeatability study. Repeatability spectra from horse and human sperms were also used to evaluate specimen dependent measurement limits.

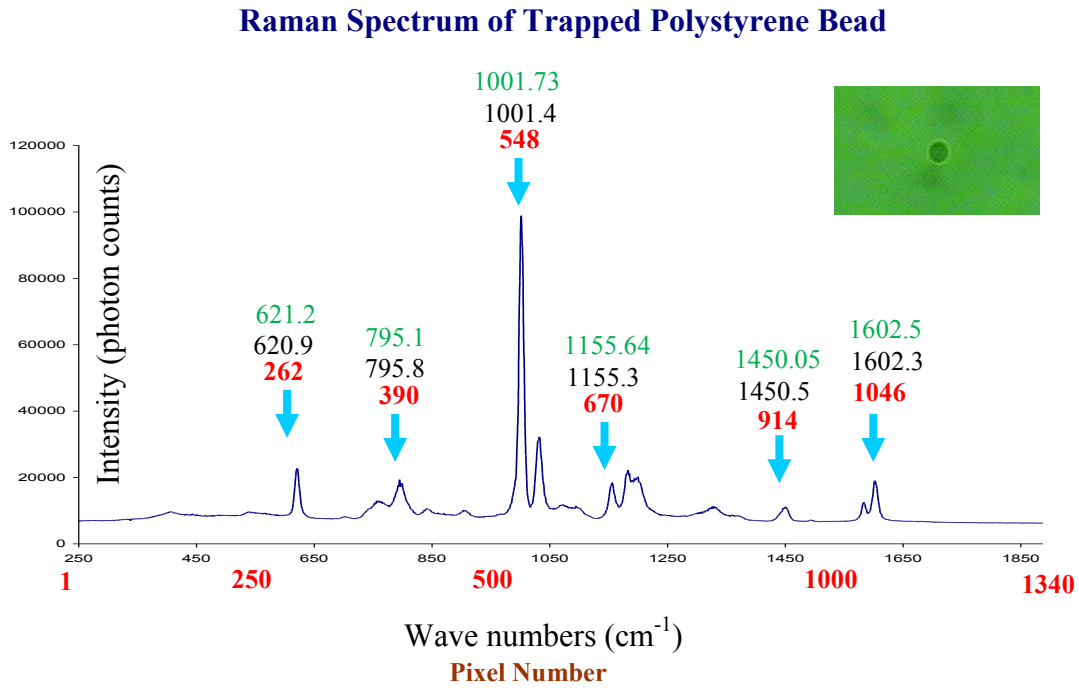

Figure 5.2: A Raman spectrum of a trapped polystyrene bead (image inlay, top right); with pixel values (red) & wavenumbers (black). The six calibration peaks (blue arrows) are shown with standard (Aldrich #18,243-5) wavenumber (black), measured wavenumber (green) and corresponding pixel numbers (red) [10].

5.5 Sperm DNA Damage Assessment using Raman Spectroscopy

Raman spectra of sperm cells were acquired after the calibration was completed. Both motile and immotile cells, sperms with distorted tails, abnormally shaped heads and abnormal motility were discernable in the live webcam image. Each cell was exposed to ~ 25 mW of focused laser beam intensity during data acquisition.

5.5.1 Raman Spectra of Stressed and Membrane damaged Stallion Sperms

Diluted cell suspension droplets (50 µl - 100 µl) were placed on a clean quartz cover slip mounted in the sample plane of the inverted microscope. A specially devised lid was placed over the sample to minimise liquid evaporation. Cells with morphologically normal appearance were selected for repeatability and reproducibility studies. If the trapped cell escaped, or a cosmic ray artefact was observed in the fingerprint region, the spectrum was rejected and a new spectrum was taken. Due to the short data acquisition time, cosmic rays were a rare event.

The experimental work consisted of two independent studies. **Study One** lasted over a month during early winter season and tested for oxidative and osmotic stress damage. The motile or immotile cells were labelled only in a few data sets. Some motility related spectral differences were observed in these data sets and no significant difference between osmotic and oxidative stress damage was observed. **Study Two** was designed to separately analyse immotile and motile cells from each aliquot. Membrane damage study was added to the study and osmotic stress damage study was retained. The number of spectra per data set was doubled; about 20 to 80 spectra were obtained from each aliquot. The study was conducted in summer and lasted a month.

Study One: Stress evaluation (**Section 6.2.1**)

- Three stallions and five collections were used
- Each data set consists of spectra from ~20 cells/process; the spectra from motile/immotile cells were not separately identified in most of the data sets
- Motile and immotile cells were identified in two processed aliquots
- Extended trapping was tested on two specimens

Study Two: Membrane damage evaluation (**Section 6.2.2**)

- Three stallions and four semen collections were used.
- Spectra consisted of ~ 20 motile and 20 immotile cells per data set
- Motile and immotile cells were separately analysed on all processed aliquots
- Extended trapping was tested on 3 specimens

The sperm spectra were acquired for 30 seconds each, using three accumulations of 10 seconds in **Study One** and 20 seconds each, with 4 accumulations of 5 seconds in **Study Two**. The trapping time of cells used in extended trapping study ranged from 10 minutes to 40 minutes; the data set was acquired with 30 seconds interval in **Study One** and 40 seconds interval in **Study Two**. Raman spectra were acquired on 20 or more randomly selected cells from each aliquot, taking a minimum of an hour per aliquot. This required frequent sample change to minimise medium evaporation. Raman spectral acquisition on a data group lasted anywhere between 10 hours to 15 hours average; one study extended over 3 days, with 40 spectra per dataset.

5.5.2 Raman Spectra of Prepared Human Sperm Cells

A data group in the human sperm study consisted of a fresh prepared, frozen or swim-up specimen. The Raman data acquisition procedure for human cells was identical to that of stallion sperm cells, as described in the previous section. Due to the use of only a few simple process conditions, each data group were completed in 2 to 5 hours. A drop of sperm cell suspension was diluted in sperm media, so as to contain 60 to 100 cells in the droplet. Raman spectrum from each randomly trapped cell was acquired for 30 seconds, with 3 accumulations of 10 seconds duration. Extended trapping on motile and immotile specimens was tested using the same procedure as that of stallion sperms.

5.6 Statistical Analyses of Raman Spectra

The application of statistical methods to extract useful information from the Raman spectra of the different samples or processes is becoming a standard procedure using spectral pre-processing, simple statistical methods and advanced multivariate analysis. The basic technique is described in the following sections.

5.6.1 Spectral Pre-processing

Each raw spectrum is plotted with wavenumber on the x-axis and Raman intensity profile on the y-axis. Fluctuations in laser intensity, variation in scattering cross-sections of the environment of each trapped specimen, and molecular differences between cells, contribute to spectral intensity variation between a given channel in each spectrum in a data set. An underlying broad background spectrum is frequently superimposed on all the acquired spectra from the Raman microspectrometer. Channel specific artefacts that are independent of the specimen, are also observed in the spectra. Each raw/acquired spectrum is pre-processed to eliminate most of these observed artefacts and random events, chiefly, cosmic ray spikes. Background subtraction and normalisation is completed to establish a common scale prior to statistical analysis. Some spectra were corrupted by evaporation of the medium or escape of live trapped cell or by cosmic rays. Such spectra were discarded during data acquisition and removed prior to statistical analysis.

5.6.1.1 Background subtraction

Each acquired spectrum in a data set is corrected for the broad background signal; there are several techniques developed for background subtraction. In this research, the background was simulated using Leiber's polynomial algorithm [11] adapted by CBST and designed for background subtraction on the LTRS [9, 12].

5.6.1.2 Normalisation

Normalisation was done using peak intensity, in this research. A stable and well resolved peak is identified and its peak height set to '1'. The intensity profile of all other channels of the spectrum is rescaled and expressed in units of this normalised peak height, to establish a common intensity scale for statistical analyses.

- Polystyrene spectrum is normalised to the height of 1001.4 cm^{-1} peak.
- Sperm spectrum is normalised to the DNA band with peak at 1092 cm^{-1}.

Smoothing the spectrum minimises noise contributions; at the same time, it can modify real peaks or eliminate the peaks in the noise range. Hence smoothing has to be performed carefully. A detailed knowledge of the specimen under study,

equipment contribution to the signal quality and the use of standards for characterisation and cross–correlation with complementary instruments are necessary for identifying peaks, spectral processing, and application of smoothing to prevent introduction of pre-processing artefacts and for comparing spectra from different instruments. A detailed literature review was used to gain insight into the cells under investigation. Smoothing was not used on the spectra prior to statistical analyses in this feasibility study.

5.6.2 Basic Statistical Analyses of Raman Spectra

Average, standard deviation, minimum, maximum, range, variance and difference spectra (in some cases) of each pixel in a data set were studied. Covariance and principal component analysis (PCA) are advanced statistics used to discriminate between samples, and are described in the next sections**.**

5.6.3 Covariance

Covariance is used to compare variance between pairs of variables. Linearity in scatter plots of variance between variable pairs reflects the degree of covariance. The covariance ($\sigma_{\text{cov}}{}^2$) of *n* pairs of variables x and y is defined by

$$\sigma_{\text{cov}}{}^2 = \frac{\left(\sum_{i=1}^{n} (x_i - \bar{x})(y_i - \bar{y}) \right)}{n-1}$$

where $\bar{x}$ and $\bar{y}$ are the averages of the two variables.

A scatter plot of a data set consisting of 2 variables *x* and *y* can be represented in a Cartesian plane. A data set with three variables, *x, y* and *z* has three pairs of covariance - *xy, xz* and *yz* that can be represented in a Cartesian space. When the number of variables in the data set exceed 3, the ability to identify and visualise the covariance in the scatterplot becomes complex. The covariance between variable pairs increases rapidly with the number of variables. In general, the number of covariance in a data set with *n* variables is,

$$\frac{n!}{(n-2)!2!}$$

The number of variables n (energy channels), in Raman spectroscopy, range from a few 100s to a few 1000s, resulting in millions of covariance data for analysis. Practically, examining several hundreds of covariance scatterplots to identify hidden or submerged patterns in the data set is not straightforward, and principal component analysis (PCA) is used.

5.6.4 Principal Component Analysis (PCA)

PCA is a multivariate statistical technique used to reveal hidden relationship between a pair of variables from large complex data sets, in a short time, by using a different pair of orthogonal axes along which the variability pattern is maximised. PCA is used to reduce large data sets with many correlated variables to smaller data sets with a few significant but uncorrelated variables – principal components that magnify majority of the variance between the variables. This feature of PCA has made it a popular tool in rapid extraction of information [13, 14].

A scatter plot is used to identify relationships between two variables in a data set. If the relationship is not evident, a different pair of axes, rotated with respect to the original axes is selected, along which the small differences are magnified. As an example, the scatter plot of a function between *2* variables x_1 and x_2 is shown in **Figure 5.3**. The covariance between the variables is maximised along a coordinate axis known as the first principle component (PC), or PC1. PC1 coincides with the least squares fit line of the scatter plot, and is rotated with respect to the original axis. PC2, the second PC, is an orthogonal coordinate to PC1, along which the next highest separation or variance in the scatterplot is observed.

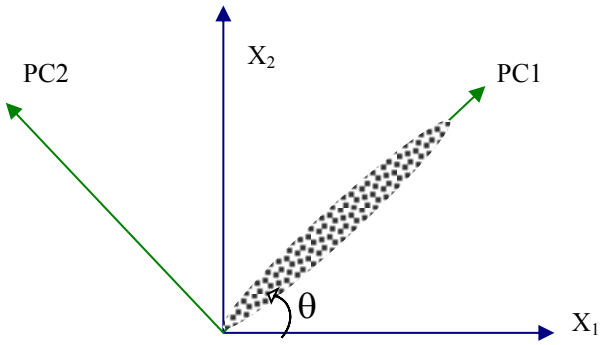

Figure 5.3: Schematic scatter plot of highly correlated variables, x_1 and x_2. Variability is maximised along the rotated axis or first PC1 (green coordinate).

The process in **Figure 5.3** can be repeated for n variables, $x_1, x_2, x_3 \ldots x_n$. PC3, orthogonal to PC1 and PC2 has the 3rd highest variance; and so on. The linear relationship between the PCs and the variables $x_1, x_2, x_3 \ldots x_n$ is expressed using least squares fit and linear algebra,

$$\begin{aligned} \text{PC1} &= \alpha_{11}\mathbf{x_1} + \alpha_{12}\mathbf{x_2} + \alpha_{13}\mathbf{x_3} + \ldots + \alpha_{1n}\mathbf{x_n} \\ \text{PC2} &= \alpha_{21}\mathbf{x_1} + \alpha_{22}\mathbf{x_2} + \alpha_{23}\mathbf{x_3} + \ldots + \alpha_{2n}\mathbf{x_n} \\ &\ldots \\ \text{PCm} &= \alpha_{m1}\mathbf{x_1} + \alpha_{m2}\mathbf{x_2} + \alpha_{m3}\mathbf{x_3} + \ldots + \alpha_{mn}\mathbf{x_n} \end{aligned} \tag{5.1}$$

This relationship can be expressed in matrix form as,

$$\mathbf{P = AX} \tag{5.2}$$

where **P** is a 1-d column matrix with m elements, **A** is an m x n matrix and **X** is 1-d column matrix with n elements; the solution to the linear equations can be used to find the PCs. The first few linear equations contain most of the significant information. Singular value decomposition can be used to solve for the coefficients of matrix **A**, where two orthogonal square matrices M of mxm elements, and N of nxn elements, are identified such that the matrix A is transformed from its original

vector space to a rotated vector space **F**, with

$$\mathbf{A = MFN}$$

The matrix **F** with *m*x*n* elements, has non-zero, positive diagonal elements arranged in descending order of magnitude; and each value is proportional to the least squares fit (variance)^2.

Another approach is to use covariance data set. Covariance matrix of the *n* variables is represented by an *n*x*n* matrix **C**,

$$\mathbf{C} = \begin{pmatrix} C_1 \\ C_2 \\ \dots \\ C_n \end{pmatrix} = \begin{pmatrix} \mathrm{cov}(x_1, x_1) & \mathrm{cov}(x_1, x_2) & \dots & \mathrm{cov}(x_1, x_n) \\ \mathrm{cov}(x_2, x_1) & \mathrm{cov}(x_2, x_2) & \dots & \mathrm{cov}(x_2, x_n) \\ \dots & \dots & \dots & \dots \\ \mathrm{cov}(x_n, x_1) & \mathrm{cov}(x_n, x_2) & \dots & \mathrm{cov}(x_n, x_n) \end{pmatrix} \tag{5.3}$$

Since $\mathbf{C}$ is a symmetric matrix, the values are represented by the non-diagonal $\frac{n(n-1)}{2}$ covariance elements in the matrix. Using eigenvalue decomposition to identify the principal components of C,

$$\mathbf{C\beta} = \gamma\boldsymbol{\beta} \tag{5.4}$$

is a symmetric real matrix equation, where $\boldsymbol{\beta}$ is a non-zero eigenvector, and γ is a positive, real value, known as its eigenvalue.

$\mathbf{B} = (\boldsymbol{\beta}_1, \boldsymbol{\beta}_2, \boldsymbol{\beta}_3, \dots \boldsymbol{\beta}_n,)$ is a matrix consisting of *n* orthonormal eigenvectors that diagonalise the covariance matrix $\mathbf{C}$, using the matrix equation

$$\mathbf{B'\,C\,B} = \boldsymbol{\gamma} \tag{5.5}$$

The elements of the matrix $\boldsymbol{\gamma}$ are eigenvalues $\gamma_1, \gamma_2, \gamma_3, \dots \gamma_n$ of $\mathbf{C}$ with $\gamma_1 \geq \gamma_2 \geq \gamma_3 \geq \dots \geq \gamma_n$ that can be determined, and represent the PCs. The information contained in the first few PCs, derived from the linear equations (**Equation 5.1)** or from eigenvalues of covariance data (**Equation 5.5)** is sufficient

to differentiate between samples, in a well designed and sampled data set. PCA can maximise the information contained in a few significant coefficient of variables and eliminate redundant/dependent variables to reveal underlying patterns.

Noise level, sampling size and quality, statistical design and artefacts of background subtraction/normalisation could also negatively impact PCA results. If sample to sample variation is greater than the spectral differences between classes, PCA could eliminate the differences, leading to erroneous conclusions. PCA is used in this research to differentiate between spectra created by different process conditions.

5.6.5 Application of PCA in Raman Spectroscopy

The complexity of PCA increases with the numbers of variables in Raman spectra, the heterogeneity of the material and molecular composition. A Raman spectrum can have energy channels in excess of 1000 wavenumbers. A data set consisting of 100 variables has 4950 covariance; hence PCA of Raman spectra requires the use of reduced PCA matrices and computer codes, to separate different process conditions, materials in a mixture or chemical compositions.

A data set consisting of *m* independent spectra and *n* energy channels (wavenumbers) in real space is represented by an *m*x*n* matrix **R**. **R** is expressed as a product of two simplified matrices in a transformed vector space known as PCs; this is represented by **Equation 5.6.** Any submerged pattern or structure in the original matrix can emerge in the simplified component matrices in the transformed vector space.

$$\mathbf{R}(mxn) = \mathbf{S}(m)\ \mathbf{L}^{T}(n) \qquad \text{or} \qquad \mathbf{S} = \mathbf{R}.\mathbf{L} \tag{5.6}$$

where

$$\mathbf{S} = \begin{bmatrix} s_1 \\ s_2 \\ s_3 \\ \dots \\ s_m \end{bmatrix} \qquad \text{and} \qquad \mathbf{L} = \begin{bmatrix} l_1 \\ l_2 \\ l_3 \\ \dots \\ l_n \end{bmatrix}$$

with **L** orthonormal to $\mathbf{L}^{\mathbf{T}}$.

S in (**Equation 5.6)** is an orthogonal column matrix, with each element known as

Score of a spectrum. The score of the m^{th} spectrum is

$$s_m = \sum_i \mathbf{r}_{mi} \bullet \mathbf{L} \qquad (5.7)$$

The column matrix **L** is known as loading spectra or coefficients and represents the most significant variations in the variables/wavenumbers. Loading is used to separate chemical mixtures or identify dissolved chemicals in solutions. Scores are used for separation of spectra and reveal variations in a data set and differences in spectral pattern between data groups. The *m* elements are the same (within error limits), if the *m* rows correspond to spectra from the same sample. A score plot is a map of each spectrum in the PC plane, with the highest variation plotted in PC1 - PC2 plane.

5.6.6 PCA of Raman Spectra of Sperm Cells

Minitab 16 was used for PCA of the Raman spectra. A raw spectrum consisted of 1340 wavenumber channels, out of which 500 - 800 channels carried information on DNA molecular vibrations. Data pre-processing and reduction were completed using Matlab, Excel and Minitab 16. The spectral range used for PCA were ~ 600 cm^{-1} to 1700 cm^{-1}, permitting ~ 900 variables (~ half a million covariance elements) in the full matrix. Due to the high variability within each data set, F-value statistics was used to identify the PCs that captured variations between processes. F-value compares the contribution from the variability between data sets to the variability within the data set, in each PC with high F-values indicating a higher likelihood of contribution from the processes. The first few PCs in the vertical section of the Scree plot account for the most variations in the spectra but do not have to account for the most variation from the processes. The high F-values were analysed for process related variations. The two PCs that maximised the dataset separation by processes are used in the results; both PC scores and the wavenumber loadings of coefficients are used in the analyses. Score and loading of coefficients were investigated on

- Data sets from stallion sperms exposed to stress and membrane damage
- Data groups to compare different preparations of human samples.
- Data sets to compare motility, individual specimen and processes

5.7 Chapter Summary

The experimental technique used in the research was summarised. This included the chemical preparations of stallion and human sperms and the measurement techniques. The spectroscopy equipment, characterisation and calibration were also described in detail. The basic statistical methods were described, with a detailed section on the theory of PCA, which has become an important tool in data reduction, qualitative pattern recognition and quantitative regression analyses. The application of PCA has been confined to simple qualitative analyses of the Raman spectra of samples investigated.

Reference

1. Pertoft, H., et al., *Density gradients prepared from colloidal silica particles coated by polyvinylpyrrolidone (Percoll).* Analytical Biochemistry, 1978. **88**(1): p. 271-282.
2. Dunkley, P.R., P.E. Jarvie, and P.J. Robinson, *A rapid Percoll gradient procedure for preparation of synaptosomes.* Nature Protocols, 2008. **3**(11): p. 1718-1728.
3. Baumber, J., et al., *Reactive Oxygen Species and Cryopreservation Promote DNA Fragmentation in Equine Spermatozoa.* J Androl, 2003. **24**(4): p. 621-628.
4. Baumber, J., et al., *The effect of reactive oxygen species on equine sperm motility, viability, acrosomal integrity, mitochondrial membrane potential, and membrane lipid peroxidation.* J Androl, 2000. **21**(6): p. 895-902.
5. Pommer, A.C., J. Rutllant, and S.A. Meyers, *The role of osmotic resistance on equine spermatozoal function.* Theriogenology, 2002. **58**(7): p. 1373-1384.
6. Rutllant, J., A.C. Pommer, and S.A. Meyers, *Osmotic Tolerance Limits and Properties of Rhesus Monkey (Macaca mulatta) Spermatozoa.* J Androl, 2003. **24**(4): p. 534-541.
7. McCarthy, M.J., et al., *Osmotic Stress Induces Oxidative Cell Damage to Rhesus Macaque Spermatozoa.* Biology of Reproduction, 2010. **82**(3): p. 644-651.
8. Moritz, T.J., et al., *Evaluation of Escherichia coli Cell Response to Antibiotic Treatment by Use of Raman Spectroscopy with Laser Tweezers.* Journal of Clinical Microbiology, 2010. **48**(11): p. 4287-4290.
9. Chan, J.W., D.S. Taylor, and D.L. Thompson, *The effect of cell fixation on the discrimination of normal and leukemia cells with laser tweezers Raman spectroscopy.* Biopolymers, 2009. **91**(2): p. 132-139.
10. National Institute of Nanotechnology, *Standard spectra of the following materials polystyrene (Aldrich #18,243-5)* in *Raman Shift Frequency Standards* 2012, McCreery Research Group: University of Alberta.
11. Lieber, C.A. and A. Mahadevan-Jansen, *Automated Method for Subtraction of Fluorescence from Biological Raman Spectra.* Appl. Spectrosc., 2003. **57**(11): p. 1363-1367.
12. Moritz, T.J., et al., *Characterisation of FXTAS related isolated intranuclear protein inclusions using laser tweezers Raman spectroscopy.* J of Raman Spectroscopy, 2010. **41**(1): p. 33.
13. Jolliffe, I.T., *Principle Component Analysis, Second Edition*. Second ed. Springer Series in Statistics, ed. P. Bickel, et al. 2002: Springer. 487.
14. Ferraro, J.R., K. Nakamoto, and C.W. Brown, *Introductory Raman Spectrosopy*. Second Edition ed. Vol. 1. 2003: Academic Press. 434.

6

The Experimental Results

You road I enter upon and look around,
I believe you are not all that is here,
I believe that much unseen is also here.

Walt Whitman (1819–1892)

6.0 *Analyses of Data*

The data analysis is arranged into three main sections,

6.1 LTRS calibration and measurement parameters using polystyrene beads,

6.2 Statistical analyses of Raman spectra of stallion sperms exposed to oxidative and osmotic stress damage (Study One) and membrane damage (Study Two),

6.3 Statistical analyses of Raman spectra of fresh human sperms, cryopreserved sperms and residual cells from swim-up technique.

6.1 Characterisation of the Laser Tweezers Raman Spectrometer

The LTRS was calibrated using polystyrene beads (described in **Chapter 5)**. A raw spectrum and the persistent low frequency background signal (magnified view in inlay), superimposed on all the spectra are shown in **Figure 6.1**. The baseline corrected and normalised spectrum is shown in **Figure 6.2**.

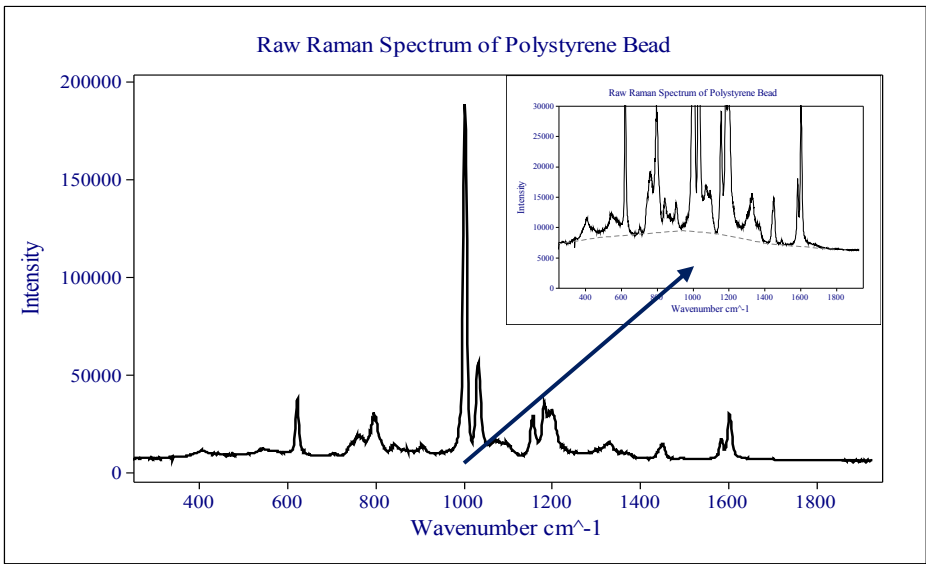

Figure 6.1: A Raman spectrum of polystyrene bead superimposed on a low background signal, highlighted in the embedded image.

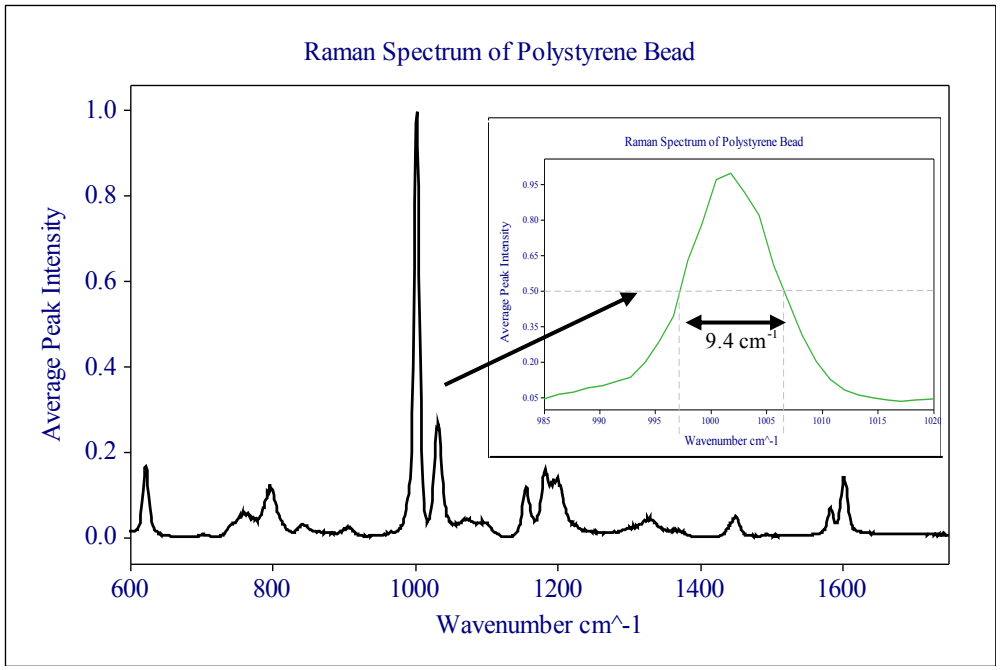

Figure 6.2: Baseline corrected and normalised polystyrene spectrum (averaged over 21 repeatability spectra) with a magnified view of the 1001.4 cm^{-1} peak.

6.1.1 The LTRS Measurement Limits

Polystyrene spectra were used to obtain the measurement limits of the LTRS. Spectral resolution (PR) in wavenumbers per pixel (wn/px) was measured using 3µm beads and 3rd order polynomial fit in **Study One** and with 4 µm beads and 2nd order polynomial fit in **Study Two**; the results are summarised in **Table 6.1.**

Spectral resolution analysis	**3rd order fit**	**2nd order fit**
Median spectral resolution (wn/px)	1.25	1.25
Standard deviation of PR	0.119	0.121
Range of PR (wn/px)	1.06 - 1.48	1.07-1.49

Table 6.1: Spectral resolution from two calibration conditions

The measured peak width and height fluctuations are summarised in **Table 6.2.** **P1-1** and **P1-2** are spectra from **Study One** and **P2** is from **Study Two**. The range of normalised peak intensity fluctuations were obtained from the fluctuations of the sharp peaks at 620.3 cm^{-1}, 795.1 cm^{-1}, 1032.2 cm^{-1}, 1182.1 cm^{-1} and 1603.3 cm^{-1}. The range for each peak from a data set was calculated as the difference between the maximum and minimum of that peak; the standard deviation of all the peaks were used to estimate the error limits in the intensity. The maximum variance of the intensity fluctuations is also used to estimate the error limits in variance.

Measurement limits of peak width and height from repeatability and reproducibility study of polystyrene beads			
Description	**P1-1**	**P2-1**	**P2**
Number of spectrum	21	40	20
Average FWHM of 1001.4 cm^{-1} peak	9.4 cm^{-1}	9.2 cm^{-1}	9.3 cm^{-1}
Range of 1001.4 cm^{-1} peak width	9.3 to 9.5 (cm^{-1}) (0.2 cm^{-1})	9.0 to 9.3 (cm^{-1}) (0.3 cm^{-1})	9.1 to 9.5 (cm^{-1}) (0.4 cm^{-1})
Range of peak intensity	0.004 – 0.007 (0.004)	0.003 - 0.011 (0.008)	0.003 - 0.013 (0.010)
Standard deviation of peak intensities	0.001	0.002	0.002
Variance of peak intensities (max var)	0.000017	0.000097	0.00014

Table 6.2: Measurement parameters from repeatability and a reproducibility study of polystyrene beads.

The 1001.4 cm^{-1} peak of select spectra **P1** and **P2**, from the repeatability studies taken six months apart are shown in **Figure 6.3.** Every 5^{th} spectra of **P1** (in black) and every 10^{th} spectra of **P2** (in red) are overlaid for comparison. Fluctuations in peak width (δw) of 0.2 cm^{-1} and peak intensity (δI) of 0.002 iu are within the measurement limits.

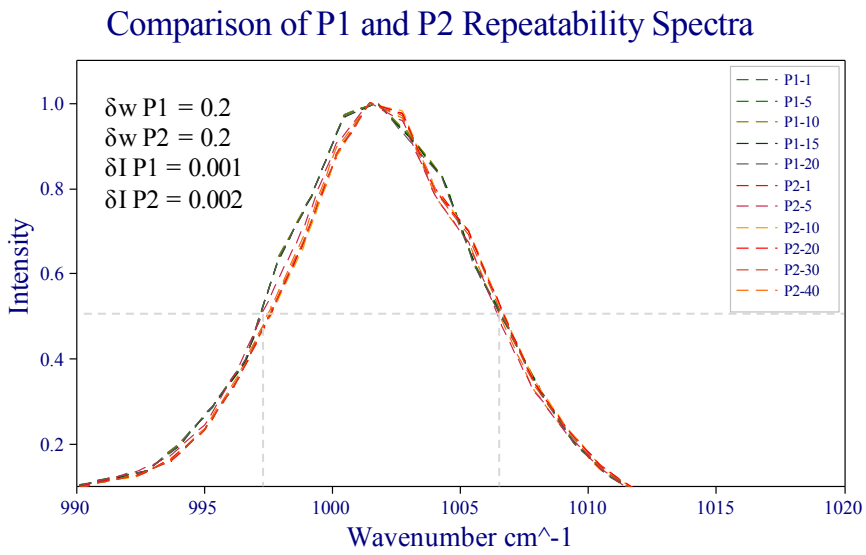

Figure 6.3: Peak 1001.4 cm^{-1} overlay from two repeatability spectra of polystyrene beads (colour coded green and red) using two bead sizes of 3 μm and 4 μm. Fluctuations in peak width, δw, and peak intensity, δI, are shown on top left.

6.2 Raman Spectroscopy of Stressed Stallion Sperms

Raman spectra of oxidative and osmotic stress damage to stallion sperm cells are analysed in **Section 6.2.1.** The spectra of membrane damaged and osmotic stress damaged cells are analysed in **Section 6.2.2.** Analytical details of a data group each, from **Study One** and **Study Two** are presented in **Section 6.2.1.1** and **Section 6.2.2.1,** respectively. The rest of the data groups are analysed using the same procedure; only relevant statistical analysis and graphs are shown. Repeatability spectra of five random sets of data taken on stallion sperms are reviewed in **Section 6.2.3** and summary of analyses of sperm DNA damage is discussed in **Section 6.2.4**.

Raman spectra of sperm cells were acquired in the wavenumber range ~ 200 cm^{-1} to 1900 cm^{-1}. The raw/unprocessed spectra consist of all the spectra collected, including corrupt spectra that were not discarded when the datasets were saved. Statistical analyses of the data sets were completed on the wavenumber range, 630 cm^{-1} to 1630 cm^{-1}. Motile and immotile cells were marked separately on some data sets during data acquisition. A raw Raman spectrum of a live stallion sperm with a low resolution webcam image of the cells in suspension, and a normalised spectrum with DNA markers are shown in **Figures 6.4 (top) and 6.4 (bottom)** respectively**.**

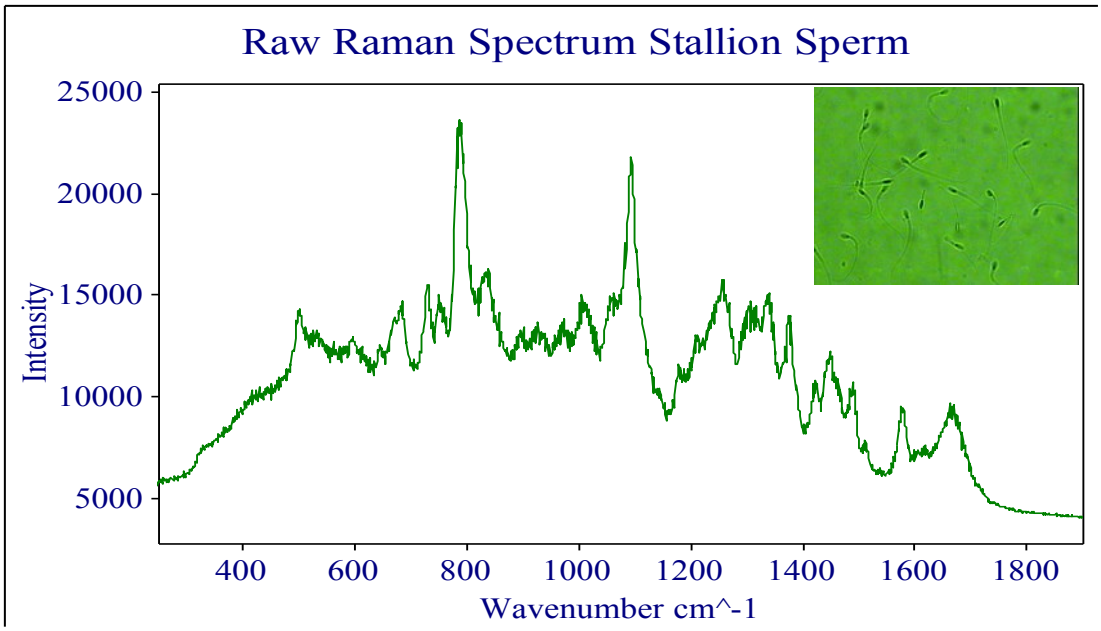

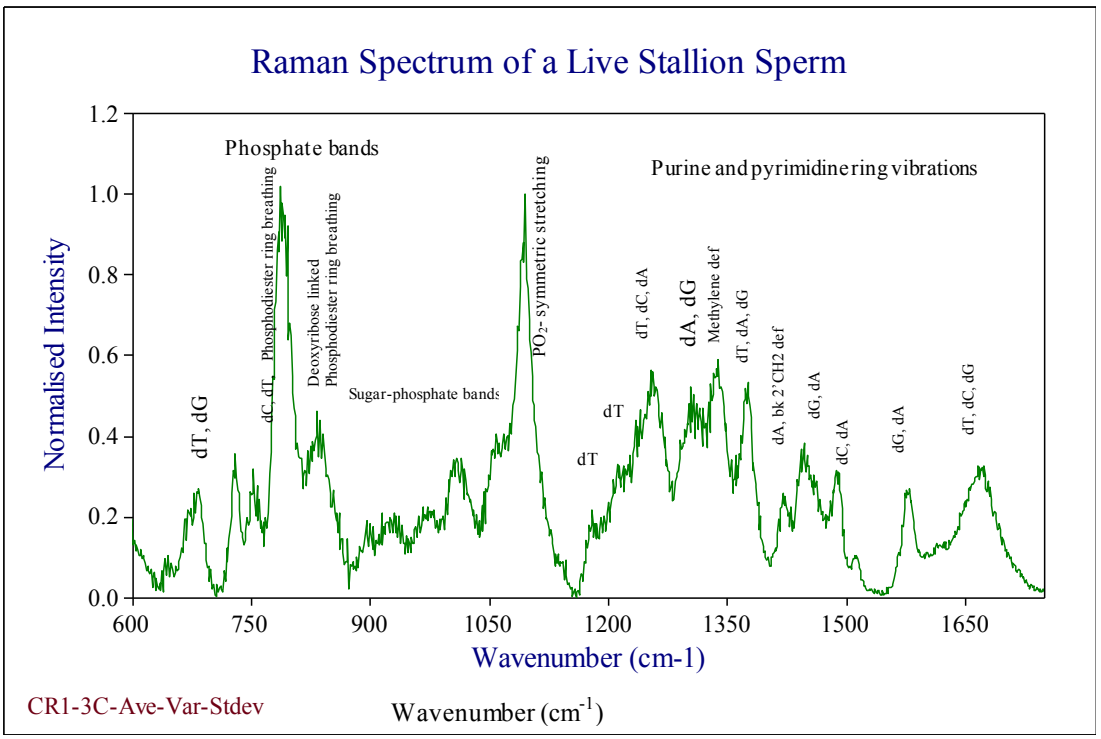

Figure 6.4 **(top)** A Raman spectrum of a live stallion sperm cell before background subtraction. A low magnification webcam image of highly diluted stallion sperm cells in suspension is shown at the top right corner of the figure. **(bottom)** Raman spectrum (baseline corrected and normalised to the PO^-_2 symmetric stretching peak of a motile stallion sperm cell, with some well-known DNA bands and some protein peaks shown (Ref: Chapter 4, Section 4.4.3). **Abbreviations:** def: deformation, bk: backbone

6.2.1 Study One: Osmotic and Oxidative Stress Damage in Stallion Sperms

Five semen collections (DN, HD1, CR1-1, CR1-2, and CR1-3) taken in early winter from three stallions, DN, HD and CR were used in this study. Three of the collections were taken from CR (CR1-1, CR1-2, and CR1-3) and were used to compare semen variations within a stallion. The five data groups exposed to the seven process conditions - three grades of osmotic stress and four grades of oxidative stress, are tabulated (**Table 6.3)**. The motile and immotile cells were identified only in a few cases in this study, as shown in the table. Some of the data were blinded and hence the given identification and actual identifications are different.

Table of Osmotic and Oxidative Stress Data Groups and Data Sets

Stallion (Data groups)	Data Sets (process conditions)												Cells/spectra per data group	Comments
	Osmotic Stress						Oxidative Stress							
	100 (hypo)		300 (iso)		600 (hyper)		XL (low)	XM (medium)	XH (high)	XC (control)	Extra	Repeatability (rpt)		
	Motile cells	Immotile cells	Motile cells	Immotile cells	Motile cells	Immotile cells	No of cells	No of cells	No of cells	No of cells	No of cells	No of spectra		Study One Total cells = 786 Total spectra = 844
DN	20		20		20		20	19	20	22	x	40	142/181	Rpt on 300 motile
HD1	20		20		9	11	20	19	19	20	x	x	138	
CR1-1	15	15	x	20	x	20	20d	x	20	20/20	20	x	150	Extra - BN from XC. XL-immotile only
CR1-2	23		22		22		21	22	22	22,21	20,20	x	215	20,21=XC,XC-aft + Extra: 20, 20 dd/lv sets
CR1-3	20		20		20		20	20	20	20	x	20 XC	141/160	Extra - rpt on XC motile cell

Table 6.3: Seven data sets of stress damage study on five sperm collections (data groups) from three stallions. Cells that have letters at the end of the cell numbers: 'd' or 'dd' for immotile, 'lv' for motile, 'BN' for bend neck, 'aft' for after.

The statistical techniques used to study the five data groups are illustrated next, using data group CR1-3. The basic statistical analysis is summarised in **sub-section 6.2.1.1** and the details of PCA are in **sub-section 6.2.1.2.** The procedures are applied to the remaining data groups; the summary of findings of the three CR data groups is summarised in **sub-section 6.2.1.3**. The results from all five data groups are summarised in **sub-section 6.2.1.4.**

6.2.1.1 Details Statistical Analyses of Data Group CR1-3

Data group, **CR1-3**, consists of eight data sets and 160 spectra (**Table 6.3**). Raman spectra were acquired between 2 and 24 hours after sample preparation. No corrupt spectrum was found in CR1-3 data group. Extended trapping was investigated using a 'control' cell from the 'oxidative stress' sub-group. Basic analysis of each data set is shown in panels of four graphs each (**Appendix**: **Figures 6.5a - 6.5h**)

(top left) the raw, unprocessed spectra,

(top right) baseline subtracted and normalised spectra,

(bottom left) average spectrum and variance

(bottom right) the average spectrum with error (standard deviation).

The complete acquisition range from ~ 250 cm^{-1} to 1930 cm^{-1} is shown in the raw/unprocessed spectra in the panel; the spectral range used to display the raw spectra is 200 cm^{-1} to 2000 cm^{-1}. The spectral range used to display the other three plots in the panel is 600 cm^{-1} to 1750 cm^{-1}.

The average spectrum from each dataset is overlaid in **Figure 6.5i** and the variance within each data set is displayed in **Figure 6.5j**.

Note: Three out of the five data groups had blind study done on one or more data sets. The information was not available at the time of data processing and hence the legends and titles in the spectra and the legends in the PCA plots show the blinded process identification and not the real identification. The labels used to describe the PC plots of the data groups were added in to describe the real process. **Table 6.4** summarises the real and blind process identification and the descriptive labels and abbreviations used to explain the plots. The term 'aniso' or 'anisotonic' is used to describe the combined '100' (hypotonic) and '600' (hypertonic) data sets.

Real data set	**Legend/Blind data set**	**Label**	**Comments**
CR1-1 100	CR1-1 300	100	Iso/300 and hypo/100 exchanged
CR1-1 300	CR1-1 100	300	
CR1-2 XC	CR1-2 XH	Control	High and Control exchanged
CR1-2 XH	CR1-2 XC	High	
HD1-300	HD1-600	Iso/isotonic/300	Hyper and iso exchanged
HD1-600	HD1-300	Hyper/hypertonic/600	

Table 6.4: Legends, based on the blind study and the actual processes and labels

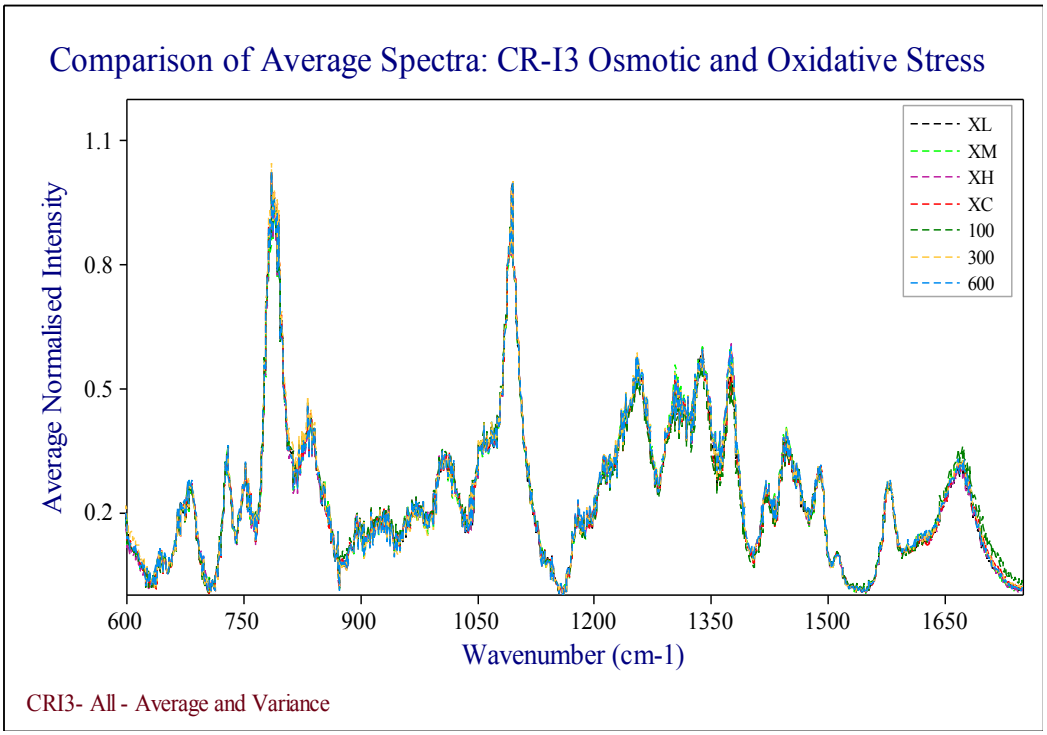

Figure 6.5i: Comparison of average spectra of CR1-3 data group.

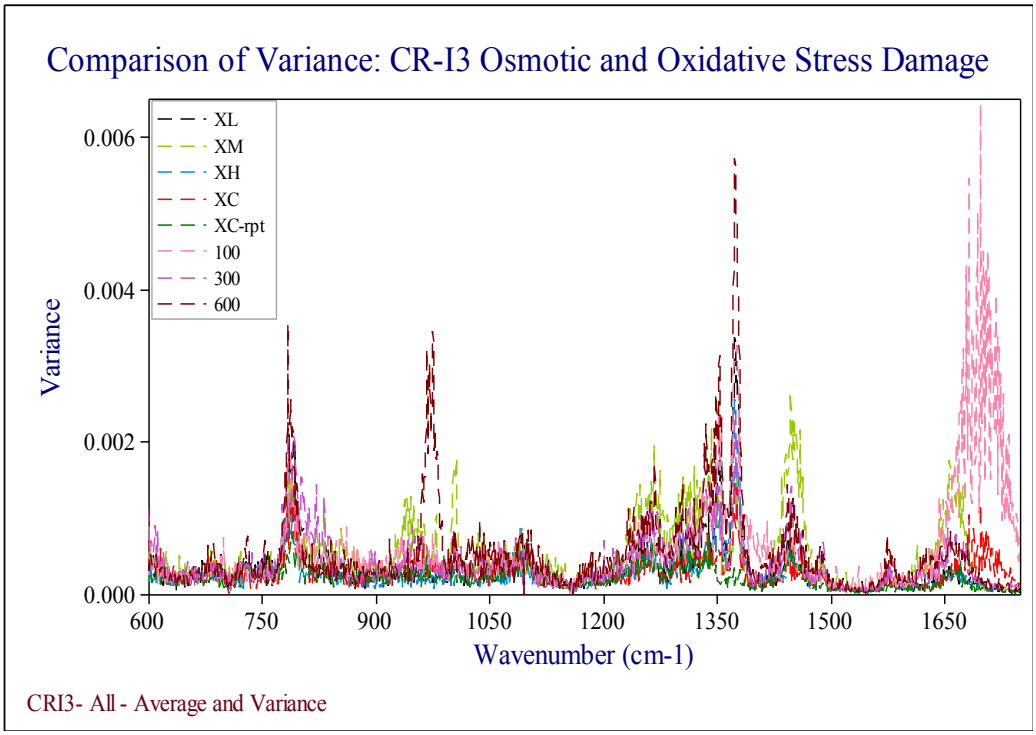

Figure 6.5j: Comparison of Variance in the spectra due to process conditions.

6.2.1.2. Principal Component Analysis of the Data Group CR1-3

PCA analysis was carried out in detail on the 160 spectra from the data group; the results are shown in the next set of figures. Eigenvalue scree and cumulative proportion of the first 50 PCs is shown in **Figure 6.5k**. The first PC accounts for 30% of the spectral variations and the first eight PCs account for 65% of the spectral variations.

After the first 8 values, the PCs showed very little variation (< 0.005). After the first 28 values, the variation in the PCs changed slowly with magnitudes ~ 0.001. The first nine PC scores plotted (as mean and standard deviation) in **Figure 6.5l** show high overlap between the PC scores of the different processes. F-value statistics are used to identify data sets that show process related variation with high F-values indicating strong process contribution to the PC scores. PC scores are plotted as a function of F-values in **Figure 6.5m**. PC coefficients corresponding to the first six PC scores with high F-values are plotted in **Figure 6.5n** as a function of wavenumber. The solid coloured legends indicate the mean value of the PC scores and the grey outlines show the distribution of the PC scores from the same processes. The vertical error bars shown in the figure are scaled 8:1, to enhance the error details.

Scatter plots of the six PC scores for oxidative stress are shown in a matrix format in **Figure 6.5o**. The scatter plot of the PC score pairs that show maximum process related difference is plotted in **Figure 6.5p**. A similar matrix for osmotic stress is shown in **Figure 6.5q** and the scatter plot showing the most process related separation is shown in **Figure 6.5r**. The PC coefficients that contributed to the maximum separation between the processes in oxidative and osmotic stress are plotted in **Figure 6.5s**. The spectral bands responsible for the process related spectral difference is identified from this overlay plot.

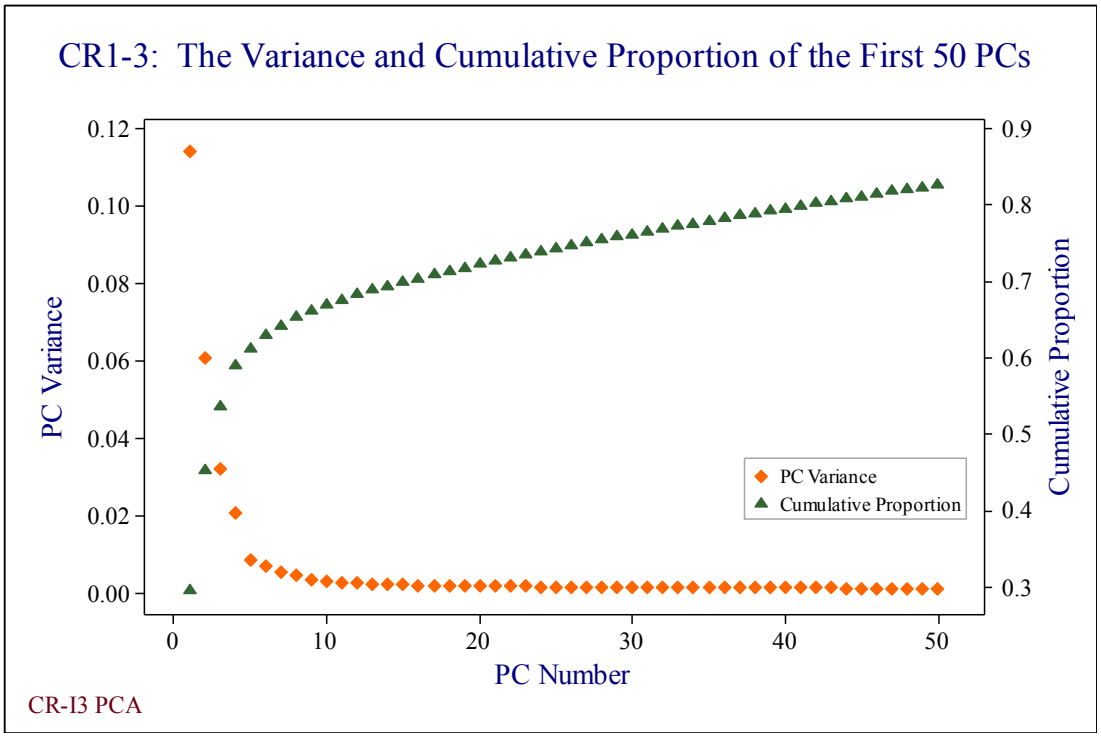

Figure 6.5k: Scree plot of the first 50 Eigenvalues and their cumulative proportion.

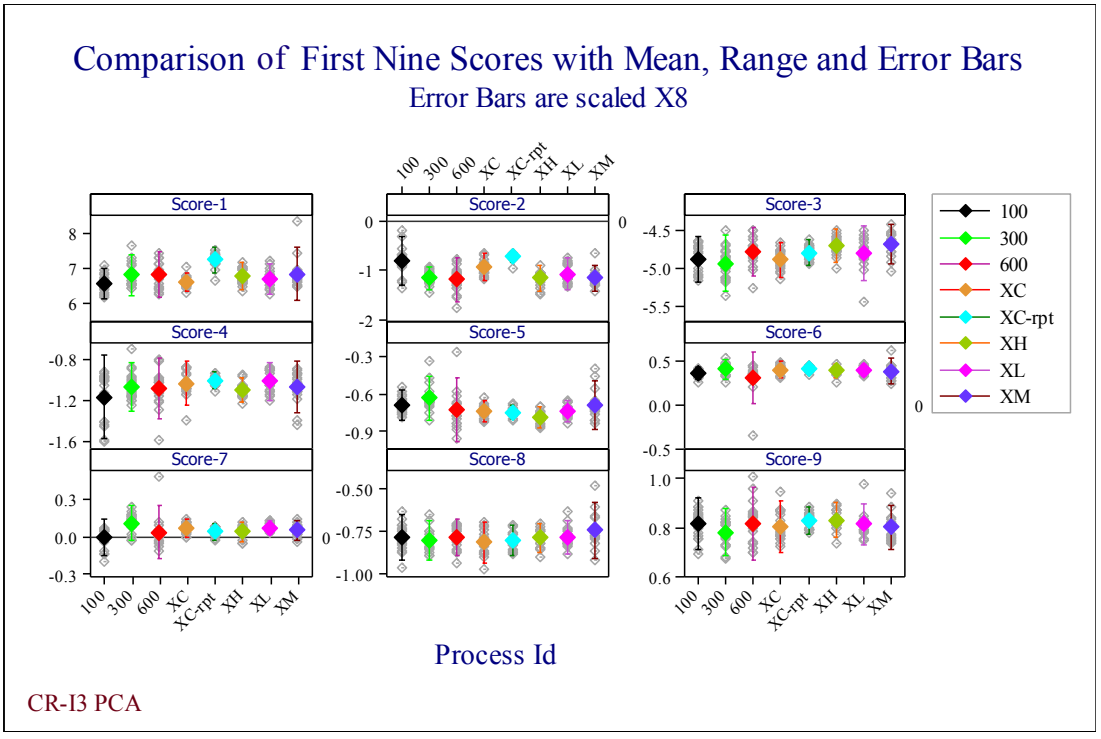

Figure 6.5l: Mean values (solid coloured symbols), distribution of the scores in each data set (grey outline) and the standard deviations (vertical bars) magnified 8 times to show the details corresponding to the first nine PC scores.

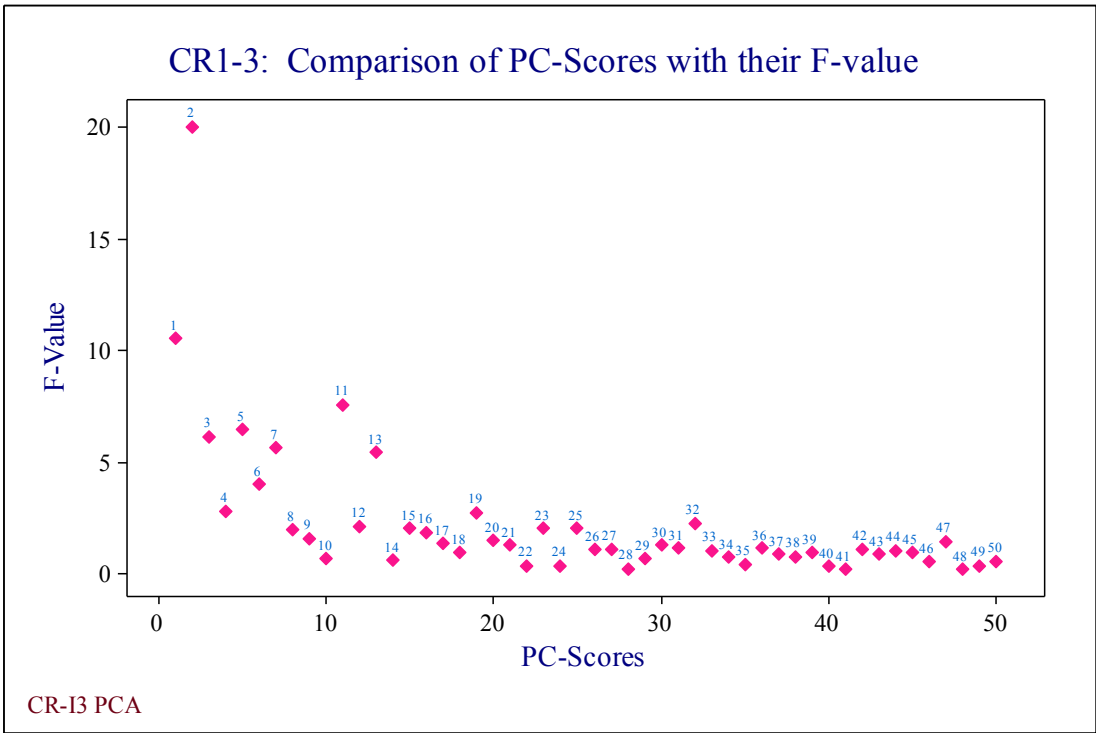

Figure 6.5m: The first 50 PC scores plotted as a function of high F-values.

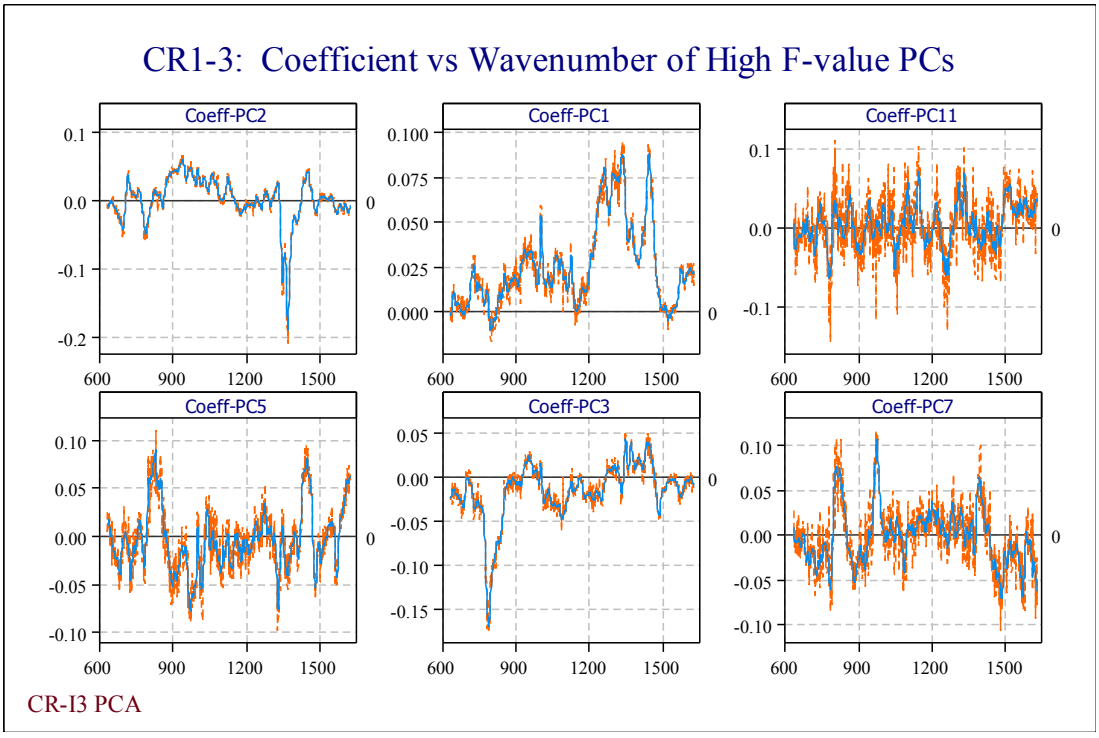

Figure 6.5n: PC coefficients plotted as a function of wavenumber for the top six PCs with high F-value scores.

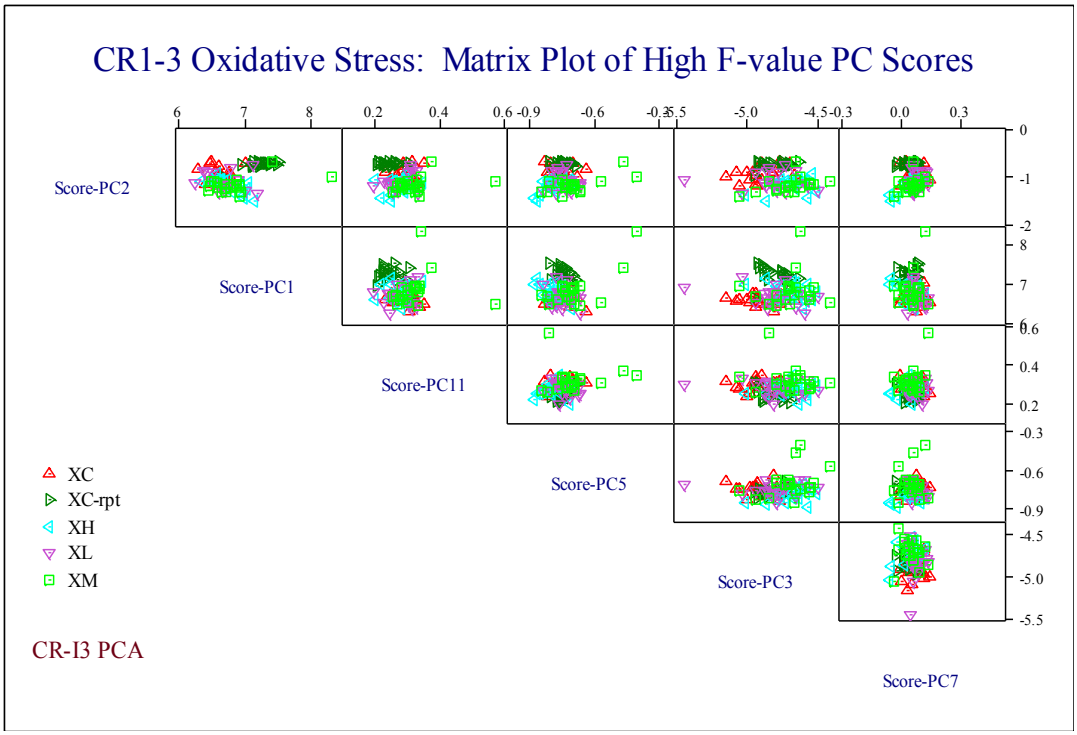

Figure 6.5o: Matrix display of PC Scores with high F-values of the data sets from cells exposed to oxidative stress. Score 2 and 3 shows maximum cluster separation.

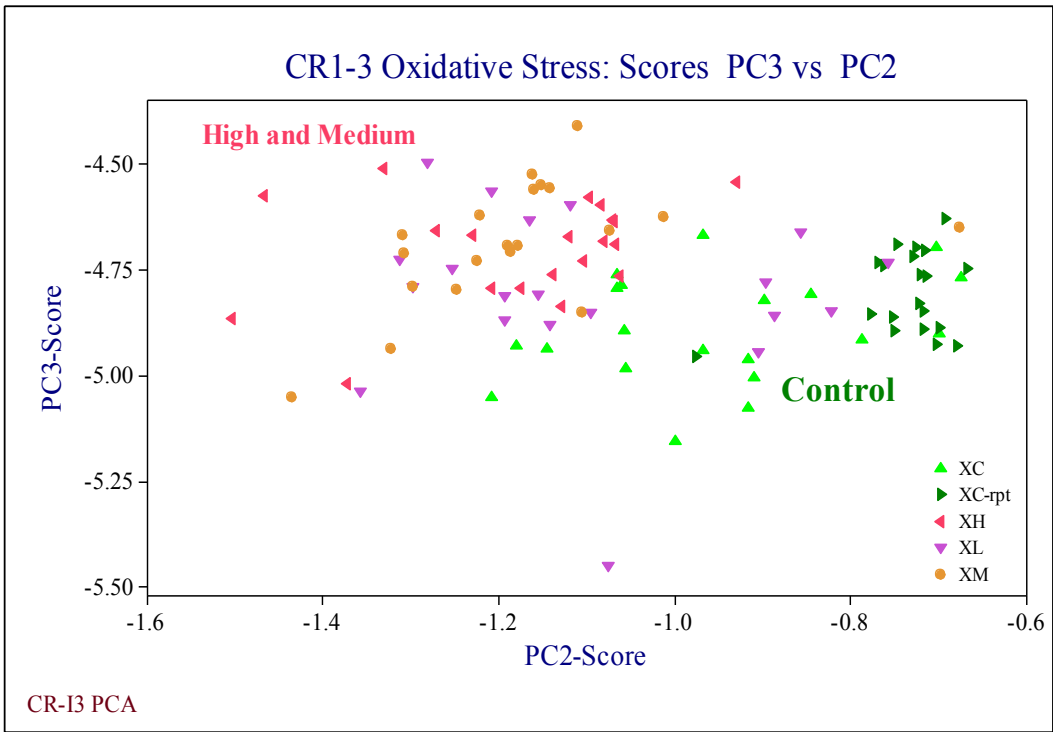

Figure 6.5p: Plot of PC scores, 3 vs 2 for Oxidative Stress. The regions with concentration of 'High'/'Medium' are shifted to the left; the 'Control' is shifted to the right. 'Low' is distributed across both regions. 'High' and 'Medium' cannot be separated.

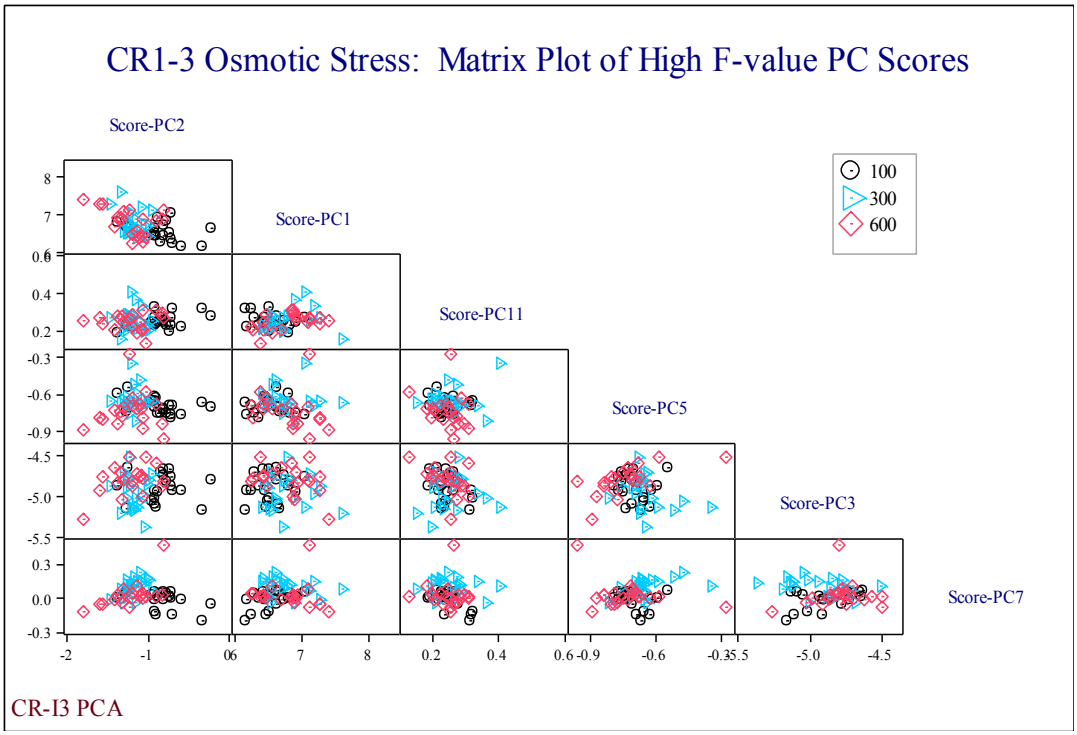

Figure 6.5q: Matrix display of PC Scores with high F-values of the data sets from cells exposed to osmotic stress processes. PC scores 7 vs 3 shows maximum separation.

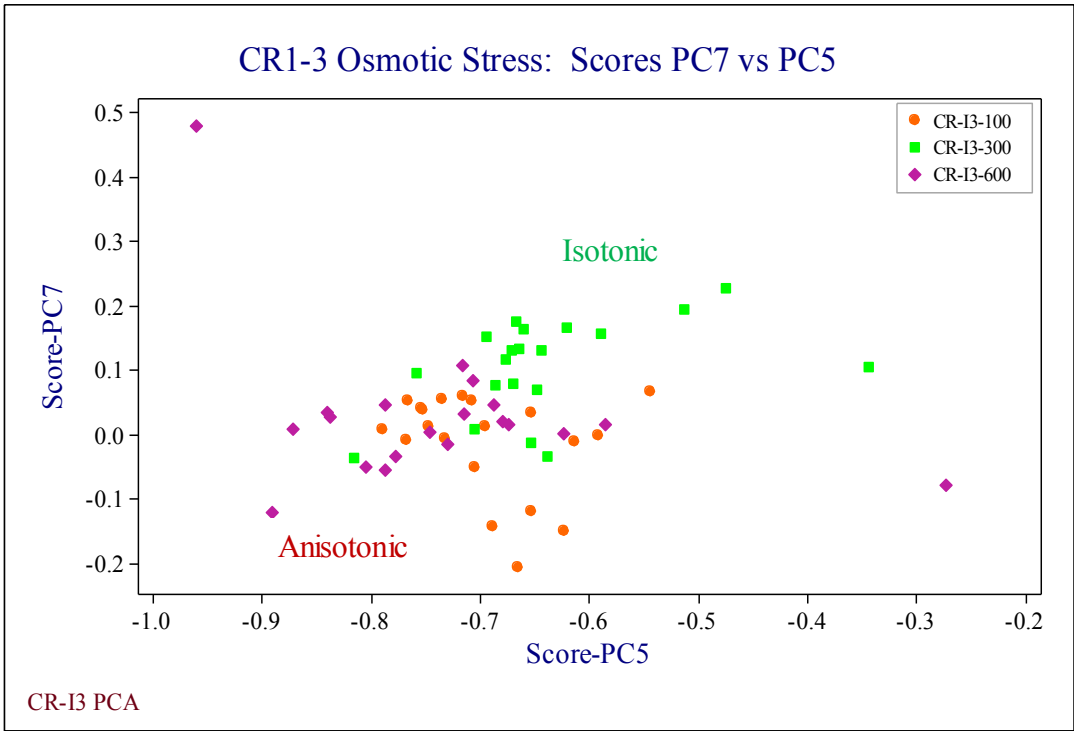

Figure 6.5r: Plot of PC scores 7 vs 5 showing overlap between 'isotonic' and 'anisotonic' stress data sets. 'Hypo' and 'hyper' cannot be separated.

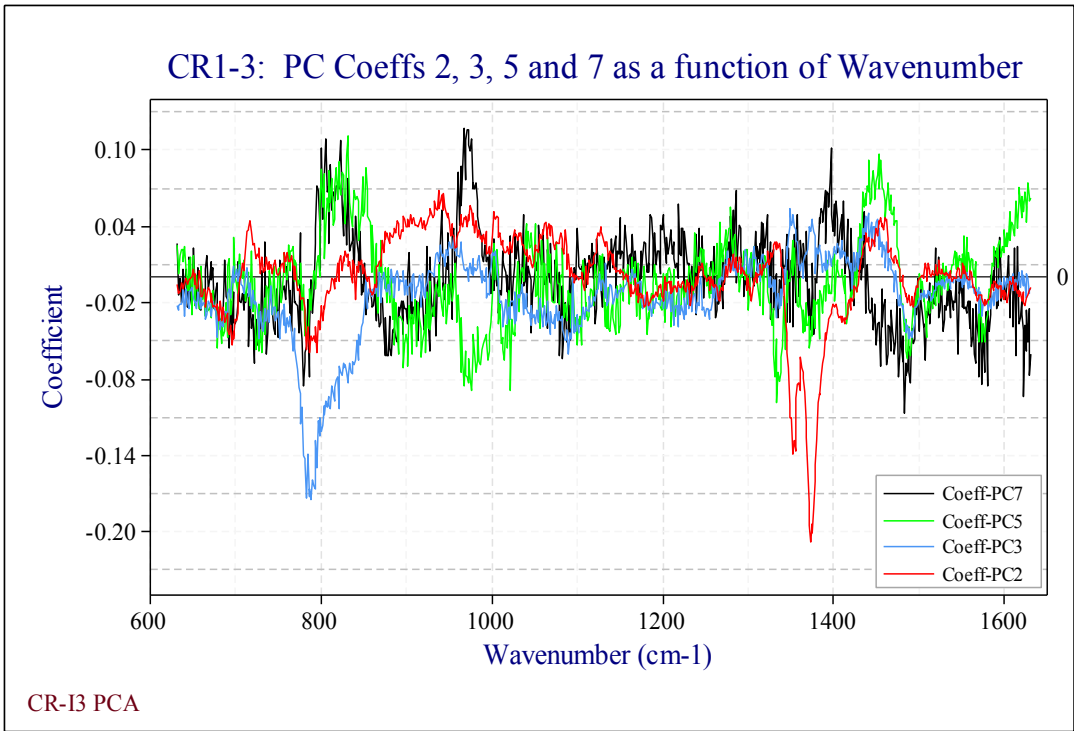

Figure 6.5s: Overlay plot of PC coefficients, 2, 3, 5 and 7 for comparison of spectral regions/bands contributing to the induced oxidative and osmotic stress damage.

6.2.1.3 Comparison of Stress Damage in CR Groups

The CR data groups are analysed separately to provide information on sperm cells from different semen collections from a stallion. Motility and viability test results by the Veterinary School team is included; the charts show percentage of total motility, progressive motility and viability of a sample population of the cells, taken prior to each stress damage and after completion of each stress damage process.

Figure 6.6a consists of a set of three bar charts that show TM, PM and viability of sperm specimens taken on three different days from stallion CR, before and after exposure to the seven process conditions. The variations in the CR data groups are highlighted in the set of plots of statistical variance in **Figure 6.6b,** with CR1-1 (top), CR1-2 (middle) and CR1-3 (bottom). **Figures 6.6c** and **6.6d** are plots of PC scores that show maximum separation in osmotic and oxidative stress data in the CR data groups. **Figure 6.6e** compares the coefficients of the PCs that show maximum process related separation in data groups CR1-1, CR1-2 and CR1-3.

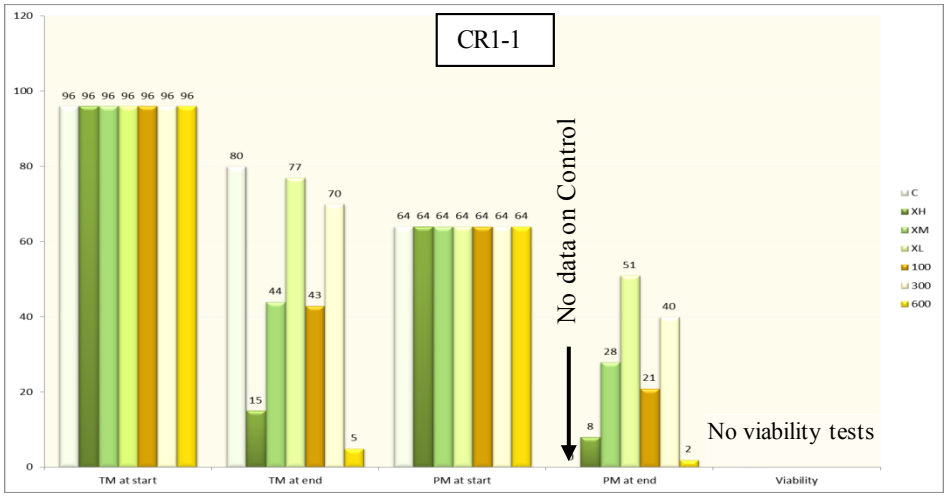

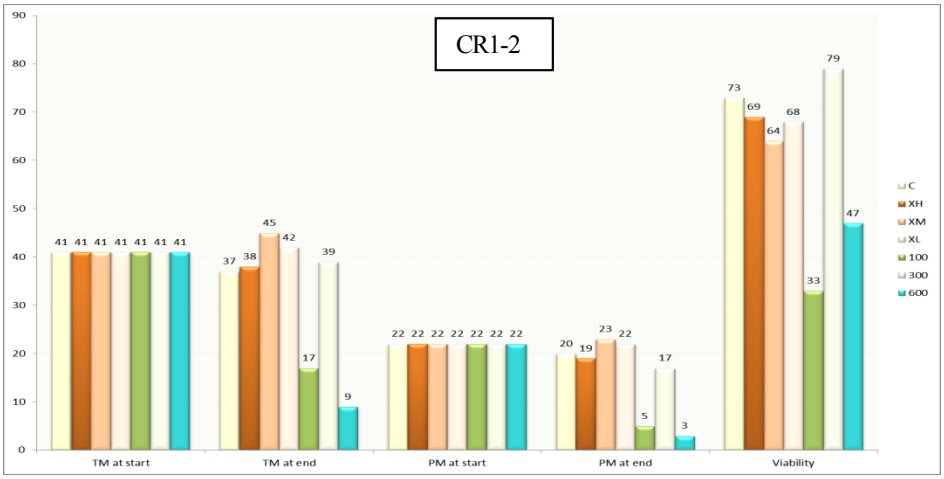

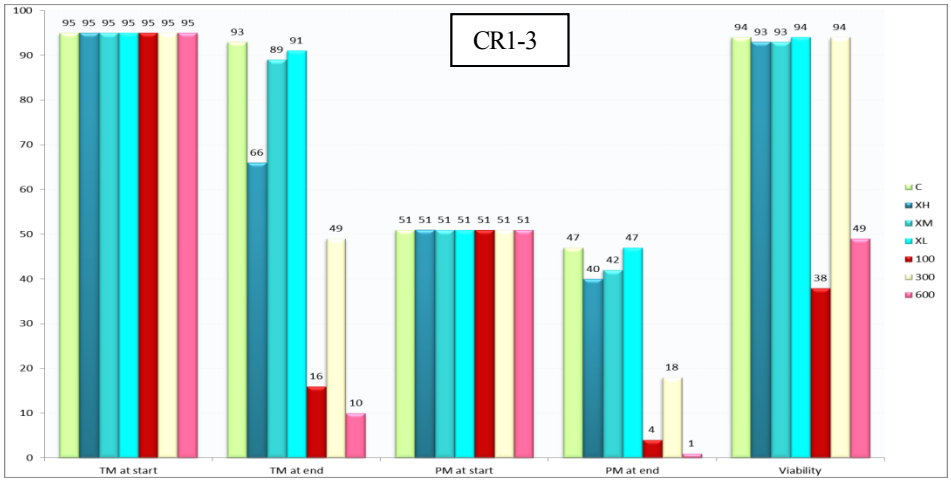

Figure 6.6a: Graph showing percent motility, both TM and PM and cell viability for the three data groups from stallion CR.

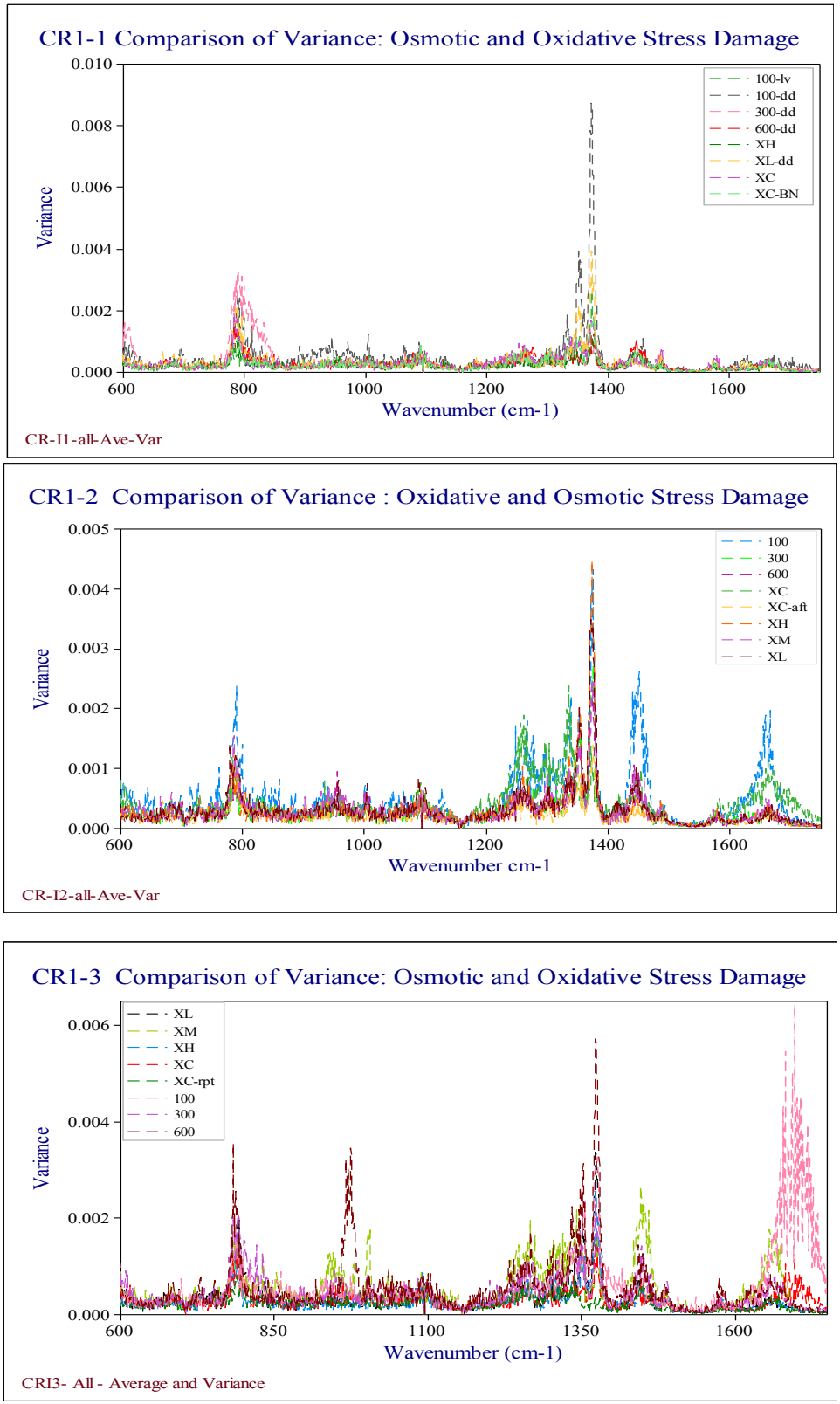

Figure 6.6b: Comparison of Variance within each data set for the three data groups from stallion CR, CR1-1, CR1-2 and CR1-3.

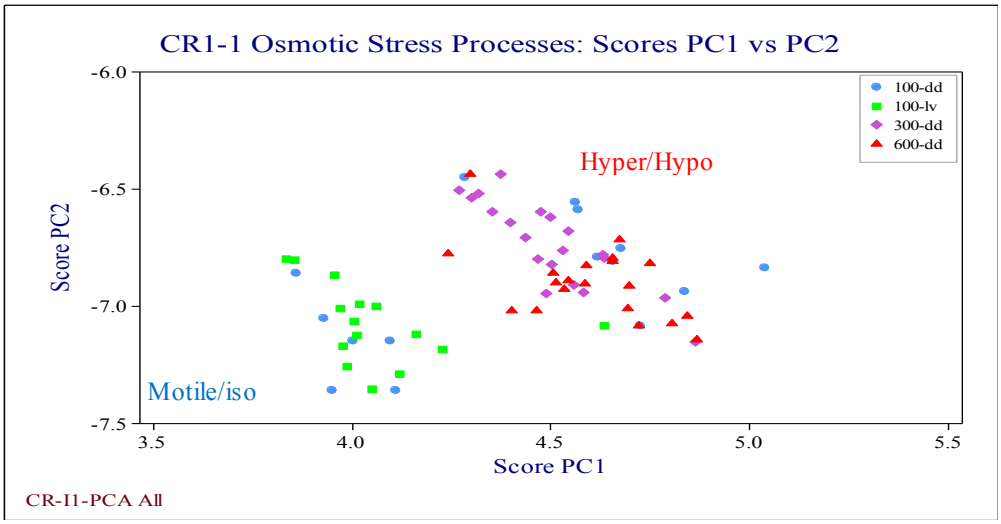

'No separation for osmotic stress on CR1-2'

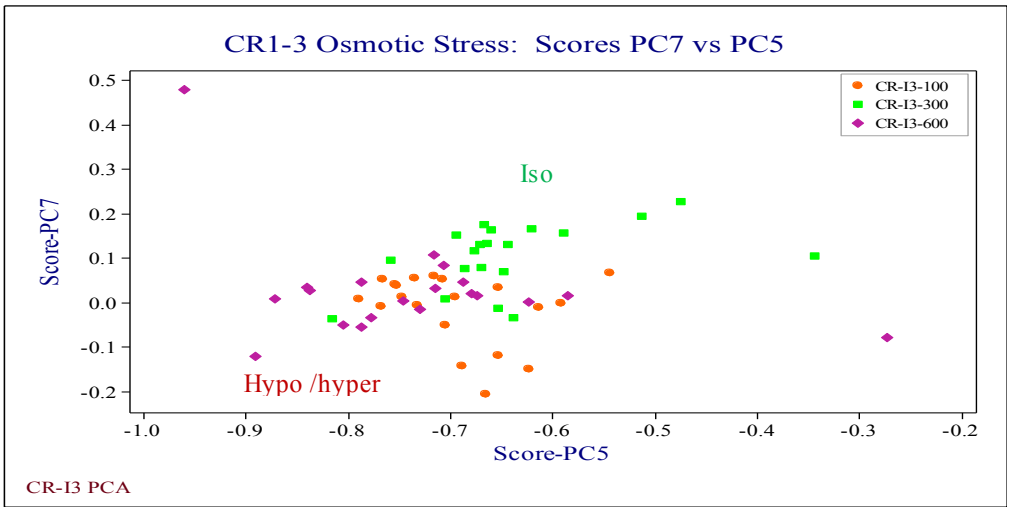

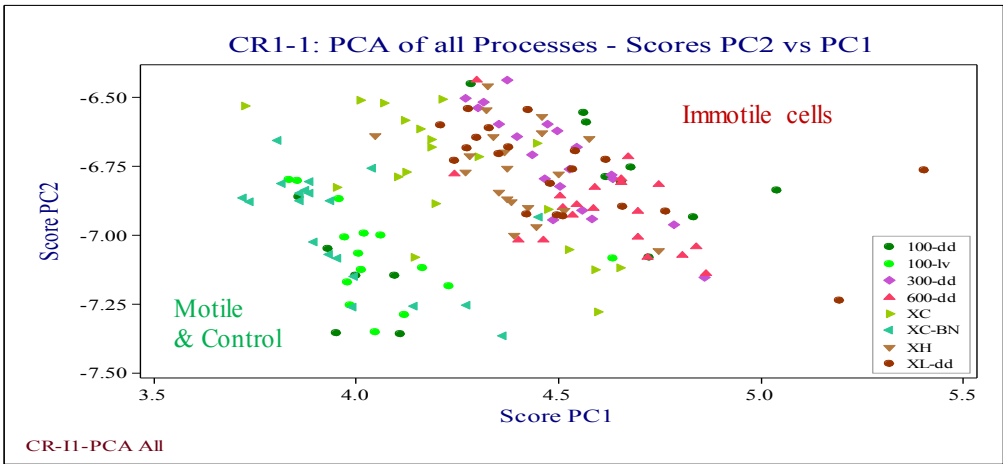

Figure 6.6c: (**Top & Centre**) Scatter plot of PC scores showing process related clustering in CR1-1 and CR1-3 osmotic stress. (**Bottom**) PC scores of CR1-1 showing some separation by motility (where applicable) after oxidative and osmotic stress damage. Iso immotile and control of CR1-1 are distributed in both regions (**Top & Bottom**).

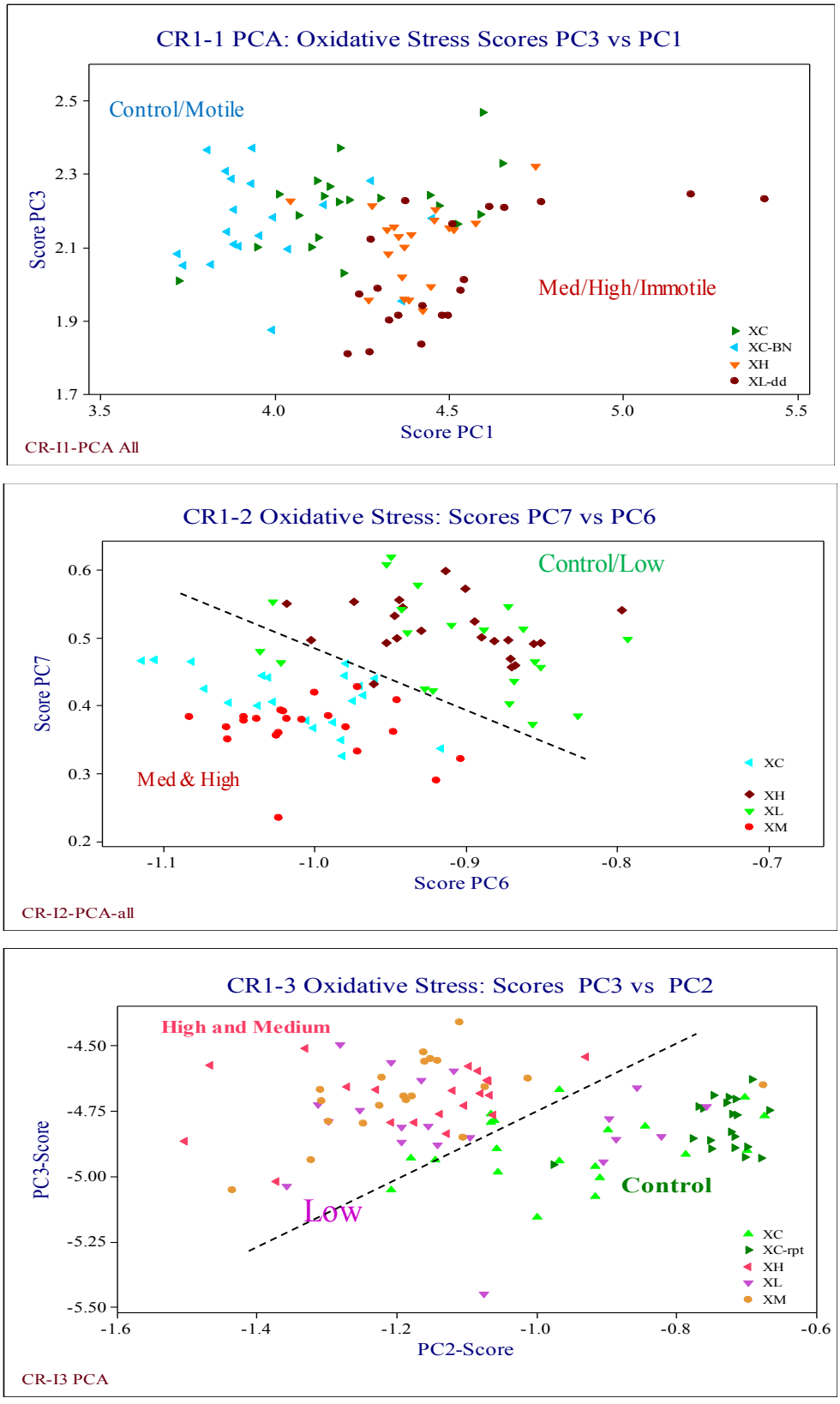

Figure 6.6d: Scatter plot of the PC scores that show separation after oxidative stress in CR13. (Top) 'High', 'Medium' and 'immotile' separated from 'Control'. (Middle and Bottom) 'High and 'Med' separated from Control. 'Low' is spread across the two regions.

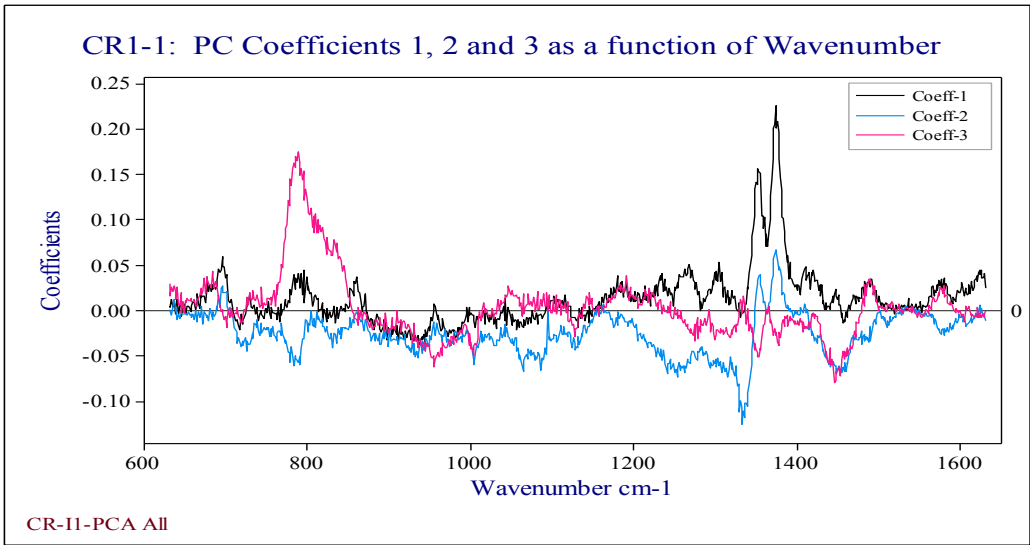

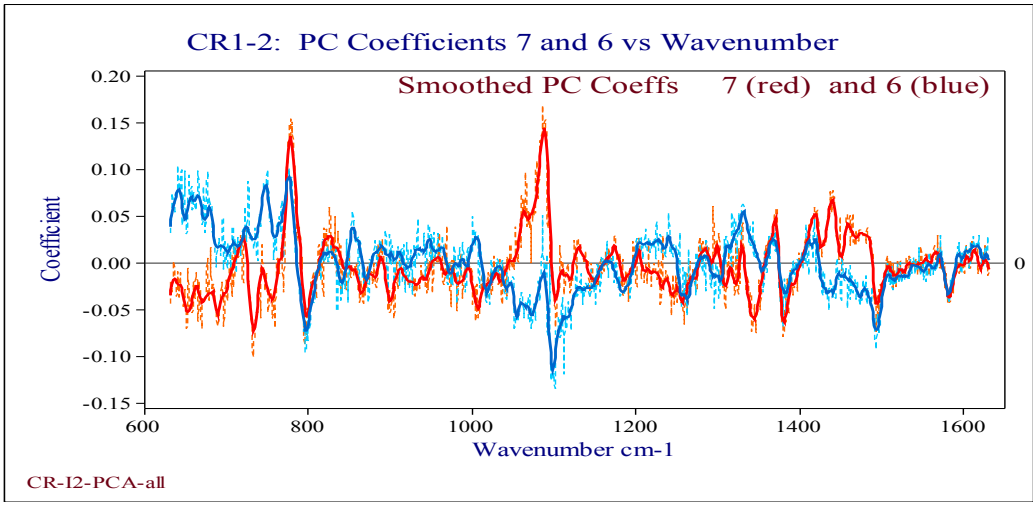

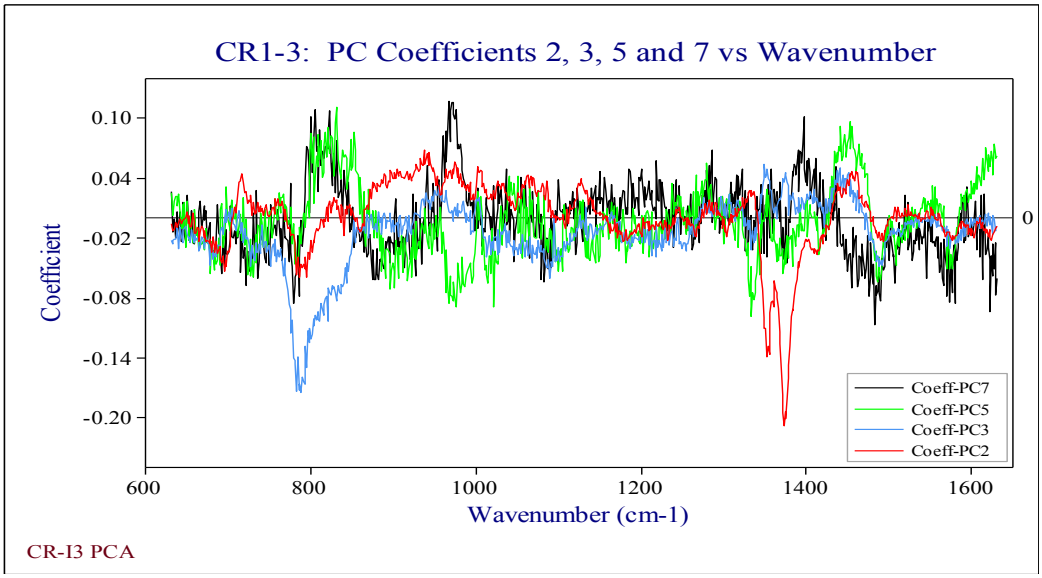

Figure 6.6e: Comparison of coefficients of the PCs that showed maximum separation of the PC scores by osmotic and oxidative stress processes in CR1-1, CR1-2 and CR1-3.

6.2.1.4 Comparison of Stress Damage in the Five Data Groups

The remaining two data groups DN and HD1 are from two different stallions; they are analysed using the same procedure described in **sections 6.2.1.2** and **6.2.1.3. Figures 6.7a – 6.7e** are plots of motility & viability, variance, PC scores and coefficients that maximise process related clustering or separation of data sets in data group, DN. **Figures 6.8a – 6.8e** show a similar set of results from data group HD1.

The findings from the stress damage study of the five data groups are summarised in **Figures 6.9a** and **6.9b**. **Figures 6.9a** are a set of three bar charts (A, B & C) that compares motility and viability data from all the five stallion collections. Since motility data from the prepared aliquots is not available on all the data sets, the post-treatment motility data is used in the plots. (**A**) Compares cell viability on CR1-2, CR1-3 and HD1. Data was not available for the other two groups. (**B**) Compares TM and PM by process. (**C**) Plot of PM to TM ratio, after each stress processes.

Figure 6.9b is a plot of the PC scores of the entire 844 spectra from the 43 data sets and five data groups. This analysis was done to identify PC clustering by the any of the variables - process conditions, stallion/data group or motility. No process related separation or grouping could be identified. **Table 6.5** summarises the spectral regions that contribute to the variability in the spectra in the five data groups.

Average intensities of the peaks/bands at 785 cm^{-1}, 1050 cm^{-1} and 1445 cm^{-1} (with standard deviations) from CR1-1, CR1-3 and HD1 are tabulated in **Table 6.6** (CR1 represents CR1-1 and CR3 represents CR1-3). This table is used to compare the results from the stallions with the results from published papers on Raman spectroscopy on sperms and is discussed in Chapter Seven. CR and HD are also used in **Study Two**; correlation between the two studies is explored.

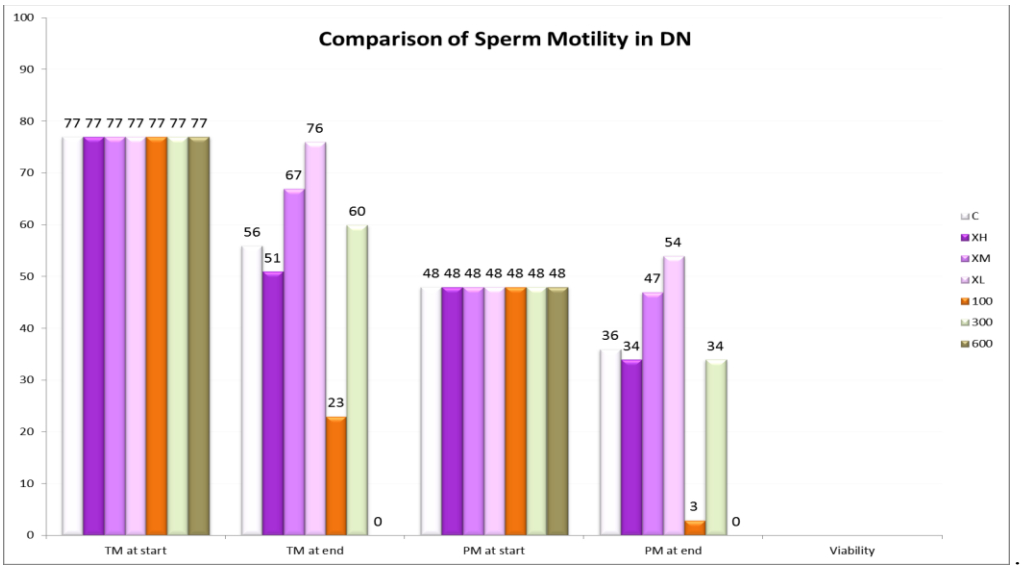

Figure 6.7a: Comparison of sperm motility (TM and PM) before and after stress damage in DN. No viability data is available

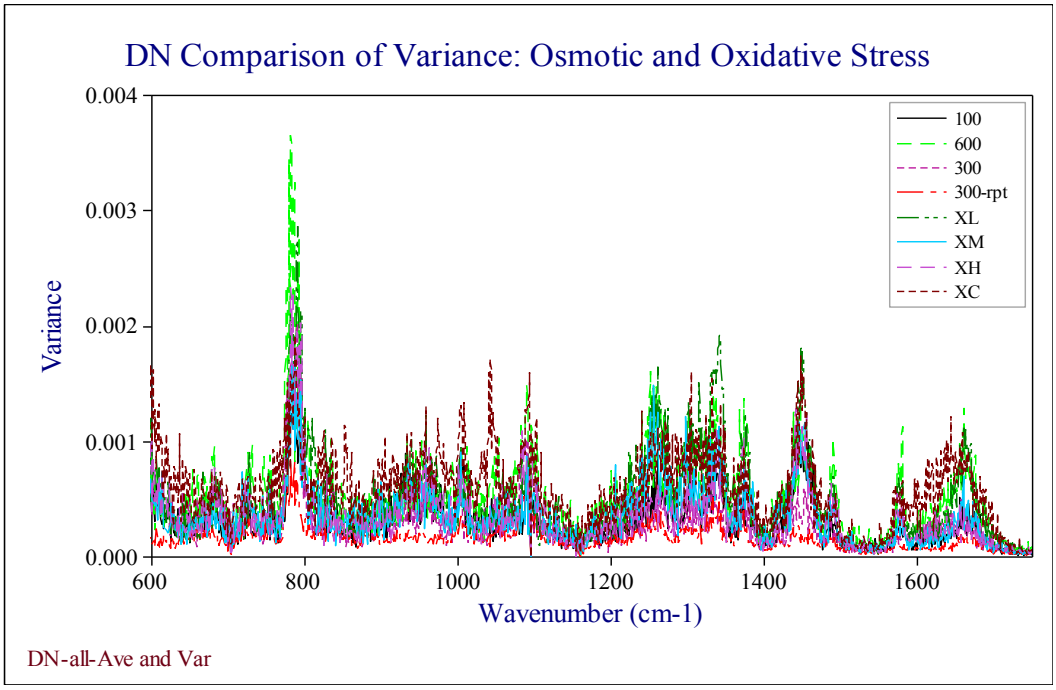

Figure 6.7b: Plot of variance of all the stress damage data sets in data group DN.

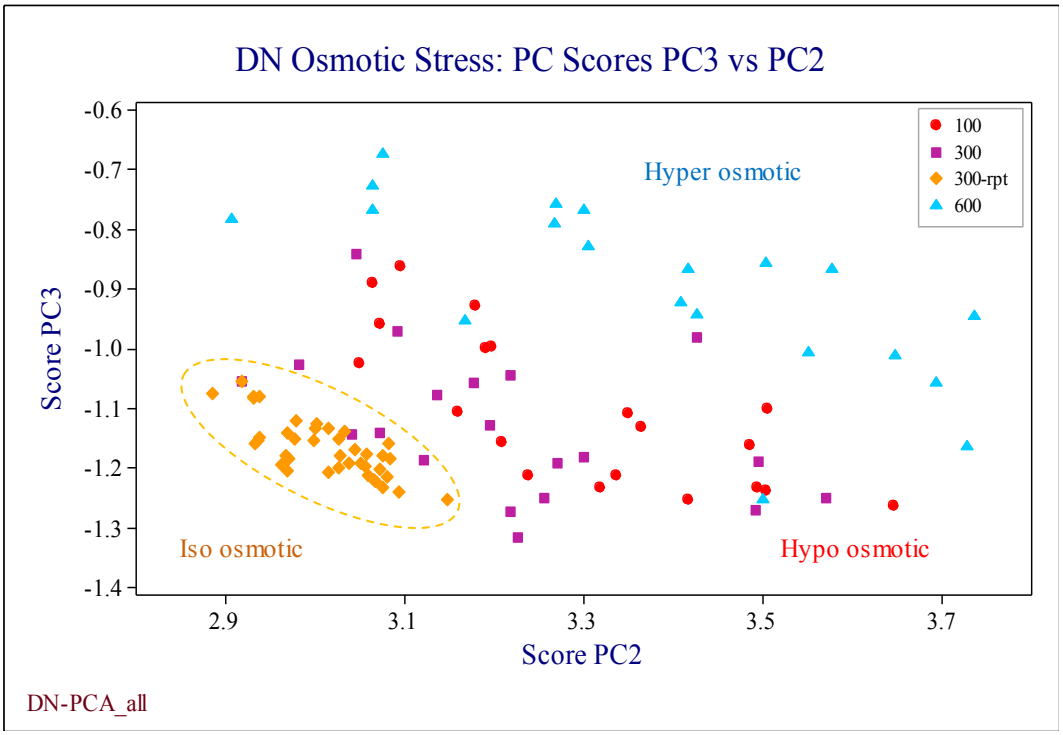

Figure 6.7c: The PC scores that show grouping by osmotic stress processes in data group DN. The circled data set is from extended trapping.

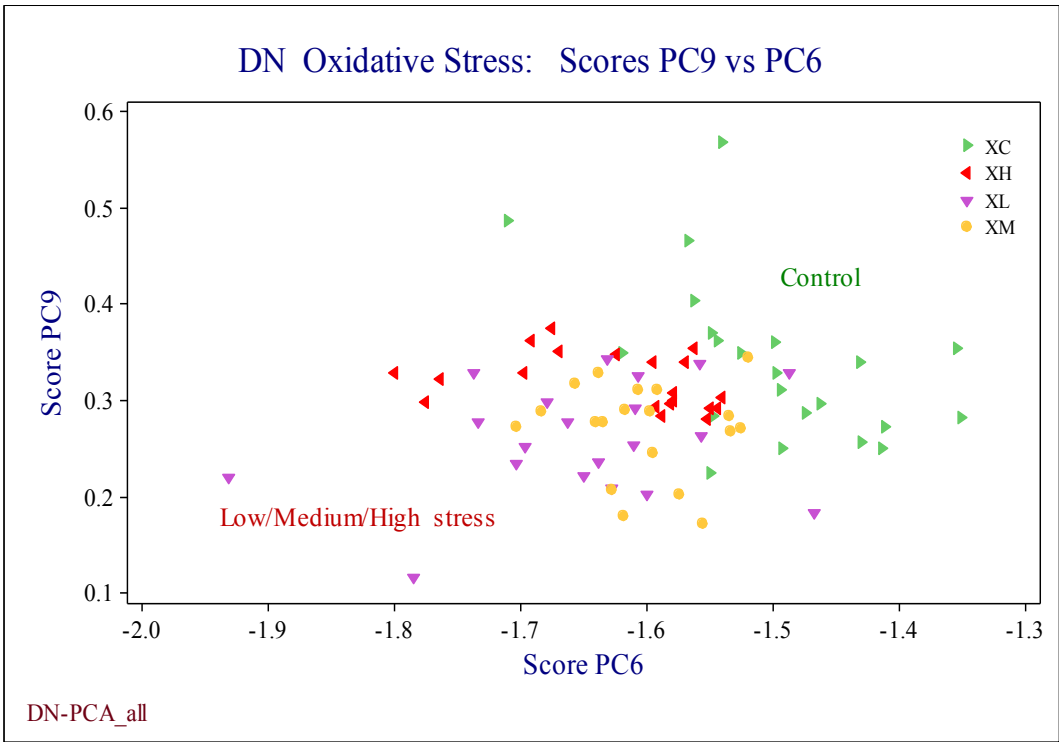

Figure 6.7d: Scatter plot of PC score grouping by oxidative stress damage processes in data group DN. The stressed samples could not be separated.

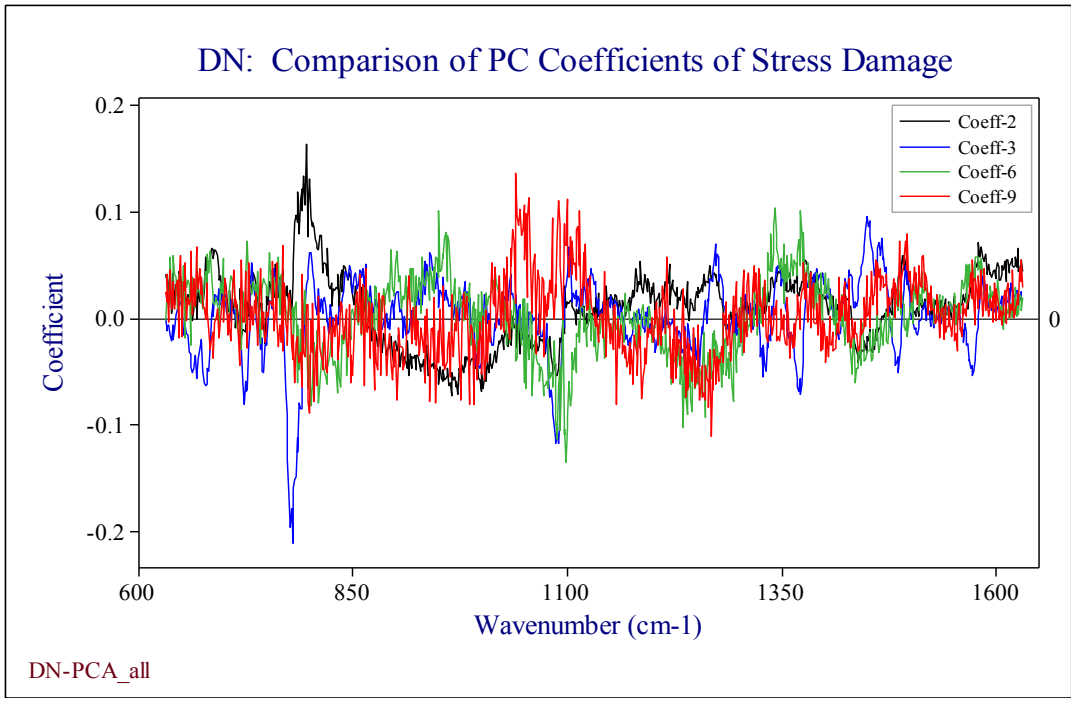

Figure 6.7e: Comparison of PC coefficients that correspond to the PC scores in DN data group.

The following data plots correspond to stallion HD

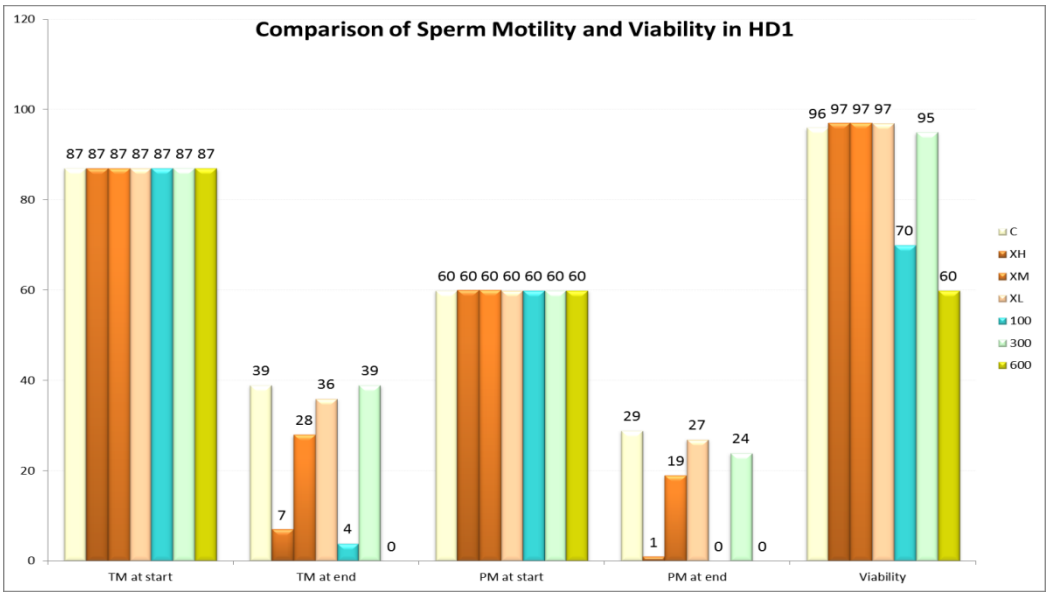

Figure 6.8a: Comparison of sperm motility before and after stress damage processes in data group HD1.

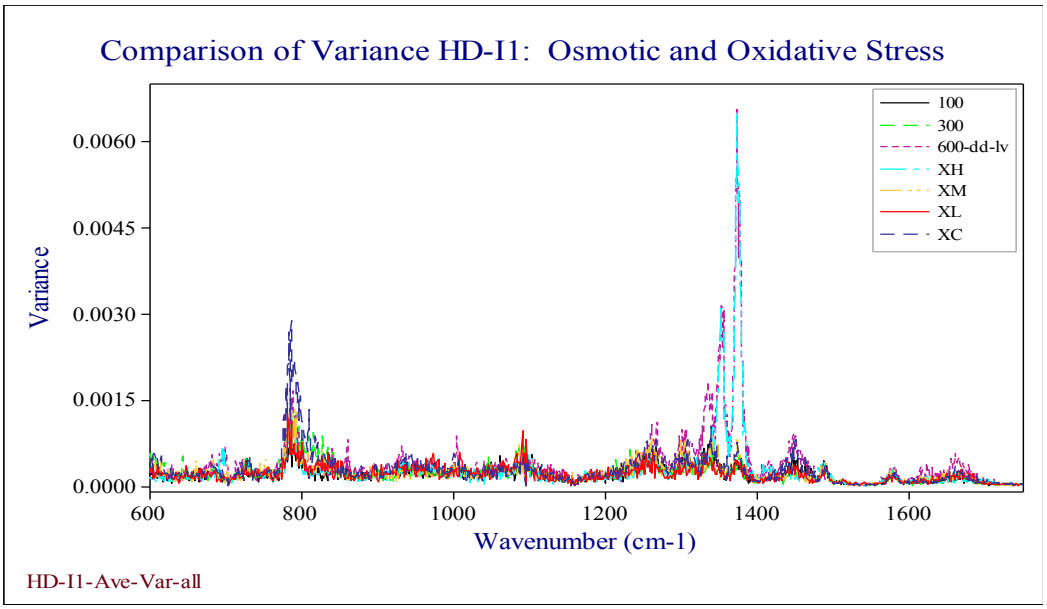

Figure 6.8b: Plot of variance in the stress damage datasets in data group HD1.

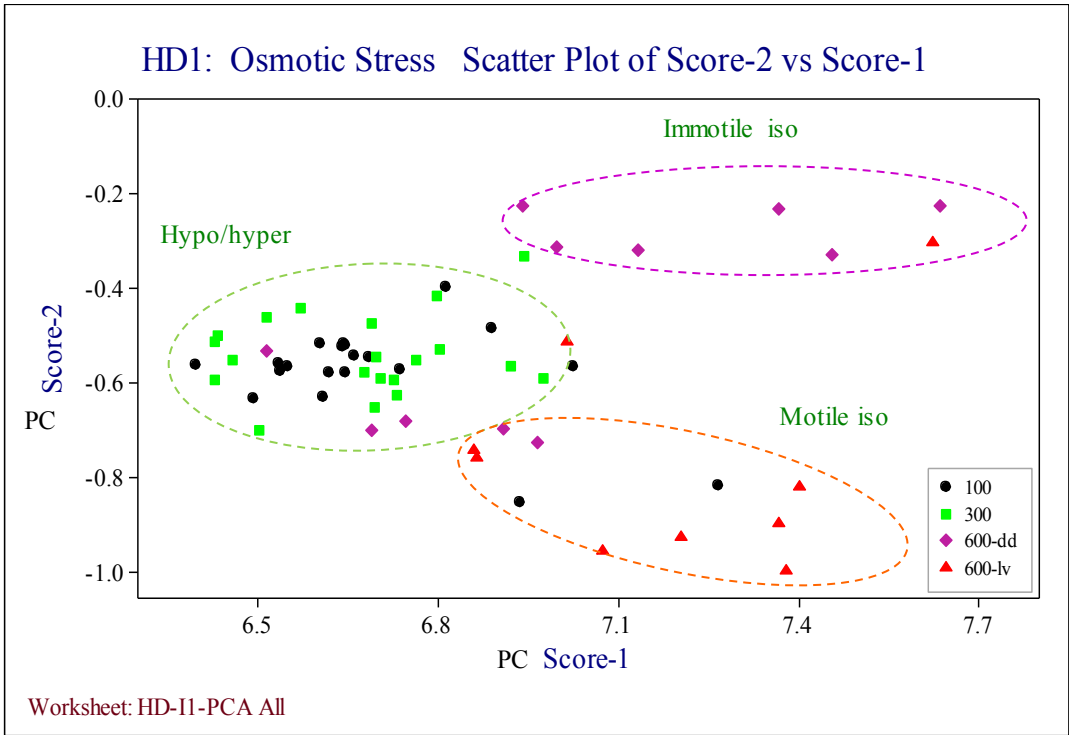

Figure 6.8c: Scatter plot of PC score groups after osmotic stress exposure in HD1.

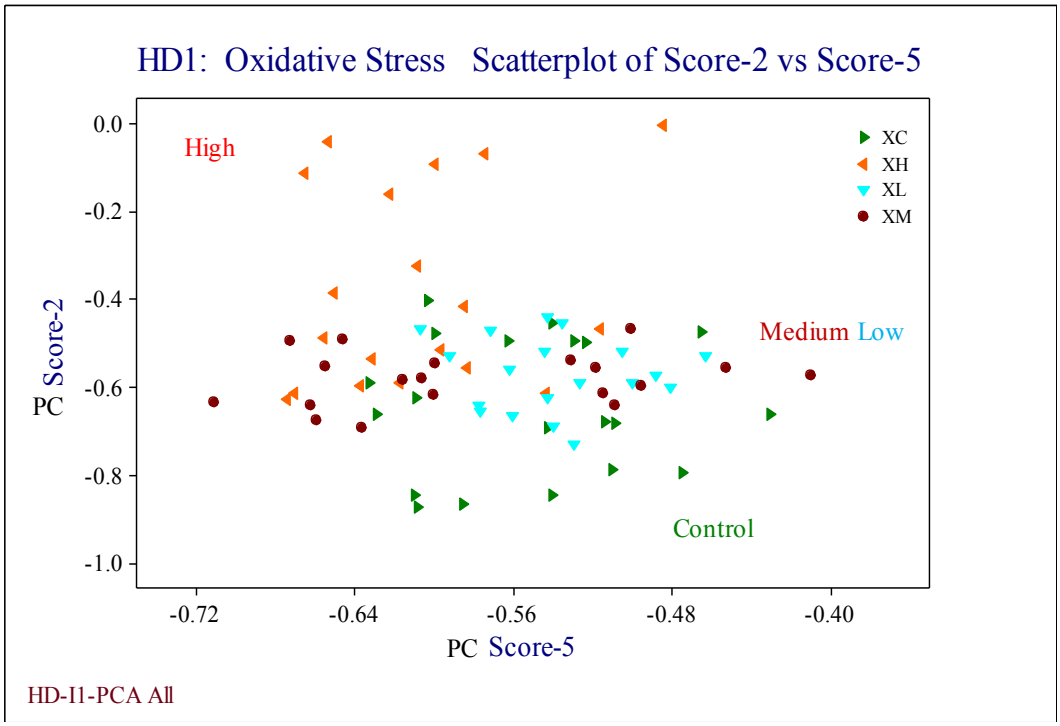

Figure 6.8d: Scatter plot of PC scores that group by oxidative stress damage processes in data group HD1. The Medium, Low and Control could not be separated.

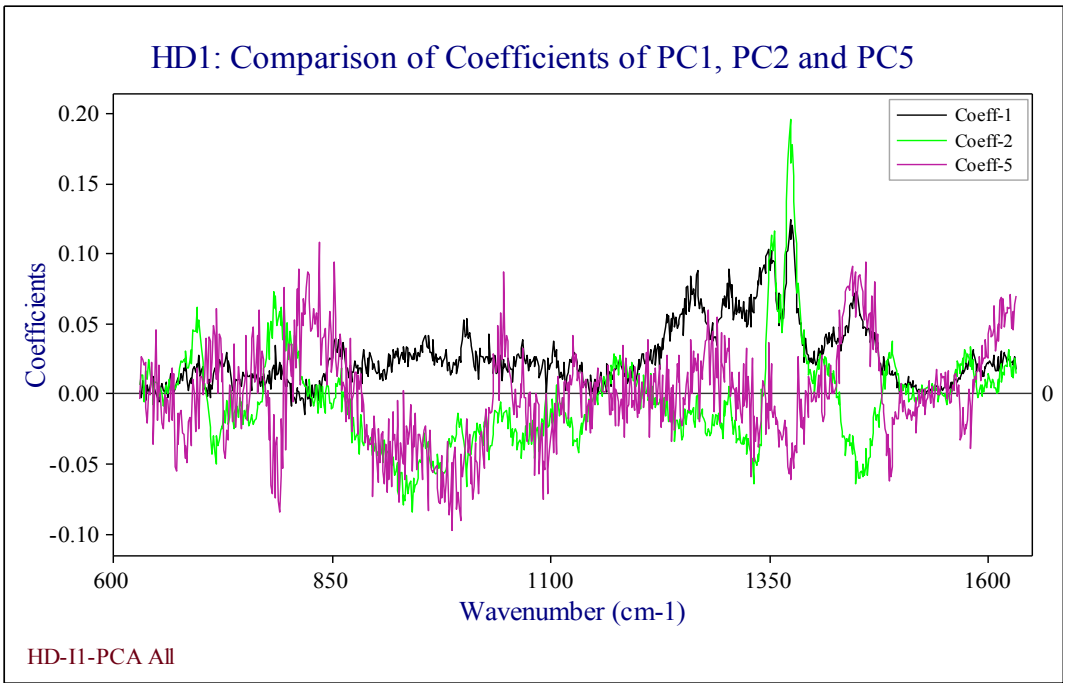

Figure 6.8e: Comparison of PC coefficients for stress damage in HD1 data group.

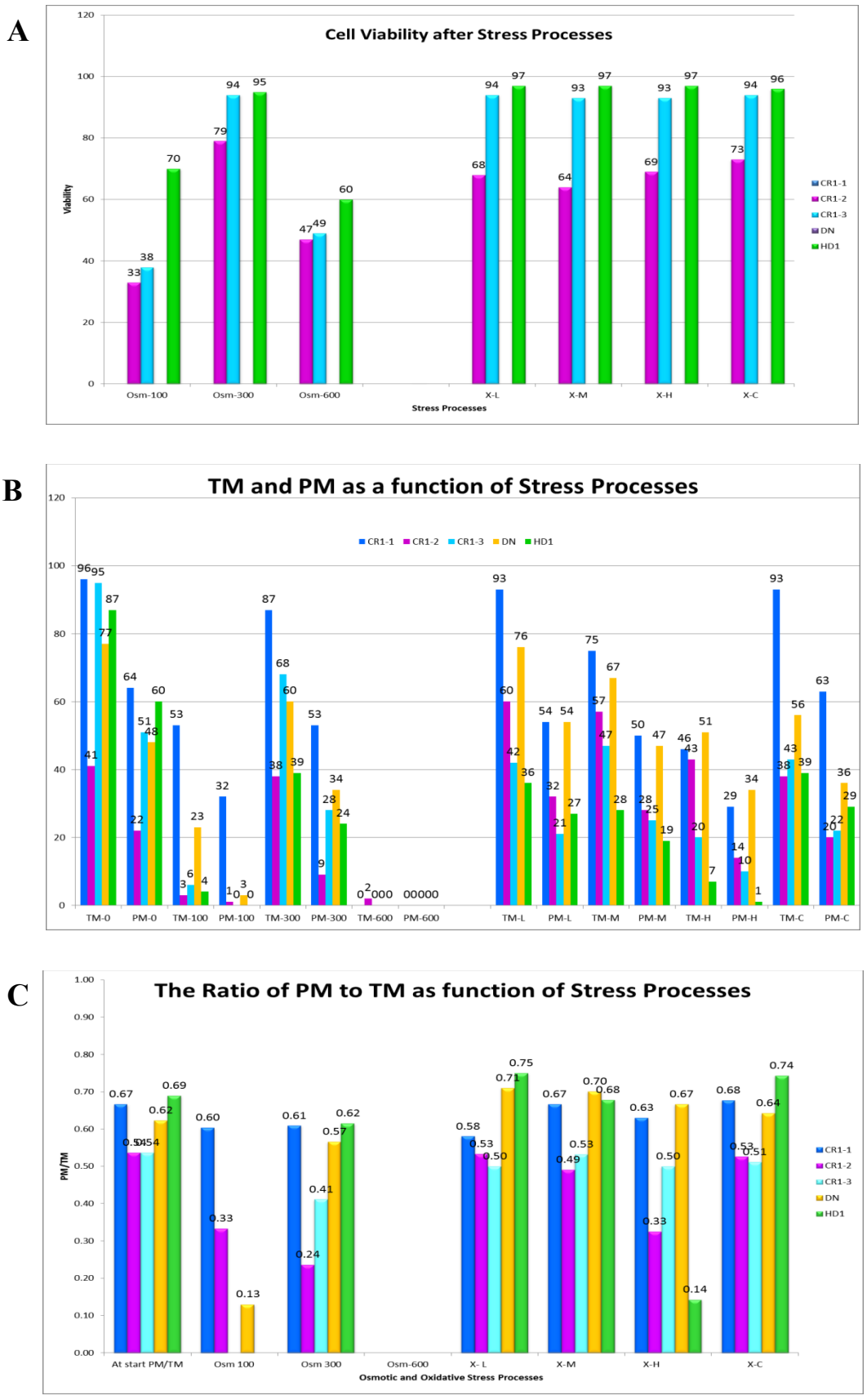

Figure 6.9a: Comparison of (A) sperm viability, (B) sperm motility and (C) ratio of PM/TM of the five semen collections representing CR1-1, CR1-2 and CR1-3, DN and HD1.

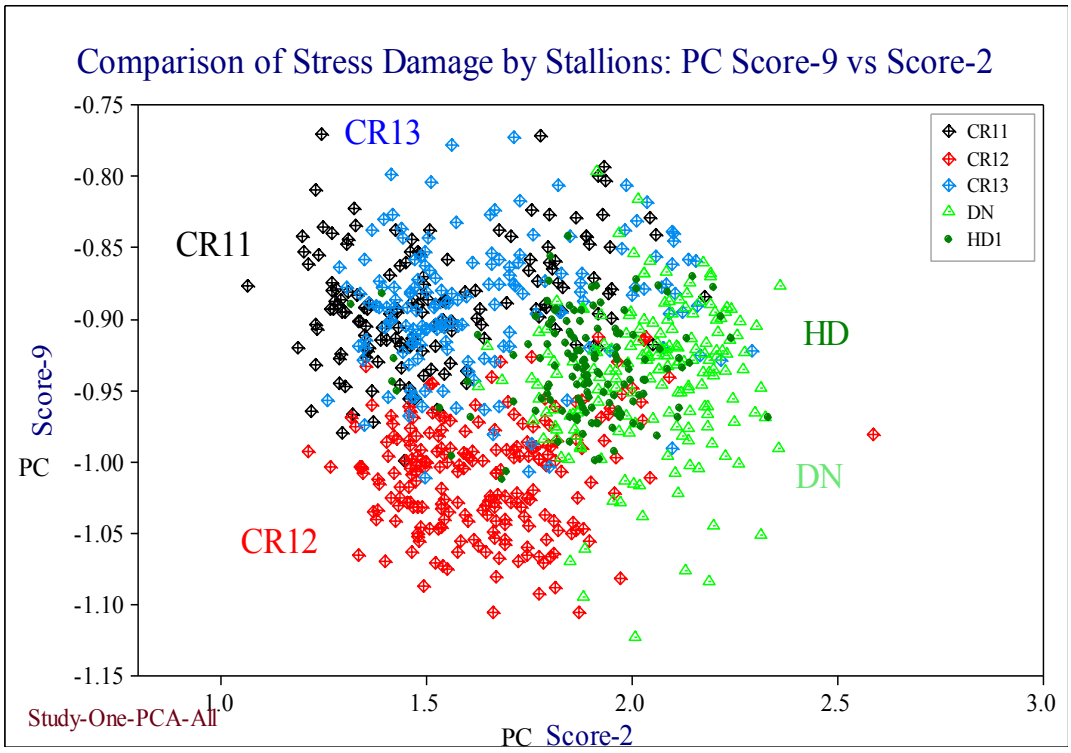

Figure 6.9b: Score plots of all the stress data separated by stallion and data groups show clustering by ejaculates. (Note: CR11 is CR1-1, CR12 is CR1-2, CR13 is CR1-3 and HD is HD1).

Description	CR1-1	CR1-2	CR1-3
Variance max (1375 cm^{-1})	≃ 0.009	≃ 0.0045	≃ 0.006
All variance (in cm^{-1})	680, 730, 785, 835, 945, 1001, 1088, 1250, 1335-1375, 1445, 1486, 1575, 1620	785, 835, 956, 1001, 1088, 1130, 1250-1375, 1445, 1486, 1575, 1620	680, 725, 750, 785, 835, 956, 1001, 1088, 1180, 1250-1375, 1445, 1486, 1575, 1620
High variance (in cm^{-1})	785, 945, 1001, 1335-1375, 1445	785, 956, 1130, 1250-1375, 1445,	785, 956, 1001, 1250-1375, 1445
Common CR Variance	785, 835, 945-956, 1001, 1088, 1250, 1335-1375, 1445, 1486, 1575, 1620		
Regions of high PC Coefficients	695, 725, 785, 835, 935, 957, 1005, 1045, 1050-1095, 1130, 1180, 1220-1320, 1331, 1350, 1370, 1445, 1485, 1575, 1602, 1621	725, 750, 780, 800, 825, 860, 900, 1002, 1055, 1070, 1090, 1130, 1185, 1200, 1250, 1330, 1345, 1370, 1380, 1415, 1435, 1490, 1580,	695, 725, 785, 795-830, 880-950, 970, 1005, 1030, 1050, 1085, 1280, 1320, 1335, 1350, 1370, 1395, 1410, 1445, 1485, 1570, 1620
Common PC coefficients	725, 770-850, 860, 950-970, 1002, 1180, 1250, 1300-1500, 1350, 1370, 1445, 1485, 1575,		
High PC coeff	770-850, 1300-1500, 1575		

Description	DN	HD1
Variance max at	≃ 0.0037 at 785 cm^{-1}	≃ 0.0045 at 1375 cm^{-1}
All variance (in cm^{-1})	Due to noisy data, this could not be measured	680, 785, 835, 956, 1001, 1090, 1250-1375, 1445, 1486, 1575, 1620,
High Variance (in cm^{-1})	785, 635, 956, 1001, 1040, 1088, 1250, 1300, 1335, 1375, 1445, 1485, 1575	785, 1001, 1090, 1250-1375, 1445,
Common variance	775-795, 835, 950-970, 1001, 1088, 1250, 1335, 1375, 1445, 1486, 1575	
Regions of high PC Coefficients	686, 725, 785, 835, 940, 960, 1005, 1045, 1050-1095, 1145, 1180, 1215, 1260, 1330, 1340, 1370, 1400, 1435, 1455, 1495, 1515, 1575	680, 695,725, 785, 825, 860, 890, 905, 935, 956, 1002, 1045, 1065, 1090, 1120, 1175, 1235, 1265, 1280, 1300, 1325, 1345, 1375, 1380, 1420, 1456, 1485, 1575, 1600, 1620
Common PC coefficients	725, 785, 825-835, 1002, 1170-1180, 1250-1280, 1300-1500, 1320-1340,, 1370-1380, 1420-1455, 1485-1495, 1570-1580,	
High PC coeff	770-850, 1300-1500, 1570-1580	

Table 6.5: Summary of Variance and PC coefficients of the five data groups.

Study One: DNA and Protein Peak Ratios (Average)						
Stallion	**785**	**Stdev (785)**	**1055**	**Stdev (1055)**	**1445**	**Stdev (1445)**
CR1-100-lv	1.01	0.022	0.42	0.020	0.42	0.024
CR1-100-dd	1.03	0.046	0.42	0.022	0.42	0.020
CR1-300-dd	1.01	0.055	0.41	0.014	0.42	0.017
CR1-600-dd	1.01	0.036	0.41	0.014	0.44	0.035
CR1-XL-dd	1.02	0.046	0.41	0.010	0.41	0.020
CR1-XH	1.02	0.028	0.42	0.014	0.41	0.024
CR1-XC	1.04	0.036	0.41	0.020	0.4	0.022
CR1-XC-BN	1.03	0.022	0.42	0.014	0.41	0.022
HD1-100	1.02	0.022	0.42	0.014	0.38	0.014
HD1-300	1.03	0.037	0.43	0.017	0.38	0.014
HD1-600	1.02	0.039	0.43	0.017	0.42	0.026
HD1-XL	1.02	0.033	0.42	0.017	0.37	0.014
HD1-XM	1.03	0.032	0.42	0.017	0.37	0.014
HD1-XC	1.02	0.054	0.43	0.020	0.39	0.020
HD1-XH	1.03	0.035	0.42	0.017	0.37	0.017
CR3-100	1.02	0.045	0.42	0.022	0.39	0.028
CR3-300	1.05	0.039	0.42	0.022	0.40	0.036
CR3-600	1.03	0.047	0.41	0.024	0.40	0.026
CR3-XL	1.03	0.040	0.41	0.017	0.39	0.028
CR3-XM	1	0.041	0.41	0.022	0.41	0.052
CR3-XC	1.02	0.030	0.41	0.017	0.38	0.026
CR3-XC-rpt	1.02	0.022	0.43	0.017	0.45	0.022
CR3-XH	1.01	0.036	0.41	0.014	0.39	0.022

Table 6.6: Summary of Average peaks at 785, 1050 and 1445 in 3 data groups.

6.2.2 Study Two: Osmotic Stress and Membrane Damage in Stallion Sperms

This study was designed to compare membrane damaged, freshly prepared and osmotic stress damaged cells and the effect of cell motility on the induced damage. Six process conditions were examined in the study - three grades of osmotic stress and three grades of membrane damage. The three grades of osmotic stress damage process are the same as in **Study One**. The three grades of membrane damage include 90% membrane damaged cells mixed with 10% fresh prepared cells. These data sets are identified as 'dmg' or 'MD' in the figures. Data sets from 50% membrane damaged cells mixed with 50% fresh prepared cells are identified as '50-50' or '50' in the figures. The data sets from 100% fresh prepared cells are identified as 'FRS' or 'FR' in the figures. Spectra were acquired from motile, (identified as 'lv'), and immotile cells (identified as 'dd') separately, in each data set. The analytical procedure is the same as the one used in **Study One**.

Four semen collections (JZ, HD2, CR2 and WL) taken in midsummer from four stallions, JZ, HD, CR and WL were used in this study. Two collections were from the stallions, HD and CR, used in **Study One**. Each data group and its data sets, the process conditions they were exposed to, and the number of spectra in each data set, are summarised in **Table 6.6**. Extended trapping was tested on three cells; 'rpt' is used to identify these data sets.

The statistical techniques used to study the four data groups are illustrated next, using data group JZ. The procedure used is the same as in **Study One** and hence many of the detailed are not included. The basic statistical analysis is summarised in **sub-section 6.2.2.1** and the details of PCA are in **sub-section 6.2.2.2.** The procedures are applied to the remaining three data groups and the results of the statistical analysis on all the four data groups are summarised in **sub-section 6.2.2.3**.

Study Two Table

Stallion Data Groups	Osmotic Stress						Membrane Damaged (MD)	Prepared cells (Fr)		50-50		Extended trapping (Rpt)	Total spectra =1135	Comments
	Hypo (100)		Iso (300)		Hyper (600)									
	motile	immotile	motile	immotile	motile	immotile	immotile	motile	immotile	motile	immotile			Total cells = 1022
JZ	32	40	28	40	x	20	30	30/20	40	21	40	Fr29/MD	412/341	Rpt on Fr 29 and MD 45 Fr motile (before30/after20)
HD2	30	40	30	20	30	40	30	30	40	29	40	43	402/360	Rpt on Fr-lv 402 spectra 360 cells
WL	10	10	9	10	x	9	10	10	10	10	10	x	98	
CR2	20	30	x	x	20	30	30	20	21	22	30	x	223	

Table 6.7: Summary of spectra from six sets of damage study on four separate stallion semen collections with motile and immotile cells separated from the same aliquot. Abbreviations: Fr – fresh/prepared, MD – membrane damaged, rpt – extended trapping.

6.2.2.1 Overview of Data Group JZ

Six process conditions and thirteen different data sets were investigated between 8 and 60 hours using stallion JZ; each data set is shown in **Appendix** (**Figures 6.10a – 6.10m)**. Panels of four graphs show the raw unprocessed spectra (top left), baseline subtracted and normalised spectra (top right), average spectrum with variance of the data set (bottom left) and average spectrum with standard deviation (bottom right); The full acquisition range is shown in the raw spectra; some of these spectra contain corrupt spectra that were discarded during data acquisition. Two spectra in **Figure 6.10a** were discarded, as the cells had escaped the trap. The pink spectrum in **Figure 6.10d** was discarded, as the specimen had started to dry. A raw spectrum in **Figure 6.10i** has a cosmic ray spike outside the range of interest and is not discarded. Statistical analyses were completed on the 412 normalised spectra from this data group. Extended trapping was investigated using a 'fresh' cell and a 'damaged' cell.

6.2.2.2. Principal Component Analysis of the Data Group JZ

The spectral region used for PCA is 630 cm^{-1} - 1630 cm^{-1} and results are shown in the next set of figures. The procedure is the same as the one used in **Study One** on CR1-3 data group; hence, many of the details presented in **Study One, section 6.2.1.2** are omitted from this section. The impact of the grades of osmotic stress damage process on each data group is explored together, as in **Study One**. Fresh and membrane damaged data sets are explored together to test the grades of membrane damage. In addition, motility and other parameters that can contribute to variations in the data sets are explored and presented in this sub-section and the next.

Figure 6.10n is the matrix plot of the eight data sets with high F-value PC scores that separate 'fresh' cells, '50-50' mixture and 'membrane damaged' cells by process conditions. The three sets of figures - **Figures 6.10o – 6.10q,** investigate the details of each process conditions on the data sets from the stallion cells. **Figure 6.10o** is a scatter plot of PC scores 1 and 9 that almost separates the eight data sets into two regions – fresh/motile cells on the right, membrane damaged and immotile cells on the left. The scatter plot in **Figure 6.10p** shows the PC score distribution of fresh motile and immotile cells taken within 24 hours and 'fresh' motile cells taken nearly 60 hours later. The spectra from fresh motile and membrane damaged cells are shown in **Figure 6.10q**. The plot on the top shows fresh and membrane damaged cells exposed to 'extended trapping', separated by the PC scores.

The three grades of osmotic stress are examined together; **Figure 6.10r** is the matrix plot of the high F-value PC scores that separate the data sets by osmotic stress grades. Spectra on motile and immotile cells in 'iso' and 'hypo' were acquired on day-1. By day 3, there were no motile cells in the hyperosmotic stressed data set; the data sets taken on day-1 and day-3 were separated by PC scores 1 and 2 and is illustrated in **Figures 6.10s**. The motile and immotile cells could not be separated.

PCA of the remaining data groups are summarised in **section 6.2.2.3**. The PC coefficients that separate the various processes and the variances of all the data groups in **Study Two** are also summarised in the section**.**

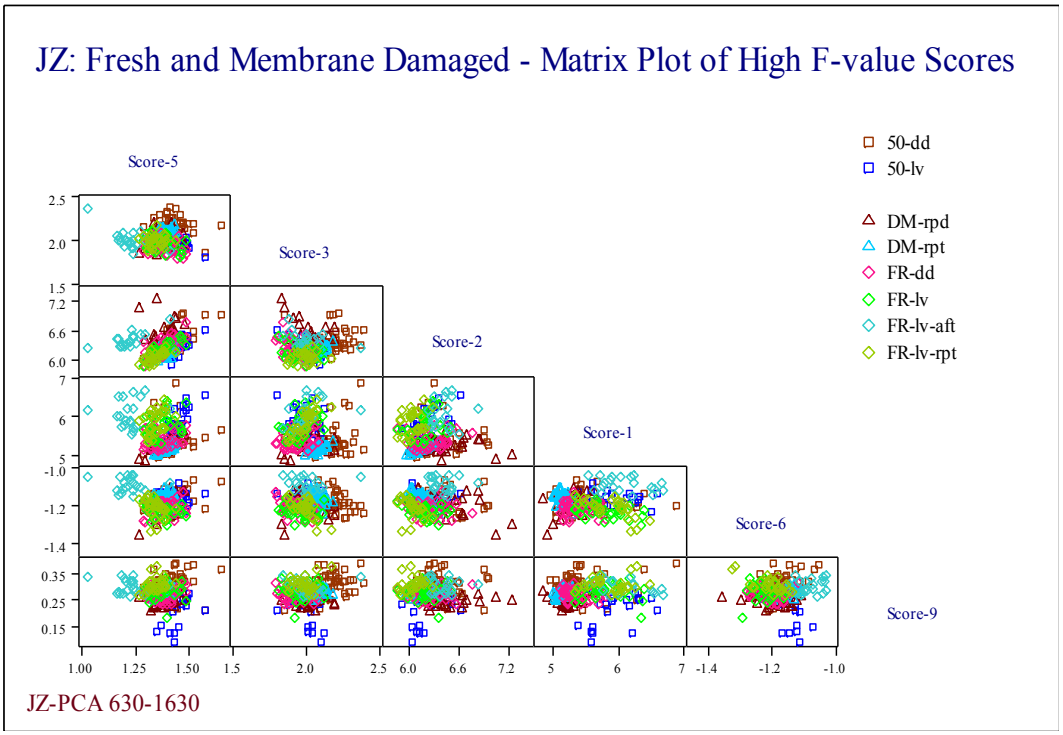

Figure 6.10n: Matrix display of PC scores with high F-values that separate fresh prepared, membrane damaged and 50-50 mixture of fresh and damaged cells.

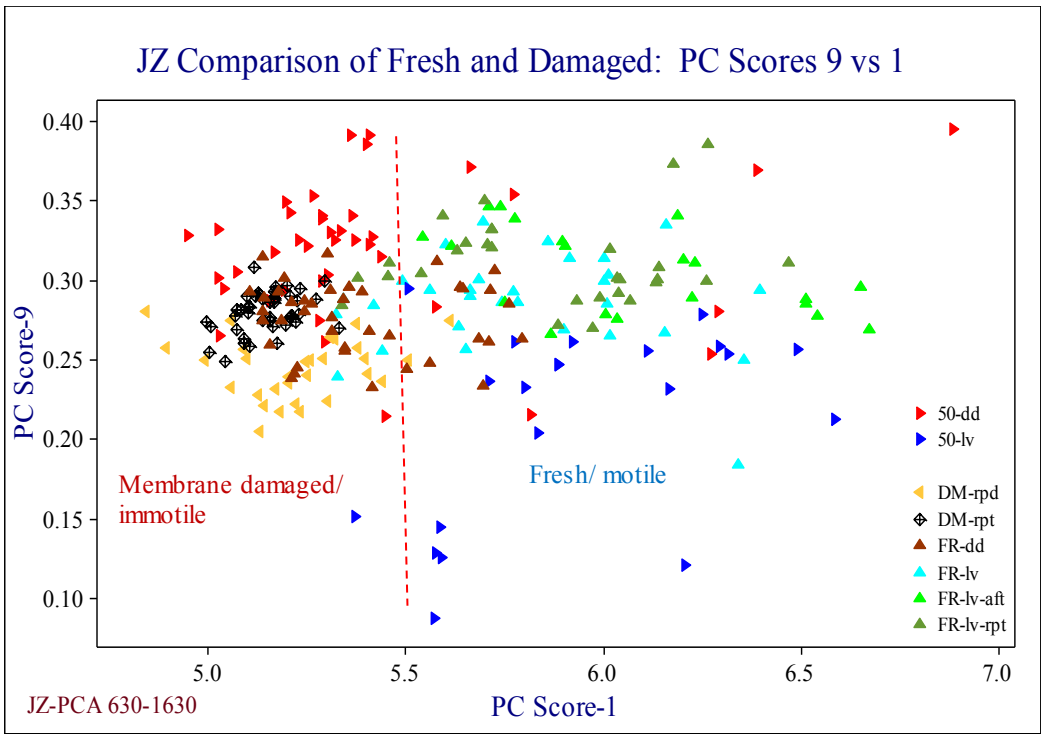

Figure 6.10o: PC scores of membrane damaged and fresh motile cells.

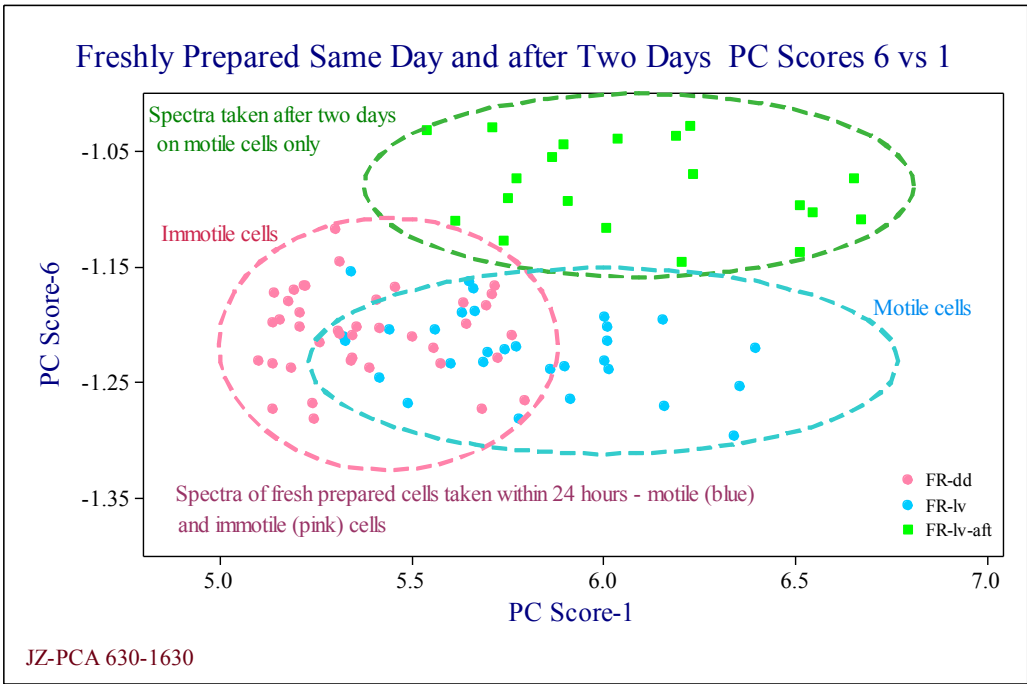

Figure 6.10p: PC scores 6 and 1 separate fresh motile and immotile cells studied within 24 hours and fresh motile cells studied nearly 60 hours later.

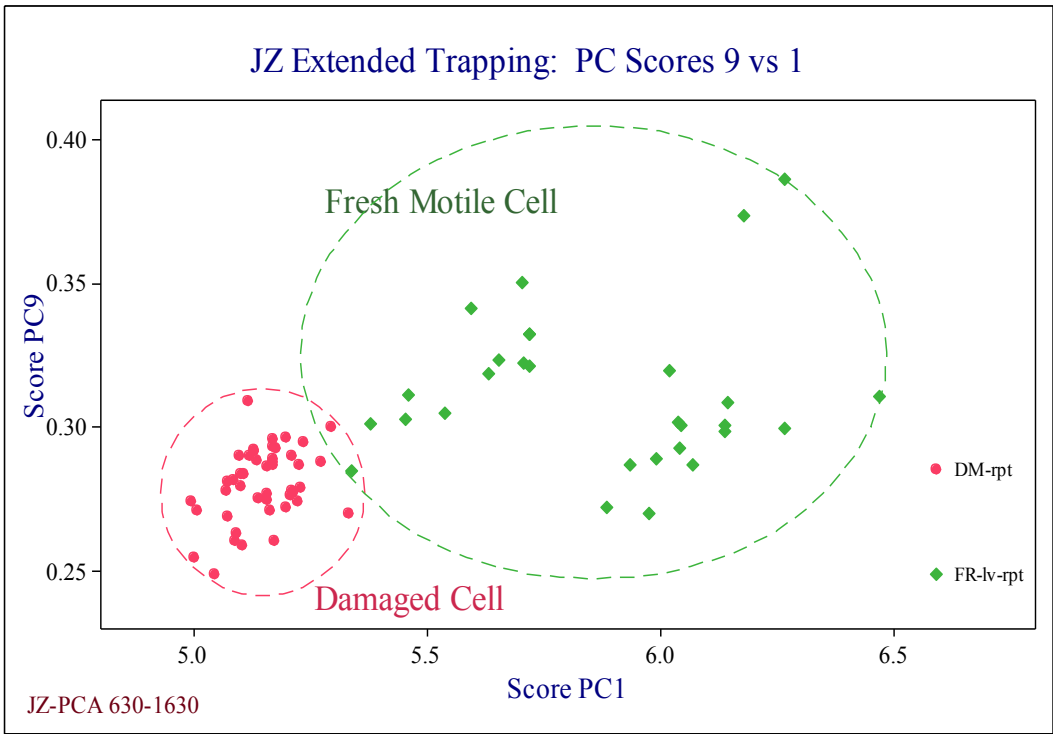

Figure 6.10q: PC scores 9 and 1 separate extended trapping using cells from fresh and membrane damaged aliquots. Fresh motile cell was trapped for 45 minutes and data collected during the first 5 minutes and last five minutes. Data from damaged cell was taken continuously for 10 minutes.

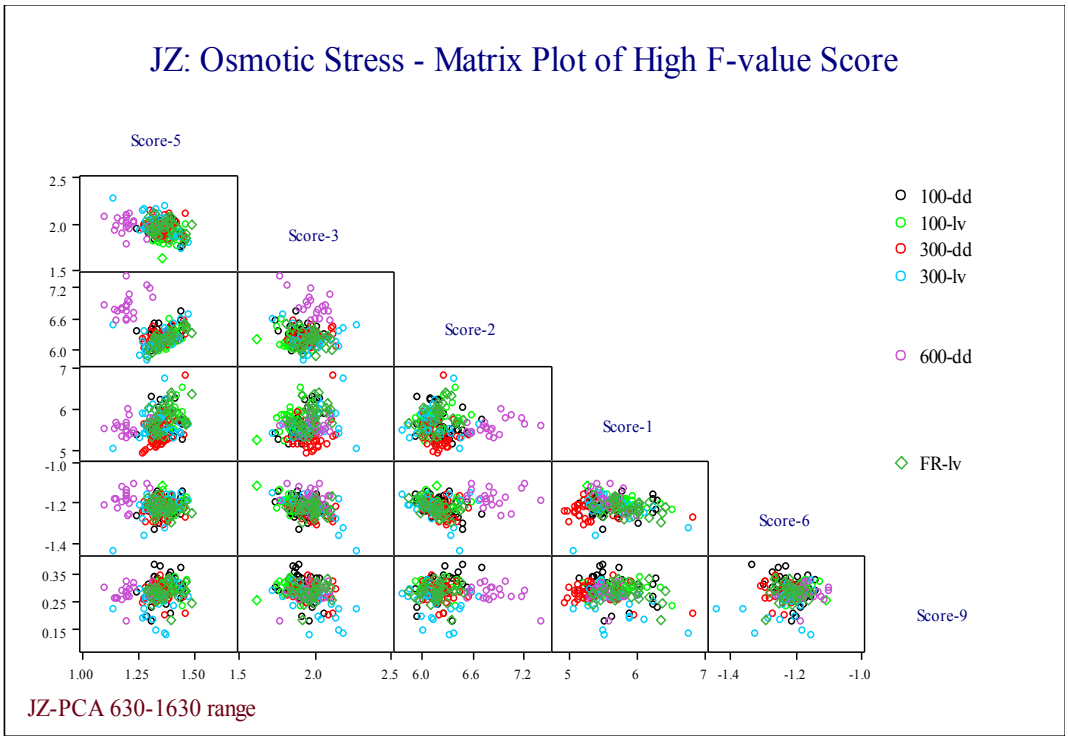

Figure 6.10r: Matrix display of PC scores with high F-values that separate osmotic stress process clusters in JZ.

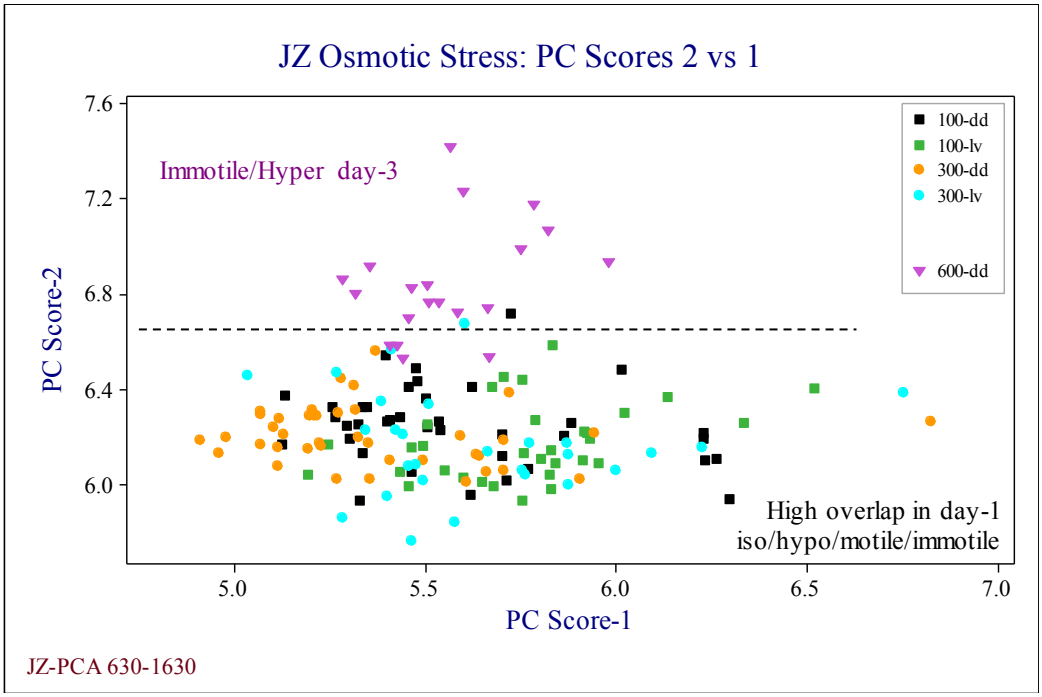

Figure 6.10s: PC scores of osmotic stress damaged cells. The data on hyper-osmotic stress cells were taken ~ 50 hours after collection.

6.2.2.3 Osmotic and Membrane Damage Study of JZ, HD2, WL and CR2

The procedure used to analyse these data groups is the same as detailed in the previous **sections.** Osmotic stress damage process and membrane damage on each data group is explored separately; where applicable, motility and other parameters that contribute to variations in the data sets are also included.

Figures 6.11 are a set of scatter plots of the PC scores that maximise process related variations between data sets in the three data groups HD2, WL and CR2. The PC scores that show separation between processes in the data group HD2 are shown in the two plots in **Figures 6.11a**. The top figure shows the score plots that separate the data sets by grades of osmotic stress damage. The bottom figure is a score plot that separates the data sets by grades of membrane damage. The two plots in **Figure 6.11b** show score plots corresponding to osmotic and membrane damage in the data group WL and the two plots in **Figure 6.11c** show similar plots of CR2 data groups.

Figure 6.12 is a set of plots of statistical variance from all the four data groups in Study Two. The top plot is the variance overlaid from all the data sets in JZ data group. The second plot is the variance from data group HD2, the third from data group WL and the bottom plot is the variance from data group CR2. **Figure 6.13** is a comparison of the major PC coefficients that separate the data sets by process related variations within each data group. The spectral regions that correspond to high magnitude of the coefficients are shown in the plots.

Figure 6.14 is a PCA analysis of the entire 1135 spectra from 1022 cells in the four data groups taken together; the scores that show maximum separation by stallion are depicted. Process related separation or overlap could not be observed; however the PC scores of motile and immotile cells showed some clustering with high overlap (**Figure 6.15**). The plot of the PC coefficients is shown in **Figure 6.16**.

DNA peaks, 785 cm^{-1} and 1050 cm^{-1} and protein peak 1445 cm^{-1} are tabulated in **Table 6.6** for three stallions, to identify process related changes in the peak ratios. Two of the three stallions are common to **Study One** and **Study Two**. The third stallion was randomly chosen as the one with maximum number of spectra per data set.

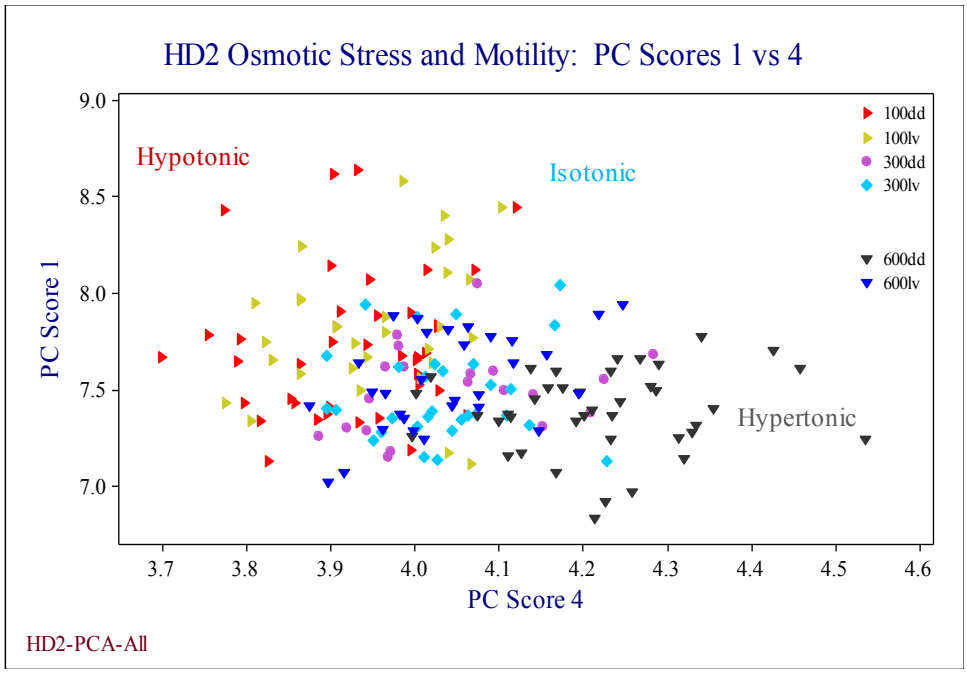

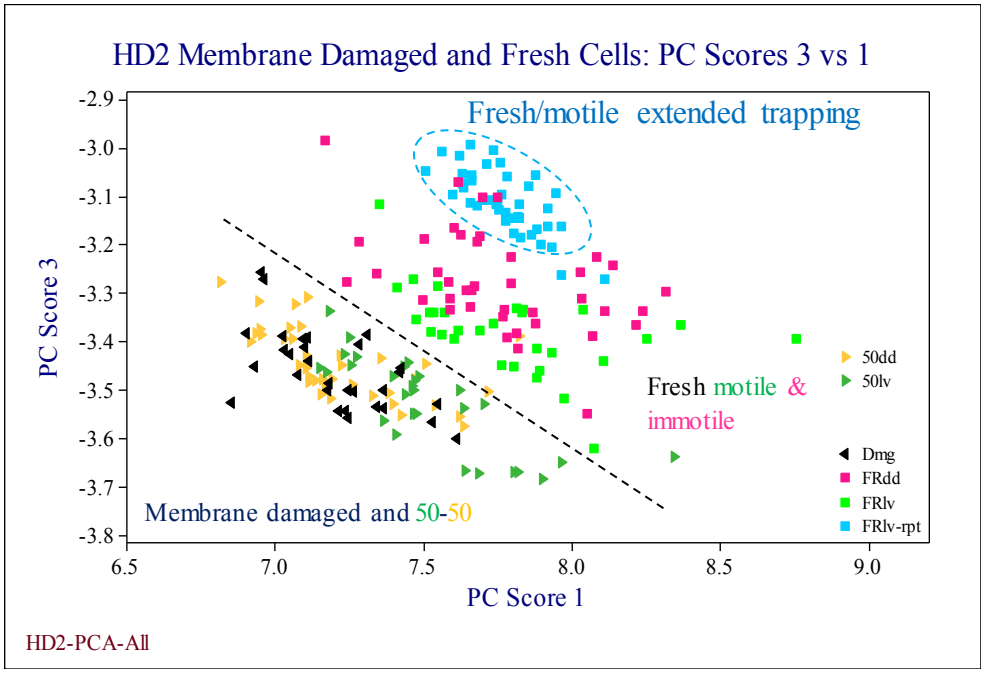

Figure 6.11a: Osmotic stress and membrane damage in HD
(Top) PC scores 4 and 7 of osmotic stress damaged cells
(Bottom) PC scores 1 and 3 of fresh and membrane damaged cells

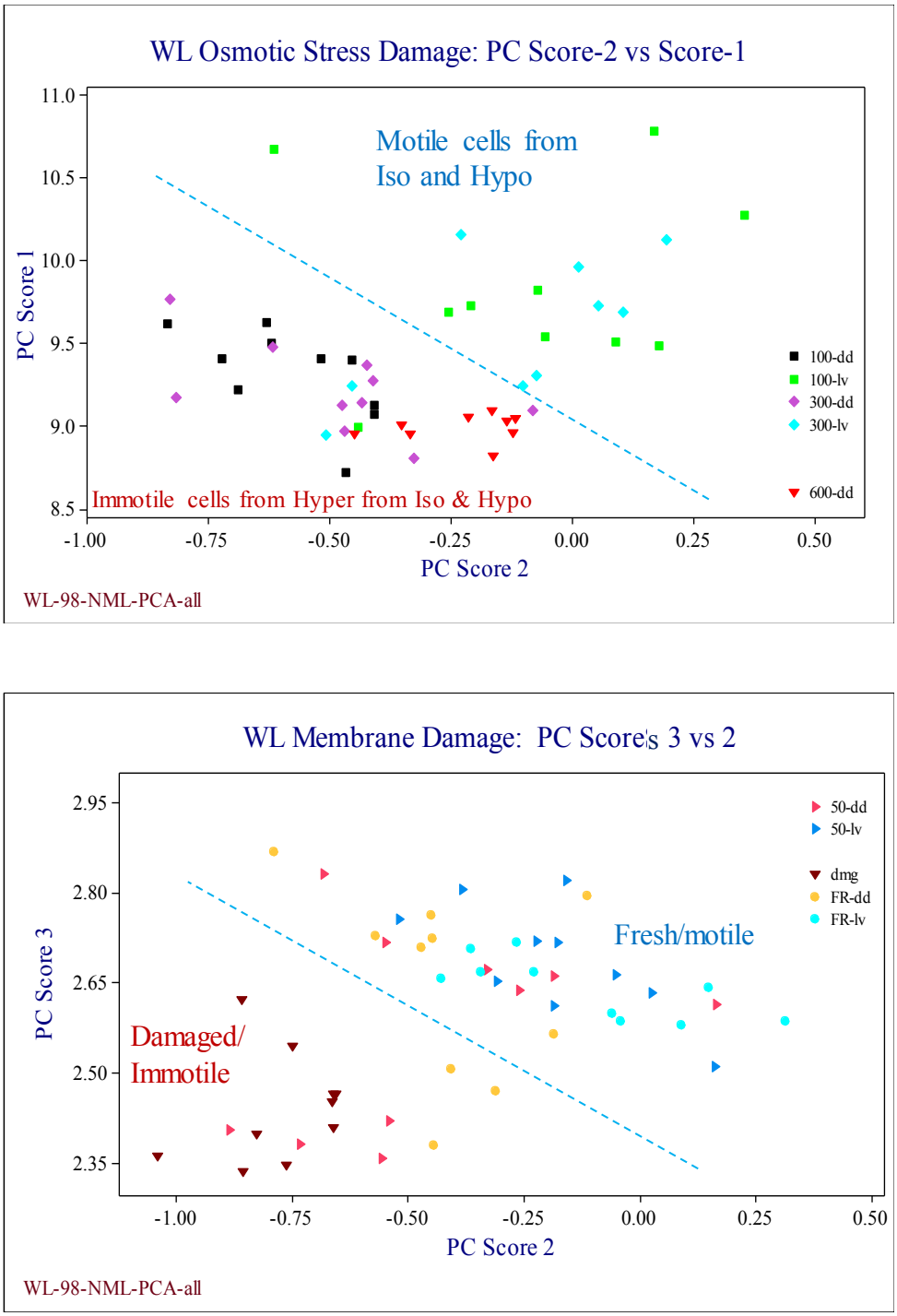

Figure 6.11b: Osmotic stress and membrane damage in WL;
(Top) PC scores 1 and 2 of osmotic stress damaged cells;
(Bottom) PC scores 2 and 3 of fresh and membrane damaged cells.

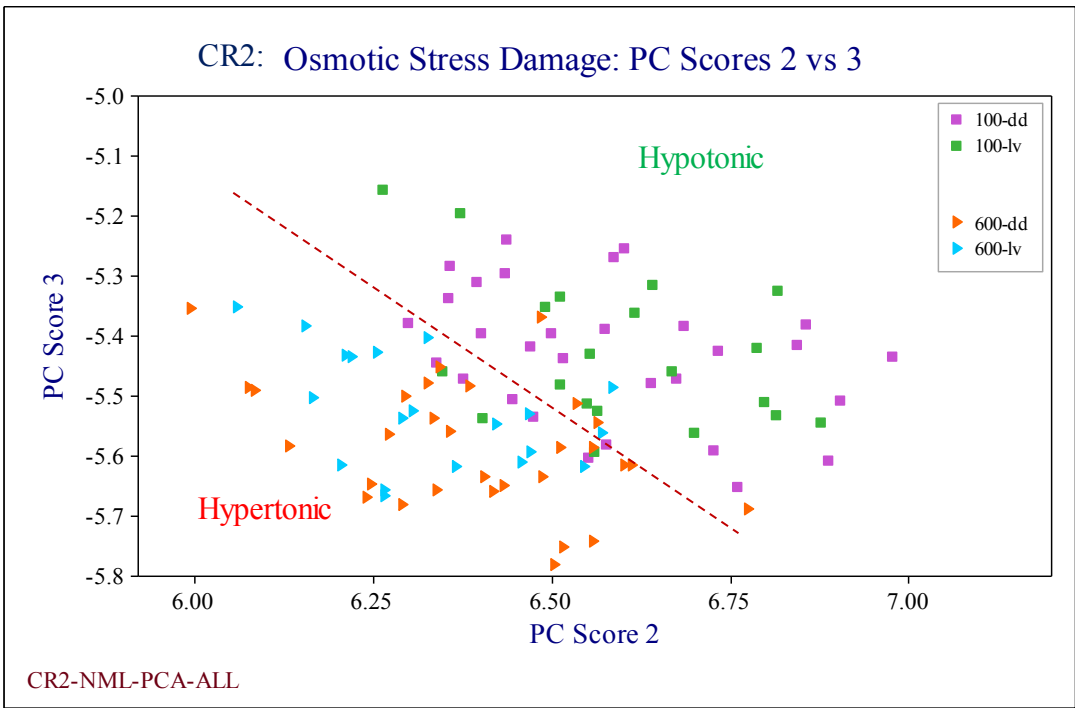

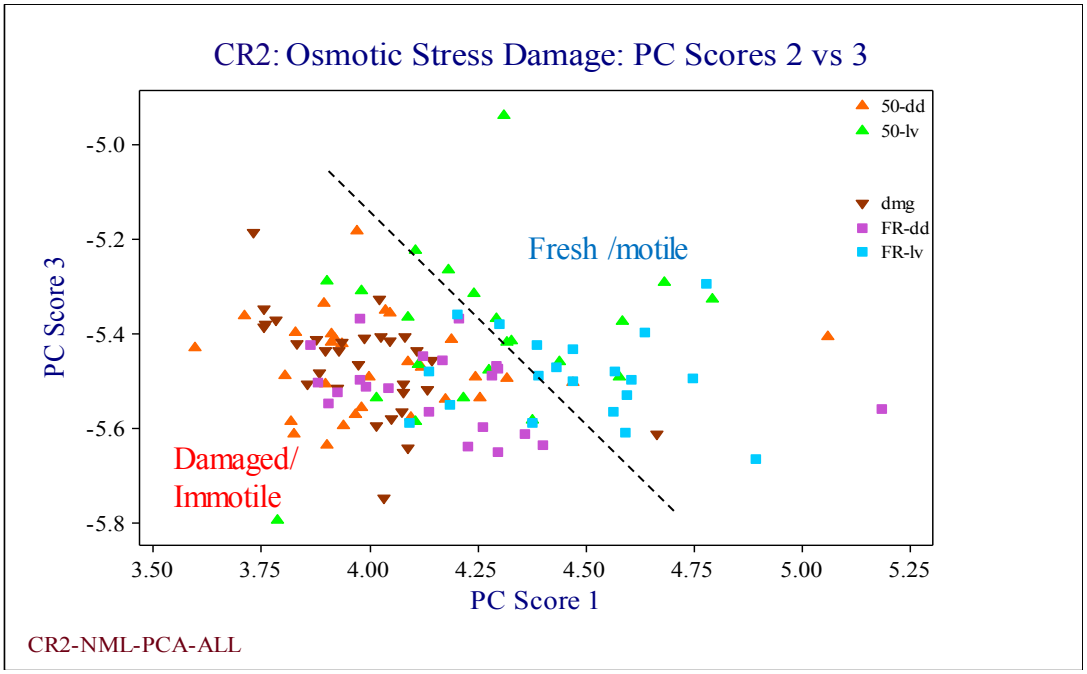

Figure 6.11c: Osmotic stress and membrane damage in CR **(Top)** PC scores 2 and 3 of osmotic stress damaged cells **(Bottom)** PC scores 2 and 3 of fresh and membrane damaged cells.

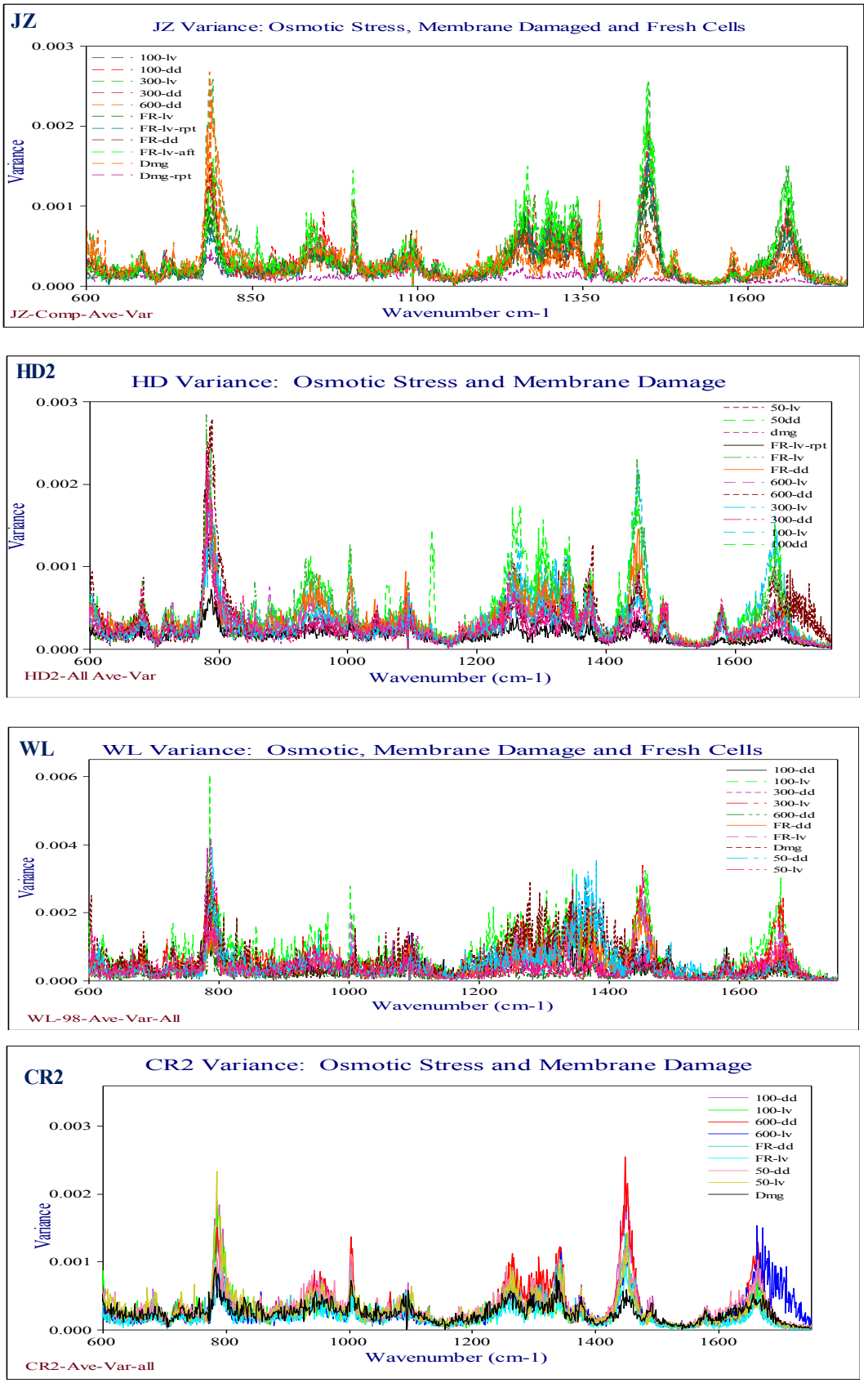

Figure 6.12: Comparison of Variance in the four data groups JZ, HD2, WL & CR2.

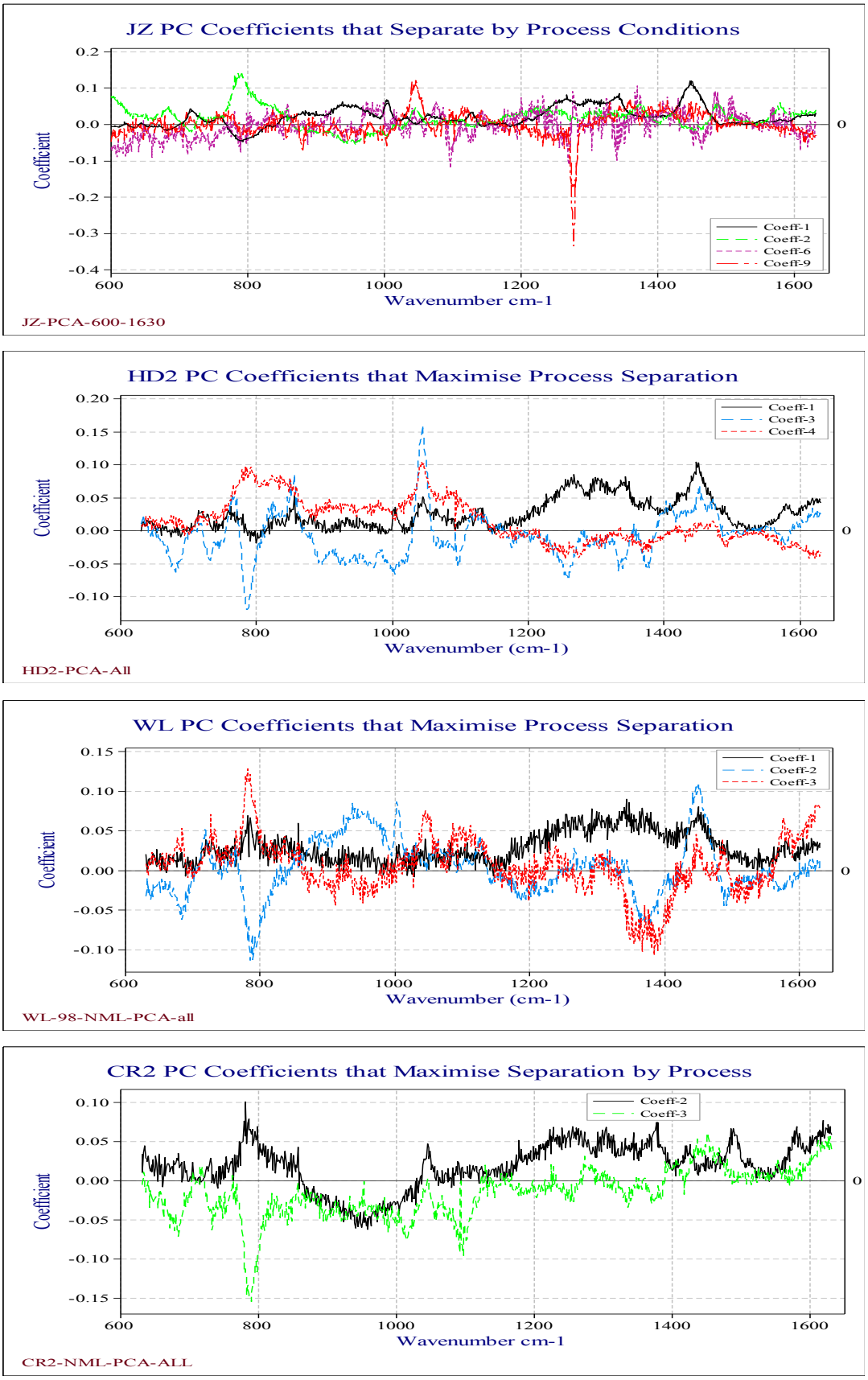

Figure 6.13: Comparison of PC Coefficients of data groups that separate processes.

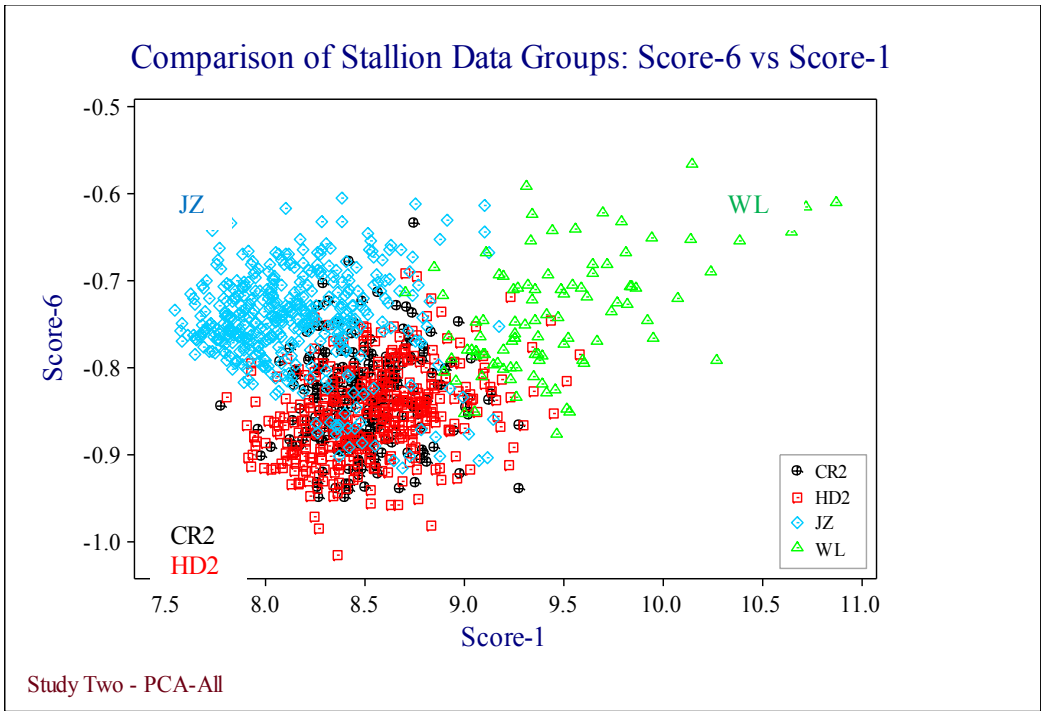

Figure 6.14: Plot of PC Scores that show clusters by stallions/data groups.

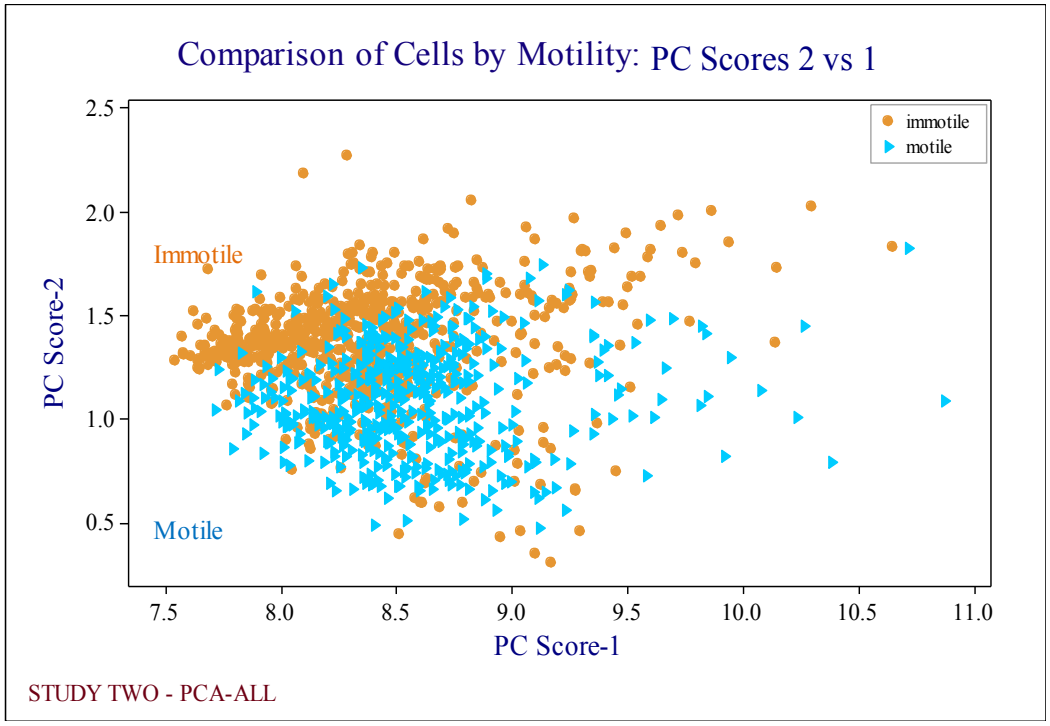

Figure 6.15a: Plot of PC Scores that group motile and immotile cells.

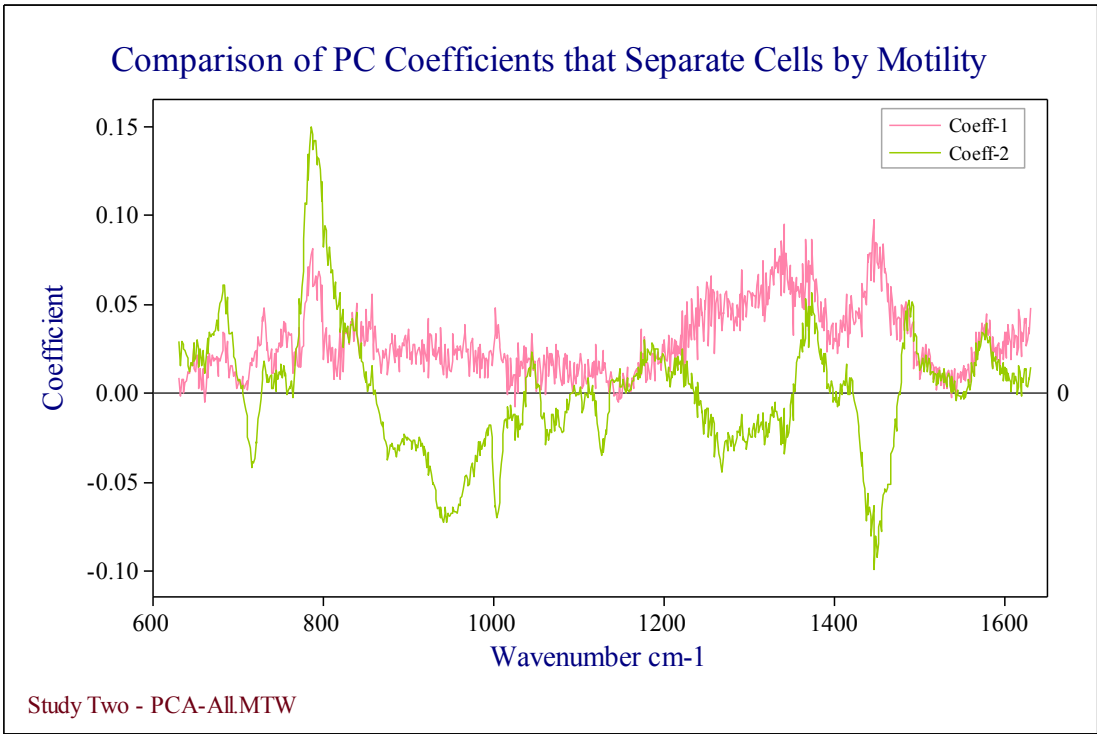

Figure 6.15b: Plot of PC coefficients that show separation of cells by motility

Description	JZ	WL
Variance max	~ 0.0027 at 785, 0.0025 at 1445 (0.0003 max at dmg-rpt)	~ 0.006 at 785 cm^{-1}
All variance (in cm^{-1})	680, 725-730, 785, 830, 856, 880, 920-980, 1004, 1060, 1088, 1128, 1175, 1260, 1295, 1335, 1375, 1445, 1486, 1575	650, 680, 730, 785, 956, 1005, 1095, 1250-1400, 1445, 1490, 1580
High variance (in cm^{-1})	785, 1004, 1260, 1295, 1335, 1375, 1445	Noisy 785, 1004, 1375, 1445
Common variance (in cm^{-1})	680, 725, 775-795, 950, 1001, 1090, 1260-1300, 1340, 1375, 1445, 1490, 1575	
Regions of high PC Coefficients	680, 720, 785, 850s, 880, 935b, 1001s, 1043s, 1098, 1125, 1260s, 1300,1338, 1375, 1445, 1489, 1575	680, 725, 785, 890, 950b, 1002s, 1045, 1090s, 1170, 1250, 1300, 1345, 1375, 1445s, 1485s, 1575s
Common PC coefficients	680, 720 - 725, 785, 880-890, 935-950, 1002, 1043 - 1045, 1098, 1250-1260, 1300, 1338-1345, 1375, 1445 – 1450, 1485 – 1490, 1575	
High PC coeff	785, 1002, 1230-1345, 1375, 1445-1450	
Description	**HD2**	**CR2**
Variance max at	~ 0.0028 at 785 cm^{-1}	~ 0.0023 at 785 cm^{-1} and 0.0026 at 1445 cm^{-1}
All variance (in cm^{-1})	680, 725, 785, 850, 880, 935, 1001, 1088, 1125, 1180, 1260, 1300, 1340, 1375, 1445, 1486, 1575,	680, 725, 785, 890, 950, 1001, 1088, 1170, 1250-1300, 1345, 1375, 1445, 1486, 1575
High variance (in cm^{-1})	680, 785, 935, 1001, 1260, 1300, 1340, 1375, 1445	785, 935, 1002, 1265, 1340, 1445, 1375, 1445
Common variance (in cm^{-1})	680, 725, 775-795, 950, 1001, 1090, 1260-1300, 1340, 1375, 1445, 1490, 1575,	
Regions of high PC Coefficients	686, 720, 760, 785, 850s, 880 - 1000, 1002s, 1045s, 1095, 1175 , 1256b, 1301, 1335, 1375s, 1445s, 1490, 1575	680, 730, 785, 840, 950b, 1014, 1045, 1090, 1175s, 1228b, 1256b, 1300b, 1336b, 1375, 1420, 1450, 1490s, 1580s
Common PC coefficients	680 - 686, 720-730, 785, 1002-1014, 1045, 1095, 1175, 1256b, 1300, 1335, 1375, 1445 - 1450, 1495, 1575 - 1580,	
High PC coeff	680, 785, 1045, 1375	

Table 6.8: Summary of the Variance and PCA analyses of the four data groups (Abbreviations: ps – partial separation, s- strong)

DNA and Protein Peak Ratios (Average)						
Stallion	**785**	**stdev**	**1055**	**stdev**	**1445**	**stdev**
JZ-100-lv	1.03	0.031	0.43	0.014	0.48	0.032
JZ-100-dd	1.04	0.037	0.43	0.014	0.46	0.039
JZ-300-lv	1.06	0.049	0.44	0.014	0.47	0.047
JZ-300-dd	1.07	0.029	0.43	0.014	0.43	0.044
JZ-600-dd	1.15	0.044	0.45	0.017	0.46	0.024
JZ-FR-lv	1.05	1.032	0.44	0.018	0.49	0.038
JZ-FR-dd	1.08	0.039	0.43	0.014	0.43	0.028
JZ-dmg	1.11	0.052	0.44	0.017	0.41	0.021
HD2-100-dd	1.01	0.043	0.44	0.016	0.50	0.044
HD2-100-lv	1.07	0.041	0.44	0.014	0.52	0.046
HD2-300-dd	1.12	0.042	0.44	0.018	0.47	0.022
HD2-300-lv	1.09	0.041	0.43	0.014	0.48	0.025
HD2-600-dd	1.13	0.047	0.44	0.014	0.46	0.027
HD2-600-lv	1.08	0.046	0.44	0.016	0.49	0.029
HD2-FR-dd	1.10	0.038	0.46	0.019	0.49	0.034
HD2-FR-lv	1.09	0.046	0.44	0.016	0.51	0.048
HD2-dmg	1.11	0.037	0.42	0.019	0.43	0.017
CR-100-dd	1.08	0.044	0.44	0.015	0.5	0.043
CR-100-lv	1.07	0.043	0.43	0.016	0.51	0.031
CR-600-dd	1.08	0.039	0.44	0.015	0.47	0.051
CR-600-lv	1.07	0.024	0.44	0.018	0.48	0.035
CR-FR-dd	1.08	0.022	0.44	0.014	0.47	0.038
CR-FR-lv	1.07	0.026	0.44	0.013	0.50	0.028
CR-dmg	1.1	0.027	0.43	0.016	0.45	0.022

Table 6.9: DNA peak/band intensities at 785 cm^{-1} and 1050 cm^{-1} and the protein peak 1445 cm^{-1} are tabulated for three stallions, to identify process related changes in the peak ratios and compare with published reports.

6.3 *Raman Spectroscopic Analyses of Human Sperms*

The Raman spectra of three categories of human sperms are examined in this exploratory work. A typical Raman spectrum of a freshly prepared, motile human sperm cell is shown in **Figure 6.16**. The molecular assignment is the same as that of the stallion sperm shown in **Figure 6.4**. A low magnification webcam image of the cells in suspension is embedded in the figure.

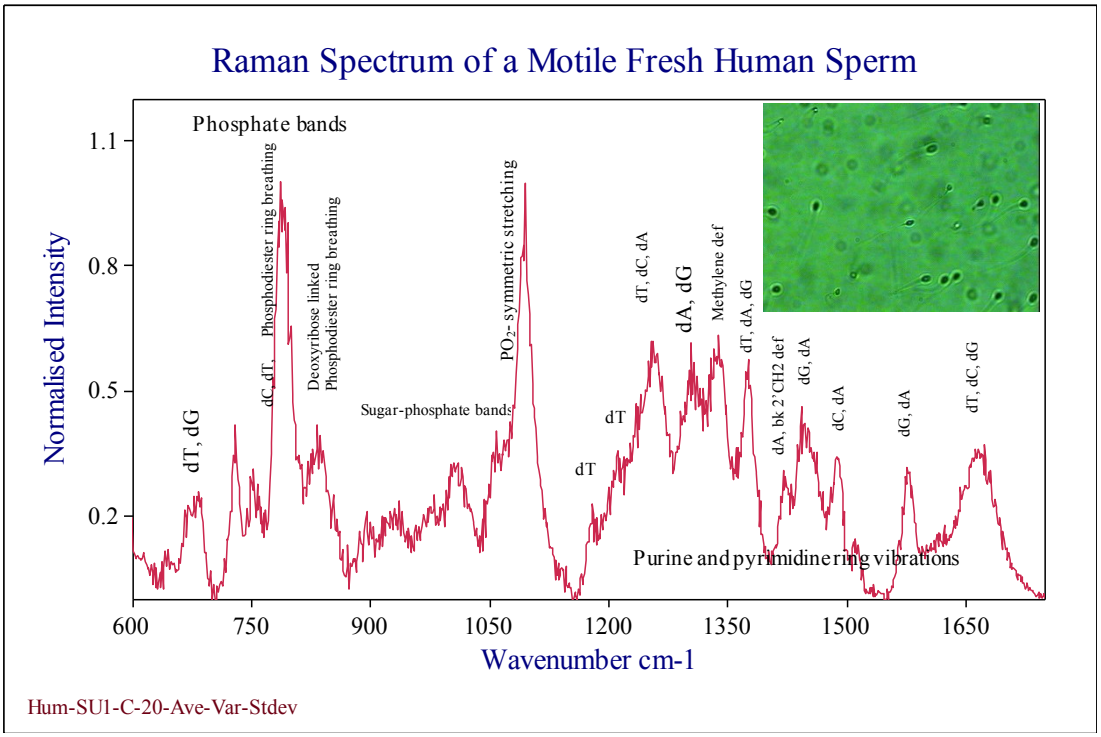

Figures 6.16: Raman spectrum of a live motile freshly prepared human sperm. A low magnification webcam image of human sperms in suspension is inlayed in the spectrum.

The three categories used in the study are:

FR freshly prepared specimens of unknown fertility;
SU sperms with high PM extracted using the swim-up technique;
FZ a cryopreserved donor specimen of normal fertility.

The spectra from some of the eight specimens were grouped into 'motile' and 'immotile' cells with 'lv' denoting motile and 'dd' denoting immotile cells.

There were eight specimens in the three categories. The three FR specimens were remnants from the andrology lab and were from different men; these cells had normal morphology and a range of sub-normal sperm count. The four swim-up (SU group) samples included a remnant from the fertility clinic, SU, and the remaining samples (SU1, SU2 and SU3) were specimen from the andrology lab. The single FZ specimen from the fertility clinic was the remnant from a donor of known fertility. Twenty data sets with approximately 20 cells per data set were used in this study, with a total of 406 spectra acquired for statistical analysis.

Three processes were examined in a limited way on some of these specimens, as the access to these specimens could not be planned in advance. The processes were

- day1 motile vs 'other days';
- disintegration with time – day1, day2, day3 and day4;
- day1 oxidative stress.

Extended trapping was tested on two cells – a fresh motile cell and a day4 immotile cell. The data sets, categories and process conditions are tabulated in **Table 6.10.**

The statistical method used is the same as the ones used for stallion sperms; Raman spectra of sperm cells were acquired in the energy range ~ 200 cm^{-1} to 1900 cm^{-1} and the analyses was completed using the region, 630 cm^{-1} to 1630 cm^{-1}. F-values were used to identify the PC scores responsible for maximum clustering/separation by process. Plots of variance and PC coefficients of the data sets are shown in the range, 600 cm^{-1} to 1650 cm^{-1}. Statistical analysis including PCA are summarised in **Figures 6.17** to **6.28**.

Specimen/data set	Day 1	Time series				Peroxide		Extended trapping	Comments (20 data sets and 406 spectra)
		Motile Day 2	Immotile Day 2	Motile Day3	Immotile /Day4	1 mMol	2 mMol		
FR	21							21	
FR1	21								
FR2	19	20	20	20	21			20/ Day4	Ext trp on dy4 immotile cell
FZ	20			20					Fertility Clinic
SU	23								Fertility Clinic
SU1	20					20	19		
SU2	20						20		
SU3	20					20	22		

Table 6.10: Human sperm data sets, test conditions and the number of spectra.

The three process conditions are examined in some detail using statistical variance and PCA. Many of the datasets from 'day1' were not separated by motility and were acquired within 24 hours. The cells exposed to oxidative stress were also not separated by motility. The eight specimens, listed in column one in **Table 6.10** were further grouped into four categories - 'fresh', 'swim-up', 'cryopreserved' and 'stressed'.

Statistical analyses of the spectral data sets taken on day 1 that were not exposed to any processes are reviewed in **Figures 6.17**. **Figure 6.17a** is a panel of plots that show statistical variance by specimens taken within 24 hours of obtaining them. Plot **A** in the panel shows the variance of spectra from all the unprocessed specimens including the variance in the spectra from extended trapping. The spectra of cells from 'swim-up' exposed to oxidative stress are not included. Plot **B** shows the

variance from 'swim-up' specimens. Plot C shows variance of the three FR specimens and plot **D** shows variance from the cryopreserved sample. The results of PCA and F-value analysis of the corresponding day1 data sets by specimen and category are shown in **Figure 6.17b**. The plot of the PC coefficients of these data sets is shown in **Figure 6.17c**.

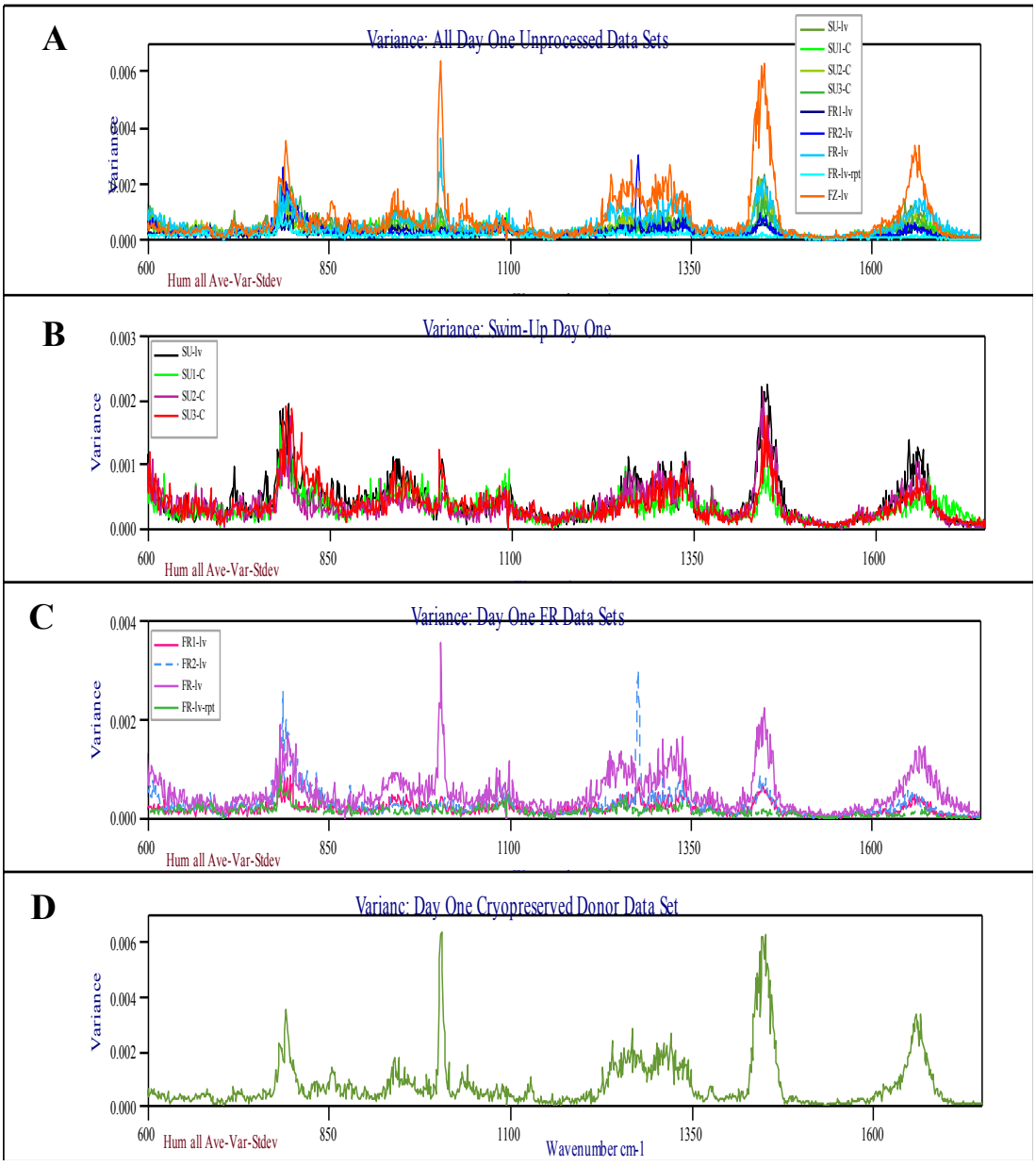

Figures 6.17a: Panels show variance of spectra from 8 specimens grouped by specimens and category **A:** all nine 'day1' groups not exposed to stress **B:** swim-up **C:** FR **D:** FZ specimen

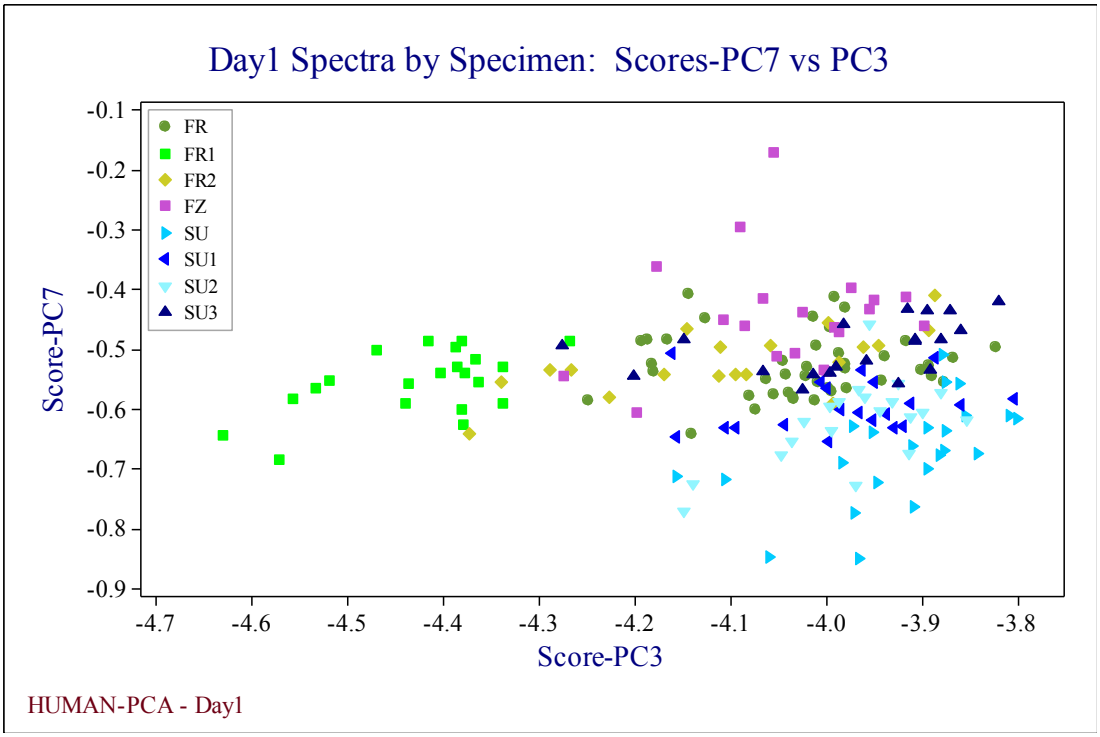

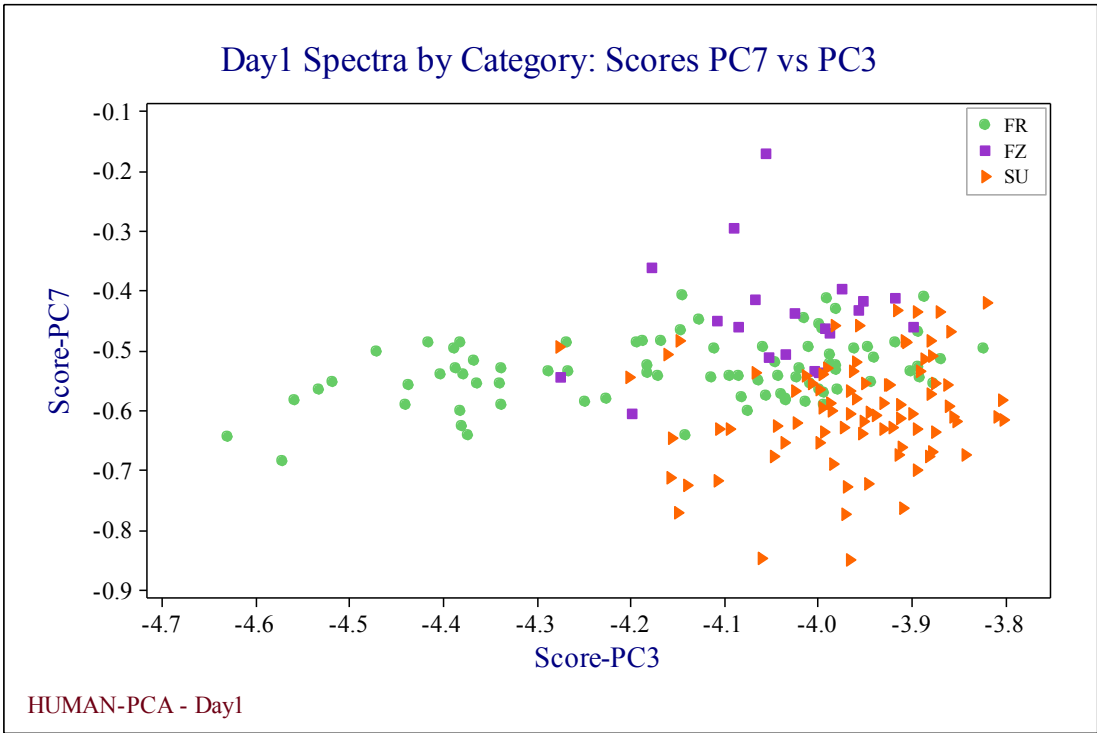

Figure 6.17b: (Top) Plots of PC Scores of unprocessed Day1 data sets **(Bottom)** PC scores by specimen category

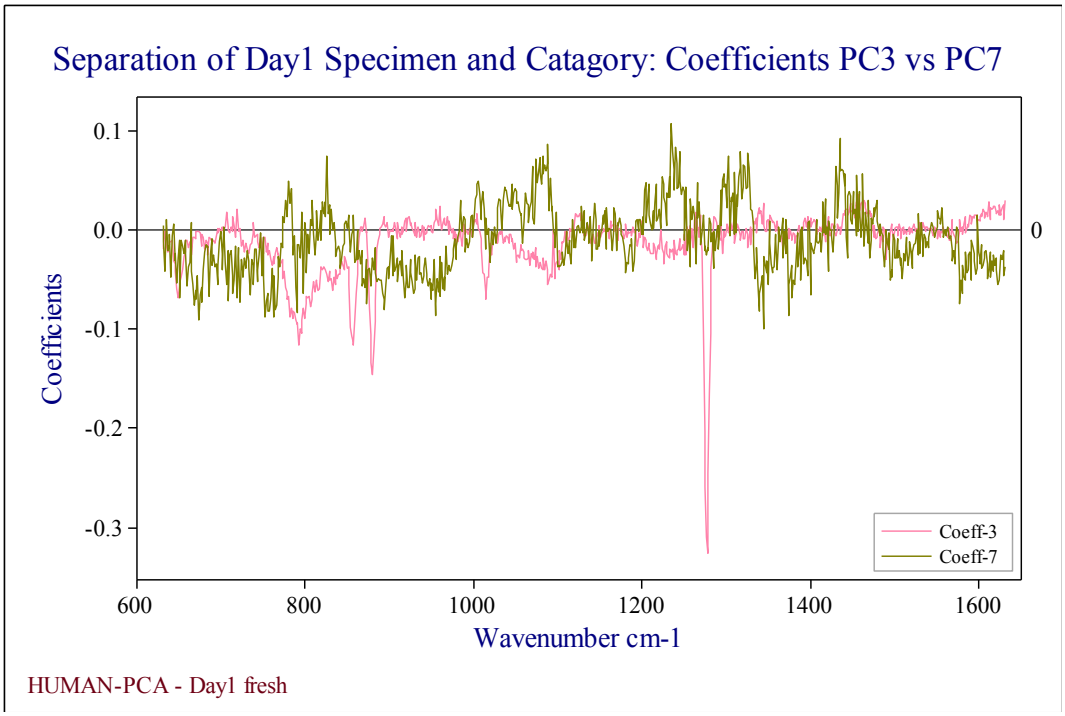

Figure 6.17c: Plots of Coefficients of the PCs that separate the Day1 unprocessed specimens by category and specimens

Comparison is made between 'Day1' and 'Other days' to identify deterioration in sperm quality after 24 hours in the sperm media. **Figures 6.18a** and **6.18b** show the statistical variance and PC plots that represent the spectra from cells taken on Day1 versus the spectra taken on other days – Day2 to Day4. The panel in **Figure 6.18a** shows three categories of variances investigated. The variance of all the data sets from 'day1' is plotted in the top panel. The middle panel shows the variance of all the data sets from day2 to day4. The bottom panel includes all day2-day4 and the stressed samples from day1. The results of PC scores and coefficients using F-value analysis of the corresponding data sets are shown in **Figure 6.18b**.

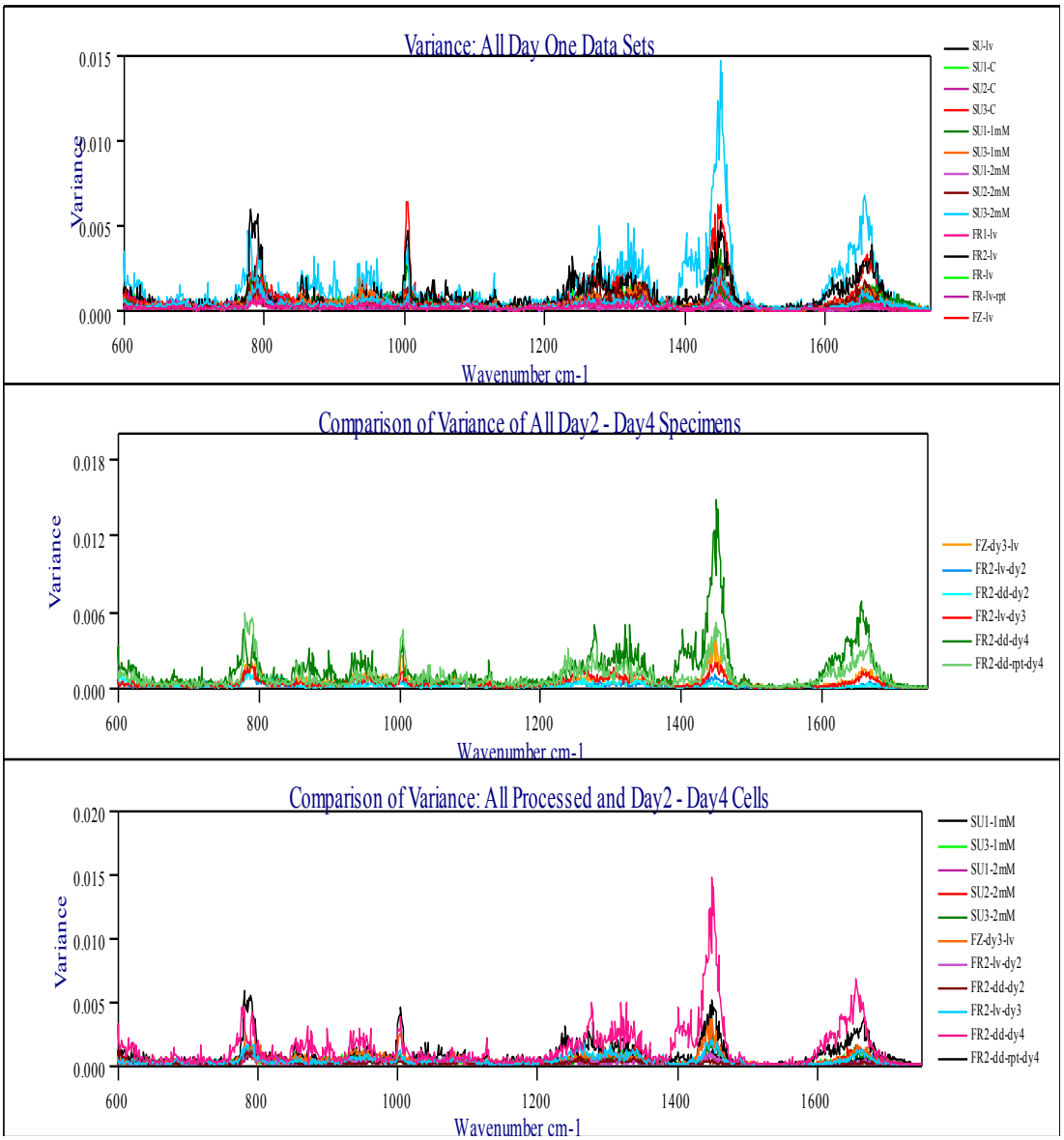

Figures 6.18a: Statistical variance plots (**Top**) Day1, (**Middle**) Day2 - Day4 and (**Bottom**) all specimens.

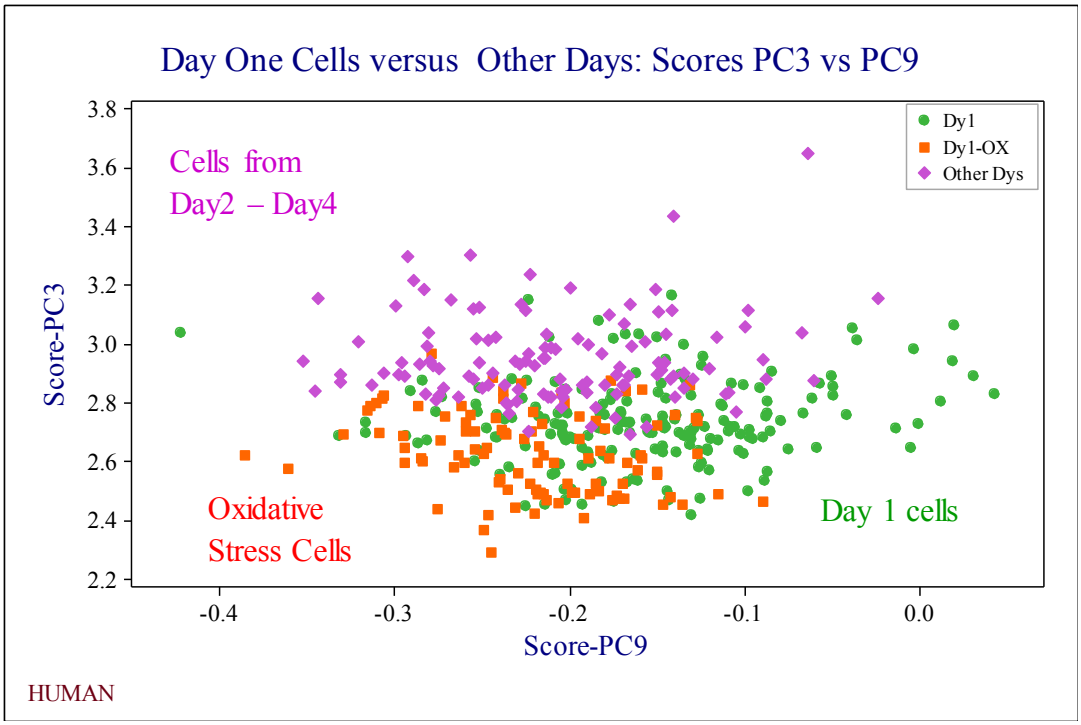

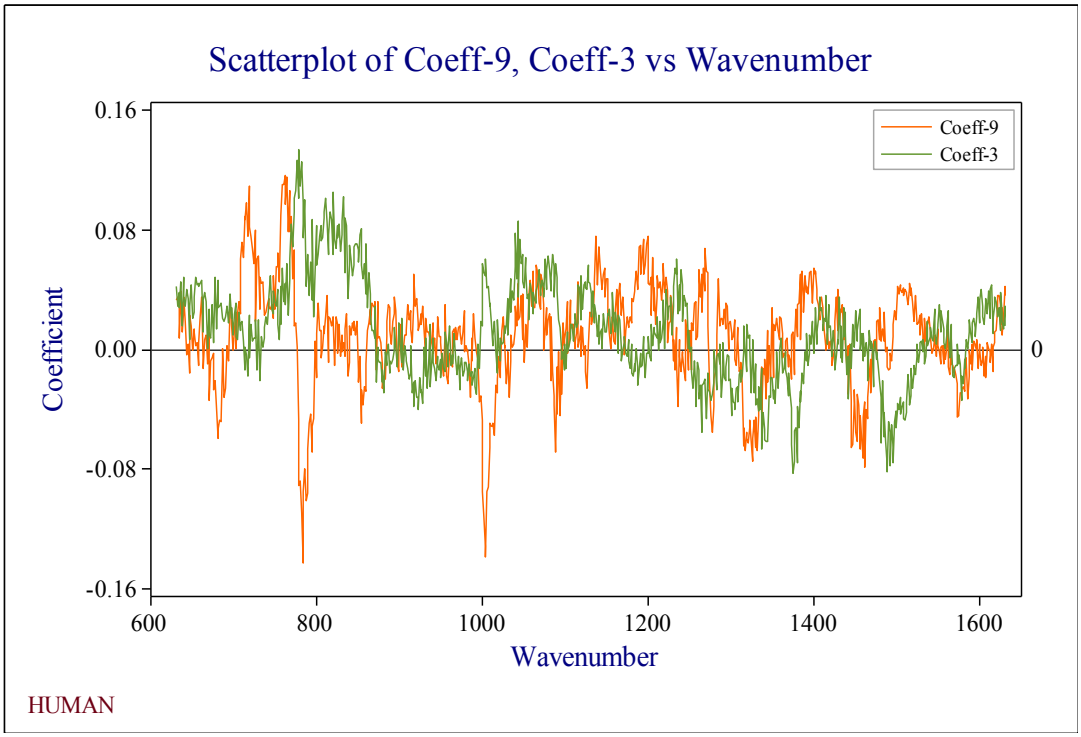

Figure 6.18b: **(Top)** Plot of PC Scores that group Day1 vs other days and processes. **(Bottom)** Coefficients of PC 3 & 9 as a function of wavenumber.

Cell disintegration with time was tested on two specimens (FR2 and FZ) kept at laboratory temperature for four days. Raman spectra were acquired once a day on a droplet from the specimen FR2. These processes were identified as day1 or dy1, day2 or dy2, day3 or dy3 and day4 or dy4 in the data sets. There were no motile cells on the fourth day. Spectra could only be acquired on 'day1' and 'day3' from the FZ specimen. Variance and PCA of data sets, separated by 'Days', are shown in **Figures 6.19.**

The 'swim-up' specimens Su1, Su2 and Su3 were exposed to oxidative stress using hydrogen peroxide. Samples from these specimens were incubated in 1mMol and 2mMol of hydrogen peroxide for 60 minutes each, then extracted and re-suspended in the sperm media. The spectra from the stressed cells are identified as 1mMol or 1mM and 2mMol or 2mM respectively in this chapter. All three specimens were exposed to '0' and 2mM oxidative stress; Su1 and Su3 were exposed to 1mM of oxidative stress; Su2 could not be exposed to 1mM oxidative stress. **Figures 6.20** is a plot showing PC scores of the datasets that maximise the separation by processes. Plot of oxidative stress is shown at the top. PCA of the data sets by all the process conditions – stress, day2, day3 and day4 are shown in the bottom figure. The same PC scores that maximised the data set separation by stress also contributed to the separation by all the process conditions.

Statistical variance, PCA and F-value were used to identify the scores that separated all the data sets by specimen and category (**Figures 6.21)**. PC scores that separate the data sets by motility are shown in **Figures 6.22.** The cells were grouped into motile (lv), immotile (dd) and unseparated by motility (x).

Extended trapping is also examined on motile cells from a FR day1 dataset cells and from a day4 dataset. The plot of the spectra, variance and PCA are shown in **Figures 6.23 - 6.25**.

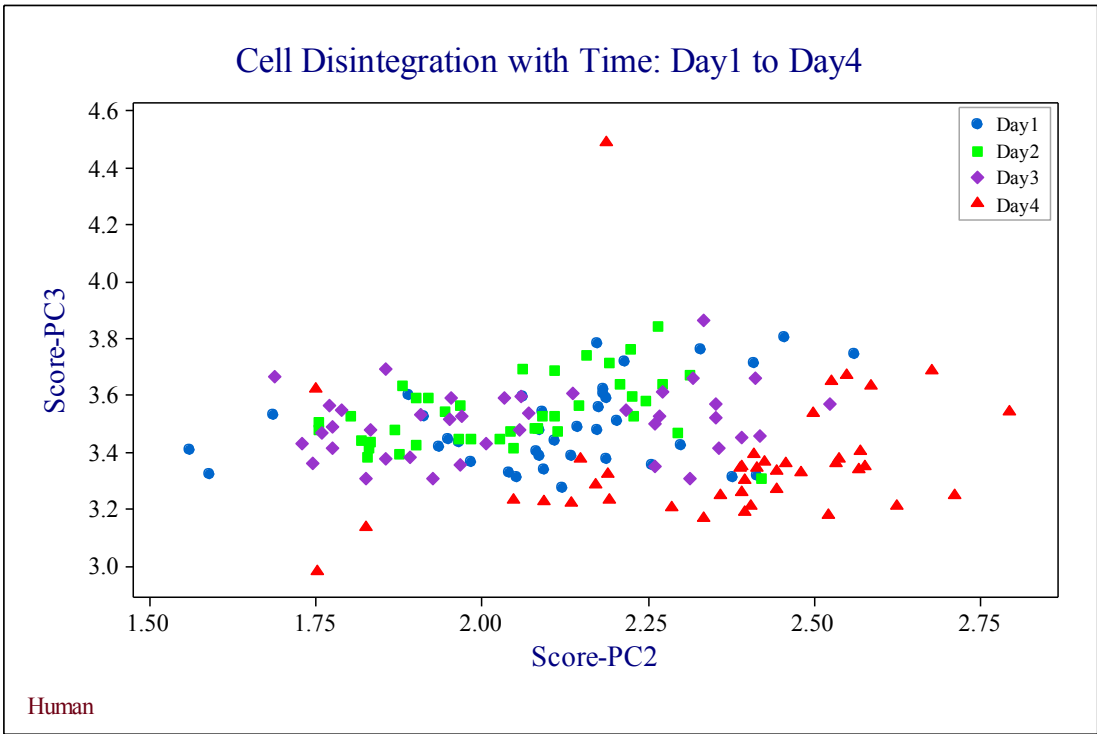

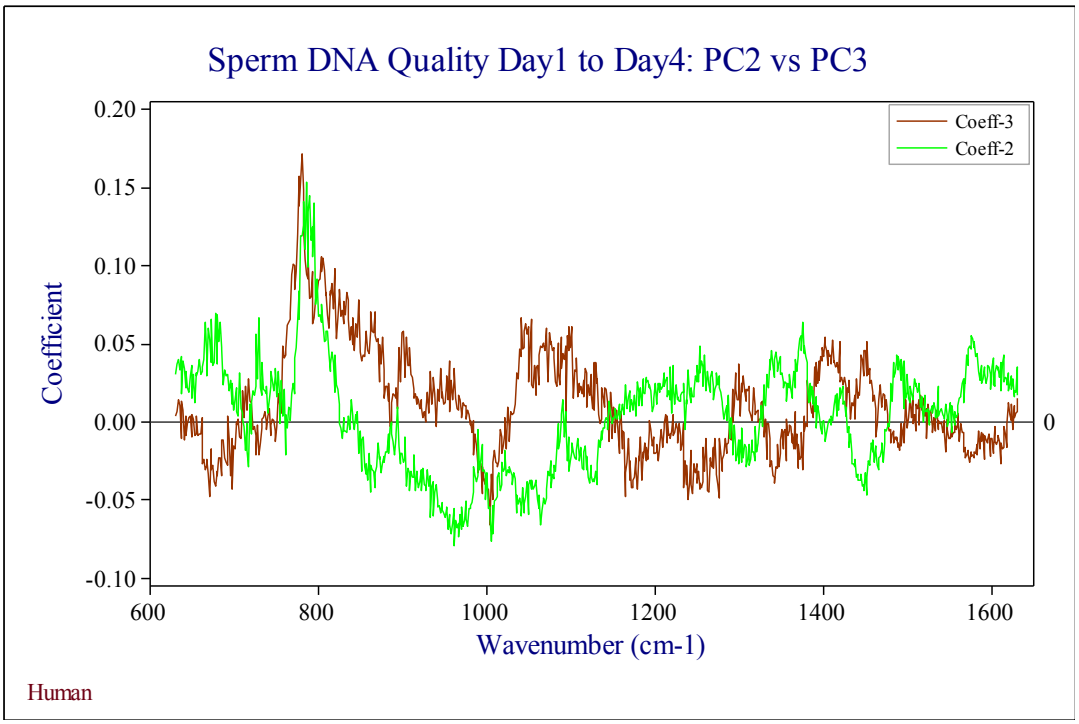

Figure 6.19: Changes in sperm cells by day **(Top)** PC scores **(Bottom)** PC coefficients

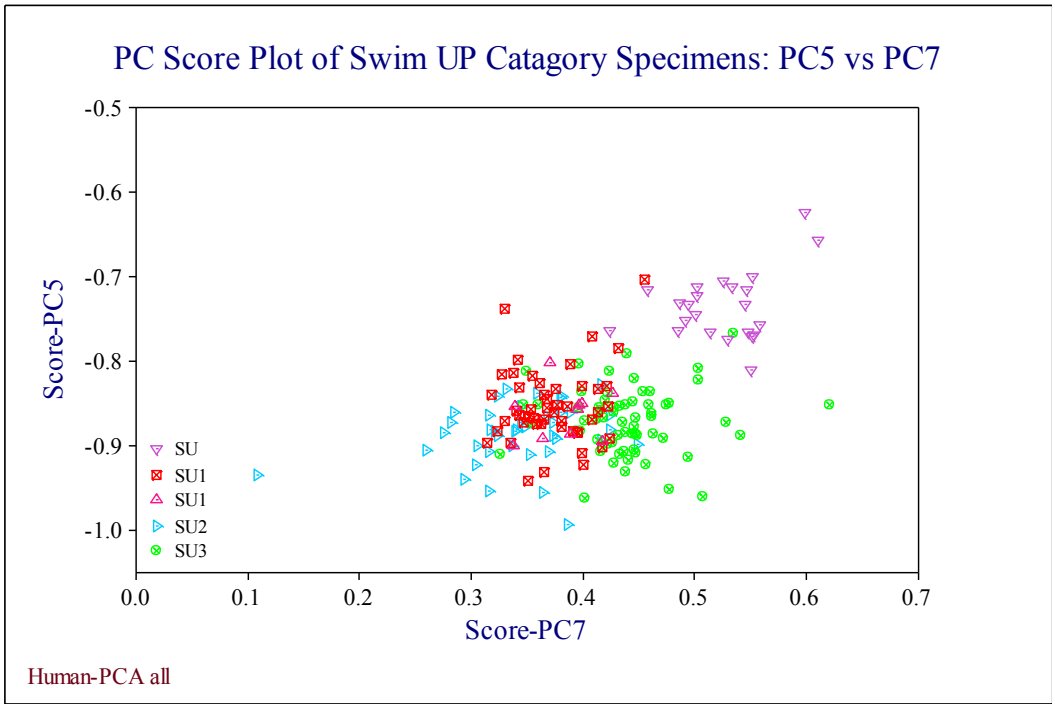

Figures 6.20: Swim-up category of data sets grouped by specimens

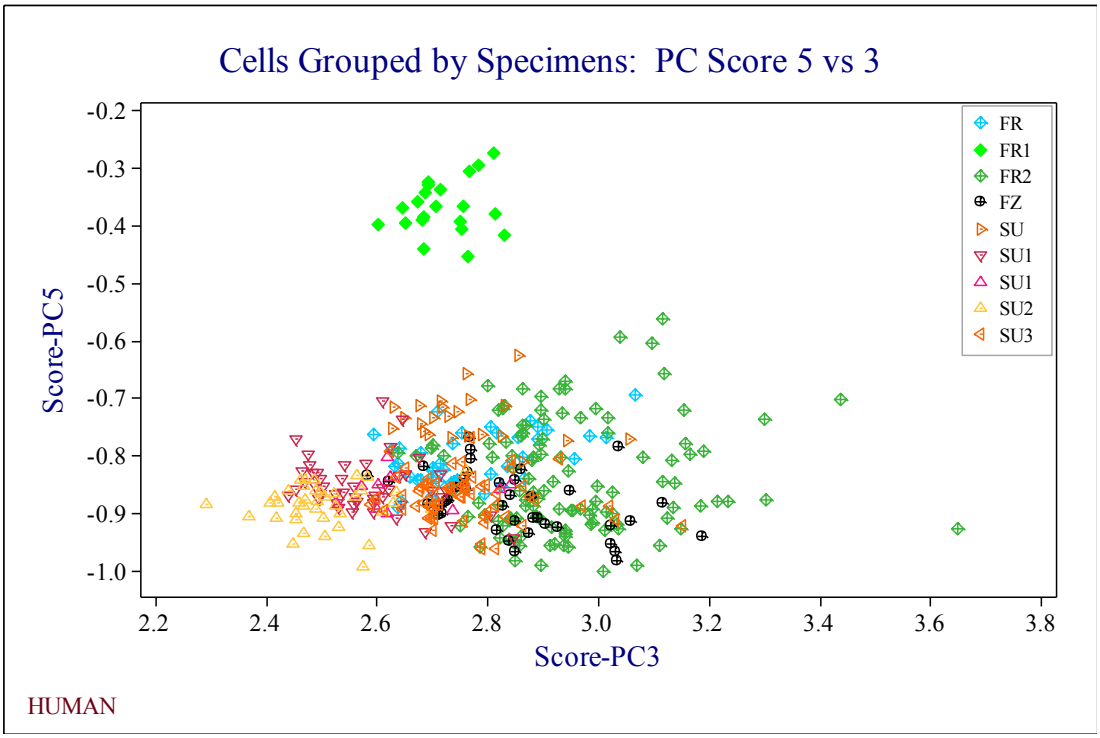

Figure 6.21a: Plots of PC Scores of all the datasets grouped by specimen

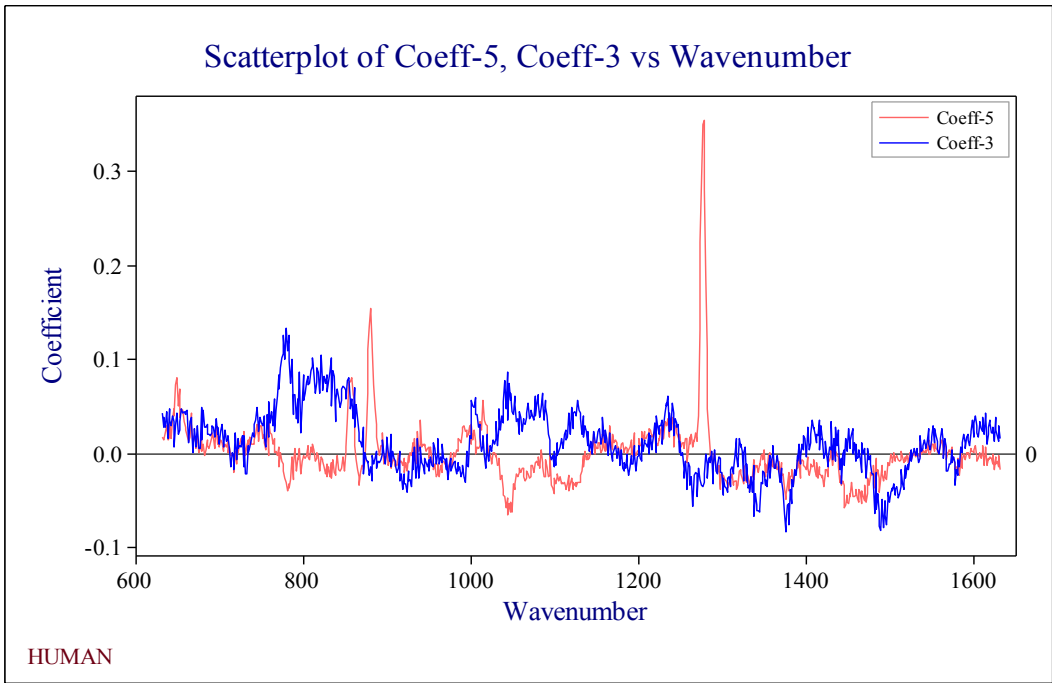

Figure 6.21b: Plots of coefficients that separate by specimens

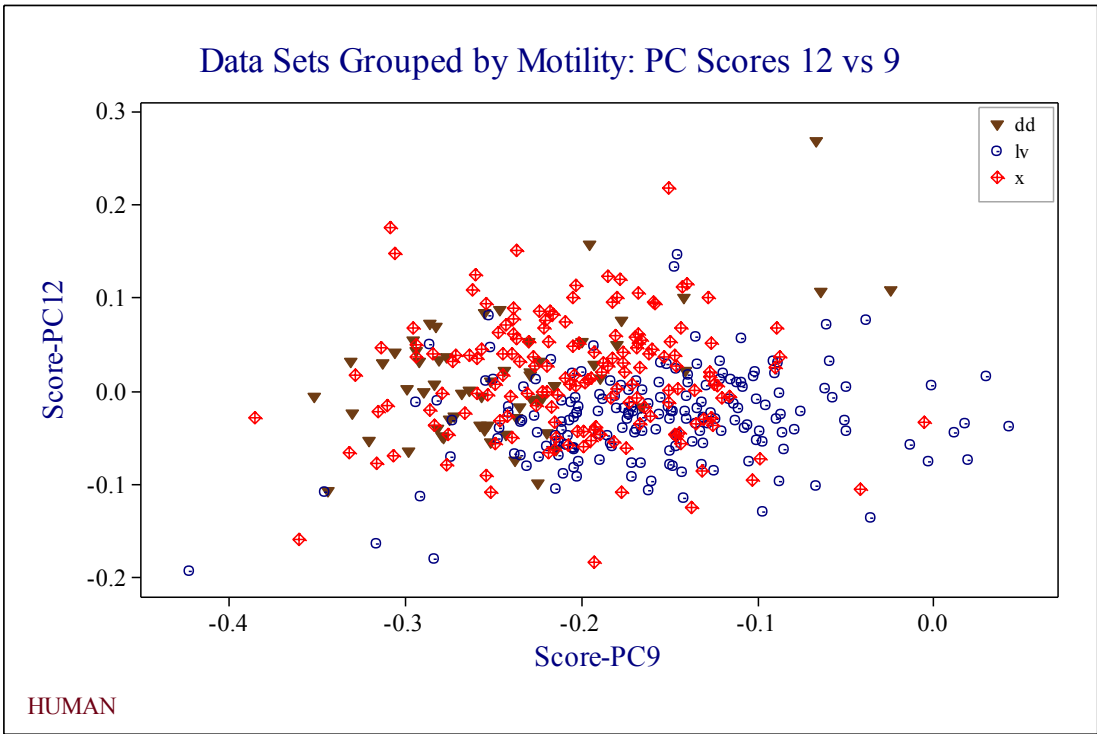

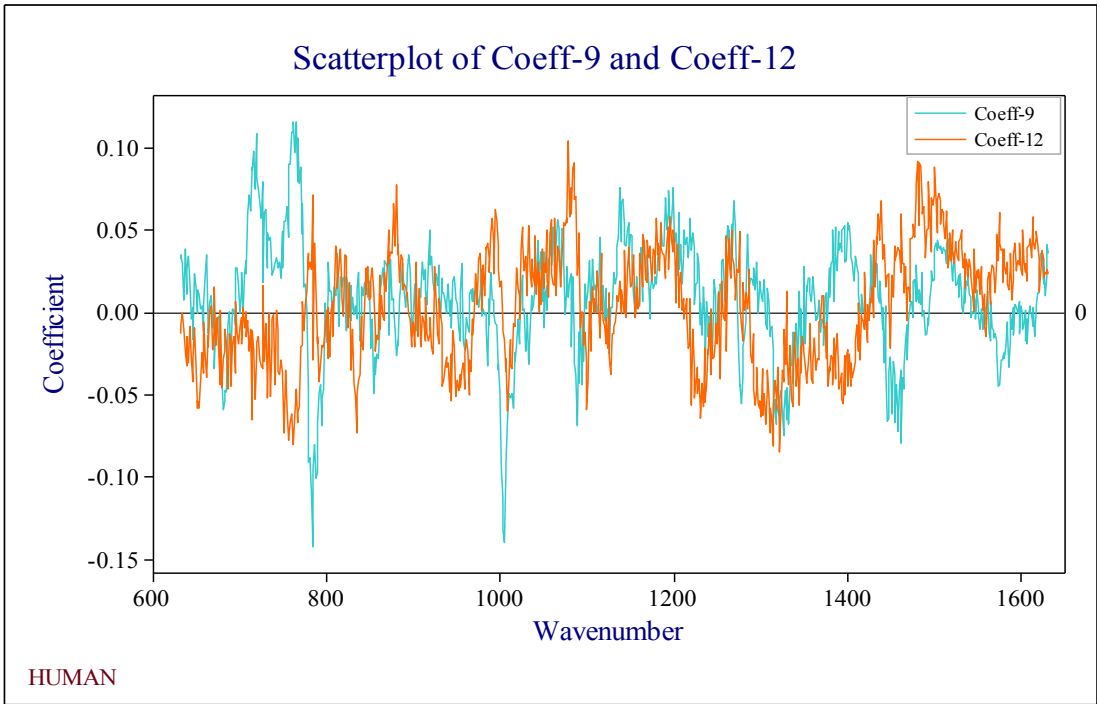

Figure 6.22: Plot of PC (**Top**) Scores and (**Bottom**) Coefficients that separate motile and immotile cells

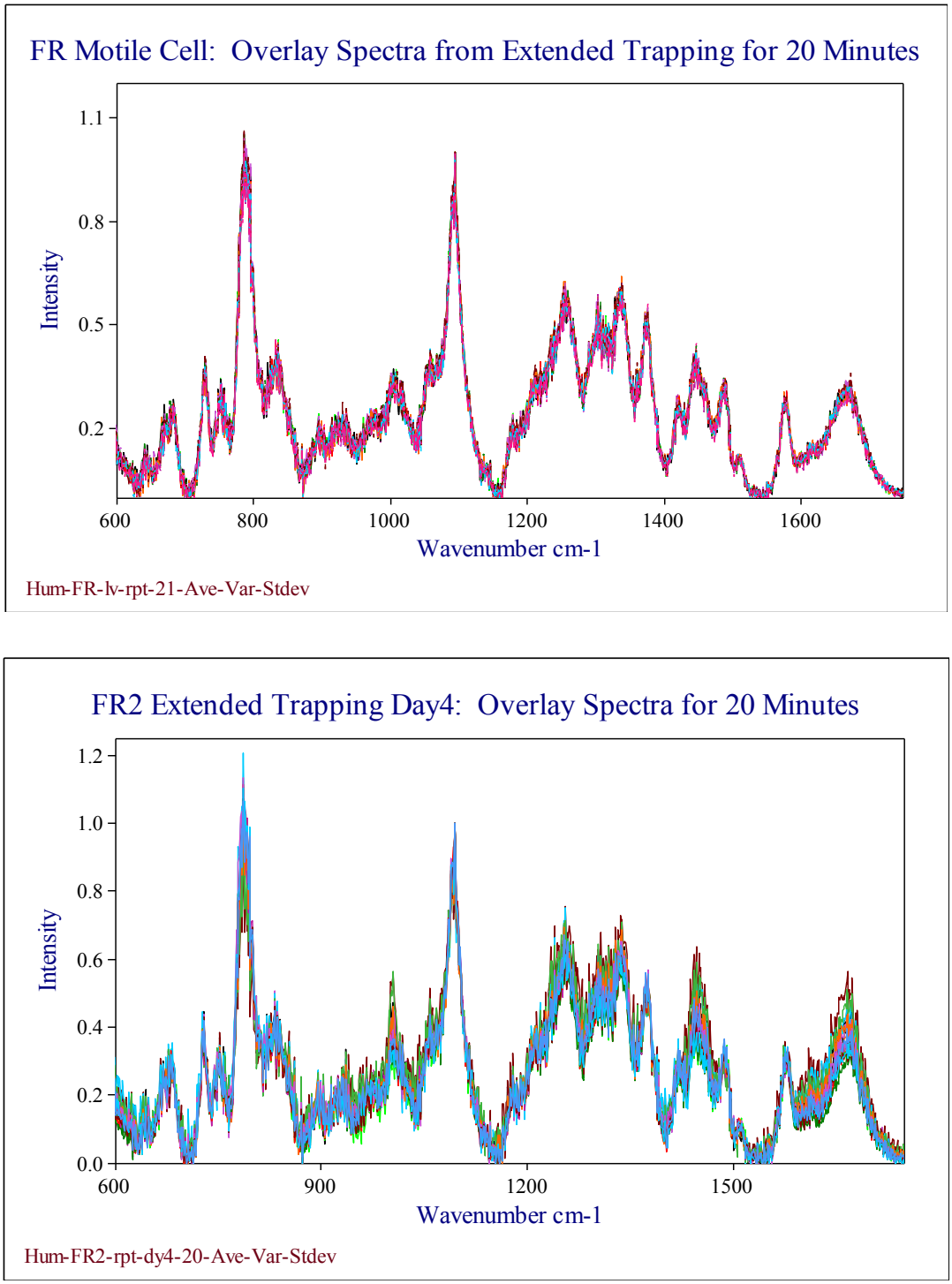

Figures 6.23: Overlay spectra from extended trapping (**Top**) FR motile Day1 (**Bottom**) FR2 Day4 specimens

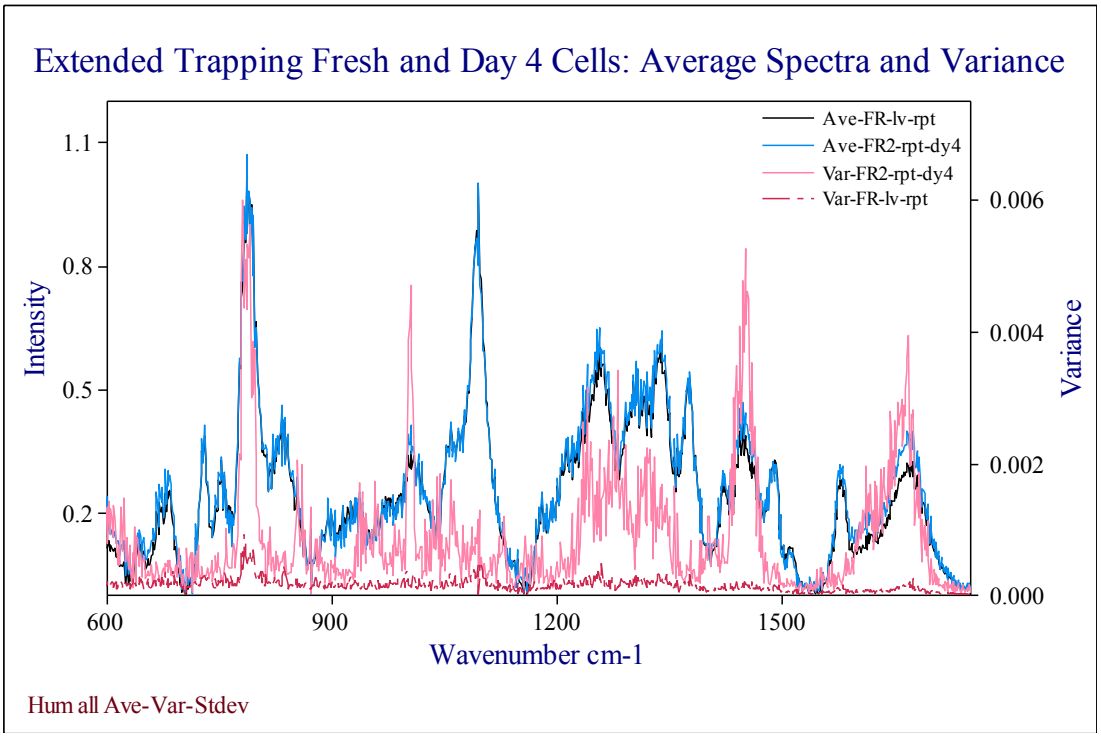

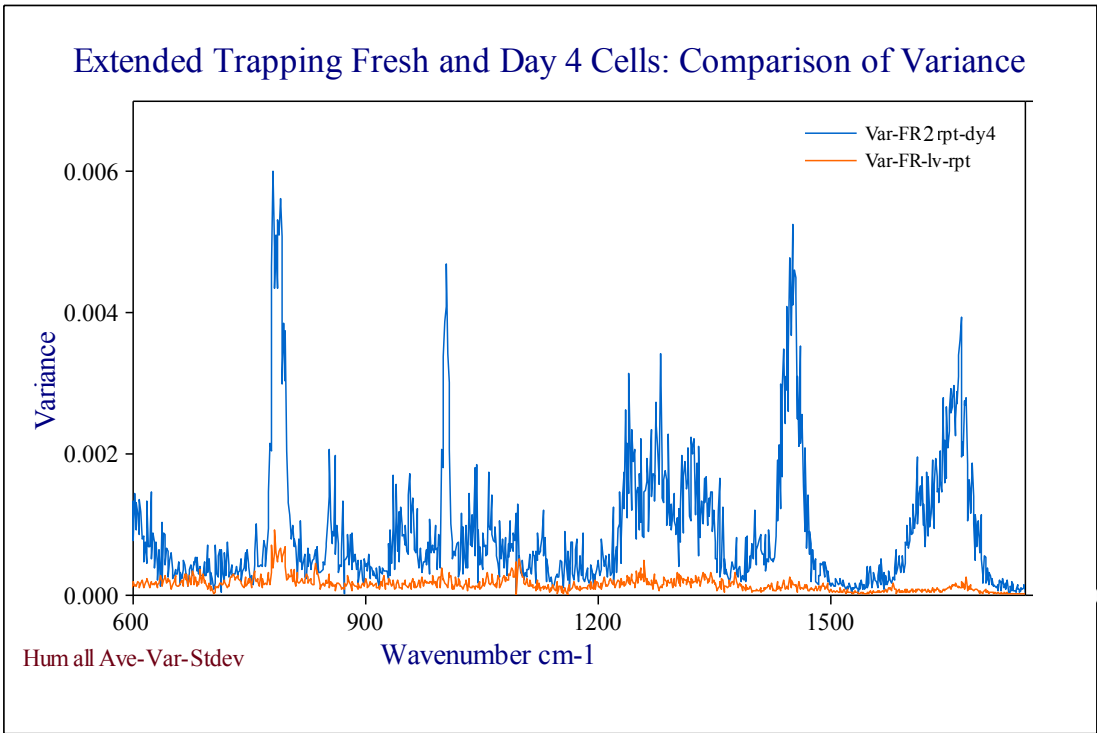

Figures 6.24: Extended trapping: (**Top**) Overlay of average spectrum and variance from the two datasets (**Bottom**) Comparison of variance from the two extended trapping data sets

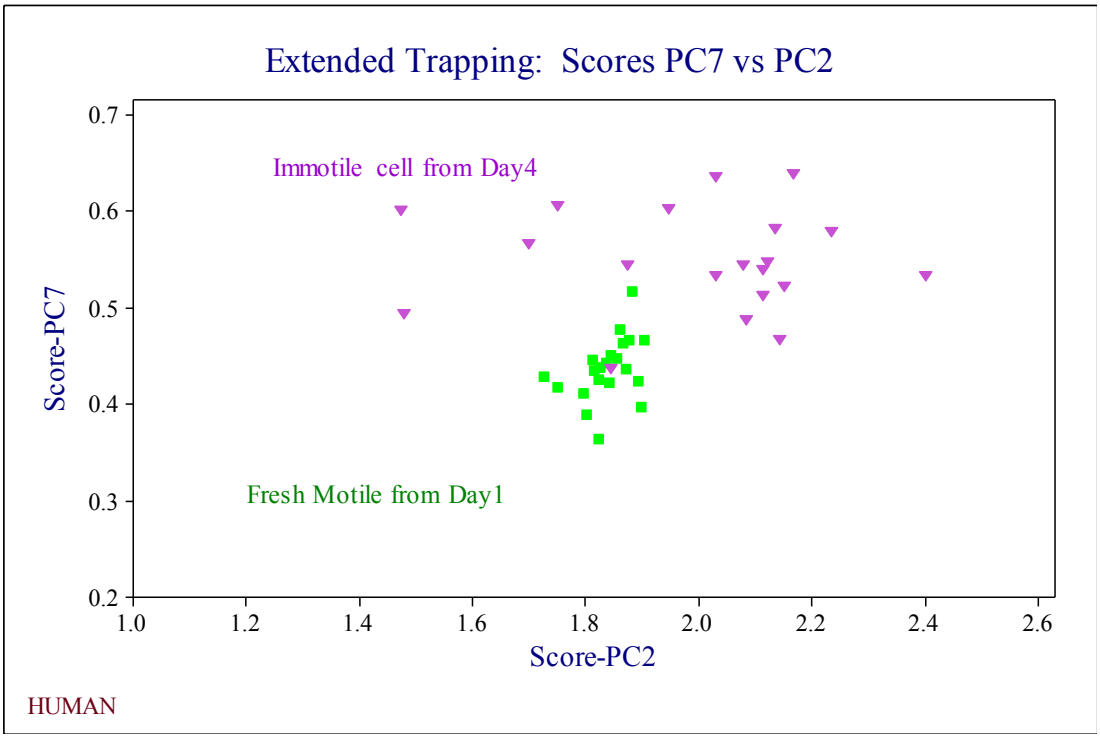

Figures 6.25: PC scores group cells by extended trapping – day1 motile vs day4 immotile

The peaks at 785 cm^{-1}, 1050 cm^{-1} and 1446 cm^{-1} and their intensity ratio to the stable DNA backbone peak at 1092 cm^{-1} for the human samples using the same procedure that was used in the case of stallion sperms are summarised in **Table 6.11** for comparison with published papers. No specific grouping of these peaks by process or category or specimen was identified.

DNA and Protein Peak Ratios (Average)						
Human	**785**	**stdev**	**1055**	**stdev**	**1445**	**stdev**
FR-Dy1-lv	1.04	0.039	0.40	0.024	0.43	0.046
FR1-Dy1-lv	1.03	0.021	0.40	0.019	0.41	0.024
FR2-Dy1-lv	1.06	0.051	0.41	0.022	0.47	0.047
FR2-Dy2-lv	1.02	0.040	0.42	0.019	0.41	0.030
FR2-Dy2-dd	1.06	0.033	0.41	0.019	0.37	0.017
FR2-Dy3-lv	1.01	0.036	0.42	0.025	0.45	0.043
FR2-Dy4-dd	1.07	0.043	0.40	0.021	0.55	0.111
FZ-Dy1-lv	1.04	0.041	0.41	0.025	0.48	0.079
FZ-Dy3-lv	1.04	0.043	0.42	0.022	0.48	0.044
SU-Dy1-lv	1.01	0.042	0.41	0.024	0.43	0.046
Su1-Dy1-lv	1.04	0.036	0.40	0.023	0.46	0.034
Su1-1mM	1.04	0.029	0.39	0.016	0.44	0.033
Su1-2mM	1.03	0.031	0.40	0.014	0.45	0.026
Su2-Dy1-lv	1.03	0.039	0.40	0.017	0.50	0.043
Su2-2mM	1.01	0.031	0.40	0.013	0.50	0.052
Su3-Dy1-lv	1.06	0.041	0.40	0.019	0.44	0.044
Su3-1mM	1.04	0.030	0.40	0.013	0.46	0.051
Su3-2mM	1.05	0.035	0.40	0.019	0.5	0.043

Table 6.11: Peaks/bands intensities at 785 cm^{-1}, 1055 cm^{-1} and 1445 cm^{-1} by specimen and processes from day1 spectra.

7

The Discussion

Nature uses only the longest threads
To weave her patterns, so that each small piece
Of her fabric reveals the organisation
Of the entire tapestry.

Richard P. Feynman (1918 – 1988)

7.0 Discussion of the Experimental Results

The purpose of this research was to investigate the feasibility of using Raman spectroscopy to identify chemically induced DNA damage in live, motile sperms. The discussion of the experimental results from the previous chapter (**Chapter Six**) is sub-divided into three main sections:

- **7.1** LTRS calibration and measurement limits
  - **7.1.1** Laser Trapping Conditions
- **7.2** Raman spectroscopy of Stallion and Human Sperms
  - **7.2.1** Osmotic and Oxidative Stress in Stallion Sperms
  - **7.2.2** Membrane Damage in Stallion Sperms
  - **7.2.3** Study of Stress and Disintegration in Human Sperms
  - **7.2.4** Laser Trap induced Cellular Changes
  - **7.2.5:** Summary of Stallion and Human Sperm DNA Damage Study
- **7.3** Discussion of Literature on Spectroscopy of Sperms

7.1 LTRS Calibration and Measurement Limits

Polystyrene beads of NIST standard quality [1] was used for frequency calibration of spectral region, 600 cm^{-1} - 1800 cm^{-1} on the LTRS – the DNA fingerprint region of the Raman spectra [2]. The spectral resolution using 2^{nd} and 3^{rd} order polynomial fits are within measurement limits (**Table 6.1 Section 6.1**). Most of the published work on Raman spectroscopy of sperm DNA uses the fingerprint region 600 cm^{-1} - 1800 cm^{-1} and was identified as a useful range to explore in this investigation. Since the frequency region below 600 cm^{-1} was unreliable due to significant contribution from the quartz substrate, and the region above 1650 cm^{-1} was dominated by contributions from the sperm media, the region used for statistical analysis is 630 cm^{-1} - 1630 cm^{-1} and contains most of the DNA fingerprint peaks. CaF_2 substrates are free from strong bands in the low energy and DNA fingerprint region and would have provided a wider range to investigate; however, CaF_2 substrates were not available in the right thickness for use on this LTRS and are not critical for the

feasibility study where the analysis is based on comparing the spectra from sperm cells subject to different processes.

The spectral resolution of the LTRS is about 1.25 cm^{-1} per pixel and the peak resolution limit is about 4.7 +/- 0.2 cm^{-1} with the 600 lines/mm grating used in this work. While higher spectral resolution could have been achieved using a grating with 1200 lines/mm or 1800 lines/mm, it would have been at the cost of frequency range. This resolution is considered adequate to measure biological specimens [1].

The accuracy of the Raman peak frequency is critical when comparing spectra taken on different days. The accuracy of the peak frequencies can be compromised when the optical path is disturbed by frequent re-alignment or shift of components. Gratings are often moved and exchanged daily on the multi-purpose and multi-user LTRS used in this research. Frequency stability over the six months period was measured using calibration spectra generated with the NIST standard polystyrene beads; the 1001.4 cm^{-1} peak was reproduced within the measurement limits as shown in **Chapter Six**, **Figure 6.3**. A similar comparison between the stable DNA PO_2^- band at 1092 cm^{-1} (**Figure 7.1**) also shows high reproducibility in the frequency of the peak, within the same six months period. DNA specific standards were not needed for this feasibility study; the published research from this equipment also did not use such standards except when doing quantification.

Average Spectra of Stallion and Human Sperms taken Six Months Apart

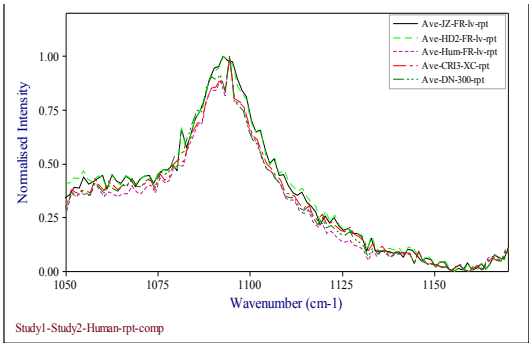

Figure 7.1 Average spectra from five repeatability datasets on motile stallion and human cells taken six months apart.

The intensity difference in **Figure 7.1** is due to the different peak profile and normalisation to the sharp region of the peaks. When working with live specimens with short life span, this LTRS has the advantage of system stability, short laser exposure time coupled with good spectral range, single mode laser beam and wavelength of 785nm that is suitable for trapping live biological specimens. Several papers on live cells in culture and bacteria have been published using this equipment and experimental setup [3-6].

7.1.2 Laser Trapping Conditions

Individual sperm cells were trapped using the 785 nm single mode diode laser with beam intensity of ~ 25 mW in the sample plane of the microscope. The size of the trapping beam has to be comparable to the size of the trapped specimen or the section of the trapped specimen from which the data is being extracted.

The exact size of the condensed mature sperm nucleus is not directly reported in the literatures researched. Indirect reference to the size of the sperm nucleus indicates that the sperm nuclear size ranges from ~ 1μm to 8μm; this range may apply to the sperm cells of different mammals. Stallion spermatid (large, round, early stage, haploid cell) has nuclear dimensions of about 5 microns [7]. When the nucleus of the spermatid condenses during maturation phase, the sperm nucleus occupies a space that is $1/20^{th}$ of the size of a somatic cell [8-10]. A somatic cell is 10 μm – 20 μm based on the book Chapter 21, 5^{th} Edition [11]. The mature sperm nucleus is a 13^{th} of the diameter of the egg [12]; the size of the human egg is about 100 microns based on the book Chapter 20, 4^{th} Edition [11]). These reports imply that the sperm nucleus is ~7 to 8 microns in size.

Based on electron microscopy research, TEM images of mature sperm heads indicate the nuclear size to be ~ 3 to 5 microns [13]. AFM images of the sperm nucleus indicates ~ 4 – 5 μm in length and ~ 2 – 3 μm in width [14]. Raman mapping of human sperm [15] also indicate a sperm nuclear dimension of ~4 μm [16]. If the sperm nucleus is assumed to be approximately the same size as the sperm head then its frontal size is ~ 3μm in human and ~ 5 μm in stallions. Raman spectra were taken on sperms trapped at the top (frontal surface).

The diffraction limited spot size of the optical trap is about 0.5 microns; with scattering from multiple boundaries and diffuse medium, the spot size would be slightly larger (< 1 μm) but not large enough to fill a 3 μm sperm head. This implies that the laser trap interacts with a small fraction of sperm nuclear content and the Raman spectrum is derived from the densest region - the densely packaged DNA - protamine complex in stallion sperms and DNA–protamine–histone complex in human sperms [17]. Thus the Raman spectra from the sperm head do not contain information from the entire sperm nuclear DNA-protamine complex. This feature of LTRS experiment has to be taken into consideration when comparing the results with biochemical assays and cell viability tests that test the entire sperm head.

The laser trap of the LTRS used in this research is a single mode 785 nm laser of ~25mW in the sample plane, exposing the sperm head to a power of ~ MW/cm^2 per second. Can this laser trap cause photo-damage to the stallion and human sperm cells?

The damaging effects of laser traps on sperms have been researched extensively. Literature review of laser induced cellular damage is discussed extensively in **Chapter Four, section 4.6**. Laser powers in sufficiently high doses can inflict damage to live cells [18]. Two photon interactions from a tuneable continuous wave laser beam of 760 nm and 70 mW intensity caused damage to sperm cells after 65 seconds of trapping and impacted their cloning efficiency [19, 20]. Sperms trapped with a single mode 70mW, 780 nm laser source had an average lifetime of 580 seconds, and a range from 400 to 1000 seconds. Damage to sperm cells by UV lasers was significantly high at very low powers and exposure time [18, 21-23]. Short pulse length, laser intensity and low coherence in NIR lasers have been implicated in multiphoton effects and photodamage [24, 25]. Thus the types of laser, choice of wavelengths, intensity, trapping time and environment have to be evaluated to prevent cell damage.

The energy and intensity of the laser trap used in this research is less than the wavelength and intensity of the 780 nm 70mW laser; the trapping time of 20 - 30 seconds is also much less than the minimum trapping time of ~ 6 minutes, used to

demonstrate the damaging effects of CW single mode laser tweezers. From these reports, it is reasonable to assume that the LTRS used in this work did not damage the trapped sperm cells.

Due to lack of high power laser sources and resources for conducting the laser induced damage experiment, such a study was technically untenable during this research and could not be undertaken. Instead, the cells were continuously trapped for 10 – 20 minutes and released without impacting their motility. The Raman spectra did not reveal any spectral changes that could correlate with the laser damage. It is essential to subject statistically significant number of sperm cells to laser flux comparable to that at the laser trap focal plane, before it can be conclusively established that healthy sperms of the species under study cannot be damaged by the laser power used.

7.2 Raman Spectroscopy of Stallion and Human Sperms

Mammalian sperms have many common characteristics, including the molecular makeup of the genomic DNA. The horse and human sperms are similar in morphology. The size of the genomic DNA is comparable in horse and human sperm cells (**Chapter Two, section 2.6)**. The nuclear proteins in the sperms of both species have similar molecular content. Stallion sperms are not bound by nuclear histones and as a result, the tight nuclear-protamine crosslinks are very difficult to break when compared to human sperms.

The dense DNA packing in the small sperm head has complex hexagonal close packed (hcp) and liquid crystal like structures [9]. Raman spectra of the trapped cells (**Figures 6.4 and 6.16**) have several strong peaks. These peaks correlated with spectra of purified calf thymus DNA [26] and synthetic DNA [27]. The frequency assignments to the DNA peaks after calibration using polystyrene beads also correlated well with the published works on DNA [26, 28] and DNA-protein complexes [29].

The Raman spectra from both horse and human sperms were normalised to the peak height of the stable symmetric stretching of PO_2^- at ~ 1092 cm^{-1} band [2, 30]. The

stability of the 1092 cm^{-1} band has been reported in several papers (**Chapter Four, section 4.4.4**). This band has been reported to have reliable intensity and frequency in both A and B conformation models of DNA and genomic DNA, with stability maintained even when exposed to temperatures up to 90 ^{o}C [2, 31]. UV exposure to herring sperm [32], calf thymus [33] and human [15] DNA showed comparatively high stability of the 1092 cm^{-1} peak at very low doses; the stability of the peak is disturbed at medium to high UV radiation exposure. While the vibrational mode of the phosphodiester component of the DNA backbone at 785 cm^{-1} is also stable, the peak is a superposition of the ring breathing mode of the DNA bases, dC and dT, making this an unreliable band for intensity normalisation [27].

Section 7.2.1: Osmotic and Oxidative Stress Damage in Stallion Sperms

Sources and methods of inducing stress damage to sperms and measuring them are discussed extensively in **Chapter Three, Sections 3.4 – 3.6**. Since oxidative and osmotic stress is associated with sperm DNA damage, especially during cryopreservation, artificial methods have been used to induce different grades of stress damage to stallion sperms [34] for this research. The outcome of the stress and membrane damage results presented in chapter six are analysed in the next sections.

Five stallion data groups were used to identify similarities and differences in the sperm cell response to applied stress. The cell motility and viability data as well as Raman spectra are reviewed to identify how sperm cells from a single stallion and from different stallions respond to applied stress.

Little information is available on the fertility potential of the selected stallions, rest between collections or the state/health of the stallions just before the collection. This information is useful to understand differences in the sperm quality and their response to the applied stress [35].

Computer aided motility and viability measurements were done on tens of 1000s of cells during this study and are plotted in **Chapter Six, Figures 6.6a and 6.9a**. A direct comparison is not possible with the Raman analysis, where ~20 cells were used. The trends provide useful information, even though the sample size is not statistically significant [36].

The three CR data groups are results from sperms collected from a single stallion, CR with high sperm count and quality. CR data groups are analysed separately to provide information on the variation between ejaculates from a single stallion. CR1-1 and CR1-2 were collected nearly three weeks apart and CR1-3 was taken two days after CR1-2. This does not imply that the stallion was used only on these three days, as all the stallions are available for use by other researchers.

The starting TM and PM (**Figures 6.6a, and 6.9a**) are comparable in CR1-1 and CR1-3, but there is a sharp decrease in TM and PM in CR1-2. The starting TM and PM and cell viability after the stress processes for CR1-2 show consistently low values with magnitude of approximately 50% of the other CR data groups in many of the processes. No explanation is available for this difference.

TM after Oxidative stress treatment in CR data groups: 'Control' (XC) had the highest TM, followed by 'low' (XL), 'medium' (XM) and 'high' (XH). The TM of XH ranged from ~ 20% in CR1-1 to ~ 70% in CR1-3. The three data groups had different levels of TM after exposure to the stress processes.

TM after Osmotic stress treatment in CR data groups: The motility of cells exposed to osmotic stress was much lower than that of cells exposed to oxidative stress. The control (300) has the highest TM in all three cases and hypertonic stress (600) has the least motility, with TM dropping below 10% in the cells. TM of the control dropped to ~50% in CR1-3. This difference has not been explained.

PM: Approximately 50% of the motile cells displayed progressive motility (PM) in all three cases; the motility trends were similar to that of TM with XC having the highest PM and '600' having the lowest PM. The PM of CR1-2 and CR1-3 after exposure to oxidative stress was comparable to their PM before exposure. This was not the case with CR1-1; PM in XC dropped to ~ 15% of the starting PM. There is no explanation for this. The PM of CR1-1 '600', CR1-2 and CR1-3 dropped to 10% of the starting PM, after exposure to osmotic stress.

Cell viability was high (>90%) in the cells exposed to oxidative and isotonic stress, in CR1-2 and CR1-3; no data was available on CR1-1. The viability of cells exposed

to hypo and hyper osmotic stress dropped to below 50%, with cells exposed to hypotonic stress having the least viability.

The PM, TM and viability data from the two stallions, DN (**Figure 6.7a**) and HD1 (**Figure 6.8a**), have similar trends to the three CR data groups. The TM, PM and viability of the five data groups are compared in **Figures 6.9a**. The motility of the 'control' in DN appears to be slightly lower than the stressed cells.

Summary: There was considerable variation in TM, PM and cell viability between collections from the same stallion and between stallions; each sperm collection also showed different starting TM and PM. All sperm collections showed different response levels after exposure to the stress processes that did not correlate with their motility before exposure to the stress processes. The TM, PM and viability responses common to the five sperm collections after oxidative and osmotic stress treatment are summarised below:

- The motility of cells exposed to oxidative stress are comparatively higher than that of cells exposed to osmotic stress;
- Motility decreased with increased grade of oxidative stress exposure;
- Oxidative stress does not significantly impact cell viability;
- Cells exposed to hypertonic stress have lower motility than cells exposed to hypotonic stress;
- Cells exposed to hypertonic stress have higher viability than cells exposed to hypotonic stress;
- PM is ~ 50% of TM
- The ratio of PM to TM (**Figures 6.9a (C))** after exposure to oxidative stress is comparable to that before the stress;
- PM/TM is comparably low after exposure to osmotic stress with the lowest ratio observed after hyper osmotic stress

- There is stallion to stallion and within stallion differences in the TM, PM, viability and cellular response to the applied stress

How do the results from motility and viability tests taken on several 1000s of cells compare with the Raman spectra taken on ~ 20 cells? The overlaid normalised spectra show spectral variation across the 630 cm^{-1} to 1630 cm^{-1} range; the statistical variance are highlighted in the set of plots in **Figures 6.6b, 6.7b** and **6.8b**; the peaks and regions of high variance are summarised in **Table 6.5**. Weak to strong variance, common to the five data groups, are observed in spectral bands at 785 cm^{-1}, 835 cm^{-1}, 950 cm^{-1}, 1004 cm^{-1}, 1094 cm^{-1}, the broad multi-band region at 1200 -1400 cm^{-1}, as well as bands at 1445 cm^{-1}, 1485 cm^{-1} and 1570 cm^{-1}. The regions with high variance are observed at 785 cm^{-1}, 1350 cm^{-1} and 1375 cm^{-1} in the three CR data groups. The variance patterns were, otherwise, unique to each data group. The variation in Raman spectra also reflects the variation in cell viability and motility plots in **Figure 6.9a**.

How does the variance and PCA of the CR data groups compare with the remaining two data groups from DN and HD? DN was the first data group prepared for Raman spectroscopy in **Study One**. The statistical variance in DN has high background noise when compared with the other four groups **(Figures 6.7b)**. Unlike the other four stallions, DN media contained debris and bacteria as the sperms were not filtered using gradient percoll wash prior to stress damage exposure and Raman spectroscopy. This may contribute to the noisy variance but it had no visible impacted on the Raman spectra.

Statistical variance is also observed at 680 cm^{-1} and 1620 cm^{-1} in some of the data groups. The spectral region between 1200 cm^{-1} and 1400 cm^{-1} has a distribution of localised high variance regions, consisting of several narrow bands with at least four separate peaks/bands. The highest variance is observed at 1375 cm^{-1} in the three CR data groups but not in the other data groups. A single cell from the hyperosmotic stress group is responsible for high variance at 972 cm^{-1} in CR1-3; this is not reproduced in the other two data groups.

The examination and comparison of statistical variance, as discussed above, is insufficient to shed light on the process contribution to spectral variation. PCA has been used for analysing the complex relationship between peaks and bands in spectroscopy and is described in **Chapter Five, section 5.6.4**. PCA is able to reveal submerged spectral patterns, identify correlations between the peaks/bands and extract relevant information using a reduced set of translation and rotation invariant vectors and their components known as PCs [37-39].

A total of 844 Raman spectra were generated on 786 trapped sperm cells from 43 data sets and analysed using PCA. The first PC accounts for 28% of the variation within the entire spectra. The second PC accounts for 18% and the third PC accounts for 8% of the variations. The first 14 PCs account for 70% of the variations and the first 210 PCs account for 90% of the variations. Thus the first few PCs do not account for the majority of the variability in the stallion spectra. This is not surprising as the dataset consisted of ~ 20 cells; this is small for statistically significant results [36, 40]. Secondly, the spectral differences are not specific to a few bands in the spectra; there is a spread of variance across the entire spectral range. In addition there is considerable variation within the data groups/ejaculates. The high number of processes tested (3 grades of osmotic and 4 grades of oxidative stress in **Study One**) also may have contributed to the low variability in the first PCs.

While low 1st PCs of the order of 40% to 50% are not unusual in biological specimens there are no previous reports that discuss the PCA of Raman spectra from stallion sperms. The combined 1st and 2nd PC from the Raman spectra of bull sperms contained ~97% of the variability in the entire data [41]. This is high for biological specimens; the use of stained and sorted cells (using flow cytometry) and the few processes tested may account for the high proportion in the first PCs. The number of spectra appeared to be about 15 per test condition (the number of spectra taken is not in the report). There are not many published reports on the use of LTRS in the study of sperm cells. Bull sperms have been easy to cryopreserve and respond differently to the protocols than stallion sperms [42].

PCA of CR1-3 data group is shown in detail in **section 6.2.1.2.** The high overlap in the mean PC scores from the first 9 PCs of the eight processes (**Figure 6.5l**) indicates that these PCs cannot separate the spectra by the processes. Inherently high variability within each data set and between data sets (from the review of the statistical variance), account for this. F-value is used to identify those PCs (illustrated using **Figures 6.5n – 6.5s**) associated with variability between processes.

The PC scores and coefficients from the analysis of the CR data groups are plotted in **Figure 6.6c** – **Figure 6.6e**. '600/hyper' and '100/hypo' osmotic stressed cells cannot be separated in CR1-1. The motile cells in the 300/iso is separated; the immotile cells are spread across two regions. This can be explained by the fact that immotile cells can consist of damaged cells and healthy sperm heads with dysfunctional midpiece or tail. The three grades of osmotic stress cannot be separated in CR1-2 and hence was not plotted. There is considerable overlap in the three grades of osmotic stressed cells in CR1-3. The 'control', XC, is separated in oxidative stress study. XM and XH cannot be separated and XL has wide distribution in the two groups CR1-2 and CR1-3. Healthy cells are not easily damaged and can account for the two clusters in the 'low'. An additional data set, XC-BN, acquired on motile sperms with bent neck from the same XC preparation, is almost completely separated from the stressed cells (**Figure 6.6d** (top)). XC consists of both motile and immotile cells. The extended trapping (XC-rpt) in CR1-3 has comparatively tighter distribution of PC scores.

The PC coefficients of the stress damage data sets (**Figure 6.6e)** has some correlation with the plots of variance in **Figure 6.6b** but the spectral regions that contribute to the high coefficients and variance have no unique association with the applied stress.

PCA of the remaining data groups DN and HD1 also show different responses. '300' and '100' cannot be separated in DN; the three grades of oxidative stress also cannot be separated. The '600' and '100' cannot be separated in HD1 and there is overlap in the oxidative stress data groups. Spectral data sets from cells labelled as motile or immotile cells were taken on a couple of samples in CR1-1 and HD1.

In summary,

- The PC scores were able to separate the motile and immotile cells in the few cases studied;
- The PCA of the five data groups do not show unique patterns in the spectral regions that contribute to the process related variations;
- The three CR data groups have responded differently to the applied osmotic and oxidative stress damage protocol in this study;
- The data groups did not show spectral responses that recognised different grades of applied stress damage
- The plots of the PC coefficients do have some broad correlation with the plots of variance;
- The PCA of the five data groups do not have any correlation with the motility and viability data.

Figure 6.9b is a PC score plot of the entire spectra from 786 cells used in **Study One**. The five data groups form three distinguishable and overlapping clusters. The findings from the study of the entire spectra are summarised:

- the three CR data groups did not show stallion specific clustering;
- the CR1-1 and CR1-3 clusters could not be separated;
- CR1-2 formed the third cluster;
- the DN and HD1 clusters could not be separated;
- HD1 has a tighter distribution compared to the other four data groups which have comparable spread in the PC scores;
- There was no clustering or partial clustering by the applied oxidative and osmotic stress, or the different grades of stress.

Study One results show that the motility, viability and spectral characteristics in the five data groups have some common pattern within which the five data groups showed unique behaviour. This is also reflected in the distribution of the PC scores from this study. The three sperm collections from the same stallion did not have unique characteristics that set them apart from the rest of the data groups. The spectral analysis did not directly correlate with motility and viability tests.

Table 6.6 was created using the average normalised peak intensities at three bands discussed in two published reports [16, 43]. Data analysis did not show process related trends or changes to the peaks at 785 cm^{-1}, 1050 cm^{-1} and 1445 cm^{-1} and will be discussed in **Section 7.3**.

Section 7.2.2 Stallion Sperm Membrane damage Study

The PC scores of the Raman spectra from the limited data on motility from **Study One** separated motile and immotile cells (**Figures 6.6d and 6.8c**). PCA did not produce stress related clusters in the data sets. Published work on stress damage to stallion spermatozoa suggests that the membrane surrounding the midpiece (housing the mitochondria) are more susceptible to osmotic stress induced damage [44]. This may account for the loss of motility observed after exposure to hypo-osmotic stress [45]. Osmotic stress in spermatozoa are also a source of oxidative stress [46]; however, there is no indication of where the damage occurs.

Thus **Study One** raised more questions – does the cell viability test differentiate between membrane damage to sperm head versus membrane damage to the midpiece? Does the PI stain nDNA as well as mtDNA? **Study Two** was designed to:

- examine the spectral response from motile and immotile cells;
- test the spectral response of direct injury to the cell membrane using cold shock;
- test the reproducibility of the results from **Study One** with Osmotic stress;
- Since the data sets used in the Raman analysis was very small compared to the 1000s of cells analysed by CASA, the membrane damage test was also designed to test the reproducibility of the sampling size. Hence the

membrane damage sample preparation was grouped into 50-50 (consisting of 50% damaged and 50% fresh cells) and 90-10 (90% damaged and 10% fresh cells) detailed in **Chapter Five**.

Four stallions (two common with **Study One**) were used in this study and the details of the analytical parameters tested is summarised in **Table 6.7**. The membrane damage process was tested on the first stallion JZ. The cells from the other three stallions were exposed to the same protocol for inducing membrane damage. The osmotic stress procedure was the same as the one used in **Study One**. No CASA viability and motility (TM and PM) tests were included with this study. Membrane damage study compares fresh cells with the membrane damaged cells. Osmotic stress is analysed using the same method in **Study One**.

The data size in **Study Two** is nearly 1.5 times the data size in Study One. The 1st PC accounts for 45% of the spectral variation, 2nd PC accounts for 18% and 3rd PC accounts for 7% of the total variation. The larger data size may account for the higher concentration of variability in the 1st PC.

Stallion JZ was rigorously analysed, acquiring ~ 40 motile and 40 immotile cells in each data set; this extended the data acquisition over three days. Most of the data acquisition was completed within 48 hours. Membrane damage study was completed within 24 hours and the '600' and a repeat set of spectra on 'fresh' samples were completed on the third day. This repeat was done to see if there were spectral changes in the fresh cells on the third day.

The raw and normalised spectra, average with variance and average with standard deviation are plotted in four panels for each data set in JZ; these can be found in the **Appendix (Figure 6.10a – Figure 6.10h)**. Some of these plots illustrate the different types of corrupt spectra that were not discarded at the time of saving the acquired data. The corrupt spectra were primarily due to cells escaping the trap as the media warmed. The slides with the cell suspensions were changed frequently to also avoid trapping cells from a drying media. A rare cosmic ray captured in one of the spectrum was not removed since it was located outside the ROI.

A matrix plot of the PCs with high process related variation was created using the same technique of **Study One**. **Figure 6.10o** shows the PC scores of membrane damaged cells separated from the fresh cells. During data acquisition, motile cells were not found in the membrane damage preparations. PC scores from 50-lv and 50-dd datasets almost completely separated the fresh/motile cells from the damaged and immotile cells. The immotile cells located in the fresh/motile region is very likely from the fresh immotile cells in the 50-50 mixture. The PCA distribution of the spectra from 50-50 cells was proportional to the 50-50 mixture in the dataset.

The PCA of fresh cells (**Figure 6.10p**) produced distinct clusters by motility and time, with the cells taken on day1 and day3 forming separate clusters. Extended trapping was done on a fresh motile and a membrane damaged cell; the data sets from these cells were also separated (**Figure 6.10q**) and discussed in some detail in the **section 7.2.4**.

PCA of the osmotic stressed datasets had unexpected results. The spectra from '100' and '300' were acquired on the second day and the spectra from '600' were acquired on the third day. There were no motile cells in '600'on day3. The '100' and '300' did not form separate clusters and the motile and immotile cells could not be separated (**Figure 6.10s**). However, the '600' was almost completely separated. The PC coefficient associated with a narrow band in the 1270 cm^{-1} region contributed to the high variability from '600'.

The spectra from the remaining four data groups were acquired within 24 hours. **Note: -** HD2 and CR2 data groups are from the stallions HD and CR respectively that were used in **Study One**.

The motile and immotile cells could not be separated in HD2 (**Figure 6.11a**); there was high overlap in the three grades of osmotic stress. Membrane damaged cells were separated from the fresh cells; the cells did not form clusters by motility. Extended trapping was tested on a fresh cell from this group and the spectra from this study showed a tighter distribution.

The small data sets from WL (**Figure 6.11b**) with 10 cells per test showed separate clusters of motile and immotile cells. The PCs could not separate the data sets by the different grades of osmotic stress. The '600' cells were all immotile. Motile fresh cells were separated from immotile and membrane damaged cells. The 50-50 cells also showed almost proportionate (40-60) separation of damaged/immotile cells indicating randomness in the trapping and good mixture of the 50-50 cells in the dataset.

The aniso-osmotic stressed cells exposed to '600' and '100' were separated with a small overlap (**Figure 6.11c (top)**) in CR2 data sets; the cells did not separate by motility. No data was obtained on '300'. Interestingly, the membrane damaged cells contained a large fraction of motile cells. Motile and immotile cells were separated in the 'fresh' dataset but the motile cells formed a cluster with the membrane damaged cells.

In summary, the PCA of the four data groups produced very different response to the applied processes. Osmotic stress causes multiple types of damage – oxidative and membrane damage as well as loss of motility; separating osmotic and oxidative stress damage from the sperm spectra is complex [34, 45, 46].

The statistical variance from the four data groups is compared in **Figure 6.12** and summarised in **Table 6.8**. As in **Study One**, high variance is observed in the 785 cm^{-1} band. Both 1004 cm^{-1} and the 1450 cm^{-1} bands displayed much higher variance than in **Study One**. The PC coefficients in **Figure 6.13** has high contributions from the 785 cm^{-1} band in all four data groups. The 1004 cm^{-1} and 1450 cm^{-1} bands also contributed to the coefficients. Both PCA and variance show that the response of each data group to the applied stress or damage is different. **Table 6.9** is also a summary of the average intensities of the three peaks at 785 cm^{-1}, 1050 cm^{-1} and 1445 cm^{-1}. There was no process related changes in the intensities at these peaks.

The experiment was designed, expecting to see significant separation by motility in the PCA analysis of these data groups, as was seen in the few datasets in **Study One**. Interestingly, the cell separation by motility also appears to have strong stallion and process dependence as is evident in the review of the figures (**Figure 6.10 – 6.13**).

Different stallion cells responded differently with some stallion cells not separated by motility at all.

PCA analysis of the 1135 spectra from 1022 cells could not separate the processes – osmotic, membrane damage and fresh cells. However, the PC scores formed three distinct clusters by stallion/ejaculate; both HD2 and CR2 formed a common cluster and JZ and WL formed two separate clusters (**Figure 6.14**). PC scores formed highly overlapping clusters by motility. The PC coefficients had high contributions from the entire spectral range investigated (**Figure 6.15 and 6.16**).

The two studies showed that each stallion ejaculate had different responses to the applied stress/damage. Since multiple collections from a single stallion were not used in **Study Two**, the variability within a stallion could not be tested. The stallions are seasonal creatures and seasonal changes in hormones have been found in stallions [47]. This could be an added complexity when comparing the two studies from two different seasons. Can some of the observed motility related separation in **Study One** be due to the season the test was done? A reformed set of studies to test the reproducibility of 'stallion to stallion' and 'within stallion' differences by season and by motility, using the process conditions - osmotic stress, membrane damage and fresh cells may provide some answers to these questions.

Section 7.2.3 Study of Stress and Disintegration in Human Sperms

A normalised spectrum of the human sperm is shown in **Figure 6.16**; it is similar in frequency and intensity profile to that of the stallion sperm spectrum. The Raman peak assignments are also the same as these peaks are from the same molecular vibrations.

Three categories of human cells were analysed using PCA and statistical variance; the analytical matrix is presented in **Table 6.10**. The datasets consist of specimens ranging from fertile donor of known fertility to unknown specimen from sub-fertile and infertile patients. The 'FR' group consists of sperms from different sub-fertile patients with normal morphology. The 'FZ' group consists of a single cryopreserved donor specimen. Donor specimens are of high fertility. The 'SU' group consists of specimens from different patients; these cells have comparatively high PM. The

three categories of human specimens were examined for spectral features common to the category.

The major tests include cell disintegration with time, oxidative stress and motility. Human sperms have longer shelf life than stallion sperms; motile cells have been found even after two days. The study of cell disintegration with time was used to test the capability of Raman spectra to detect molecular level changes. Oxidative stress damage using 1 mM and 2 mM of H_2O_2 was tested on some of the SU specimen. Peroxide exposure at doses in this range are known to induce mtDNA damage in human sperms [48]. Can the peroxide exposure induce nDNA damage? Are immotile cells easier to damage than motile cells? Motility declines with time; many of the datasets in this study were separated by motility.

Statistical variance of the three categories is presented in **Figure 6.17a**. The top left plot is an overlay of all the Day1 specimens that were not subjected to additional stress or processes. The remaining three plots are breakdown of these Day1 specimens by category; the variance from these plots shows some unique patterns. The SU category appears to have a uniform pattern in variance with the high variances appearing in the bands at 785 cm^{-1} and 1445 cm^{-1}. Medium variance can be observed at 720 cm^{-1}, 1004 cm^{-1} and 1370 cm^{-1}. The typical broad multiband region between 1220 cm^{-1} and 1350 cm^{-1} is present in all three categories that are found in stallion. Interestingly, the 1004 cm^{-1} peak is sharp and strong; this peak is associated with the protein phenylalanine. The FR data sets are from different men with different fertility potential with definite sub-fertility indication in sperm count. There is a range of variance from this category.

Raman spectra are also analysed using PC to identify spectral patterns related to the tests and specimen quality. The 1st PC accounts for 57% of the variation in the Raman spectra of these human cells; 0.1% of the variation is accounted for by the 2nd PC and 0.05% of the variation is contained in the 3rd PC. This distribution in variation between the PCs is different from that of stallions. Interestingly, even though the 1st PC contains a high proportion of the variability in the spectra, the

higher PCs account for specific process related variability, as illustrated by the PC scores in **Figures 6.17 – 6.22**.

PCA was used to analyse the datasets from Day1 that were not exposed to any stress or processes. The eight specimens and three categories of the specimen are analysed in **Figure 6.17b**. Some clustering by specimen (top) and categories (bottom) can be observed in the two plots. The three categories form three distinct clusters with some overlap. There is a broad spread in the three FR datasets from three different men; this spread is more than the spread in the SU groups from four men. The only FZ sample also formed a distinct cluster. The plot of PC coefficients (**Figure 6.17c)** has sharp peaks with a dominant contribution from the 1275 band. This band is associated with Amide III protein molecule [49].

The specimens from FZ and FR categories were further tested for day to day disintegration in cell DNA quality. These samples were kept at laboratory temperature (18 ^{o}C) and Raman spectra acquired from 100 μl of the specimen on four consecutive days. The spectra from motile and immotile cells were marked on the day2 and day3 data sets. There were no motile cells on day4. A plot of the statistical variance (day2 – day4) from this study is shown in **Figure 6.18a** (middle). The plot shows high variance in the day4 dataset and least variance in the day2 dataset. Both FZ and FR show similar variance in the day3 dataset. No day4 or day2 spectra were acquired on FZ. The other two plots in the figure show high contribution to variance from the peroxide exposed SU specimen. The 785 cm^{-1} and 1004 cm^{-1} bands show some variance in the three sets of variance plots, but higher variance is distributed in the bands between 1200 cm^{-1} and 1600 cm^{-1}.

PCA of the datasets were used to investigate spectral differences between three processes - Day1, the combined spectra Day2 – Day4 and oxidative stress on SU specimens. Some clustering by these processes is observed (**Figure 6.18b** (top)). The plot of PC coefficients in **Figure 6.18b** (bottom) shows high contribution from 720 cm^{-1}, 785 cm^{-1} and the 1004 cm^{-1} band. The variations in the higher frequency region has some similarities to that of the stallion spectra, with broad bands involved.

The distribution of variance in **Figure 6.18a** indicates daily changes in the cells. Hence the spectra from Day1 to Day4 were analysed in some detail using PCA (**Figure 6.19**). The score plot shows considerable spread and overlap in the cells from day1 – day3; day4 cells show some separation. Based on discussions with researchers and embryologists, the human sperms have a longer shelf life than stallion sperms with very little deterioration in cell motility in the first 48 hours. The plot of PC coefficients shows high contribution from the 785 cm^{-1} band. Since this test was done with two specimens – a cryopreserved donor specimen, FZ, and a fresh sub-fertile specimen, this spread and overlap in the scores is to be expected.

PCA of the swim-up specimens SU, SU1, SU2 and SU3 show some clustering by specimen (**Figure 6.20**); SU, the donor specimen is separated from the patient groups. The SU groups were also tested for DNA damage after exposure to 1mM and 2mM of H_2O_2. The PCA showed no clustering by treatment. PCA of the entire 406 spectra, consisting of 20 data sets from 20 different individuals, are plotted in **Figure 6.21**. The cells are colour coded by category and specimen; there is some clustering by category. The FR data sets have the highest spread. The PC coefficient plot shows contribution from the entire spectral range. Motile, immotile and unclassified cells were analysed using PC. There is some clustering of motile and immotile cells with high overlap. As expected, the spectra from the unclassified are spread across the motile and immotile regions.

Human subjects were not recruited for the study of human cells; clinical discards were used as and when they were available. As a result, access to the LTRS could not be coordinated or booked in advance as with the stallion study. Only a few specimens could be studied on an ad hoc basis. Raman analysis was completed with the small set of specimens that could be analysed when the LTRS was free. Despite this limitation, some useful information has been obtained. Human sperms appear to be more sensitive to the applied processes.

Section 7.2.4 Laser trap induced cellular changes

Laser trap induced photodamage has been extensively reported and reviewed in **Chapter Four**, **section 4.6** and revisited in this chapter (**section 7.1.2**). The spectra from extended trapping of both stallion and human are discussed in this section. Seven cells, 5 from stallion and two from human were used in this study. The trapping time was about 20 minutes per cell and 20 to 40 spectra were taken on each cell. A cell (JZ-FR-lv-rpt) was trapped for about 40 minutes and the spectra acquired in the first 10 minutes and the last ten minutes. The plots of variance from these cells are shown in **Figure 7.2**. The statistical variances in these data sets have spectral regions of similarities and differences. The spectra on extended trapping showed the least spread and variance in most cases. An average high variance of ~ 0.0008 is associated with live motile horse and human cells. The damaged stallion JZ-dmg has the least variance. The stallion cell, JZ-FR-lv, subjected to ~ 40 minutes of trapping and the day4 human cell have the most variance in this category.

The regions sensitive to trapping are at:

- 785 cm^{-1} broad band producing strong variation after trapping;
- 830 cm^{-1} weak variation in all;
- 1004 cm^{-1} sharp medium variation;
- 1046 cm^{-1} broad medium variation;
- 1092 cm^{-1} broad strong variation;
- 1200 cm^{-1} to 1280 cm^{-1} – very broad and medium to strong;
- 1300 cm^{-1} band – weak to strong;
- 1370 cm^{-1} band – weak to strong;
- 1445 cm^{-1} broad band - medium to strong;
- 1485 cm^{-1} sharp weak;
- 1570 cm^{-1} sharp weak.

The terms ‘sharp’, ‘medium; and ‘weak’ are relative to the overall spectral variance. There are two possible sources of spectral variation in these regions – laser induced localised non-destructive heating [50-52] and photodamage [21, 22, 53, 54]. Further research is needed to identify the source of laser trapping induced spectral variations

within a sperm head and the minimum trapping time before laser induced damage is generated for the given instrument.

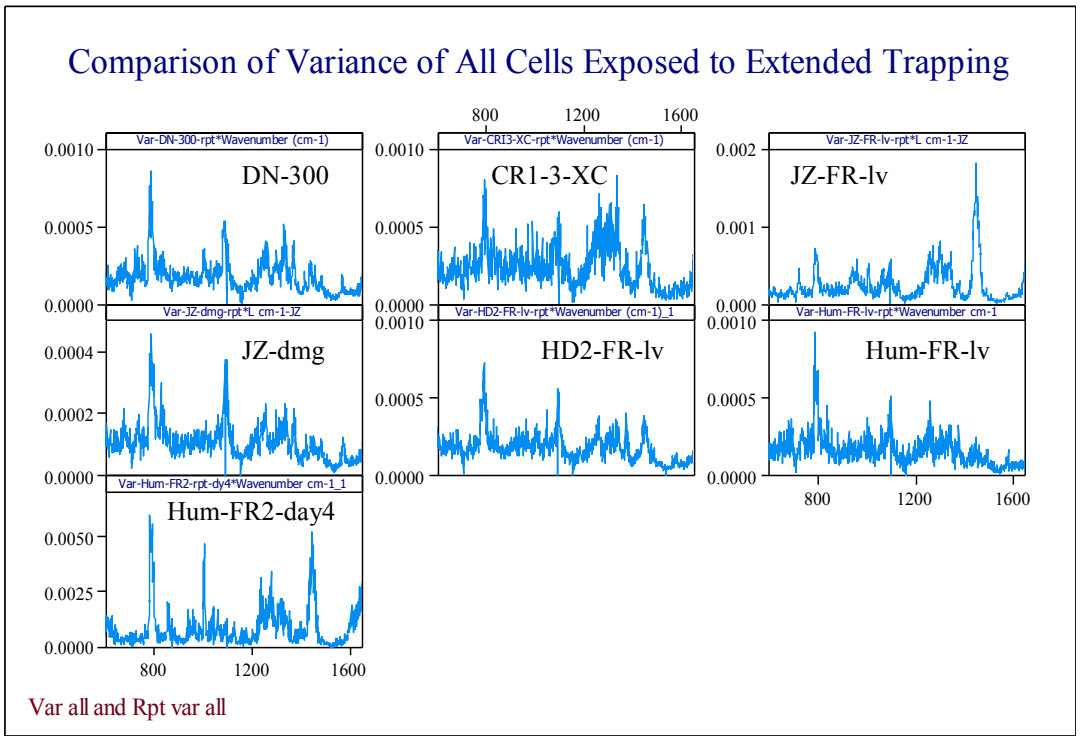

Figure 7.2: Comparison of variance from extended trapping in stallion and human

Section 7.2.5: Summary of Stallion and Human Sperm DNA Damage Study

Motility is a marker of sperm morphological normalcy and included in the human sperm evaluation criteria in the WHO manual [55]. Motility (TM and PM) and HOST of stallion sperms is not a predictor of stallion fertility, due to high incidence of structural asymmetry, circular motion, especially in cryopreserved sperms [56]. Detailed stallion sperm motility and acrosome integrity test on several stallions indicated stallion to stallion and within stallion variation, at various process stages [57, 58]. In this study, the CASA TM, PM and viability tests also indicated high variability between stallions and within stallion. The PC score test on horse (**Figure 6.15**) and human (**Figure 6.22**) are attempts to identify Raman signatures associated with motility, in this research. The plot of coefficients show a complex contribution

from the entire range analysed, with high contributions from the spectral bands at 680 cm^{-1}, 785 cm^{-1} and 1004 cm^{-1}, in both horse and human. The horse has broad spectral bands contributing to the variability, when compared to human. The histone free tight binding in stallion sperms, low levels of membrane lipids and stallion to stallion variation [58] could also contribute to this complex spectral response. The spectral regions that contribute to stress are not unique for oxidative and osmotic; this is to be expected, as literature shows that osmotic stress also induces oxidative stress [46].

PCA of stallions showed distinct clustering by ejaculate/data group. The sperms taken from a stallion on different days and from different stallions could not be differentiated. This difference between collections is seen in the two studies conducted in two different seasons, testing different applied stress/damage. Even though the study on human cells in this research is not as detailed as the two studies on stallion, there seems to be some clustering by category – swim-up, sub-fertile and donor and applied damage. It has emerged from discussions that seasonal effects are not observed in stallion sperms.

The plots of variance in human show a peak at 720 cm^{-1}. The peak is present at 725 cm^{-1} – 730 cm^{-1} in the stallions. The latter range is associated with the dA, whereas the former is associated with the SRY gene [29]. However, unless the bands are given accurate assignments and cross correlated with standards in a variety of focused tests, this remains an observation.

Summary: There are several unknowns associated with molecular level understanding of living cells. Study of molecular organisation within sperm nucleus is in its infancy [9]. Sperm cells are designed to protect the genomic DNA and are not only wrapped by proteins to make it electrically neutral and chemically inactive, it is also protected by a double membranous layer (perinuclear theca) that is highly resistant to salt and soap, commonly used to destroy cellular membranes. Thus it is not surprising that assays created to access cell nuclear DNA are not as effective in extracting the sperm nuclear DNA. The standard biochemical assays like comet assay, have been modified with the addition of harsh chemicals like proteinase,

RNAse and mercaptoethenol to break stallion sperms. Yet, it has not been easy to reproduce the comet on other stallion specimens. The difficulties encountered during such studies are seldom reported in publications. The effectiveness of a single protocol is highly limiting and controversial [59, 60]. Even biochemical tests that are easy to implement do not tell the whole story [61]; the complexity of such studies and the limitations on the limited information that emerges from such studies is beautifully summarised in a few papers [62-65].

The sperm plasma membranes of different species have different phospholipid characteristics, and these membranes show different response to cryopreservation. Equine sperm plasma membranes have 37% higher cholesterol content than bull sperms, influencing fertility as well as sperm cryopreservation potential in stallions. However, high variations between breeds, between stallions within a breed and between ejaculates of a stallion have been observed; this has limited the use of a single cryopreservation protocol in equine ejaculates. While cooled equine semen with semen extender at $5^{o}C$ is as effective as fresh semen, for up to 24 hours, cryopreserved equine sperms have reduced fertility potential due to membrane damage following centrifugation [66].

Comparing sperm cells exposed to biochemical damage with Raman spectroscopy requires a detailed understanding of the mechanism of damage induction through biochemical techniques. If the mitochondrial membrane and mtDNA are damaged by stress chemicals, then the spectra from the sperm head will not correlate with the induced damage.

7.3 Review of Literature on Raman Spectroscopy of Sperms

There are very few published reports on the use of Raman spectroscopy and PCA to study sperm cells [15, 16, 41, 43, 67]. The techniques used are different and hence a direct comparison is difficult. The two stable DNA backbone peaks at 785 cm^{-1} and 1092cm^{-1}, and the 1445 cm^{-1} protein peak and an additional peak at 1050 cm^{-1} and their measured intensity ratio has been compared in human sperms in two of the published literatures [16, 43]. Bull sperms have been evaluated using LTRS and the

results are very different from the study on stallion sperms. Similarities and differences are compared in this section.

Sperm cells in suspension on quartz coverslip were studied on stallions of unknown fertility and humans of mixed fertility. The sperm head is trapped, with little contribution from the tail or mid-piece in this study using LTRS. Due to the high trapping intensity and crystalline-like dense nuclear content, the spectra are highly resolved with high scattering cross sections. The spectra from motile trapped sperms were normalised to the stable 1092 cm^{-1} peak. The DNA peaks, 785 and 1092 were of comparable intensities in both stallion and human sperms (**Table 6.6, Table 6.9 and Table 6.11**). The intensity of 785 cm^{-1} increased slightly after membrane damage in stallion cells but remained within the error range. The spectral intensity of the 1055 cm^{-1} and 1445 cm^{-1} peak are comparable and has less than 50% of the 785 peak height. Process related changes in their peak intensities were observed.

Abnormal human sperms from infertile men and abnormal protamine ratios were studied in the paper by Husar et al [68]. The Raman spectra were acquired from sperm cell nucleus on quartz coverslips with a 488 nm laser source. The spectra were not from intact sperm head, but were maps from regions of the membrane-free content. As a result, the spectra and their ratios are different from that of whole trapped cells, even though the spectra were normalised to the 1092 cm^{-1} peak. So a simple comparison between the two studies is not possible. Since abnormal cells were not studied in this research, it is not possible to make direct comparison.

Raman mapping using a 532 nm laser beam of healthy human cells smeared on cover slips were used to study different parts of the sperm. The impact of UV damage at different fluence was also investigated by Meister et al [15]. The Raman spectra from the nucleus and midpiece had different signatures. The Raman map shows a nuclear size of ~ 3 μm. The result of UV exposure shows the high stability of the 1092 cm^{-1} peak compared to the other bands in the spectra.

Mallidis et al [43] used a 633 He-Ne laser of 5 mW to study air dried smeared human sperms. The sample preparation is similar to that of Meister's. Both PCA and wavelet analysis were used to analyse the spectra from air dried and UV damaged

cells. The spectral signatures of the cell nucleus, tail and acrosome region were different. The DNA intensity dropped in the acrosome region. In this study, the first two PCs accounted for 25% of the total variations in the spectra. The post UV exposure samples have a pronounced peak at 1050 nm, which is not found in Meister et al paper. There is also large change in the 1092 peak compared to the 785 peak. The spectral processing technique is not clarified in the paper.

Another recent paper by Mallidis et al [67], explores oxidative stress damage to human sperm DNA using Raman and FTIR and compares it with biochemical assay tests, namely SCSA. The spectra were obtained on air-dried specimen. The intensity normalisation was done on the minimum and maximum intensity range. The band at 1050 is present in the spectra. A similar peak was not found in the human and stallion spectra analysed in this thesis. A broad band of peaks are present in the 1050 cm^{-1} to 1080 cm^{-1} range. While the optical path can suppress certain bands/peaks, such a sharp resolved peak is also not reported in the papers by Meister [15] or Li [41]. The band intensity ratios reported in the paper could not be reproduced in this research, nor was there any significant change in the band intensities in stallion and human sperms.

The organisation of the vast DNA-protein complex in the sperm head which is a small fraction of the size of the large egg has been difficult to study; molecular level study of the cell nuclear structure is about two decades old. The sperm chromatin is tightly packaged into near crystalline structure [9]. There is a need to use multiple complementary techniques to study the cellular response to stress and damage mechanism. Unless such detailed studies are repeated, the stallion to stallion and within stallion variation in the sperm response to cryopreservation protocols or spectroscopy will remain a mystery.

Reference

1. McCreery, R.L., *Raman Spectroscopy for Chemical Analysis*. Vol. 157. 2000: John Wiley and Sons. 420.
2. Movileanu, L., J.M. Benevides, and G.J. Thomas, *Temperature Dependence of the Raman Spectrum of DNA. Part I—Raman Signatures of Premelting and Melting Transitions of poly(dA–dT)·poly(dA–dT).* Journal of Raman Spectroscopy, 1999. **30**(8): p. 637-649.
3. Chan, J.W., et al., *Monitoring dynamic protein expression in living E. coli. Bacterial cells by laser tweezers Raman spectroscopy.* Cytometry Part A, 2007. **71A**(7): p. 468-474.
4. Moritz, T.J., et al., *Characterisation of FXTAS related isolated intranuclear protein inclusions using laser tweezers Raman spectroscopy.* J of Raman Spectroscopy, 2010. **41**(1): p. 33.
5. Moritz, T.J., et al., *Evaluation of Escherichia coli Cell Response to Antibiotic Treatment by Use of Raman Spectroscopy with Laser Tweezers.* Journal of Clinical Microbiology, 2010. **48**(11): p. 4287-4290.
6. Pagba, C.V., S.M. Lane, and S. Wachsmann-Hogiu, *Conformational changes in quadruplex oligonucleotide structures probed by Raman spectroscopy.* Biomed. Opt. Express, 2011. **2**(2): p. 207-217.
7. Gebauer, M.R., B.W. Pickett, and E.E. Swierstra, *Reproductive Physiology of the Stallion. II. Daily Production and Output of Sperm.* Journal of Animal Science, 1974. **39**(4): p. 732-736.
8. Balhorn, R., et al., *Applications of X-Ray Microscopy to the Analysis of Sperm Chromatin.* 1998.
9. Blanc, N.S., et al., *DNA in Human and Stallion Spermatozoa Forms Local Hexagonal Packing with Twist and Many Defects.* Journal of Structural Biology 2001. **134**: p. 76-81.
10. Balhorn, R., *The protamine family of sperm nuclear proteins.* Genome Biology, 2007. **8** (9): p. 227.
11. Alberts, B., et al., *Molecular Biology of The Cell*. Fourth ed. 2002, New York: Garland Science.
12. Martins, R.P. and S.A. Krawetz, *Nuclear Organisation of the protamine locus.* Society of Reproduction and Fertility Supplement, 2007. **64**: p. 1-12.
13. Kupker, W., W. Schulze, and K. Diedrich, *Ultrastructure of gametes and intracytoplasmic sperm injection: the significance of sperm morphology.* Human Reproduction, 1998. **13**: p. 99 - 106.
14. Lee, J.D., M.J. Allen, and R. Balhorn, *Atomic force microscope analysis of chromatin volumes in human sperm with head-shape abnormalities.* Biology of Reproduction, 1997. **56**(1): p. 42-49.
15. Meister, K., et al., *Confocal Raman microspectroscopy as an analytical tool to assess the mitochondrial status in human spermatozoa.* Analyst, 2010. **135**(6): p. 1370-1374.
16. Huser, T., et al., *Raman spectroscopy of DNA packaging in individual human sperm cells distinguishes normal from abnormal cells.* Journal of Biophotonics, 2009. **2**(5): p. 322-332.
17. Balhorn, R., et al. (1998) *Applications of X-Ray Microscopy to the Analysis of Sperm Chromatin*. 18.
18. Konig, K., et al., *Cell damage in near-infrared multimode optical traps as a result of multiphoton absorption.* Optics Letters, 1996. **21**: p. 1090.
19. Puppels, G.J., et al., *Studying single living cells and chromosomes by confocal Raman microspectroscopy.* Nature., 1990. **347**(6290): p. 301-3.
20. Puppels, G.J., et al., *Laser irradiation and Raman spectroscopy of single living cells and chromosomes: Sample degradation occurs with 514.5 nm but not with 660 nm laser light.* Experimental Cell Research, 1991. **195**(2): p. 361-367.
21. Konig, K., et al., *Effects of ultraviolet exposure and near infrared laser tweezers on human spermatozoa.* Human Reproduction, 1996. **11**(10): p. 2162-2164.
22. Liang, H., et al., *Wavelength dependence of cell cloning efficiency after optical trapping.* Biophysical journal, 1996. **70**(3): p. 1529-1533.
23. Neuman, K.C., et al., *Characterization of Photodamage to Escherichia coli in Optical Traps.* Biophysical Journal, 1999. **77**(5): p. 2856-2863.

24. König, K., et al., *Pulse-length dependence of cellular response to intense near-infrared laser pulses in multiphoton microscopes.* Optics Letters, 1999. **24**(2): p. 113-115.
25. König, K., et al., *Determination of motility forces of human spermatozoa using an 800 nm optical trap.* Cellular and Molecular Biology (Noisy-le-grand) 1996. **42**(4): p. 501-9.
26. Duguid, J., et al., *Raman spectroscopy of DNA-metal complexes. I. Interactions and conformational effects of the divalent cations: Mg, Ca, Sr, Ba, Mn, Co, Ni, Cu, Pd, and Cd.* Biophysical Journal, 1993. **65**(5): p. 1916-1928.
27. Benevides, J.M. and J. G.J. Thomas, *Characterization of DNA structures by Raman spectroscopy: high-salt and low-salt forms of double heical poly(dG-dQ in H21 and D20 solutions and application to B, Z and A-DNA*.* Nucleic Acids Research, 1983. **11**(16).
28. Benevides, J.M., et al., *The Raman spectra of left-handed DNA oligomers incorporating adenine-thymine base pairs.* Nucleic Acids Research, 1984. **12**(14): p. 5913-5925.
29. Thomas Jr, G.J., *Raman Spectroscopy of Protein and Nucleic Acid Assemblies.* Annual Review of Biophysics and Biomolecular Structure, 1999. **28**: p. 1-27.
30. Alla, S., et al., *Raman spectroscopic study of calf thymus DNA: an effect of proton- and gamma-irradiation.* Journal of Raman Spectroscopy, 2007. **38**(11): p. 1406-1415.
31. Duguid, J.G., et al., *DNA melting investigated by differential scanning calorimetry and Raman spectroscopy.* Biophysical Journal, 1996. **71**(6): p. 3350-3360.
32. Ke, W., D. Yu, and J. Wu, *Raman spectroscopic study of the influence on herring sperm DNA of heat treatment and ultraviolet radiation.* Spectrochimica Acta Part A: Molecular and Biomolecular Spectroscopy, 1999. **55**(5): p. 1081-1090.
33. Tang, Y.-L. and Z.-Y. Guo, *Raman Spectroscopic Analysis of the Effect of Ultraviolet Irradiation on Calf Thymus DNA.* Acta Biochimica et Biophysica Sinica, 2005. **37**(1): p. 39-46.
34. Baumber, J., et al., *Reactive Oxygen Species and Cryopreservation Promote DNA Fragmentation in Equine Spermatozoa.* Journal of Andrology, 2003. **24**(4): p. 621-628.
35. Langdon, W.C., *A comparative study on equine sperm chromatin using the Sperm Chromatin Structure Assay and the Sperm-Halomax kit®* in *ANIMAL SCIENCE* 2012, Texas Tech University Lubbock p. 74.
36. Kuster, C.E., R.S. Singer, and G.C. Althouse, *Determining sample size for the morphological assessment of sperm.* Theriogenology, 2004. **61**(4): p. 691-703.
37. Moreno, M., et al., *Raman Spectroscopy Study of Breast Disease.* Theoretical Chemical Association, 2009: p. 1-6.
38. Matthews, Q., et al., *Variability in Raman Spectra of Single Human Tumor Cells Cultured in Vitro: Correlation with Cell Cycle and Culture Confluency.* Appl. Spectrosc., 2010. **64**(8): p. 871-887.
39. Das, K., et al., *Raman Spectroscopy of Parathyroid Tissue Pathology.* Lasers in Medical Science, 2006. **21**(2006): p. 192-197.
40. Hidalgo, M., et al., *Effect of sample size and staining methods on stallion sperm morphometry by the Sperm Class Analyzer.* Veterinary Medecine – Czech, 2005. **50**(1): p. 24-32.
41. Li, X.X., et al., *Protective Effects of Melatonin against Oxidative Stress in Flow Cytometry-sorted Buffalo Sperm.* Reproduction in Domestic Animals, 2011: p. 1-9.
42. Foote, R.H., *The history of artificial insemination: Selected notes and notables.* Journal of Animal Science, 2002. **80**(E-Suppl_2): p. 1-10.
43. Mallidis, C., et al., *In situ visualization of damaged DNA in human sperm by Raman microspectroscopy.* Human Reproduction, 2011. **26**(7): p. 1641-1649.
44. Garcia, B.M., et al., *The Mitochondria of Stallion Spermatozoa Are More Sensitive Than the Plasmalemma to Osmotic-Induced Stress: Role of c-Jun N-terminal Kinase (JNK) Pathway.* J Androl, 2012. **33**(1): p. 105-113.
45. Pommer, A.C., J. Rutllant, and S.A. Meyers, *The role of osmotic resistance on equine spermatozoal function.* Theriogenology, 2002. **58**(7): p. 1373-1384.
46. Burnaugh, L., et al., *Osmotic stress stimulates generation of superoxide anion by spermatozoa in horses.* Animal Reproduction Science, 2010. **117**(3): p. 249-260.
47. Berndtson, W.E., B.W. Pickett, and T.M. Nett, *Reproductive Physiology of the Stallion IV. Seasonal Changes in the Testosterone Concentration of the Peripheral Plasma.* The Journal of the Society for Reproduction and Fertility, 1974. **39**: p. 115 - 118.

48. Bennetts, L.E. and R.J. Aitken, *A comparative study of oxidative DNA damage in mammalian spermatozoa.* . Molecular Reproduction and Development, 2005. **71**(1): p. 77-87.
49. Otto, C., et al., *A Raman scattering study of the helix-destabilizing gene-5 protein with adenine-containing nucleotides.* Nucl. Acids Res., 1987. **15**(18): p. 7605-7625.
50. Abondanzieri, E.A., J.W. Shaevitz, and S.M. Block, *Picocalorimetry of Transcription by RNA Polymerase.* Biophysical Letters, 2005: p. 61-63.
51. Liu, Y., et al., *Evidence for localized cell heating induced by infrared optical tweezers.* Biophysical Journal, 1995. **68**: p. 2137-2144.
52. Peterman, E.J.G., F. Gittes, and C.F. Schmidt, *Laser-Induced Heating in Optical Traps.* Biophysical Journal, 2003. **84**(2): p. 1308-1316.
53. Dasgupta, R., et al., *Hemoglobin degradation in human erythrocytes with long-duration near-infrared laser exposure in Raman optical tweezers.* Journal of Biomedical Optics, 2010. **15**(5): p. 055009-11.
54. Singh, G.P., et al., *Real-Time Detection of Hyperosmotic Stress Response in Optically Trapped Single Yeast Cells Using Raman Microspectroscopy.* Analytical Chemistry, 2005. **77**(8): p. 2564 - 2568.
55. World Health Organisation, ed. *WHO Laboratory Manual for the Examination of Human Semen and Sperm-Cervical Mucus Interaction*. 4 ed., ed. c. Published on behalf of the World Health Organization [by] Cambridge University Press. 1999, Cambridge University Press, UK, . 128.
56. Katila, T., *In vitro evaluation of frozen-thawed stallion semen: A review.* Acta vet Scand, 2001. **42**: p. 201 - 217.
57. Blach, E.L., et al., *Changes in quality of stallion spermatozoa during cryopreservation: Plasma membrane integrity and motion characteristics.* Theriogenology, 1989. **31**(2): p. 283-298.
58. Ortega Ferrusola, C., et al., *Lipid peroxidation, assessed with BODIPY-C11, increases after cryopreservation of stallion spermatozoa, is stallion-dependent and is related to apoptotic-like changes.* Reproduction, 2009. **138**(1): p. 55-63.
59. Evenson, D.P., et al., *Utility of the sperm chromatin structure assay as a diagnostic and prognostic tool in the human fertility clinic.* Hum. Reprod., 1999. **14**(4): p. 1039-1049.
60. Aitken, R.J., et al., *Analysis of the relationships between oxidative stress, DNA damage and sperm vitality in a patient population: development of diagnostic criteria.* Human Reproduction, 2010. **25**(10): p. 2415-2426.
61. Ramos, L. and A.M.M. Wetzels, *Low rates of DNA fragmentation in selected motile human spermatozoa assessed by the TUNEL assay.* Human Reproduction, 2001. **16**(8): p. 1703-1707.
62. Aitken, R.J., et al., *The source and significance of DNA damage in human spermatozoa; a commentary on diagnostic strategies and straw man fallacies.* Molecular Human Reproduction, 2013. **19**(8): p. 475-485.
63. Gonzalez-Marín, C., J. Gosalvez, and R. Roy, *Types, Causes, Detection and Repair of DNA Fragmentation in Animal and Human Sperm Cells.* International Journal of Molecular Sciences, 2012. **13**(11): p. 14026-14052.
64. Zini, A., et al., *Is sperm dna damage associated with IVF embryo quality? A systematic review.* Journal of Assisted Reproduction and Genetics, 2011. **28**(5): p. 391-397.
65. Makhlouf, A.A. and C. Niederberger, *DNA Integrity Tests in Clinical Practice: It Is Not a Simple Matter of Black and White (or Red and Green).* Journal of Andrology, 2006. **27**(3): p. 316-323.
66. Aurich, C., *Factors affecting the plasma membrane function of cooled-stored stallion spermatozoa.* Animal Reproduction Science, 2005. **89**(1-4): p. 65-75.
67. Sanchez, V., et al., *Oxidative DNA damage in human sperm can be detected by Raman microspectroscopy.* Fertility and sterility, 2012. **98**(5): p. 1124-1129.e3.
68. Huser, T., et al., *Raman spectroscopy of DNA packaging in individual human sperm cells distinguishes normal from abnormal cells.* Journal of biophotonics, 2009. **2**(5): p. 322-32.

8

The Conclusion

When you reach the end of what you should know, you will be at the beginning of what you should sense.

Khalil Gibran (1883 – 1931)

8.0 The Conclusions

The inference that can be drawn from this research is summarised in **Section 8.1**. Limitations of the work is summarised in **Section 8.2**, the project contribution to knowledge is summarised in **Section 8.3** and scope for future work in **Section 8.4**.

8.1 Conclusions and Project Contribution to Knowledge

Stallion Stress and Membrane Damage Study: The purpose of this experimental research was to investigate the feasibility of using laser tweezers and Raman spectroscopy combination to trap single live motile sperm cells and obtain the spectral fingerprint of the cell nuclear DNA without destroying the cell or damaging it. It was also anticipated that the spectra would be sensitive to various types and grades of applied chemical stress and differentiate between the induced DNA fragmentation.

Can the LTRS be used to trap single live motile sperms and obtain its spectral fingerprint without destroying the cell or damaging it?

The low power LTRS was successfully adapted to trap and obtain Raman spectra of motile stallion and human sperm cells in suspension (in sperm friendly media like BWW and Pure sperm). Strong Raman signals were obtained with exposure times of 20 to 30 seconds. The motile cells remained motile and swam away after several minutes of trapping. Hence it can be concluded that the LTRS does not destroy the trapped cells.

It has not been possible to verify conclusively, if the LTRS caused molecular level damage to the cellular DNA. Further tests using established and highly sensitive biochemical techniques will have to be completed before any conclusions can be made on the affect of trapping at the molecular level, on sperm DNA health.

Is the Raman spectrum sensitive to the different degrees of applied osmotic and oxidative stress? Can Raman spectra separate membrane damaged and fresh cells?

The Raman spectra from the stallion sperms have shown different responses to the applied osmotic and oxidative stress of different grades. There is high variability within each specimen and this variability is found in the specimens from the same stallion. The LTRS results support the findings from many other studies on stallion sperm cryopreservation and stress damage protocols discussed elsewhere in the thesis:

- there is considerable variability in the cellular response to the applied stress
- the variability is observed in the cells from the same stallion and in the cells from different stallions
- the variability is found in the cells collected in winter and in summer
- a single biochemical stress procedure produces different responses in different stallion ejaculates

PCA of the Raman spectra from sperms exposed to membrane damage was used to separate fresh and membrane damaged cells in the four stallion ejaculates investigated. The amount of separation or clustering varied between the ejaculates. The membrane damage protocol was not tested on other ejaculates from the same stallion. Human sperms, on the other hand, appeared more sensitive to the cell categories (fresh, disintegration, frozen, swim-up etc.) and applied stress.

8.2 Limitations of the Research

- The specimen used to do the detailed feasibility study – stallion sperm cells, has naturally inherent variability within and between stallions. Such high variability in the test specimens make it difficult to assess the spectral sensitivity to the parameters being tested – in this case, three grades of osmotic stress and four grades of oxidative stress.

- The sample size used in this research was small. The use of short life specimens coupled with manual data acquisition and analysis restricted the number of cells that could be studied to 20 to 40 cells per variable tested.

- Lack of complementary tests to analyse the nature of damage within the specimens under study. Example: If osmotic stress only damages mitochondria in the sperm midpiece, the Raman spectra of the sperm head will remain unresponsive to the applied stress.

- Biochemical tests and molecular level knowledge of the tiny sperm cells are still in their infancy; further detailed studies with multiple experts on sperms are needed before Raman spectral sensitivity to DNA damage can provide useful information.

- There was no information on the sperm health, fertility potential or health status of the stallions during sperm collection.

- The experiments could not be repeated in the same season

- Laser trap induced cellular changes in the stallion cells could not be investigated.

8.3 What is the research contribution to knowledge?

To the best of our knowledge, this is the first research on the use of low power NIR lasers to study live motile stallion sperms and test them for response to different grades of chemically applied stress.

With the use of PCA of Raman spectra, it has been possible to show that the variability in the cellular response from each ejaculate, whether from the same stallion or different stallions, dwarf the results from the stress damage tests. This outcome was reproduced in two independent studies in this research, even though the sample size was small.

This outcome supports the findings from other research on the stallion cells, namely - stallion sperm cells have high variability in their cellular response to biochemical treatments like cryopreservation protocols. A single protocol produces different responses in difference ejaculates from the same and different stallions. The protocols are tweaked for each stallion; this can be costly and time consuming.

The 785 nm 25mW single mode laser is capable of trapping motile cells by the head to obtain strong Raman signals in a few seconds. These signals correlate with the Raman signals from dense calf thymus DNA that was researched in the early days of Raman spectroscopy applications in biological specimens.

The Raman signal is captured from the densest region of the sperm head and there is little contribution to the signal from other parts of the cell. This conclusion is based on both the geometry of the cell trapping optics and the absence of signal from the midpiece, which is the top part of the flagella and close to the head.

The cells did not suffer motility degradation after several minutes of trapping; however molecular level degradation has not been explored so it has to be established through independent studies, if healthy stallion cells suffer damage through the low power trapping environment.

There was distinct ejaculate contribution to the applied stress and membrane damage on the sperm cells that did not show any preference by stallion. This was observed in the two independent studies conducted in early winter and mid-summer.

Why is such a study important?

Such a technique, if it can be established will play a critical role in examining the molecular level health of sperm DNA and its contribution to pregnancy outcome. Several highly sensitive biochemical assays have been in existence for several decades, to test various molecular structures within cells. Many of these assays have been modified to analyse sperm molecular structure and its DNA health. These are time consuming, labour intensive and require highly skilled and experienced people to successfully perform the experiments and interpret the results. There is

considerable variability in the results from the various techniques used and it is uncertain if the various techniques are testing the same molecular structures within the complex and highly resistant architecture of the sperm nucleus. A fast and simple technique, such as the use of LTRS would be a critical and welcome alternative to the lengthy and complex test procedures currently in use.

It is impossible to carry out these biochemical tests, without adding additional damage to the cell and possibly the nucleus and DNA. While no measurement technique is free from interacting with the material under investigation, the least invasive technique is most useful.

Raman spectroscopy using NIR lasers comes close to meeting such criteria and plays a major role in molecular and structural biology, medicine and lives cell monitoring. The use of laser trap and Raman spectroscopy for testing biological specimens and monitoring cell metabolic function is still in the research stage. If laser trap induced cell damage can be minimised to less than that induced during biochemical testing, then this fast and easy technique can be used to analyse cryopreservation protocols and other routine tests used to assess sperm health and its response to various test environment.

8.4 Scope for Future Research

Sperm DNA quality is integral to the successful reproductive outcome in mammals; the study of live sperm DNA quality is not only useful in gaining molecular level scientific knowledge, but it is also useful in the research related to preservation of the dying species. Sperm DNA damage is also implicated in human infertility, which is on the rise. Study of sperm DNA quality is useful in AI research where labour saving techniques are used to increase products from dairy and cattle farming. Such simple, fast, and easy techniques to research sperm and other cellular DNA health are in demand.

Appendix

How will fare the world whose wonder
Was the very proof of me?

Walter John Dela Mare (1873 - 1956)

The following set of plots in **Figure 6.5a** to **Figure 6.5h** correspond to the analytical work on page 162, **section 6.2.1.1** in **Chapter Six.** These plots from a representative data group are used to show the variability in the raw spectra from the data groups in **Study One**.

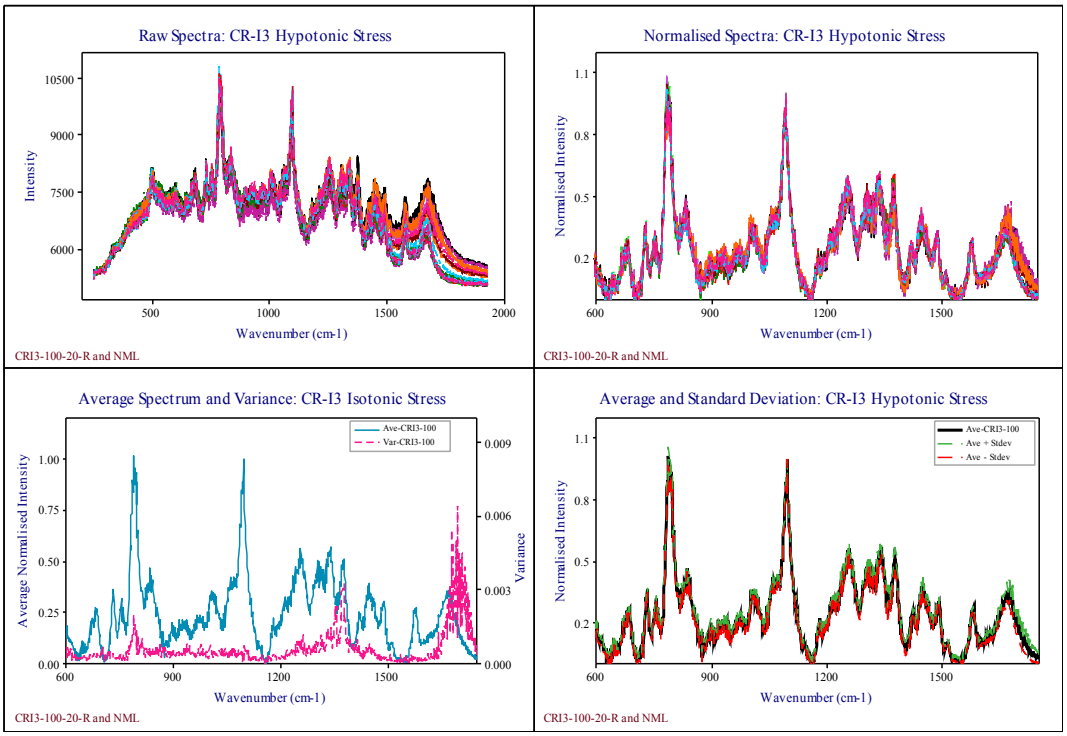

Figure 6.5a: **Hypotonic stress damage** study show spread in the raw and normalised spectra with maximum variance of ~ 0.003 in the ROI.

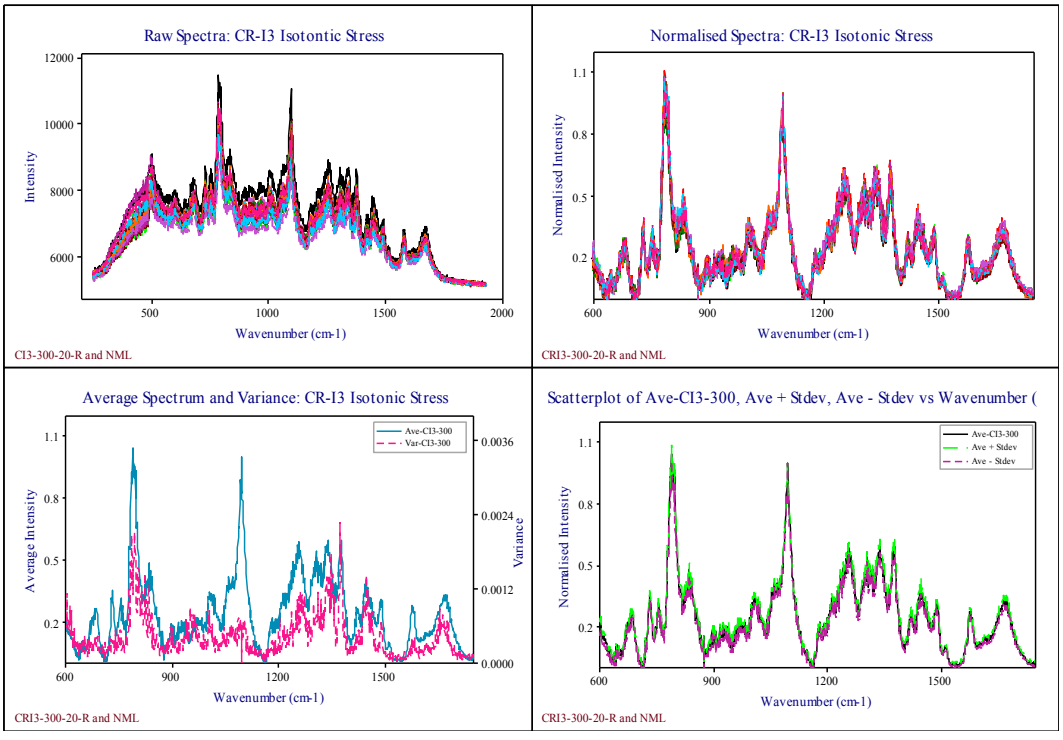

Figure 6.5b: **Isotonic stress damage** study show spread in the raw data and normalised spectra with maximum variance of ~ 0.0024 in the ROI.

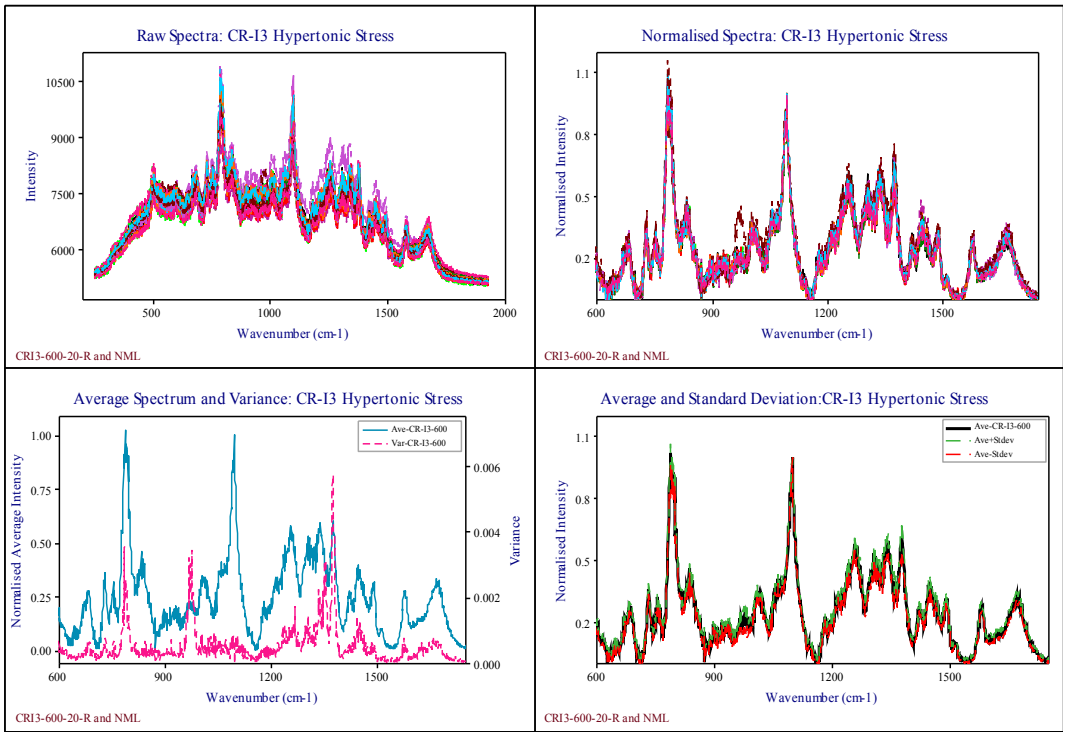

Figure 6.5c Hypertonic stress damage study show spread in the raw data and normalised spectra with maximum variance of ~ 0.006 in the ROI.

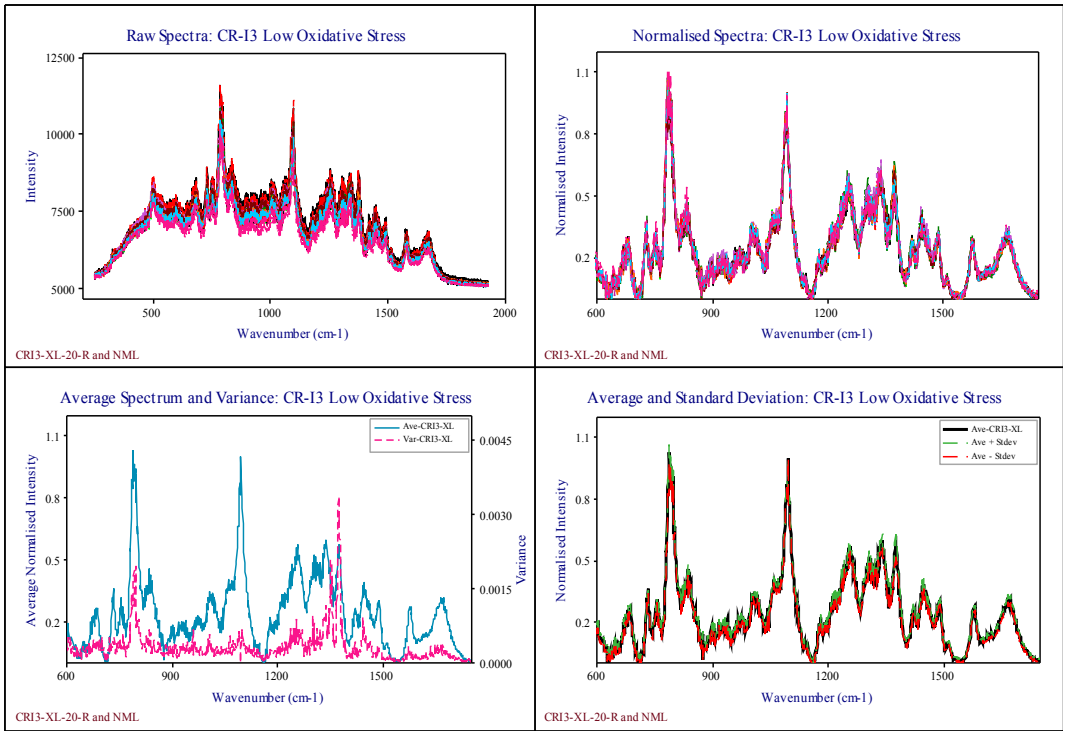

Figure 6.5d: Low Oxidative stress damage study show spread in the raw data and normalised spectra with maximum variance of ~ 0.003 in the ROI.

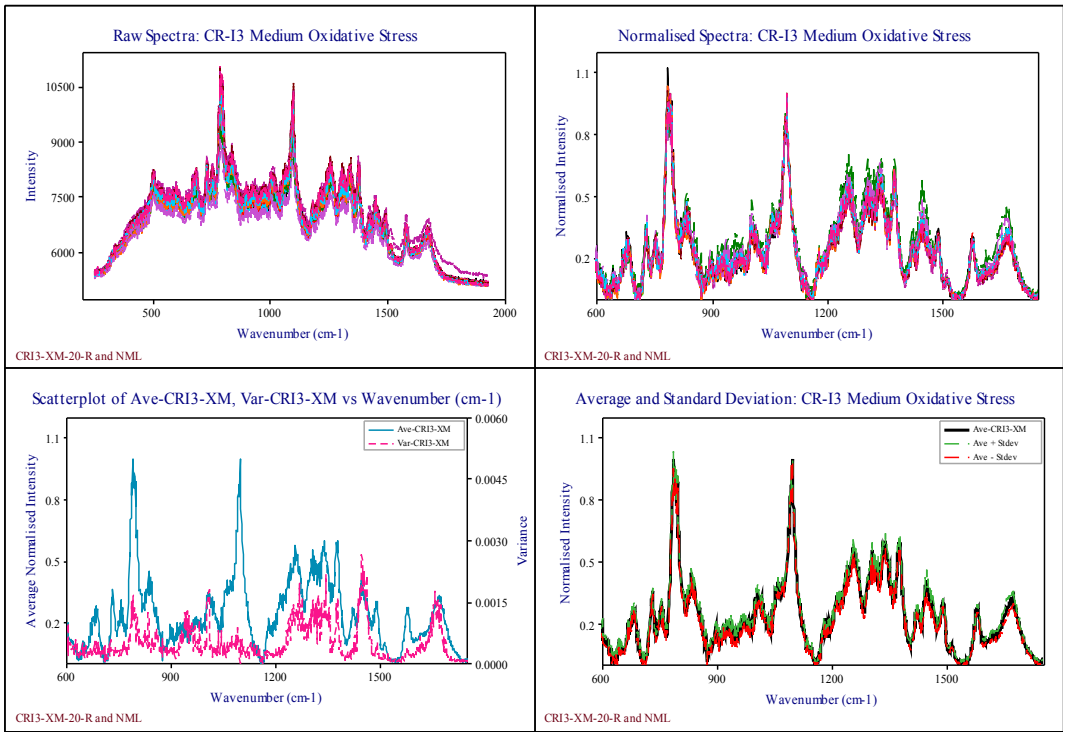

Figure 6.5e: **Medium Oxidative stress damage** study show spread in the raw and normalised spectra with maximum variance of ~ 0.003 in the ROI.

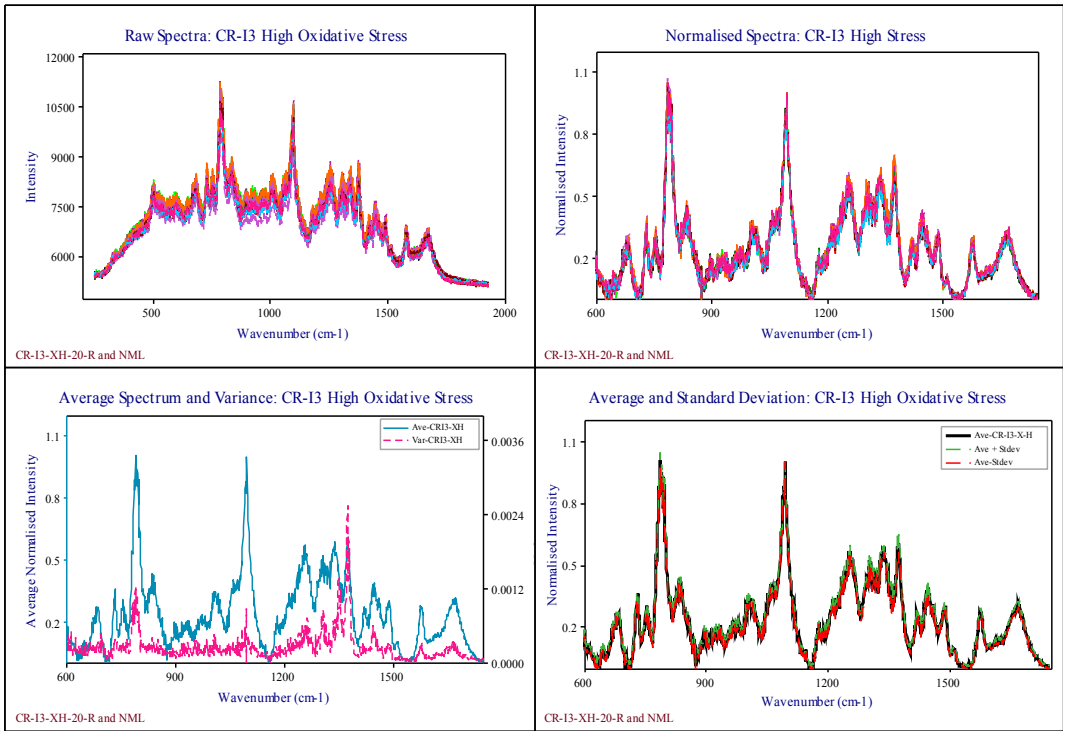

Figure 6.5f: **High Oxidative stress damage** study show spread in the raw and normalised spectra wih maximum variance of ~ 0.0024 in the ROI.

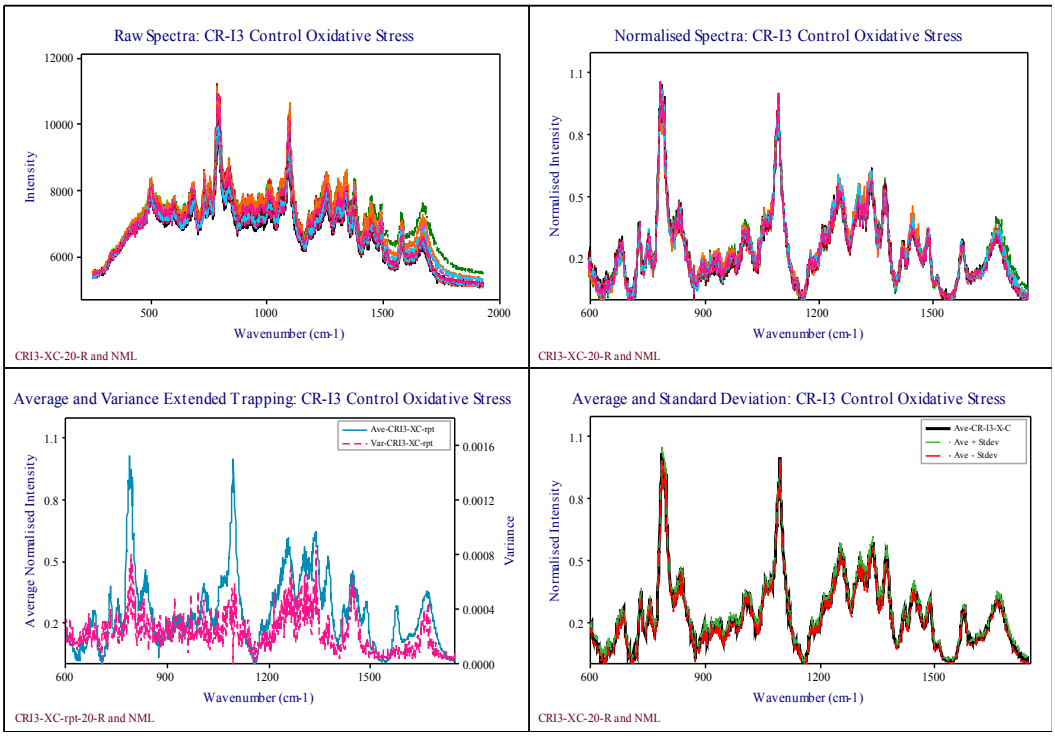

Figure 6.5g: **Control - Oxidative stress damage** study show spread in the raw and normalised spectra with maximum variance of ~ 0.0008 in the ROI.

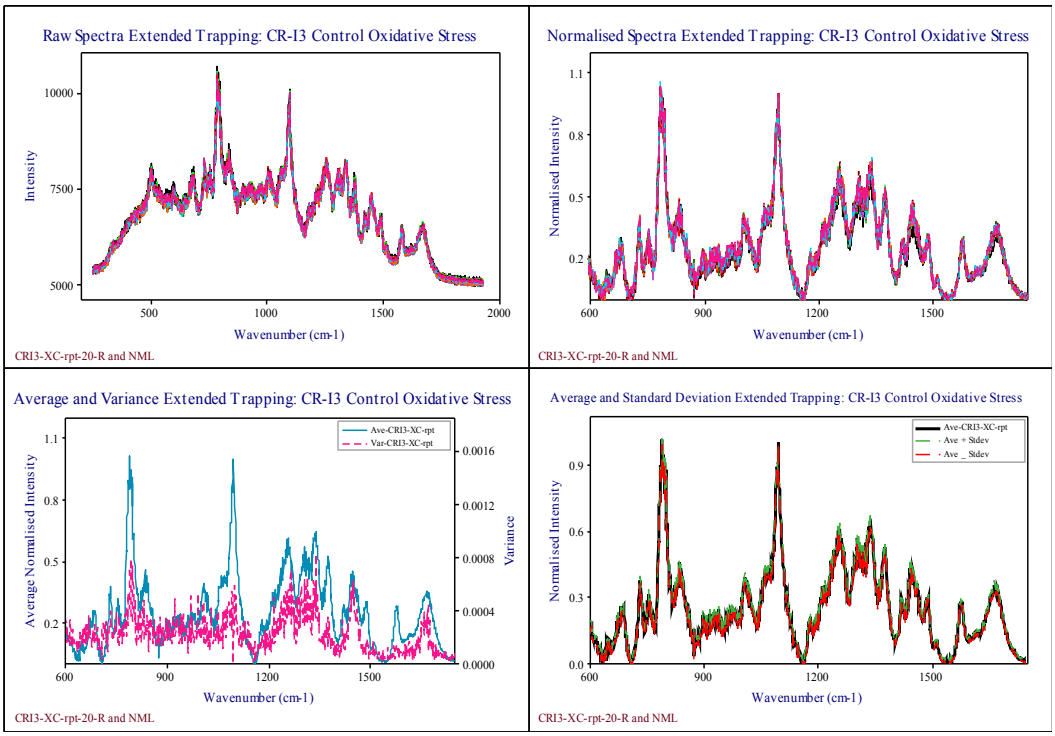

Figure 6.5h: Extended trapping study show spread in the raw and normalised spectra with maximum variance of ~ 0.0008 in the ROI.

The following set of plots in **Figure 6.10a** to **Figure 6.10h** correspond to the analytical work on page 187, **section 6.2.2.1** in **Chapter Six.** These plots were created to show the variability in the raw spectra from the data groups in **Study Two**.

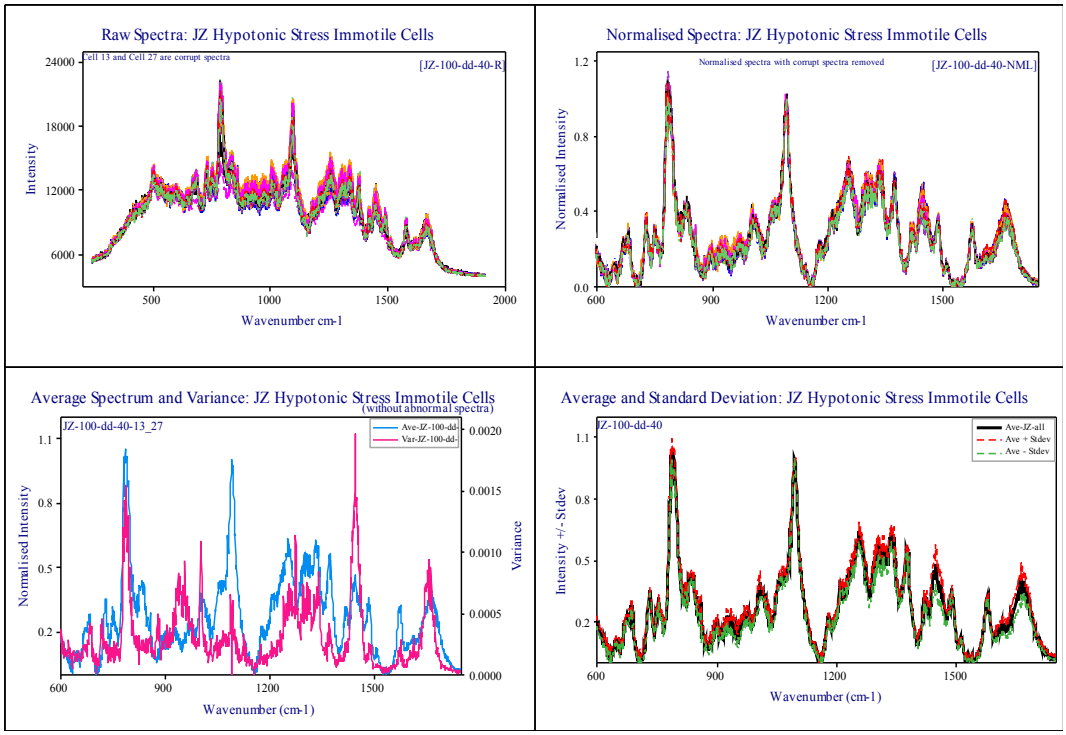

Figure 6.10a: Immotile cells from hypotonic stress damage study

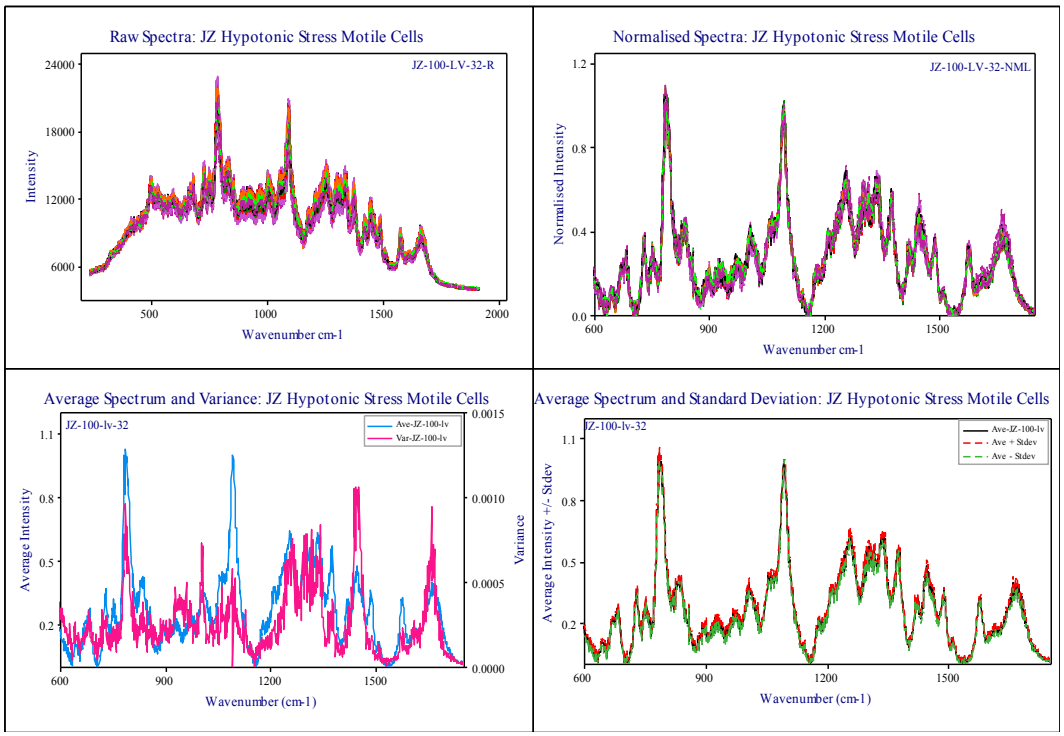

Figure 6.10b: Motile cells from Hypotonic Stress damage study

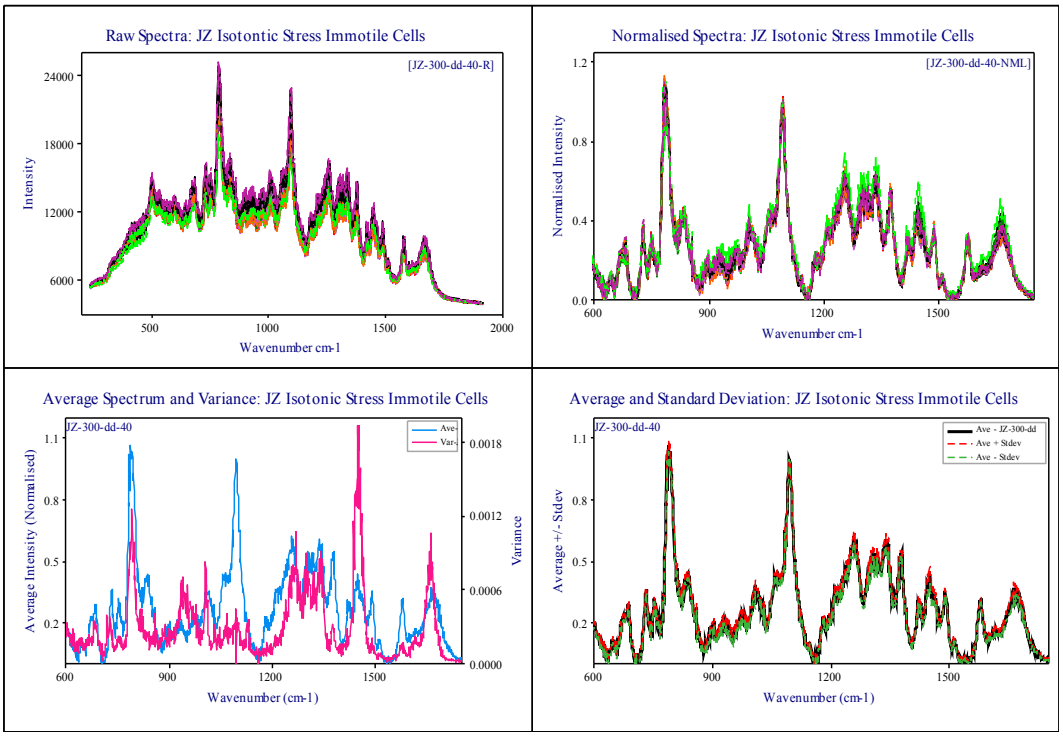

Figure 6.10c: Immotile cells from isotonic stress damage study

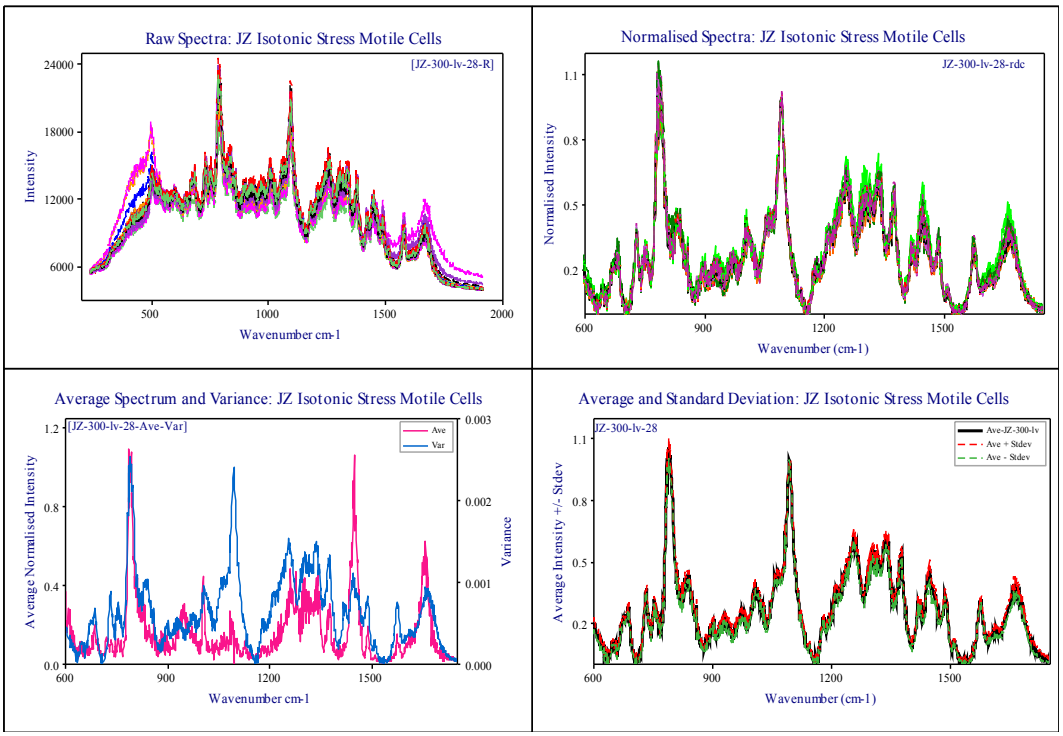

Figure 6.10d: Motile cells from isotonic stress damage study

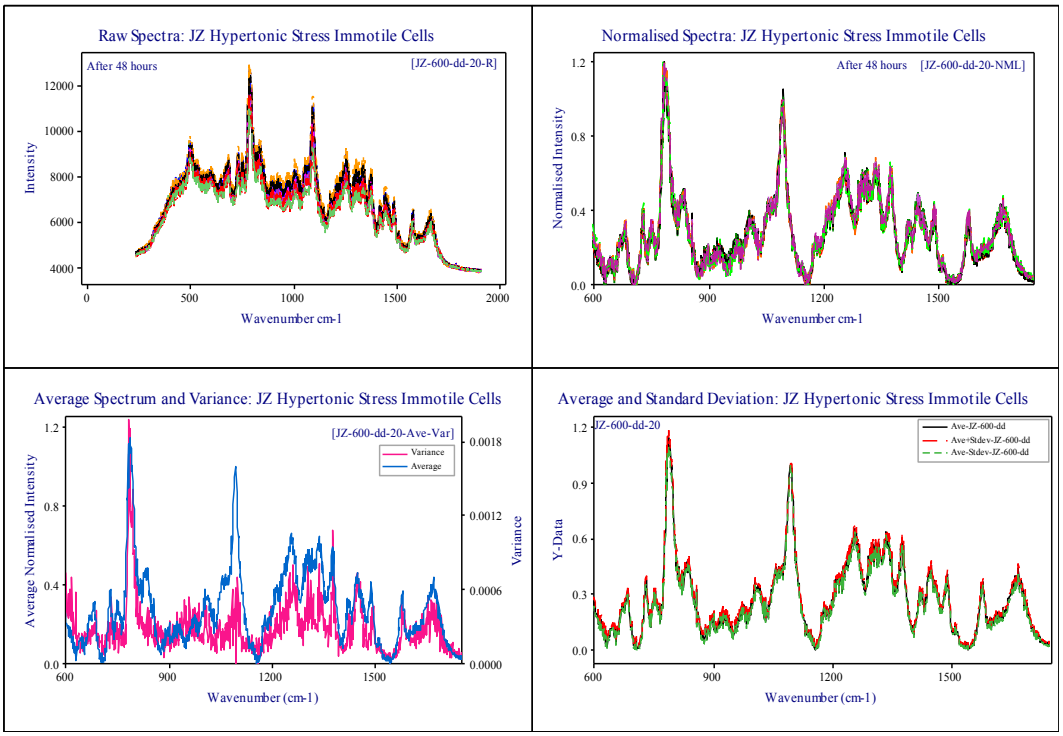

Figure 6.10e: Immotile cells from hypertonic stress damage study

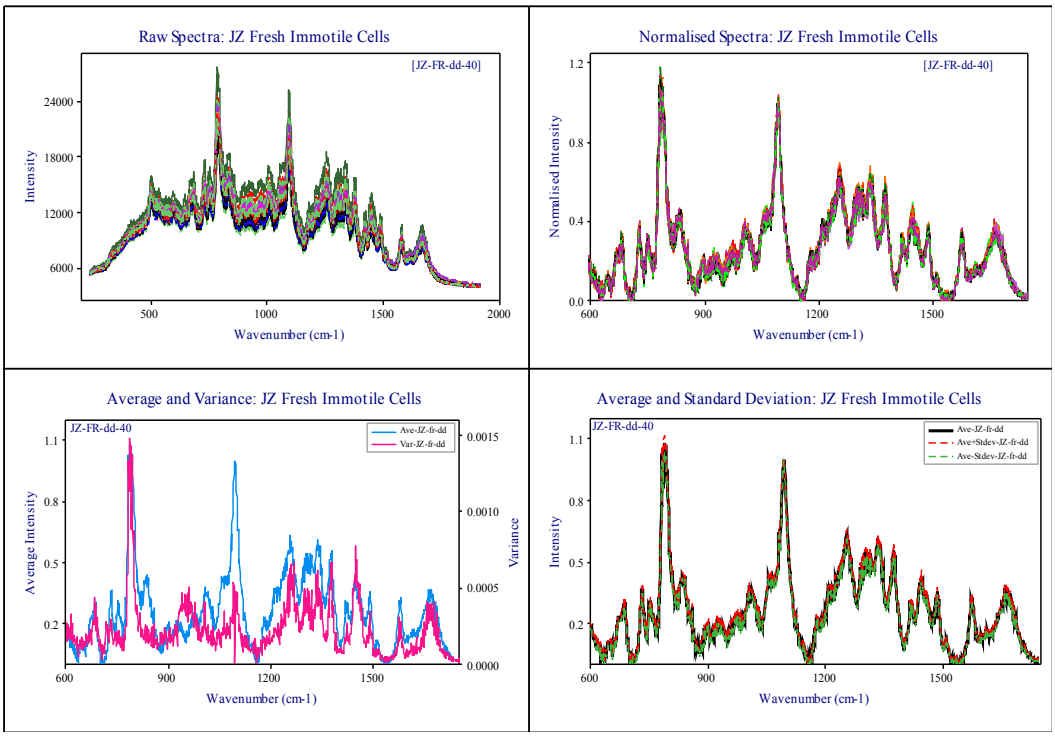

Figure 6.10f: Immotile cells from freshly prepared cells

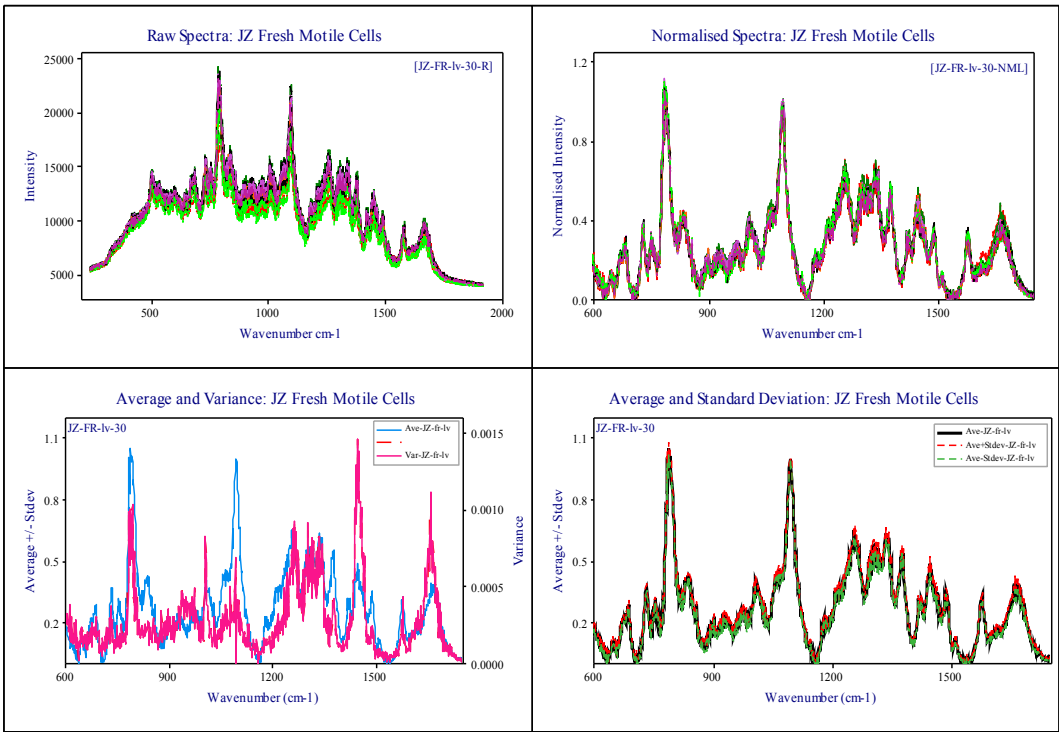

Figure 6.10g: Motile cells from freshly prepared cells

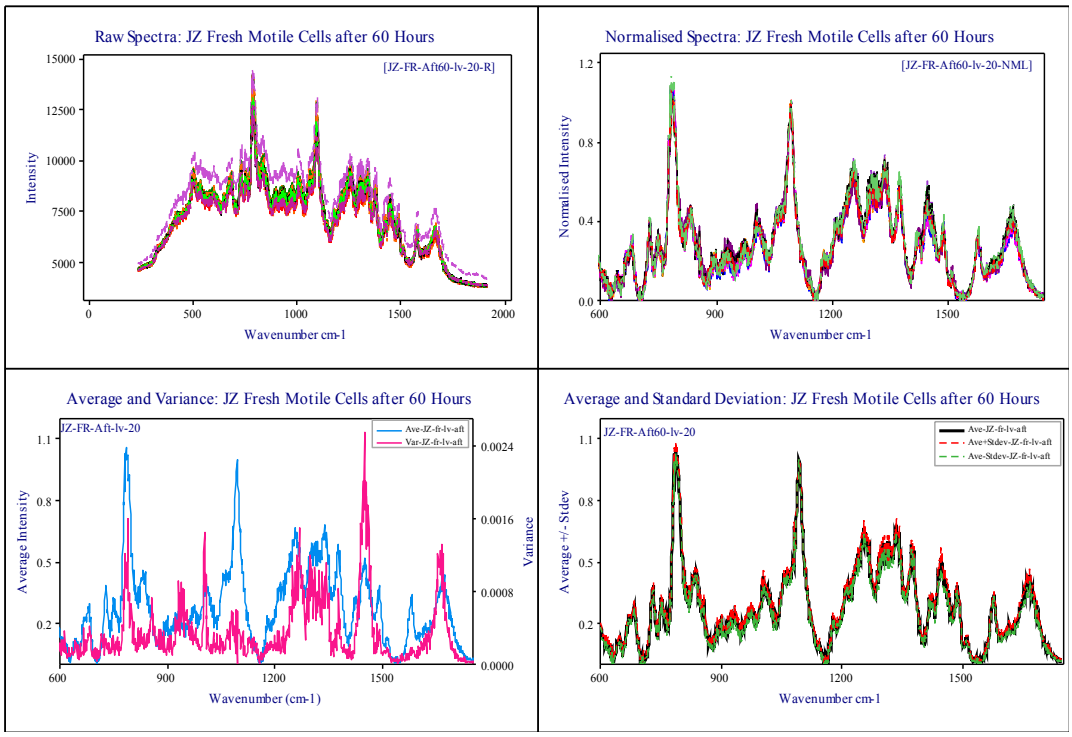

Figure 6.10h: Motile cells from freshly prepared samples after 60 hours

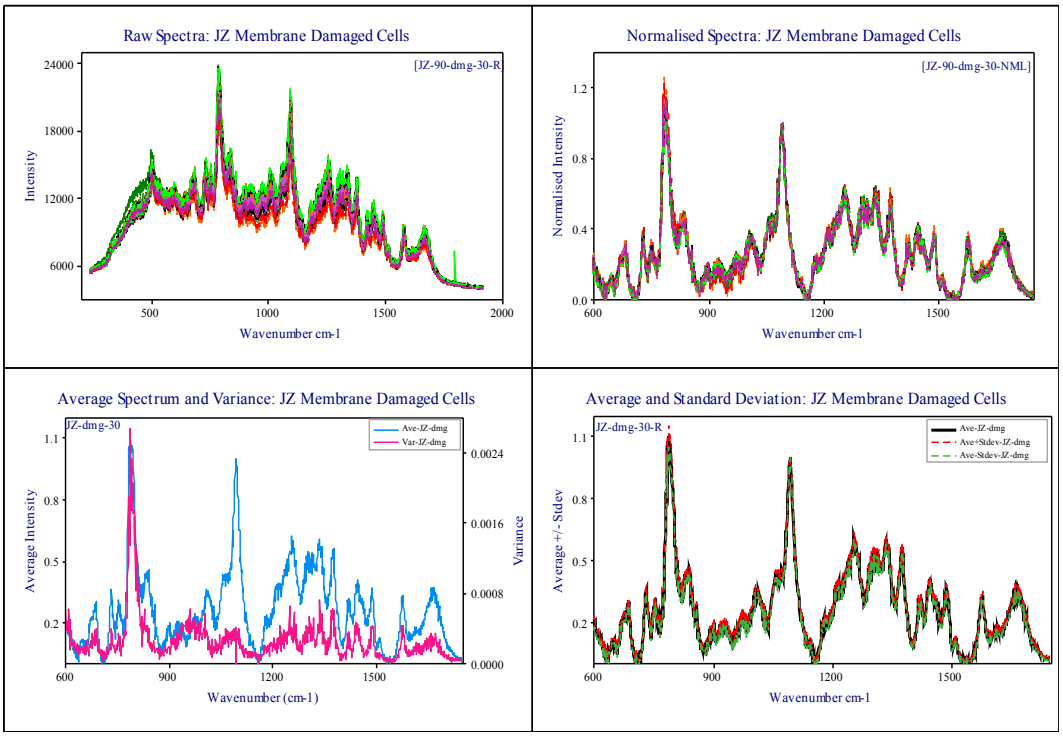

Figure 6.10i: Immotile cells from membrane damage study

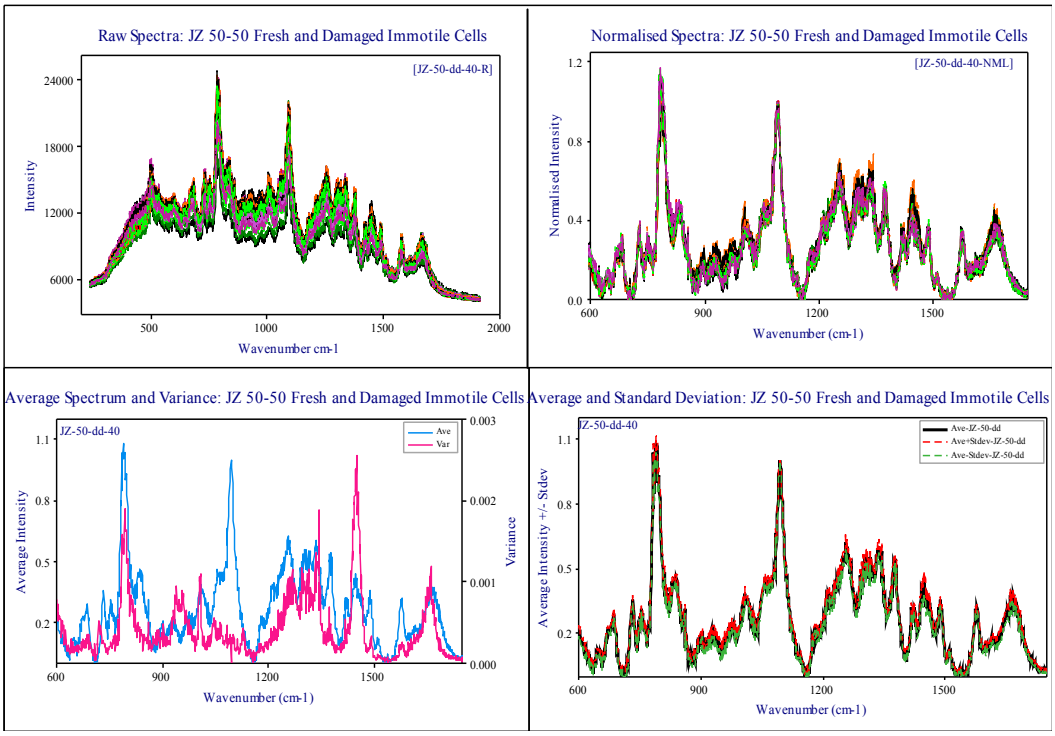

Figure 6.10j: Immotile cells from 50-50 mixture of fresh and damaged cells

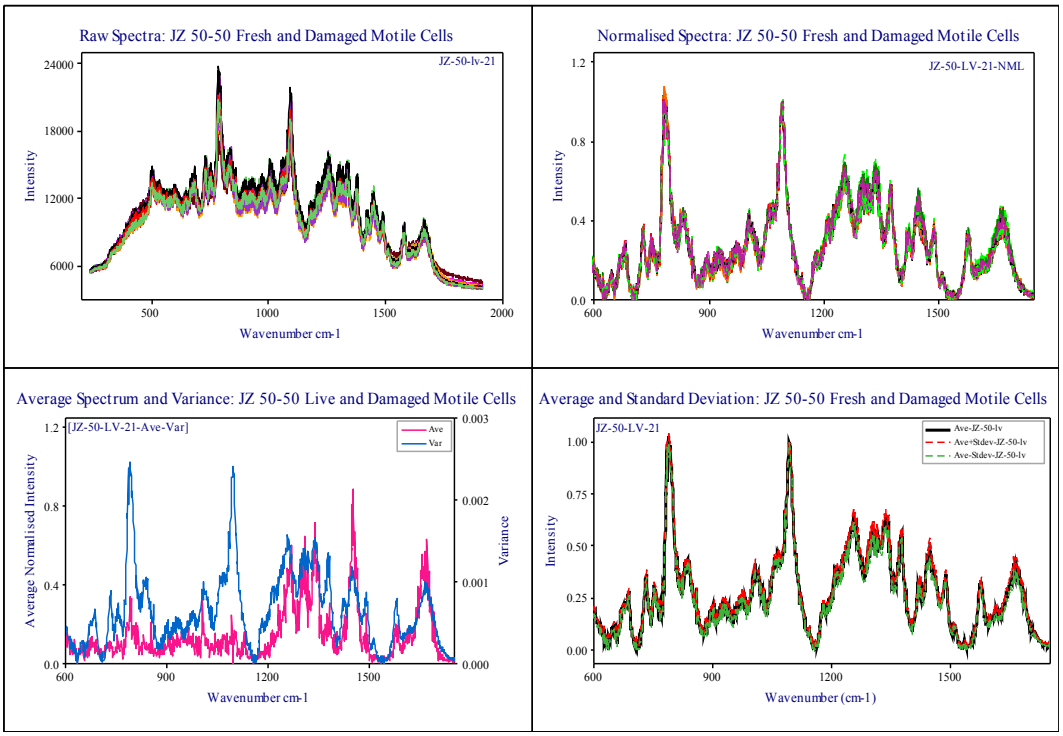

Figure 6.10k: Motile cells from 50-50 mixture of fresh and damaged cells

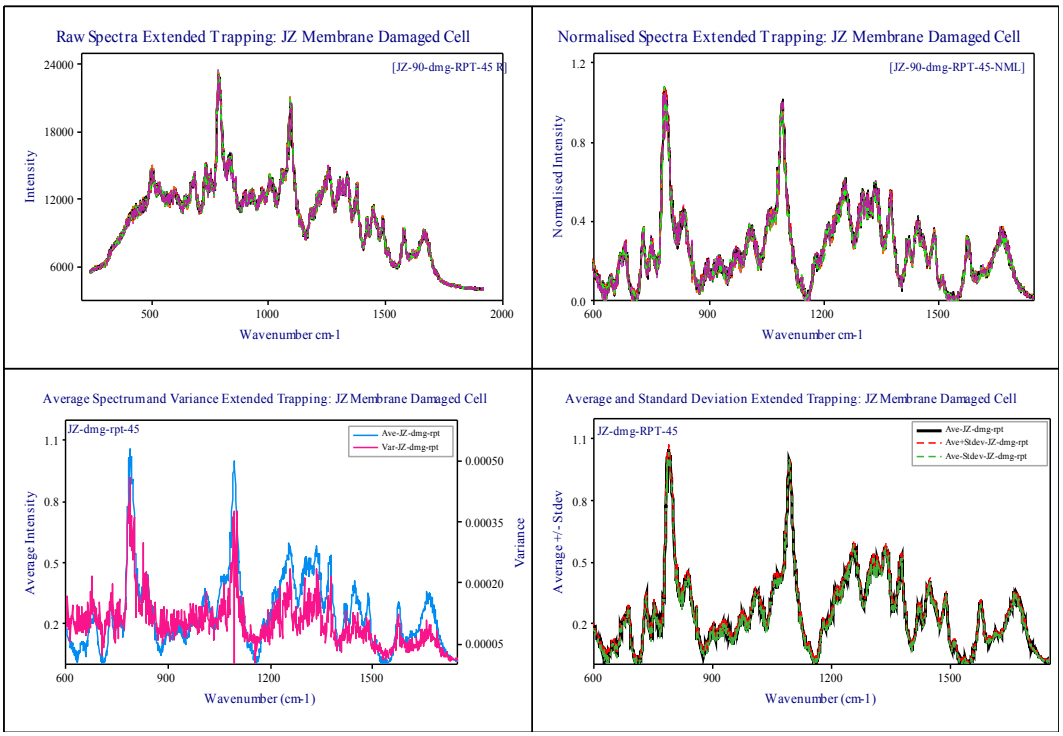

Figure 6.10l: Extended trapping: membrane damage study

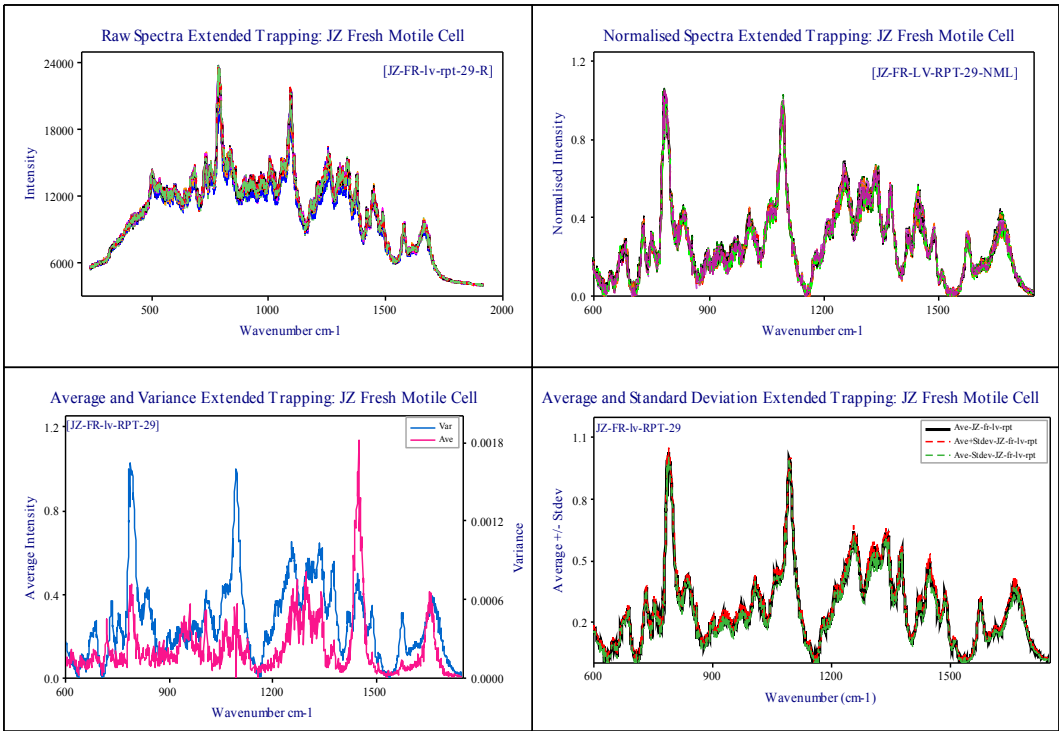

Figure 6.10m: Extended trapping: Fresh motile